THESIS DISSERTATION

Mitigating Lithium-Ion Battery Aging: Physics-Based State Estimation, Aging Prediction, and Degradation-aware Control Strategies

IKER LOPETEGI TAPIA

APRIL 2024

PHD PROGRAM IN

APPLIED ENGINEERING

Mitigating Lithium-Ion Battery Aging: Physics-Based State Estimation, Aging Prediction, and Degradation-aware Control Strategies

PhD Dissertation Presented in

MONDRAGON UNIBERTSITATEA

as Part of the PhD Program in

APPLIED ENGINEERING

Presented by

IKER LOPETEGI TAPIA

Directed by

DR. UNAI IRAOLA

Codirected by

DR. EDUARDO MIGUEL

In HERNANI, APRIL 2024

ABSTRACT

Lithium-ion batteries are the most widely adopted energy storage system (ESS) nowadays. Due to their high gravimetric and volumetric energy density, and their low self-discharge rate, they are the best option for many applications, such as consumer electronics or electric vehicles (EVs). Yet, this technology still needs improvements to meet the demands of the energy transition. The relatively fast degradation that these batteries suffer is one of the main concerns with this ESS, and alongside the safety issues associated to it, the need for optimized and safe management is urgent.

This thesis aims to improve the management of lithium-ion batteries using advanced control algorithms based on physical knowledge to mitigate battery aging. For that, simplified and reduced-order physics-based models (PBMs) are employed, such as the P2D and SPMe models, which are believed to give relevant insight about the physicochemical phenomena happening inside batteries. Lithium-ion battery aging is analyzed, and PBMs are used to develop a reliable degradation model that could be used to develop advanced degradation-aware control algorithms. For that, a new parameterization approach is proposed and tested experimentally, which could be used to significantly reduce the number of experiments to obtain an accurate aging model. To estimate the physical states of the battery through battery lifetime, new state-of-charge (SOC) and state-of-health (SOH) estimation algorithms are developed, improving current battery diagnosis algorithms by providing accurate estimates of electrode-level degradation and internal variables. Lastly, combining the knowledge provided by the state and parameter estimator, and the predictions of the degradation model, a new fast charging control strategy is proposed based on a nonlinear model predictive control (NMPC) algorithm, resulting in faster charging and reduced aging.

The developed aging modeling approach, state and parameter estimation, and control strategy, demonstrate that PBMs can improve current empirical approaches, and help in the advance of new optimized battery algorithms; for battery aging prediction purposes, for battery health diagnosis, and for improved degradation-aware control strategies that mitigate aging.

LABURPENA

Gaur egun, litio-ioizko bateriak dira energia biltegiratzeko sistemarik erabiliena. Beren energia dentsitate grabimetriko eta bolumetriko altua, eta auto-deskarga tasa baxua tarteko, aplikazio askotarako aukerarik onena dira, hala nola kontsumo elektronikarako edota ibilgailu elektrikoetarako. Hala ere, trantsizio energetikoaren aldarriarekin bat egiteko teknologia honek badu zer hobetu. Bateria hauek jasaten duten degradazioa da egungo kezka nagusienetako bat. Horregatik, premiazkoa da beraien erabilera seguruago eta optimizatuago bat bilatzea.

Tesi honek litio-ioizko baterien kudeaketa hobetzea du helburu, baterien zahartzea arintzea ahalbideratzen duten ezagutza fisikoan oinarritutako kontrol algoritmoak erabiliz. Horretarako, ordena murriztuko eta sinplifikatutako bateria modelo fisikoak (PBM) erabili dira, hots, P2D eta SPMe izenez ezagutzen direnak. Hauek, baterien barruan gertatzen diren fenomeno fisiko-kimikoei buruzko informazio garrantzitsua ematen dute. Litio-ioizko baterien degradazioa aztertzeko, bateria eredu fisikoetan oinarritzen den degradazio modelo fidagarri bat doitu da, aurrerago kontrol algoritmo aurreratuen garapena ahalbideratu dezakeena. Horretarako, esperimentu kopurua nabarmen murriztu dezakeen parametrizazio prozesu berri bat proposatu eta bere zehaztasuna esperimentalki egiaztatu da. Horrez gain, bateriaren bizitzan zehar bere uneoroko egoeraren berri ematen duten aldagai fisikoak estimatzeko, karga (SOC) eta degradazio-egoeren (SOH) estimazio algoritmo berritzaileak garatu dira, egungo bateriaren diagnostiko algoritmoak hobetuz, eta elektrodo-mailako degradazioaren eta barne aldagai fisikoen estimazio zehatzak emanez. Azkenik, aldagai fisikoen estimatzaileak emandako ezagutza eta degradazio-modeloaren iragarpenak konbinatuz, karga azkarreko kontrol-estrategia berri bat proposatu da, "*nonlinear model predictive control*" (NMPC) algoritmoan oinarritzen dena. Modu honetan, karga denbora eta degradazioa, biak murriztea lortu da.

Tesi honetan proposatu eta garatu diren degradazio modeloak, bateriaren egoera eta parametro fisikoen estimazio prozesuak, eta karga-azkarrerako kontrol algoritmoak frogatzen dute PBMek, gaur egun erabiltzen diren modelo enpirikoen aldean, baterien erabilera seguruago eta optimoago baten bidean aurreratzen jarraitzea ahalbideratzen dutela; degradazio predikzio eta diagnosiarekin, eta baita degradazioa murrizteko kontrol estrategiak hobetuz.

RESUMEN

Las baterías de iones de litio son el sistema de almacenamiento de energía más adoptado en la actualidad. Debido a su alta densidad de energía, y su baja tasa de autodescarga, son la mejor opción para muchas aplicaciones, como la electrónica de consumo o los vehículos eléctricos. Sin embargo, esta tecnología aún necesita mejoras para satisfacer las demandas de la transición energética. La degradación relativamente rápida que sufren estas baterías es una de las principales preocupaciones y, junto con los problemas de seguridad asociados, es urgente la necesidad de una gestión optimizada y segura.

Esta tesis tiene como objetivo mejorar la gestión de baterías de litio utilizando algoritmos de control avanzados basados en el conocimiento físico para mitigar el envejecimiento de las baterías. Para ello, se emplean modelos basados en la física (PBM) simplificados y de orden reducido, concretamente los modelos P2D y SPMe, que brindan información relevante sobre los fenómenos fisicoquímicos que ocurren dentro de la batería. Se analiza el envejecimiento de las baterías de litio y se utilizan PBM para desarrollar un modelo de degradación preciso que podría usarse para desarrollar algoritmos avanzados de control. Para ello, se propone y valida experimentalmente un nuevo preoceso de parametrización, mediante el cual se podría reducir significativamente el número de experimentos y obtener un modelo de envejecimiento preciso. Además, para estimar los estados físicos de la batería a lo largo de su vida útil, se desarrollan nuevos algoritmos de estimación del estado de carga (SOC) y del estado de salud (SOH), que mejoran los algoritmos actuales de diagnóstico al proporcionar estimaciones precisas de la degradación a nivel de los electrodos y variables internas. Por último, combinando el conocimiento proporcionado por el estimador de estado y parámetros, y las predicciones del modelo de degradación, se propone una nueva estrategia de control de carga rápida basada en un algoritmo de control predictivo de modelo no lineal (NMPC), que da como resultado una carga más rápida y un menor envejecimiento.

El modelo de envejecimiento desarrollado en esta tesis, la estimación de estados y parámetros de la batería, y la estrategia de control propuesta demuestran que los PBM pueden mejorar los modelos empíricos actuales y ayudar en optimizar la gestión de las baterías; mediante la predicción del envejecimiento, diagnóstico del estado y estrategias de control optimizadas que mitiguen de la degradación.

ACKNOWLEDGEMENTS

I would like to start thanking my supervisors Unai Iraola Iriondo and Eduardo Miguel Garcia de Cortazar for their guidance and support throughout this thesis. You have been an indispensable part of this work, and I will always be thankful to you for giving me the chance to perform this research.

I would like to express my deepest gratitude to Prof. Gregory L. Plett and Prof. M. Scott Trimboli. Thank you for every Friday meeting that we have had, for helping me in every technical aspect of this thesis, for receiving me at UCCS, and especially, for your humility and kindness. To the rest of UCCS colleagues that I had, Juan, Aloisio, Suchita... Thank you for making my stay at Colorado Springs even more rewarding.

Of course, to all the colleagues and friends that accompanied me through this journey; the students and professors that make every day at work such a joyful experience. I would like to make an especial mention to Manex Aizpurua, Xabier Dorronsoro and Josu Yeregui. I could not find a better team to work with. It has been such a pleasure to share so many great (and sometimes not so great) moments with you. Thank you.

Nola ez, nire familiari eta lagun guztiei eskertu nahi diet behar izan dudan guztian lagundu izana. Zuekin egoteak beti pozten eta indarberritzen nauelako, eskerrik asko!

Azkenik, Amaiari eskertu nahi dizkiot batera pasatako une guztiak, tesiko momenturik gogorrenak ere zoragarri bihurtu direlako zure alboan. Mila esker bihotz-bihotzez.

CONTENTS

ABBREVIATIONS

BMS	**B**attery **M**anagement **S**ystem
BOL	**B**egnning **O**f **L**ife
C-rate	**C**urrent **R**ate
CC	**C**onstant-**C**urrent
CCCV	**C**onstant-**C**urrent **C**onstant-**V**oltage
CRA	**C**ontinuous-time **R**ealization **A**lgorithm
CV	**C**onstant-**V**oltage
DAE	**D**ifferential **A**lgebraic **E**quation
DOD	**D**epth-**O**f-**D**ischarge
DMC	**D**i**M**ethyl **C**arbonate
DRA	**D**iscrete-time **R**ealization **A**lgorithm
EC	**E**thylene **C**arbonate
ECM	**E**quivalent-**C**ircuit **M**odel
EKF	**E**xtended **K**alman **F**ilter
EOL	**E**nd-**O**f-**L**ife
eSOH	**e**lectrode-specific **S**tate-**O**f-**H**ealth
ESPM	**E**xtended **S**ingle-**P**article **M**odel
ESS	**E**nergy **S**torage **S**ystem
EU	**E**uropean **U**nion
EV	**E**lectric **V**ehicle
FDM	**F**inite **D**ifference **M**ethod
FEM	**F**inite **E**lement **M**ethod
FVM	**F**inite **V**olume **M**ethod
FOM	**F**ull-**O**rder **M**odel
HRA	**H**ybrid **R**ealization **A**lgorithm
IMM	**I**nteracting **M**ultiple-**M**odel
KPI	**K**ey **P**erformance **Indicator**
LAM	**L**oss of **A**ctive **M**aterial
LFP	**L**ithium Iron **P**hosphate
LLI	**L**oss of **L**ithium **I**nventory
MOR	**M**odel **O**rder **R**eduction
MPC	**M**odel **P**redictive **C**ontrol
MSCC	**M**ulti **S**tage **C**onstant-**C**urrent

NCA	Lithium **N**ickel **C**obalt **A**luminum oxide
NMC	Lithium **N**ickel **M**anganese **C**obalt oxide
NMPC	**N**onlinear **M**odel **P**redictive **C**ontrol
OCP	**O**pen-**C**ircuit **P**otential
OCV	**O**pen-**C**ircuit **V**oltage
ODE	**O**rdinary **D**ifferential **E**quation
P2D	**P**seudo **2** **D**imensional model
PBM	**P**hysics-**B**ased **M**odel
PDAE	**P**artial-**D**ifferential-**A**lgebraic **E**quation
PDE	**P**artial **D**ifferential **E**quation
POD	**P**roper **O**rthogonal **D**ecomposition
pSEI	**p**ositive electrode **S**olid **E**lectrolyte **I**nterphase
RMS	**R**oot-**M**ean-**S**quare
RMSE	**R**oot-**M**ean-**S**quare-**E**rror
ROM	**R**educed-**O**rder **M**odel
SEI	**S**olid **E**lectrolyte **I**nterphase
SOA	**S**afe **O**perating-**A**rea
SOC	**S**tate-**O**f-**C**harge
SOH	**S**tate-**O**f-**H**ealth
SOL	**S**tate-**O**f-**L**ithiation
SOP	**S**tate-**O**f-**P**ower
SPKF	**S**igma-**P**oint **K**alman **F**ilter
SPM	**S**ingle-**P**article **M**odel
SPMe	**S**ingle-**P**article **M**odel with electrolyte dynamics
UDDS	**U**rban **D**ynamometer **D**rive **S**chedule
UKF	**U**nscented **K**alman **F**ilter
xRA	**R**ealization **A**lgorithm

GLOSSARY

Parameters

A_{cell} (m^2)	Total cell area
a_s (m^2 m^{-3})	Specific surface area
α (-)	Charge transfer coefficient
brug (-)	Bruggeman exponent
$c_{e,0}$ (mol m^{-3})	Initial electrolyte salt concentration
$c_{s,max}$, $c_{s,min}$ (mol m^{-3})	Maximum and minimum solid phase concentrations
D_e (m^2 s^{-1})	Salt diffusivity in the electrolyte
D_s (m^2 s^{-1})	Active material diffusion coefficient
η (V)	Overpotential
ε_e (-)	Liquid phase volume fraction
ε_f (-)	Active volume fraction of filler/binder
ε_s (-)	Solid phase volume fraction
E_{act} (kJ mol^{-1})	Activation energies
i_0 (A m^{-2})	Exchange current density
i_{app} (A m^{-3})	Applied current density
κ (S m^{-1})	Electrolyte conductivity
k (mol m^{-2} s^{-1})	Reaction rate coefficient
L (m)	Domain thickness
L_{tot} (m)	Total cell thickness
Q (Ah)	Nominal cell capacity
R_{film} (Ω m^2)	Particle film resistance
R_s (m)	Active material particle radius
r (m)	Radial coordinate
t (s)	time
σ (S m^{-1})	Solid phase conductivity
t_0^+ (-)	Transport number
T (K)	Temperature
T_{ref} (K)	Reference temperature for Ahrrenius equation
τ (-)	Electrode tortuosity
θ_0 (-)	SOL of the electrode at 0% SOC
θ_{100} (-)	SOL of the electrode at 100% SOC
U_{ocp} (V)	Open circuit potential
x (m)	Spatial coordinate across cell thickness

Superscripts

CC	Current collector
neg	Negative electrode
pos	Positive electrode
sep	Separator

Subscripts

avg	Average
e	Electrolyte
eff	Effective
max	Maximum
min	Minimum

P2D Variables

c_e $(x,\ t)$ (mol m^{-3})	Concentration of Lithium in the electrolyte
$c_s(x,\ r,\ t)$	Lithium concentration in the solid particles
$c_{s,e}(x,\ t)$ (mol m^{-3})	Lithium concentration in the solid particles on the surface
j_s $(x,\ t)$ (A m^{-2})	Side reaction flux contribution to j_{tot}
j_{tot} $(x,\ t)$ (A m^{-2})	Flux of lithium out of a particle
$\phi_e(x,\ t)$ (V)	Potential of lithium in the electrolyte
$\phi_s(x,\ t)$ (V)	Lithium in the solid particles

Constants

F	Faraday's constant (96485 sA mol^{-1})
R	Gas constant (8.314472 (J mol^{-1} K^{-1}))

Chapter 1

INTRODUCTION

This chapter introduces the research topic of the thesis. First, the framework is presented, followed by an explanation of the motivation behind the work. Subsequently, the background of the topic is provided, and the relevant literature is reviewed. The hypotheses and objectives of the thesis are outlined next, and the research methodology is explained. Lastly, the scientific contributions made through this thesis are summarized.

1.1 FRAMEWORK AND MOTIVATION

The current energetic scenario is very controversial. The economic and political interests of many countries and companies have generated conflicting perspectives on what direction should the actual energetic model take. However, due to increasing concerns about climate change and global warming, many of the most developed countries in the world are taking actions to reduce their greenhouse gas emissions to slow down climate change. The Horizon Europe [1] funding program serves as evidence of this. The main objective of the Horizon Europe program is to tackle climate change, helping to achieve the Sustainable Development Goals of the United Nations.

The Intergovernmental Panel on Climate Change reported that energy industry is the largest contributor to global greenhouse gas emissions, accounting for approximately 75% of the total emissions [2]. The adoption of more renewable energy sources should help in the reduction of greenhouse gas emissions. Naturally, as more renewable sources are installed, the amount of fossil sources necessary to meet the power requirements is reduced. However, renewable energies introduce a problem that did not exist with the traditional electrical energy generation and distribution system. As renewable energy sources depend on meteorological conditions, the power generation of these energy sources is intermittent. Therefore, they may not be able to generate the power that the electrical grid demands if the meteorological conditions are not favorable. In this sense, energy storage systems (ESSs) play a crucial role in overcoming the issues associated with the intermittent nature of renewable energy sources. Among existing energy storage technologies, lithium-ion batteries have become the most widely used due to their high gravimetric and volumetric energy densities [3].

In addition, the electrification of the transport sector is another key factor in the decarbonization process. The European Commission reported that 20 % of all European Union (EU) greenhouse gas emissions come from road transport, and for the year 2035 the EU plans to ban the sale of internal combustion engine vehicles. By 2050 the EU wants to achieve climate neutrality, and for that, zero emission vehicles will be needed. Lithium-ion batteries are the main ESS used for electric vehicles (EVs) nowadays due to their high energy density (705 Wh/L), high power density (10,000 W/L), long life cycle, high voltage, low self discharge rate (<2 %/month), and high energy efficiency (∼95 %) [4].

In consequence, lithium-ion batteries have become a key factor in the energy transition; however, despite their widespread adoption across various applications, lithium-ion batteries

continue to face significant challenges that demand improvement. Figure 1.1 shows different research areas that are being investigated nowadays, from cell-level to system-level studies.

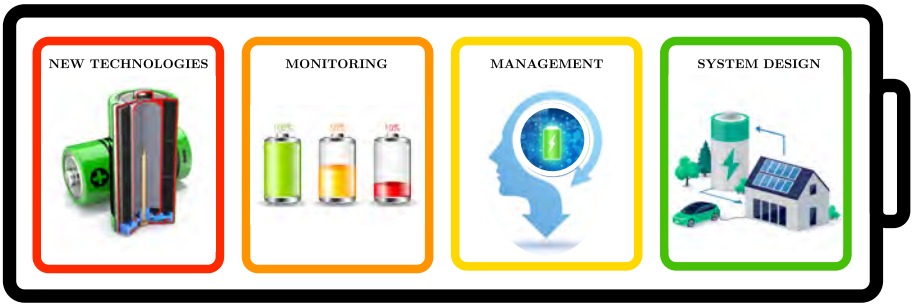

Figure 1.1: Research areas involving lithium-ion batteries.

One of the main concerns with lithium-ion batteries that impacts in almost any application, is the relatively fast degradation that these batteries suffer. As a consequence, batteries need to be changed to meet the energy and power requirements of their applications. Several questions arise from the concern on battery degradation:

- How can we know how aged a battery is?
- How can we predict the lifespan of a battery?
- What strategies can we employ to extend the lifespan of lithium-ion batteries?
- How can we charge batteries faster without increasing degradation?
- How can we ensure safe operation of aged batteries?

Many of these interesting research questions can be approached from various fields of study. For example, battery cell manufacturers and scientists may try to address them by exploring advances in materials and manufacturing processes to enhance battery robustness [5]. For example, fast charging capabilities are being investigated through electrode design [6] and electrolyte design [7].

In this PhD thesis, rather than investigating how to improve lithium-ion batteries, we focused on the improvement of lithium-ion battery management. Thus, the problem with degradation is approached from a control engineering perspective. For that, the main research question that is wanted to answer is the following:

How should we control a lithium-ion battery to mitigate its aging and optimize its performance?

With this question in mind, a literature analysis was performed, presented in Section 1.2. Subsequently, in Section 1.3, this literature analysis was used to hypothesize about the research problem, and the objectives of the thesis were defined.

1.2 BACKGROUND AND LITERATURE REVIEW

To address the challenge presented by battery aging, extensive research efforts are underway. From the battery management point of view, control engineers are focusing on optimizing battery utilization by improving battery state estimation algorithms [8–13] (to improve *diagnosis*) and control strategies [14–17]. In order to reduce battery aging by optimizing its management, it is essential to know how batteries age. This knowledge can be used to predict aging behavior (for *prognosis*) and prevent or minimize its effects on cell performance. Therefore, significant effort is being carried out in battery degradation modeling [18–24], with the goal of making aging models that describe degradation phenomena occurring inside battery cells as faithfully as possible.

In the following subsections, an overview of the state of the art is given for these three relevant topics: battery aging modeling, state estimation, and control algorithms.

1.2.1 Battery aging modeling

As mentioned above, battery aging is one of the critical problems related to lithium-ion batteries [25], and its modeling has been studied for several years [24, 26–28]. However, despite the research efforts, it is still a huge challenge due to its complex nature and difficult experimental validation. The most common approach to model battery aging are empirical models [25, 28, 29]. These models approximate some empirical information that has been collected previously (usually from laboratory aging experiments), such as cell capacity or internal resistance, using empirical equations [25]. These models can give reasonably accurate results in the prediction of capacity loss and impedance increase [29], but do not represent physical behavior, and therefore, lack the interpretability needed to be ideal for battery degradation mitigation controls. One of the factors that contributes to these type of models being so extended, is the very little battery degradation information that can be obtained without cell teardown and post mortem analysis. Furthermore, numerous mechanisms can occur in a lithium-ion battery, which are influenced by many stress factors,

and are closely related to each other [22]. Hence, it is very challenging to model specific degradation phenomena occurring inside lithium-ion batteries.

Another approach to investigate battery aging are physics-based battery aging models [18, 20, 21, 23, 24, 26, 30–36]. In this type of aging models, physical equations are used to predict battery aging. Since physical equations implicitly take into account different stress factors that can influence battery aging, these stress factors may not be explicitly investigated, as has to be done for empirical models. Physical equations are assumed to be accurate descriptions of the real degradation phenomena, and therefore, they should give relevant information to improve battery control algorithms. However, it is not feasible to investigate all the degradation phenomena that can occur inside battery cells in-situ [24], and this makes the parameterization of these aging models very difficult. Nonetheless, some specific techniques have been proposed to study specific degradation mechanisms such as lithium plating for example [37, 38]. Furthermore, due to the highly coupled nature of many degradation mechanisms, even after cell teardown, it is not trivial to discern which degradation mechanisms have occurred in the cell, and to quantify the effect of each of them in cell performance [22].

As a consequence, the parameterization of physics-based aging models is usually performed using empirical methods; fitting the capacity loss or resistance increase values of degradation experiments performed in laboratories [18, 33, 35, 39]. Thus, like empirical models, these models would also require to fit a big degradation matrix to represent the interdependencies of different degradation mechanisms accurately.

Summing up, physics-based methods were determined to be a better approach to improve the prognosis of control algorithms. However, a research gap was identified in the parameterization and validation of these models, where many works have been published but none of them demonstrate the validity of their modeling approach in predicting specific physical phenomena accurately. Thus, a better approach is needed to increase the reliability of these models and to reduce the experimental time and cost of the development process.

1.2.2 State estimation

State estimation is one of the key features to control batteries. Since many necessary internal states of batteries, such as the state-of-charge (SOC) or the state-of-health (SOH), cannot be directly measured, these values must be estimated. These estimates should be used to diagnose the battery and to evaluate which is the current state of the battery

regarding safety, aging, power, etc. To maintain batteries within safe operating limits, it is indispensable to have a state estimation algorithm in every battery management system (BMS) [10]. For that, many approaches can be adopted. As clearly explained in [10], model-based state estimators outperform current-based or voltage-based methods. Nowadays state estimators almost exclusively use equivalent-circuit models (ECMs) to emulate battery behavior. These methods are proven to be effective when estimating the SOC and SOH of the battery [40–44], however, due to their empirical nature, they are not able to describe the internal physicochemical behavior of batteries. Thus, the information obtained from these models cannot be used to mitigate aging with advanced control algorithms. Due to this lack of physical information, batteries are kept inside the safety limits that manufacturers provide. These are not the actual physical limits of the components, but a safe operating zone that defines the manufacturer in order to prevent hazardous conditions. In spite of preventing premature aging, these safety limits reduce the total capacity that batteries can store and provide. Figure 1.2 shows an illustration of the electrochemical safe operating area (SOA) of a battery, and a "datasheet" based SOA. As shown, a physics-based SOA could allow to operate safely beyond the SOA of the manufacturer, and to even contract more the SOA when the battery has aged.

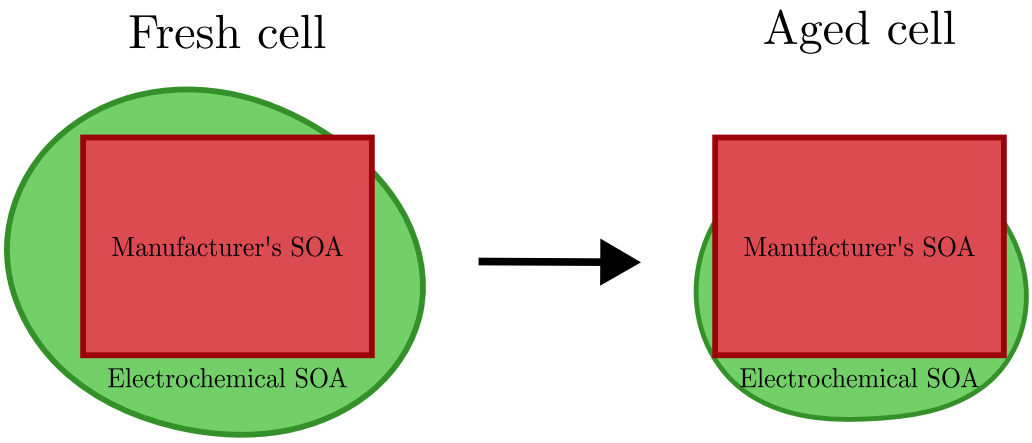

Figure 1.2: Manufacturer specified and electrochemical SOA representation for fresh and aged cells. Adapted from [17].

To overcome these issues, the use of physics-based models (PBMs) for state estimation has been proposed in the literature [9, 11, 13, 17, 45]. These models provide valuable information about the internal states of the battery, such as internal concentrations, potentials or lithium fluxes [8]. However, these models present new challenges that have to be addressed before PBMs become the main approach for state estimation.

- First, the parameterization of PBMs is much harder than that of empirical models, requiring cell teardown and complex laboratory testing to obtain an accurate set of parameters [46–50].
- Second, PBMs are composed of partial-differential-algebraic equations (PDAEs), which are computationally expensive to solve, so simplifications and reduced-order models (ROMs) are required to obtain a computationally tractable battery model [8].
- Third, battery state estimation is more difficult because the cell voltage is dependent on the potential contributions of both electrodes [11].

Nevertheless, these three topics have been investigated in the last years, and advances have been achieved. Many parameters of physics-based battery models can be obtained without performing destructive tests [51,52], reducing considerably the time and economical cost to obtain a PBM. Furthermore, ROMs and simplified models have been proven to be suitable for real-time implementation in non-expensive embedded systems [13, 53]. Lastly, despite being more complicated, several publications on physics-based state estimation have been reported in the literature [9, 11, 54], showing accurate results and even proposing advanced observer architectures to improve the observability of electrodes with flat open-circuit potential (OCP) curves [11].

These improvements have led PBMs to be closer for real-world implementations. However, an important research gap was identified in this field. As batteries age, their internal characteristics change and therefore, the models designed for the beginning of life (BOL) become inaccurate. In this sense, PBMs have an important advantage comparing to traditional ECMs: the aging of each electrode can be taken into account separately. In traditional ECMs, an open-circuit voltage (OCV) curve is calculated for the BOL value, and while battery aging occurs, this OCV curve becomes more and more inaccurate. Since the OCV of the cell is composed of the OCPs of both electrodes, the differences that come from each electrode should be taken into account to maintain an accurate OCV. This can be achieved in PBMs, whereas it cannot in traditional ECMs. However, there are not many publications on physics-based SOH estimation using PBMs [12, 55, 56], and none of them estimates the degradation that occurs in both electrodes. Therefore, the need of a new estimation approach was identified to exploit as much as possible the capabilities that PBMs offer for accurate battery diagnosis and posterior usage for control.

1.2.3 Control strategies

Controlling lithium-ion batteries can be a relatively amenable task if the objective of the control algorithm is to maintain the cell inside the SOA provided by the manufacturer. However, if a more advanced management is desired to optimize power capabilities, minimize cell degradation, or for safe fast charging applications, the control of these devices becomes particularly challenging. Due to the complex nature of the physical phenomena occurring inside lithium-ion batteries, it can be very complicated to design safe and optimized control strategies.

An indicator of the difficulty of controlling lithium-ion batteries, is the numerous accidents that happen today in consumer electronic devices or EVs that use lithium-ion batteries [57]. Many safety issues are generated due to lithium plating [58], which can produce internal short-circuits due to the growth of lithium dendrites [22], reduce thermal stability [58], and enhance gas generation [59]. Therefore, to prevent lithium plating and other degradation mechanisms, the objective of minimizing degradation or maximizing power, should require advanced knowledge of the electrochemical and mechanical processes occurring inside batteries.

Control algorithms for lithium-ion batteries can be designed seeking different purposes. Focusing on cell-level controls, the typical goals of these algorithms are to maximize power [60] and minimize degradation [61]. Most studies focus on improving the charging process since, in most applications, it is easier to control than the discharging process, which is usually governed by the demands of the user. To maximize power capabilities, state-of-power (SOP) estimation is usually performed with the objective of informing the control unit of the maximum power that the battery can deliver or receive while maintaining some safety limits. For this, model predictive control (MPC) algorithms have been proposed in the literature [17, 62]. Other control algorithms can be used, but the ability of the MPC to generate predictive estimates gives the possibility of future load planning. As in the case of SOC or SOH estimation, ECMs can be used to produce accurate and reliable SOP estimates [10], however, these SOP estimates cannot be obtained according to physical information, and hence, these algorithms cannot be used to minimize cell degradation.

With the goal of minimizing battery aging, degradation-aware control strategies can be designed. As mentioned above, the objective of mitigating battery aging is closely related to knowing how the battery ages, and therefore, it could be preferable to base these degradation-aware controls on models that can provide physical insight. These control

strategies can be classified in two main groups: passive methods and active methods [16]. Passive methods usually try to optimize a charging profile to minimize cell degradation and charging time offline, using a cell model, sometimes coupled to degradation or thermal models [16]. On the other hand, active methods are computed in-situ, using present data to calculate pseudo-optimal cell current values.

Both above-mentioned approaches can be adequate, since each of them has its advantages and disadvantages. On the one hand, passive methods can use computationally heavier degradation and thermal models to design optimal charging strategies, since this method does not require to run a real-time simulation. On the other hand, the control strategy should vary as batteries age, since its internal characteristics change, and what initially was an optimal charging strategy, may not be never more. Thus, a recomputation of the charging strategy should be done after estimating accurately the SOH of the cell and updated the model parameters. Furthermore, in this case, the charging strategy would be designed for a predefined condition, *e.g.* from 10 % to 80 % SOC at 20 ºC. If the charging process starts from a different SOC or temperature condition, for example, this charging profile may not be the optimal.

Several researches adopted this approach to design degradation-aware control strategies [16, 61, 63]. Many of them focused on using alternative charging protocols to the traditional constant-current constant-voltage (CCCV) protocol; like for example multi-stages constant-current (MSCC) protocols [64], boost charging protocols [65], or pulsed charging protocols [66]. Despite showing good results for some cases, these charging sequences typically do not consider the physical phenomena occurring inside batteries, and hence, it may be difficult to reproduce the same results in different cases.

Alternatively, active methods could be used to avoid the issues presented by passive methods. When using this approach, the controller has the information of the cell when is applying the current profile, and hence, it can design the control strategy according to the response of the cell. Furthermore, the state estimator could give more insight about the state of the battery in real time, adapting the control according to it. Nevertheless, these methods present some inconveniences too. Since the computations must be done in real time, the modeling approach cannot be as complicated as in passive methods, thus loosing modeling accuracy. Furthermore, charging optimizations can be very complicated to solve. In a fast charging application for example, the objective of the charge could be to minimize time while maintaining cell degradation below a limit. This type of optimal minimum-time problems are very challenging to solve and are generally not amenable

for real-time computation [17, 67]. To overcome these issues, Xavier *et al.* proposed a pseudo-minimum-time problem [68], which seeks to carry the SOC to its reference value.

Summing up, the degradation-aware control approaches reported in the literature can be classified in two groups: active and passive methods. Both methods present positive and negative attributes and have been widely analyzed in the literature. It was determined that physics-based approaches can give more insight to mitigate battery aging, thus being a better approach for degradation-aware controls. In this aspect, relatively few works have analyzed physics-based control, both on active and passive methods. Passive methods usually focus on mitigating plating by imposing constraints and reducing solid electrolyte interphase (SEI) layer growth in the charging process. However, these approaches did not report clear experimental proof of the performance of the control algorithm. On the other hand, the reported active methods mostly used an MPC or nonlinear MPC (NMPC) algorithm to limit the overpotentials of the side reactions [16, 69]. Thus, a main research gap was identified on the validation of the control algorithms. Furthermore, it was believed that a better use of physics-based battery aging modeling could be done, since the only mechanisms that are taken into account in the literature are the SEI growth and the lithium plating, without including any loss of active material (LAM) generating mechanism.

1.3 HYPOTHESES AND OBJECTIVES

Based on the research gaps identified in Section 1.2, the following hypotheses were tested throughout this PhD thesis:

- **H1**. Accurate PBMs could be simplified and reduce their order to decrease their computational complexity and convert them a suitable approach for battery control applications.
- **H2**. Physics-based aging equations could be coupled to physics-based battery models to describe degradation phenomena occurring inside battery cells. The parameterization of these models should be faster and cheaper than that of empirical models, and the models should be able to describe different degradation conditions more accurately.
- **H3**. PBMs could be used to obtain accurate internal physical variable estimates, improving empirical and ECM based battery state estimation. For example, instead of estimating the SOC of the battery, the state-of-lithiation (SOL) of each electrode could

be estimated, and instead of estimating an overall SOH estimate, electrode-specific SOH (eSOH) values could be obtained to improve degradation diagnosis.

- **H4**. The above mentioned state estimation algorithms, and the physics-based aging models could be used to develop advanced control strategies, mitigating battery aging and improving performance.

With the intention of validating these hypotheses, the main objective of this work was defined:

Design a control strategy to reduce lithium-ion battery aging, applicable to any operation moment, and adaptable throughout its lifetime.

In order to cope with the main goal of the PhD, four sub-objectives were specified:

- **O1**. Identify and implement the most suitable PBMs according to the accuracy and computational requirements of control oriented systems.
- **O2**. Develop an accurate physics-based battery aging model with a reduced number of experiments compared to a traditional empirical model.
- **O3**. Implement and validate a state estimation algorithm capable of estimating the internal states of the battery and its aging condition, adapting the PBM parameters during battery operation.
- **O4**. Design a control strategy to reduce battery aging based on the physical knowledge that PBMs give.

1.4 RESEARCH METHODOLOGY

The research methodology began with an extensive review of the pertinent literature concerning PBMs to establish a comprehensive understanding of existing frameworks. Following this review, the most appropriate models were selected for control-oriented purposes, and they were implemented and compared to serve as the foundation for further analyses.

Subsequently, a detailed examination of physics-based aging models was conducted, leading to the development of a novel parameterization approach. This approach aimed to enhance the accuracy and effectiveness of aging predictions, thereby contributing to the optimization of battery performance over time.

Furthermore, state estimation algorithms were rigorously scrutinized to identify their applicability in the context of battery health estimation. A new methodology, rooted in physics-based principles, was proposed to offer improved accuracy and reliability in assessing the health status of lithium-ion batteries.

Lastly, an in-depth investigation into the control strategies for lithium-ion batteries was undertaken through a comprehensive literature review. Building upon existing knowledge, a novel control proposal was formulated, aiming to optimize the operational efficiency and lifespan of batteries while addressing prevalent challenges in battery management.

The research methodology is summarized in Figure 1.3. As shown, the foundations of this work are accurate reduced-order and simplified physics-based battery models, explained in Chapter 2. Using physics-based battery models, new battery aging models can be developed, as explained in Chapter 3, useful for the prognosis of lithium-ion batteries. In addition, new state estimation algorithms are proposed to diagnose better the internal physical variables and the health of batteries in Chapter 4 and Chapter 5, respectively. Finally, combining the three previously developed methods, enhanced management of lithium-ion batteries can be achieved with new control algorithms, as detailed in Chapter 6.

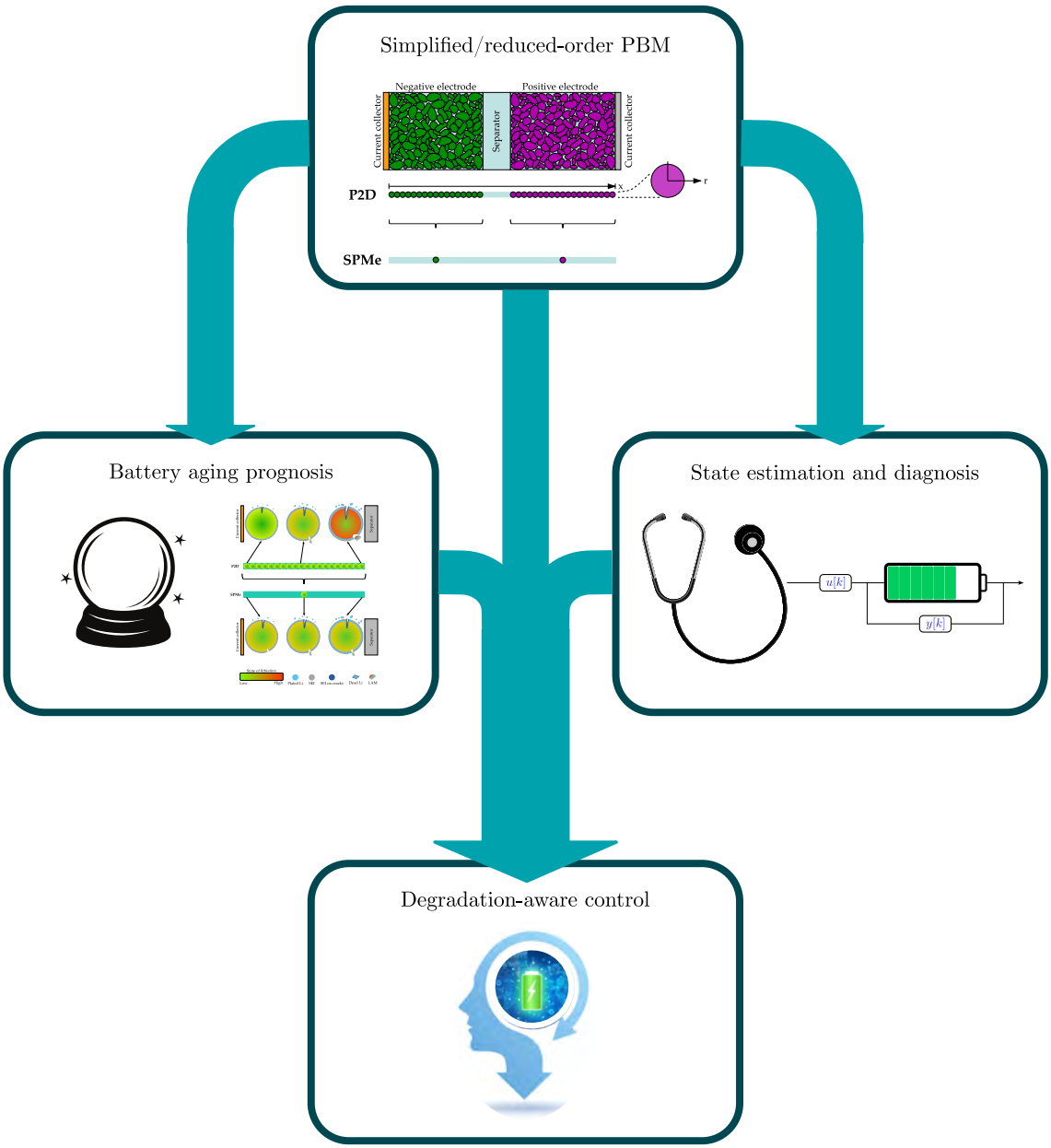

Figure 1.3: Summary of the research methodology.

1.5 SCIENTIFIC CONTRIBUTIONS

Journal articles

[1] Josu Yeregui, Laura Oca, Iker Lopetegi, Erik Garayalde, Manex Aizpurua, and Unai Iraola. "State of charge estimation combining physics-based and artificial intelligence models for lithium-ion batteries". *Journal of Energy Storage*, 73:108883, 2023. [70]

[2] C. Rojas, L Oca, I Lopetegi, U Iraola, J Carrasco. "A critical look at efficient parameter estimation methodologies of electrochemical models for Lithium-Ion cells". *Journal of Energy Storage*", 80, 110384. [71]

[3] Iker Lopetegi, Gregory L. Plett, M. Scott Trimboli, Aloisio Kawakita de Souza, Laura Oca, Eduardo Miguel, and Unai Iraola. "A new battery SOC/SOH/eSOH estimation method using a PBM and interconnected SPKFs: Part 1. SOC and internal variable estimation". *Journal of The Electrochemical Society*. [72]

[4] Iker Lopetegi, Gregory L. Plett, M. Scott Trimboli, Laura Oca, Eduardo Miguel, and Unai Iraola. "A new battery SOC/SOH/eSOH estimation method using a PBM and interconnected SPKFs: Part 2. SOH and eSOH estimation". *Journal of The Electrochemical Society*. [73]

Conferance papers

[1] Xabier Dorronsoro, Iker Lopetegi, Erik Garayalde, Unai Iraola and Josu Yeregui,"Modular Battery Energy Storage Systems for Available Energy Increase", *2022 IEEE Vehicle Power and Propulsion Conference (VPPC)*, pp.1-7, 2022. [74]

[2] Iker Lopetegi, Gregory L. Plett, M. Scott Trimboli, Josu Yeregui, Laura Oca, Clara Rojas, Eduardo Miguel and Unai Iraola, "Lithium-ion Battery Aging Prediction with Electrochemical Models: P2D vs SPMe" *2023 IEEE Vehicle Power and Propulsion Conference (VPPC)*, pp.1-7, 2023. [75]

[3] Manex Aizpurua, Erik Garayalde, Iker Lopetegi, Josu Yeregui, Xabier Dorronsoro and Unai Iraola, "Modular BESS architecture for enhanced performance and extended lifetime", *ECCE 2024*. **Submitted for publication**

[4] Sergio Fernandez, Iker Lopetegi, Laura Oca, Josu Yeregui, Erik Garayalde and Unai Iraola, "Intuitive Degradation Mode Estimation Tool: ModEst", *ECCE 2024*. **Submitted for publication**

Chapter 2

PHYSICS-BASED BATTERY MODELING

This chapter summarizes the physics-based battery modeling research carried out within the thesis. First, different battery models reported in the literature are evaluated, discussing the appropriate modeling scale and complexity for the scope of this research. Later, different solving methods and model order reduction (MOR) techniques reported in the literature are analyzed, with the aim of obtaining the best model response with the lowest computational cost. Finally, the most interesting models are implemented and compared to conclude which model should be used for each case.

2.1 PHYSICS-BASED LITHIUM-ION BATTERY MODELS

The main purpose of physics-based battery models is to describe the internal physico-chemical behavior of battery cells. Depending on the amount of detail that is desired to describe, different modeling scales may be used. Usually, the more detail described, the harder it is to execute the model, which requires more computational resources. Therefore, there is a trade-off between predictability and computational cost when choosing the appropriate model scale for the application.

Due to the framework of the thesis, the smallest scale that was analyzed is the continuum scale. Smaller scale models are very useful to investigate specific physical phenomena that occur inside battery cells, but they are computationally too expensive for entire cell simulations and control-oriented applications with the present technology [8]. Continuum-scale models are more tractable computationally, and despite being less accurate in the physical representation of the components of the battery, they can be used to simulate a general physical behavior of entire cells.

The most renowned continuum-scale model is probably the pseudo-2-dimensional (P2D) model. It consists of a PDAE system that is computationally expensive to solve compared to frequently used equivalent-circuit or empirical models [8]. However, it provides important physical information about the cell, which could be used to reduce degradation or control the safety operation limits of the battery. Consequently, many research has been performed with the intention of reducing the computational cost of the P2D model [76–83]. Typically, PDAE systems, such as the P2D model, can be discretized using finite difference (FDM), finite volume (FVM), or finite element (FEM) methods. However, these types of solution are computationally expensive and are usually used to obtain robust and accurate solutions rather than to reduce the computational cost of the model. Therefore, these solutions are named as full-order models (FOMs) in this document.

To reduce the computational cost of a model, MOR techniques can be used. These techniques are used to reduce the computational complexity of mathematical models in numerical simulations. By applying MOR, the P2D model can be reduced to a ROM, making it computationally lighter. Depending on the technique, the performance of the resulting ROM will change, having different accuracy and computational cost [83].

Another way to reduce the computational complexity of the P2D model is to simplify the model. Unlike in ROMs, in simplified models some physical phenomena representation

is lost in the simplification process. Sometimes these simplified models are also called ROMs in the literature, but in this work ROMs are defined as reduced complexity models that represent the same amount of physical phenomena as the FOM.

The most widely used simplification of the P2D model is the single-particle model (SPM) [84]. It assumes that lithium diffusion in the solid phase is the slowest process occurring inside the cell, and its dynamics dominate the rest. Therefore, the SPM represents each electrode as an average active material spherical particle. The biggest drawbacks of the SPM are that the electrolyte dynamics are neglected and that its accuracy decreases drastically at mid-high C-rates [82,85–87], when the electrolyte dynamics and the concentration gradients across the thicknesses of the electrodes become more relevant. Consequently, electrolyte related phenomena and solid-phase gradients across the thicknesses of the electrodes cannot be described with this model.

Attempting to overcome these drawbacks, many authors extended the SPM taking into account the electrolyte dynamics, and consequently improving the accuracy of the model [82, 85–91]. The resulting model is known as extended single-particle model (ESPM) or single-particle model with electrolyte dynamics (SPMe). For that extension, approximation functions and volume averaging can be used to obtain computationally less expensive equations for the electrolyte concentration and the electrolyte potential, as in [85, 86]. Nonetheless, in spite of improving the model accuracy, by including the electrolyte dynamics in the SPM, the computational cost of the model increases.

Marquis *et al.* [82] used asymptotic reduction methods [92] to obtain a more accurate SPMe than previously reported SPMe-s, and similar computational complexity [82]. In this work [82], they compared the computational requirements and accuracies obtained with the SPM and their SPMe relative to the P2D model, all of them disretized with FVM. The results showed that the accuracy of the SPMe was very good until C-rates up to 2C while the accuracy of the SPM dropped drastically, and the computational cost was very similar to the SPM. Thus, the SPMe could be a better approach than the SPM due to its better accuracy and similar computational cost.

This literature analysis showed that the simplifications of the P2D model are less accurate and provide less physical information, however, they are computationally lighter and, therefore, they could be a better option for applications where the computational cost is critical. For this reason, it was decided to implement the SPM, the SPMe and the P2D model to compare their performance and to have the possibility of implementing the most suitable model in any particular case.

In the following subsections these three models are explained in more detail. For that, the P2D model is described first, since it uses the most complete physical representation, and the SPMs can be derived from this model by making additional assumptions. After the P2D model is explained, a literature overview is presented to analyze the MOR methods that were used to reduce the P2D model complexity. Since the P2D model should be reduced for the purpose of this thesis, the different MOR techniques are compared and the selection of the technique that was used to solve all the models of this work is justified. Finally, the SPMs are described and a comparison between the reduced-order P2D and SPMs is presented.

2.2 THE PSEUDO-TWO DIMENSIONAL MODEL

As mentioned, the P2D model is a continuum-scale PBM developed by Newman, Doyle and Fuller [93–95]. It describes the electrochemical processes that occur inside a battery cell using a system of PDAEs. These PDAEs derive from the physical equations that represent the micro-scale physical phenomena occurring inside the cell. Volume averaging theorem is used to transform these micro-scale equations into continuum-scale equations [8].

The model represents the cell thickness with a linear macro-scale dimension (x). It divides the cell in three domains: the electrodes and the separator. Porous electrode theory [96] is used to describe the electrodes, which considers two superimposed phases: the solid phase and the electrolyte phase. Each x point of the electrodes is considered as the center of a solid spherical particle of radius R_s. To describe the particle radius at each x point, a micro-scale pseudo-dimension (r) is used. Therefore, the model does not take into account the current distribution along the height and length of the electrodes and assumes a homogeneous distribution of spherical particles in the electrodes. An illustration of the model can be seen in Figure 2.1.

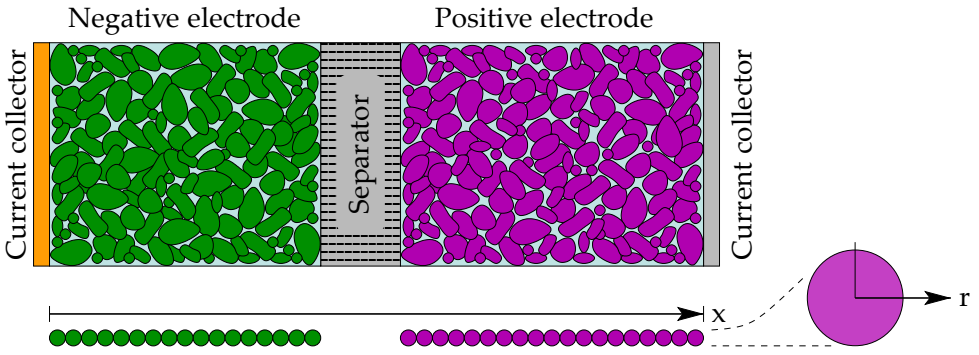

Figure 2.1: P2D model representation [8].

Using this representation and the applied current density (i_{app}) as input, the model solves the time and spatial evolution of five dependent variables: the solid phase concentration $c_s(x, r, t)$, the electrolyte concentration $c_e(x, t)$, the electric potential of the solid phase $\phi_s(x, t)$, the electric potential in the electrolyte $\phi_e(x, t)$ and the flux of lithium ions between solid particles and the electrolyte $j(x, t)$.

2.2.1 Governing equations

The system of equations is composed of four PDEs, which model mass and charge conservation in the solid and electrolyte phases, and an algebraic equation that couples all the PDEs together.

Lithium transport in the solid phase is described by Fick's diffusion equation in spherical coordinates

$$\frac{\partial c_s(x, r, t)}{\partial t} = \frac{1}{r^2}\frac{\partial}{\partial r}\left(D_s r^2 \frac{\partial c_s(x, r, t)}{\partial r}\right), \tag{2.1}$$

where D_s is the diffusivity of lithium in the solid particles, and represents how easy it is for lithium to diffuse through the solid phase. Since radial symmetry is assumed, there can be no net flux through the center of the particle. This is represented with the homogeneous Neumann boundary condition

$$\frac{\partial c_s(x, 0, t)}{\partial r} = 0. \tag{2.2}$$

At the particle surface, $r = R_s$, the module of lithium concentration variation must be equal to the flux of lithium going out of the particle. This is described with the inhomogeneous Neumann boundary condition

$$D_s \frac{\partial c_s(x, R_s, t)}{\partial r} = -j(x, t). \tag{2.3}$$

Mass conservation in the electrolyte phase is modeled by:

$$\frac{\partial(\varepsilon_e c_e(x, t))}{\partial t} = \frac{\partial}{\partial x}\left(D_{e,eff}\frac{\partial}{\partial x}c_e(x, t)\right) + a_s(1 - t_+^0)j(x, t), \tag{2.4}$$

where ε_e is the volume fraction of the electrolyte (or the porosity), t_+^0 is the transference number of the cation with respect to the solvent and $D_{e,eff}$ is the effective electrolyte diffusivity. This equation describes the movement of lithium through the electrolyte due to

diffusion, neglecting the convection and migration phenomena. However, for high current rates, this assumption may be inaccurate [97].

The electrolyte mass conservation equation is subject to two homogeneous Neumann boundary conditions. As there cannot be flux of lithium between the electrolyte and the current collector:

$$\frac{\partial(c_e(0,t))}{\partial x} = \frac{\partial(c_e(L_{tot},t))}{\partial x} = 0. \tag{2.5}$$

Charge conservation in the electrolyte is modeled by

$$\frac{\partial}{\partial x}\left(\kappa_{eff}\frac{\partial}{\partial x}\phi_e(x,t)\right) + \frac{\partial}{\partial x}\left(\kappa_{D,eff}\frac{\partial}{\partial x}\ln(c_e(x,t))\right) + a_s F j(x,t) = 0, \tag{2.6}$$

where κ_{eff} is the effective electrolyte conductivity, a_s is the specific surface area of the solid particles, F is the Faraday constant and $\kappa_{D,eff}$ is calculated as

$$\kappa_{D,eff} = \frac{2RT\kappa_{eff}}{F}\left(1 + \frac{\partial \ln f_{\pm}}{\partial \ln c_e}\right)\left(t_+^0 - 1\right), \tag{2.7}$$

where $f_{\pm}$ is the mean molar activity. It is common to assume $\frac{\partial \ln f_{\pm}}{\partial \ln c_e} = 0$ [8], however, this thermodynamic factor can deviate depending on the salt concentration. The influence of this deviation on cell performance increases at higher C-rates, as shown in [97].

Since there is no electron transfer between the current collectors and the electrolyte, the boundary conditions 2.8 and 2.9 must be met.

$$\kappa_{eff}\frac{\partial}{\partial x}\phi_e(0,t) + \kappa_{D,eff}\frac{\partial}{\partial x}\ln(c_e(0,t)) = 0 \tag{2.8}$$

$$\kappa_{eff}\frac{\partial}{\partial x}\phi_e(L_{tot},t) + \kappa_{D,eff}\frac{\partial}{\partial x}\ln(c_e(L_{tot},t)) = 0 \tag{2.9}$$

Charge conservation in the solid phase is modeled by Ohm's law

$$\frac{\partial}{\partial x}\left(\sigma_{eff}\frac{\partial}{\partial x}\phi_s(x,t)\right) - a_s F j(x,t) = 0, \tag{2.10}$$

where σ_{eff} is the solid effective conductivity. All the current flowing through the cell must be transferred through the solid phase from the collectors to the electrodes, and vice versa. Therefore, two homogeneous Neumann boundary conditions are defined at the electrode/collector boundaries

$$-\sigma_{eff}^n\frac{\partial}{\partial x}\phi_s(0,t) = \sigma_{eff}^p\frac{\partial}{\partial x}\phi_s(L_{tot},t) = i_{app}. \tag{2.11}$$

Lithium transfer between the solid/electrolyte interface is modeled by the Butler-Volmer kinetic relationship

$$j = \frac{i_0}{F}\left\{\exp\left(\frac{(1-\alpha)F}{RT}\eta\right) - \exp\left(-\frac{\alpha F}{RT}\eta\right)\right\}, \tag{2.12}$$

where α is the charge transfer coefficient, R is the universal gas constant, T is the temperature, η is the overpotential (2.13) and i_0 is the exchange current density (2.14).

The overpotential is defined as the difference between the local electric potential and the equilibrium potential on the surface of the particle. It sets the direction and the magnitude of the lithium transfer reaction in the solid/electrolyte interface, and is calculated with the equation

$$\eta = \phi_s - \phi_e - U_{ocp}(c_s) - FR_{film}j, \tag{2.13}$$

where U_{ocp} is the equilibrium potential (or open circuit potential) and R_{film} is the resistance generated by the film covering the solid particles, "isolating" them from the electrolyte. This film is known as the SEI.

The exchange current density is given by

$$i_0 = Fk_{0,norm}\left(\frac{c_e}{c_{e,0}}\right)^{1-\alpha}\left(\frac{c_{s,\max} - c_{s,e}}{c_{s,\max}}\right)^{1-\alpha}\left(\frac{c_{s,e}}{c_{s,\max}}\right)^{\alpha}, \tag{2.14}$$

where $c_{e,0}$ is the initial electrolyte concentration, $c_{s,max}$ is the maximum solid-phase concentration and $k_{0,norm}$ is defined by

$$k_{0,norm} = Fk_0 c_{e,0}^{1-\alpha} c_{s,max}, \tag{2.15}$$

where k_0 is the reaction rate coefficient.

2.2.2 Model parameters and assumptions

As can be seen in the equations of the P2D model, many parameters have to be defined before solving the equation system. The parameter measurement/estimation process is not a trivial task, it requires several parameter estimation and/or physico-chemical parameter measurement procedures to obtain values that can accurately represent the behavior of the cell [46, 50, 98–100]. Table 2.1 shows a classification of the parameters of the P2D model.

Table 2.1: Classification of the P2D model parameters.

Negative electrode	Separator	Positive electrode
a_s^{neg}		a_s^{pos}
R_s^{neg}		R_s^{pos}
$c_{e,0}$	$c_{e,0}$	$c_{e,0}$
$c_{s,max}^{neg}$		$c_{s,max}^{pos}$
ε_e^{neg}	ε_e^{sep}	ε_e^{pos}
ε_s^{neg}		ε_s^{pos}
κ_{eff}^{neg}	κ_{eff}^{sep}	κ_{eff}^{pos}
σ_{eff}^{neg}		σ_{eff}^{pos}
θ_0^{neg}		θ_0^{pos}
θ_{100}^{neg}		θ_{100}^{pos}
U_{ocp}^{neg}		U_{ocp}^{pos}
A	A	A
L^{neg}	L^{sep}	L^{pos}
D_e^{neg}	D_e^{sep}	D_e^{pos}
D_s^{neg}		D_s^{pos}
t_+^0	t_+^0	t_+^0
τ^{neg}	τ^{sep}	τ^{pos}
k_0^{neg}		k_0^{pos}
α^{neg}		α^{pos}
$\partial \ln f_\pm / \partial \ln c_e$	$\partial \ln f_\pm / \partial \ln c_e$	$\partial \ln f_\pm / \partial \ln c_e$

Since batteries are manufactured with porous electrodes nowadays, the bulk properties of the materials have to be adjusted in order to calculate effective parameter values that take into account the path that ions follow through the porous media. This is the case of the electrolyte diffusivity and the ionic and electronic conductivities. Effective parameters can be calculated using the tortuosity (τ) of the porous media. The tortuosity is defined as the ratio between the lengths of the shortest path and the real path that an ion diffusing through the porous media can take:

$$\tau = \frac{L}{L_0}, \tag{2.16}$$

where L is the length of the real path and L_0 is the shortest path length. This is shown in Figure 2.2.

To relate tortuosity to the liquid volume fraction (or porosity), the Bruggeman exponent [101] is commonly used in the P2D model [8], which is defined as

$$\tau = \varepsilon_e^{brug}. \tag{2.17}$$

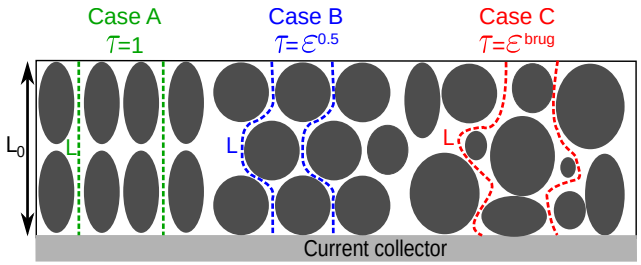

Figure 2.2: Different tortuosity scenarios [99].

Applying the Bruggeman exponent to the bulk parameters, the effective parameters are calculated:

$$\kappa_{eff} = \kappa \varepsilon_e^{brug} \tag{2.18}$$

$$\sigma_{eff} = \sigma \varepsilon_e^{brug} \tag{2.19}$$

$$D_{e,eff} = D_e \varepsilon_e^{brug}. \tag{2.20}$$

Many physicochemical properties may vary depending on temperature and concentration [102]. These variations should be taken into account to make the model more accurate at a wider range of SOCs and temperatures. The temperature dependency of the parameters can be taken into account using the Arrhenius equation [103]:

$$\psi = \psi_{ref} exp\left[\frac{E_{act,\psi}}{R}\left(\frac{1}{T_{ref}} - \frac{1}{T}\right)\right], \tag{2.21}$$

where ψ is the temperature dependent variable and $E_{act,\psi}$ is the activation energy of the evolution process of ψ.

For concentration dependent parameters, other relations can be used. One of them is the Einstein equation, proposed by Ecker *et al.* [104] to model the concentration and temperature dependence of the electrolyte diffusion coefficient:

$$D^r_{e,eff} = \frac{\kappa^r_{eff} k_B T}{e^2 N_A c_e}, \tag{2.22}$$

where k_B is the Boltzmann constant, e is the elementary charge, N_A the Avogadro constant and c_e the electrolyte concentration of lithium.

One of the parameters that varies most due to concentration variations is the solid-phase diffusion coefficient, which can change up to 2 orders of magnitude in the entire SOC range

for typical electrode materials such as NMC or graphite [47]. Baker and Verbrugge [105] suggested the following concentration dependency for the solid-phase diffusion coefficient:

$$D^r_{s,tot}(\theta, T) = -D^r_{s,tot}(T)\frac{F}{RT}\theta^r(1-\theta^r)\frac{\partial U^r_{ocp}}{\partial \theta^r}, \tag{2.23}$$

where θ is the local SOL and $\partial U^r_{ocp}/\partial\theta^r$ is the slope of the equilibrium potential at certain θ value.

The parameters of the P2D model that depend on temperature and concentration are presented in Table 2.2.

Table 2.2: Concentration and temperature dependent parameters.

Parameter	Dependency
D_e	c_e, T
D_s	c_s, T
$\partial \ln f_\pm / \partial \ln c_e$	c_e, T
k	c_s, T
κ	c_e, T
σ	c_s, T
t^0_+	c_e, T
U_{ocp}	c_s, T

2.3 MODEL ORDER-REDUCTION TECHNIQUES

The objective of MOR techniques is to convert the PDEs of the system into lower order ODEs and algebraic equations, which are less demanding computationally. In the following lines, an analysis of different MOR techniques found in the literature is presented. In order to compare them between each other, the key aspects to look at when evaluating the models are defined as key performance indicators (KPIs). The KPIs that were considered are the following: computational time, memory requirements, ROM accuracy, precomputation speed, and whether the MOR technique is analytical or numerical.

This last feature was considered to be very important for this work. Analytical techniques result in ROMs that keep the original parameters "symbolically" in the ROM, whereas numerical methods do not. The importance of this characteristic depends mainly on the aging of the cells. While the cells age, the values of the physical parameters change, making the original model inaccurate if these parameters are not updated. When this happens, analytically reduced ROMs are able to change the parameters directly, whereas

numerically reduced ROMs are not, and they would have to be recomputed after changing the parameter values on the FOM.

After identifying the most important characteristics of MOR techniques, the literature was analyzed to compare different options and decide which method was the most suitable for the purpose of this work. In result of this literature analysis, 5 MOR methods were selected to compare: the proper orthogonal decomposition (POD) [76, 77, 106–108], the realization algorithms (xRAs) [79, 81, 109, 110], the Padé approximation method [106, 111, 112], the Galerkin approximation [106, 113, 114] and the orthogonal collocation [54, 78, 80, 115]. There are different types of xRAs, such as the continuous-time (CRA), the discrete-time (DRA) or the hybrid realization algorithm (HRA) [81], however we decided to group them for this analysis, since they have many characteristics in common.

These 5 techniques have been used previously in the literature to reduce the computational complexity of the P2D model or the SPMe, so the results shown in their respective publications were used to compare the performance of the techniques in each KPI. Table 2.3 shows the qualitative comparison for each MOR method in the defined KPIs. More black circles mean better performance, so more black circles in computational time mean that the ROM requires less computational time for a simulation.

Table 2.3: Qualitative comparison of the analyzed MOR techniques (based on literature results).

MOR technique	Analytic MOR	Computational time	Memory requirements	Model accuracy	Precomputation speed	References
POD	✗	●●○○	●●●○	●●●○	●○○○	[76, 77, 108]
Realization algorithms	✗	●●●●	●●○○	●●●○	●●○○	[79, 81, 109, 110]
Padé approximation	✓	●●●○	●●●●	●●○○	-	[106, 112]
Galerkin approximation	✓	●●○○	●●●○	●●●●	-	[113, 114]
Orthogonal collocation	✓	●●○○	●●●○	●●●●	-	[54, 78, 80, 115]

As can be seen in Table 2.3, the POD and xRAs are numerical MOR techniques. Since the goal of this thesis is to reduce degradation, it is not convenient to have ROMs that cannot update its parameters directly when the cell ages. Therefore, the Padé approximation, the Galerkin approximation, and the orthogonal collocation methods were identified as a better approach for this work. However, note that these methods could be a better option for other purposes. For example, Lee *et al.* reported that their DRA-based ROM was 5000 times faster than their FOM [79], while the time reduction with the orthogonal collocation method can be of 20:1 with respect to a FOM [115]. Thus, DRA should be a better option for applications where simulation time is the most critical feature.

Among the three analytical methods, the orthogonal collocation and Galerkin approximation methods are more accurate than the Padé approximation method. This is because frequency-domain approximation methods rely on the assumption that the system is linear [83]. The Galerkin and the orthogonal collocation methods are spectral MOR methods, which are based on approximating the PDEs of the system using a sum of basis (or trial) functions [78, 114]. Depending on the number of functions used to approximate the PDE, the reduction in computational time will vary, as well as the accuracy of the solution. Compared to spatial discretization methods such as the FEM, FVM or FDM, spectral methods can achieve the same accuracy with a reduced number of discretization nodes [83], achieving faster ROMs [78, 115]. On the other hand, the Padé approximation is a faster method that consists on linearizing the transcendental transfer functions of the FOM [110] into rational functions in the Laplace domain and reducing the order of the system with moment matching [112].

These three analytical MOR techniques could be valid for this work; however, we decided to choose the orthogonal Collocation method for several reasons. First of all, regarding the additional models that have to be included in the model, such as aging and thermal models, the Galerkin approximation method or the orthogonal collocation method are easier to adapt than the Padé approximation method, due to the transfer function based nature of the Padé approximation. Between the two spectral methods, the orthogonal collocation is easier to implement in our opinion. Both methods use the weighted residual method to obtain the coefficients of their trial functions, but with different approaches. The Galerkin method consists on forcing the integral of the residual to be zero over an interval, whereas the orthogonal collocation forces the integral of the residual over a point to be zero. For these reasons, orthogonal collocation was adopted as the reduction technique to reduce the computational cost of the P2D, SPMe and SPM models that were used in this work.

For the sake of readability, the implementation of the orthogonal collocation method for the P2D model is explained in Appendix A. The implementation of the orthogonal collocation SPMe and SPM is the same as for the P2D model, but solving the solid-phase concentration equations for only one particle, and considering a uniform current density instead of using the Butler-Volmer equation. The orthogonal collocation P2D model was validated against a high-fidelity P2D model solved with FEM in COMSOL Multiphysics® implemented by Plett *et al.* [8]. The validation results are shown in Appendix B.

2.4 THE SINGLE-PARTICLE MODELS

As specified above, the SPM and SPMe are simplifications of the P2D model. They model one average active material particle per electrode, and the current density is assumed to be uniform. The only state variable of the SPM is the solid-phase concentration, which is calculated using the same solid-phase diffusion equation of the P2D model, but considering the above-mentioned uniform current density. Once the solid-phase concentration is solved, the cell voltage and overpotentials are calculated. The equations of the SPM are shown in Table 2.4.

Table 2.4: Equations of the SPM.

Description	Equation	Boundary conditions
Mass conservation in the solid phase	$\frac{\partial c_s}{\partial t} = \frac{1}{r^2}\frac{\partial}{\partial r}\left(D_s r^2 \frac{\partial c_s}{\partial r}\right)$	$\left.\frac{\partial c_s}{\partial r}\right\|_{r=0} = 0, D_s \left.\frac{\partial c_s}{\partial r}\right\|_{r=R_s} = -j$
Reaction flux	$j = \begin{cases} \frac{i_{app}}{F a_s^n L^n} & \text{for} \quad x \in [0, L^n] \\ 0 & \text{for} \quad x \in [L^n, L^n + L^s] \\ -\frac{i_{app}}{F a_s^p L^p} & \text{for} \quad x \in [L^n, L^{tot}] \end{cases}$	
Cell voltage	$V_{cell} = \overline{U}_{eq} - \overline{\eta}_r + \overline{\eta}_c - \overline{\Delta\phi}_e - \overline{\Delta\phi}_s$ $\overline{U}_{eq} = U^p_{ocp}(c^p_{s,e}) - U^n_{ocp}(c^n_{s,e})$ $\overline{\eta}_r = \frac{2RT}{F} sinh^{-1}\left(\frac{j^p F}{2i_0^p}\right) + \frac{2RT}{F} sinh^{-1}\left(\frac{j^n F}{2i_0^n}\right)$ $i_0 = F k_{0,norm} (1-\theta)^{1-\alpha} \theta^{\alpha}$	

Unlike the SPM, the SPMe considers the electrolyte dynamics and models more physical phenomena that occur inside battery cells. However, it cannot model the solid-phase concentration gradients that occur through the thicknesses of the electrodes due to its single-particle approach. The equations of the SPMe are shown in Table 2.5. As can be observed, the equations of the SPMe are very similar to the equations of the P2D model. One of the main differences that results in the reduced computational cost of the SPMe is the assumption of a uniform current density. The Butler-Volmer Equation 2.12 that is used in the P2D model to calculate the reaction flux creates an algebraic loop that converts the system of ODEs into a DAE system. Consequently, a specific DAE solver for stiff systems is required to solve the P2D model (if a frequency-domain approximation method is not used, as the xRAs or Padé approximation).

Table 2.5: Equations of the SPMe.

Description	Equation	Boundary conditions
Mass conservation in the solid phase	$\frac{\partial c_s}{\partial t} = \frac{1}{r^2}\frac{\partial}{\partial r}\left(D_s r^2 \frac{\partial c_s}{\partial r}\right)$	$\left.\frac{\partial c_s}{\partial r}\right\|_{r=0} = 0, D_s \left.\frac{\partial c_s}{\partial r}\right\|_{r=R_s} = -j$
Mass conservation in the electrolyte	$\frac{\partial(\varepsilon_e c_e)}{\partial t} = \nabla \cdot (D_{e,eff} \nabla c_e) + a_s(1-t_+^0)j$	$\left.\frac{\partial c_e}{\partial x}\right\|_{x=0} = \left.\frac{\partial c_e}{\partial x}\right\|_{x=L^{tot}} = 0$
Reaction flux	$j = \begin{cases} \frac{i_{app}}{F a_s^n L^n} & \text{for} \quad x \in [0, L^n] \\ 0 & \text{for} \quad x \in [L^n, L^n + L^s] \\ -\frac{i_{app}}{F a_s^p L^p} & \text{for} \quad x \in [L^n, L^{tot}] \end{cases}$	
Cell voltage	$V_{cell} = \overline{U}_{eq} - \overline{\eta}_r + \overline{\eta}_c - \overline{\Delta\phi}_e - \overline{\Delta\phi}_s$ $\overline{U}_{eq} = U_{ocp}^p(c_{s,e}^p) - U_{ocp}^n(c_{s,e}^n)$ $\overline{\eta}_r = \frac{2RT}{F} sinh^{-1}\left(\frac{j^p F}{2i_0^p}\right) + \frac{2RT}{F} sinh^{-1}\left(\frac{j^n F}{2i_0^n}\right)$ $i_0 = F k_{0,norm} \left(\frac{c_e}{c_{e,0}}\right)^{1-\alpha} (1-\theta)^{1-\alpha}\theta^{\alpha}$ $\overline{\eta}_c = \frac{2RT}{F c_{e,0}}\left(1-t_+^0\right)(\overline{c}_e^p - \overline{c}_e^n)$ $\overline{\Delta\phi}_e = \frac{i_{app}}{\kappa_e(c_{e,0})}\left(\frac{L^n}{3\varepsilon_e^{n\,brug}} + \frac{L^s}{\varepsilon_e^{s\,brug}} + \frac{L^p}{3\varepsilon_e^{p\,brug}}\right)$ $\overline{\Delta\phi}_s = -\frac{i_{app}}{3}\left(\frac{L^p}{\sigma^p} + \frac{L^n}{\sigma^n}\right)$	

An illustration of the difference between the P2D model and the SPMe can be seen in Figure 2.3. As shown, the SPMe models just one active material particle per electrode, and the P2D model needs to model various particles to obtain an accurate solution.

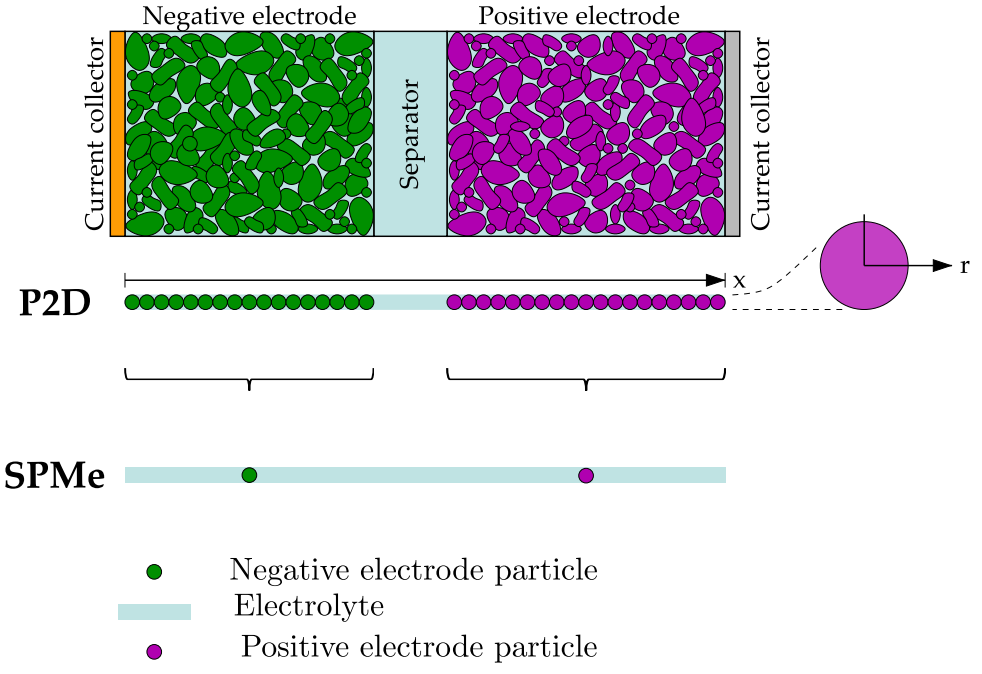

Figure 2.3: P2D vs SPMe representation.

To analyze how accurate the SPMe is compared to the SPM, various constant-current discharge simulations were performed and compared with the P2D model. The orthogonal collocation method was used to convert the PDEs of the models into ODEs, and the MATLAB® *ode15s* solver was used to perform the simulations. Figure 2.4 shows the simulation results for 2C, 1C, C/2 and C/5 CC discharges for an LG M50 battery cell. The parameters for the simulations were acquired from [49], and are specified in Appendix C.1.

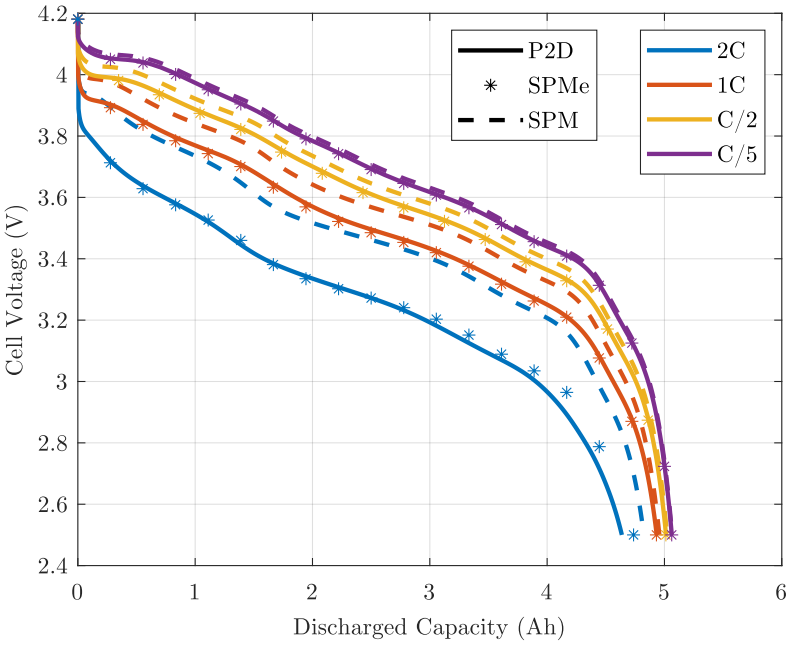

Figure 2.4: Cell voltage prediction comparison for 2C, 1C, C/2 and C/5 C-rates for an LG M50 cell between the P2D (solid lines), SPMe (markers) and SPM (dashed lines) models.

As can be seen in Figure 2.4, the SPMe is very accurate until the 2C simulation, were the errors become notorious at the end of the discharge. This error occurs because the SPMe is unable to represent the solid-phase concentration gradients across the negative electrode, and when the negative electrode OCP becomes more nonlinear, the average particle approach of the SPMe is not sufficient to represent it. It has to be noted that the maximum continuous discharging C-rate is of 1.5C (7.5 A) for the LG M50 cell, so it is not designed to work at much higher C-rates. High energy density cells, such as this one, have thicker electrodes than high-power density cells, making the single-particle approach less reliable for both SPM and SPMe models. For this reason, it is often claimed in the literature that the SPM and the SPMe are not able to give accurate results at high C-rates; however, this strongly depends on the type of cell that is being used.

To demonstrate that the SPMe can work appropriately at relatively high C-rates, the same type of discharge simulations were performed with a 28 Ah high-power cell. The

parameters of the cell were acquired from [47, 48], and are specified in Appendix C.2. The simulation results are shown in Figure 2.5. As can be seen, the voltage response of the SPMe can be very accurate until C-rates up to 5C, and the SPM can also be accurate at 1C. Since the electrodes of this cell are much thinner, the SPM and SPMe remain accurate until higher C-rates. Nevertheless, if a very high energy density cell is going to be used with high currents, maybe the P2D model would be a better option to better model the dynamics of the cell.

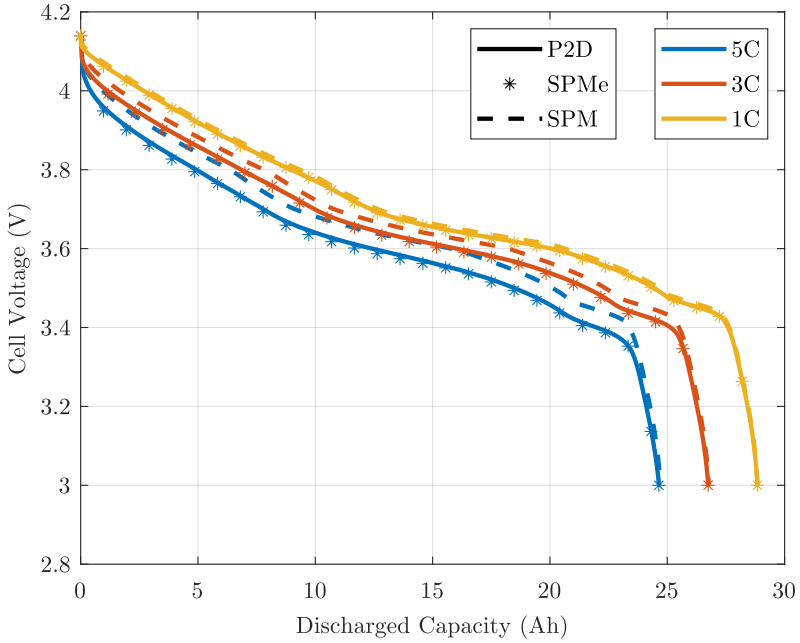

Figure 2.5: Cell voltage prediction comparison for 2C, 1C, C/2 and C/5 C-rates for an LG M50 cell between the P2D (solid lines), SPMe (markers) and SPM (dashed lines) models.

Summing up, the SPMe was proved to be much more accurate than the SPM, with a similar computational complexity. Therefore, it seems that the SPMe would be a better option than the SPM for most applications. When comparing these two models to the P2D model, it must be noted that the computational complexity of the P2D model is much higher, so it seems more reasonable to use the SPMe or the SPM for control oriented applications.

Chapter 3

BATTERY AGING PREDICTION

The research performed on battery aging modeling and prediction is discussed in this chapter. First, an overview of battery aging is given, explaining which are the effects of degradation in battery performance, which are the modes of degradation and how they affect in the performance of the battery, and which are the main aging mechanisms that can occur in lithium-ion batteries. After this overview, the importance of the degradation modes is highlighted, and a degradation mode estimation tool that was developed in our research group is introduced. Later, the modeling of degradation mechanisms is discussed, and a comparison is presented to evaluate which battery model should be used for aging prediction. Finally, the experimental study that was developed is presented, describing a new method to enhance the parameterization and improve the reliability of physics-based aging models.

3.1 LITHIUM ION BATTERY AGING OVERVIEW

As explained in Chapter 1, one of the biggest drawbacks of nowadays lithium-ion batteries is their aging. Aging occurs continuously in lithium-ion batteries, at any storage or working condition [22, 116]. However, depending on the chemistry and characteristics of the cell, and the operating conditions (SOC ranges, C-rates, temperatures...), batteries can suffer from different aging phenomena and at higher or lower rates [22, 116]. Therefore, it is of critical importance to optimize the usage of these batteries so they can last more while improving their performance.

3.1.1 Aging mechanisms, modes and effects

Battery aging can be analyzed at different levels or scales. As users, we often experience the consequences of battery aging when we notice that the battery of our cell phone does not last as long as it used to. The reason behind this capacity fade could be in different components of the battery. The amount of cyclable lithium inside the battery could have been reduced, some fraction of the electrode could have become inactive for lithium intercalation due to mechanical stresses or electrolyte dry-out. These form of degradation can be observed in the OCV of the battery using differential voltage [117] or incremental capacity [118] techniques for example. However, they are more difficult to measure comparing to capacity fade or power fade. The lowest level of degradation that can be analyzed are the actual physical phenomena that occur inside specific regions of the battery, which provoke LLI, LAM or impedance increase, consequently affecting the capacity and power capabilities of the cell. Figure 3.1 shows a summary of the predominant aging mechanisms that can occur in lithium-ion batteries.

The three scales of degradation forms are defined below:

- *Aging or degradation **mechanisms** are the physical phenomena that occur in battery cell components (in the electrodes and the electrolyte), causing battery aging. The mechanisms can be mechanical or chemical.*
- *The degradation **modes** are a method to group the degradation mechanisms depending on their impact on the kinetic and thermodynamic behavior of the cell.*
- *The degradation **effects** are the consequences of the mechanisms that can be directly observed in the cell performance. Which are mainly capacity fade and power fade.*

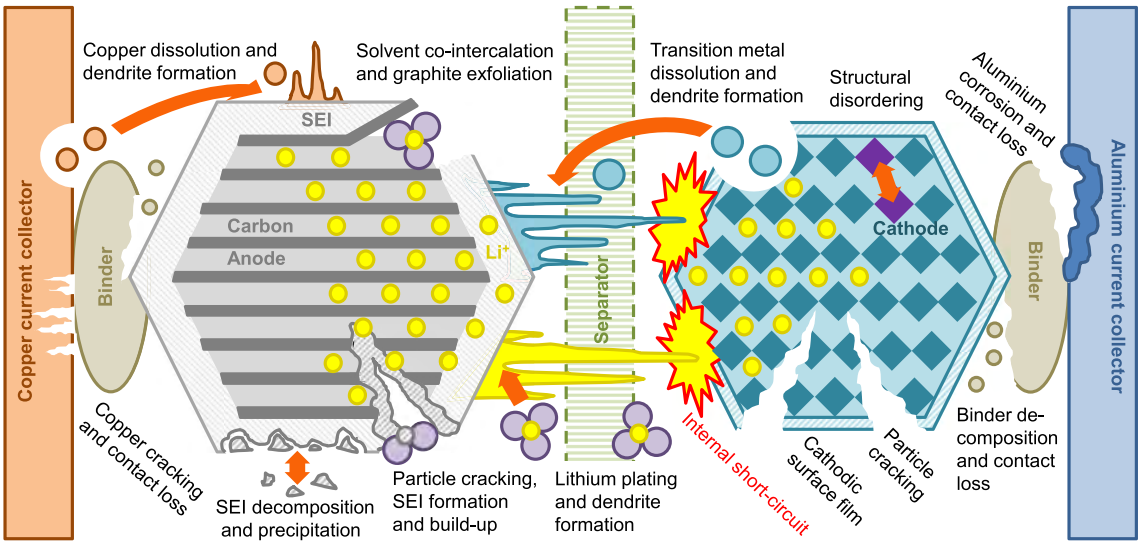

Figure 3.1: A graphical representation of the main degradation mechanisms that occur in Li-ion cells [119].

Extensive work has been done to analyze each of the degradation mechanisms that occur inside battery cells [22, 35, 119–125]. Nevertheless, many of them are not completely understood yet, and many others probably have not still been discovered. In this section, the most common aging mechanisms will be analyzed, defining to which observable degradation modes they impact and the effects they produce in cell performance. The three degradation modes that were defined are the following:

- ***Loss of Active Material (LAM)***. *It groups the mechanisms that reduce the active material available for electrochemical reactions, either on the positive or the negative electrode.*
- ***Loss of Lithium Inventory (LLI)***. *It groups the mechanisms that reduce the amount of cyclable lithium. This results in capacity fade and, depending on the mechanism, if a resistive film is formed, it may also result in power fade.*
- ***Impedance change***. *It groups the mechanisms that affect the kinetic behavior of the cell.*

The interplay between different mechanisms, modes and effects is summarized in Figure 3.2. Green squares denote the five principal degradation mechanisms that Edge *et al.* considered [22], and the red ones the secondary mechanisms. The gray squares contain the observable aging modes, and the two pink squares are the two degradation effects: power and capacity fade. The mechanisms related to the negative electrode are located in the blue rectangle (which are the most critical ones generally [116, 120, 122]), and below, in the

brown rectangle, the ones related to the positive electrode. As can be seen, the different aging mechanisms are closely related to each other, and one can help originating many others. This indicates how difficult it would be to model all the mechanisms together.

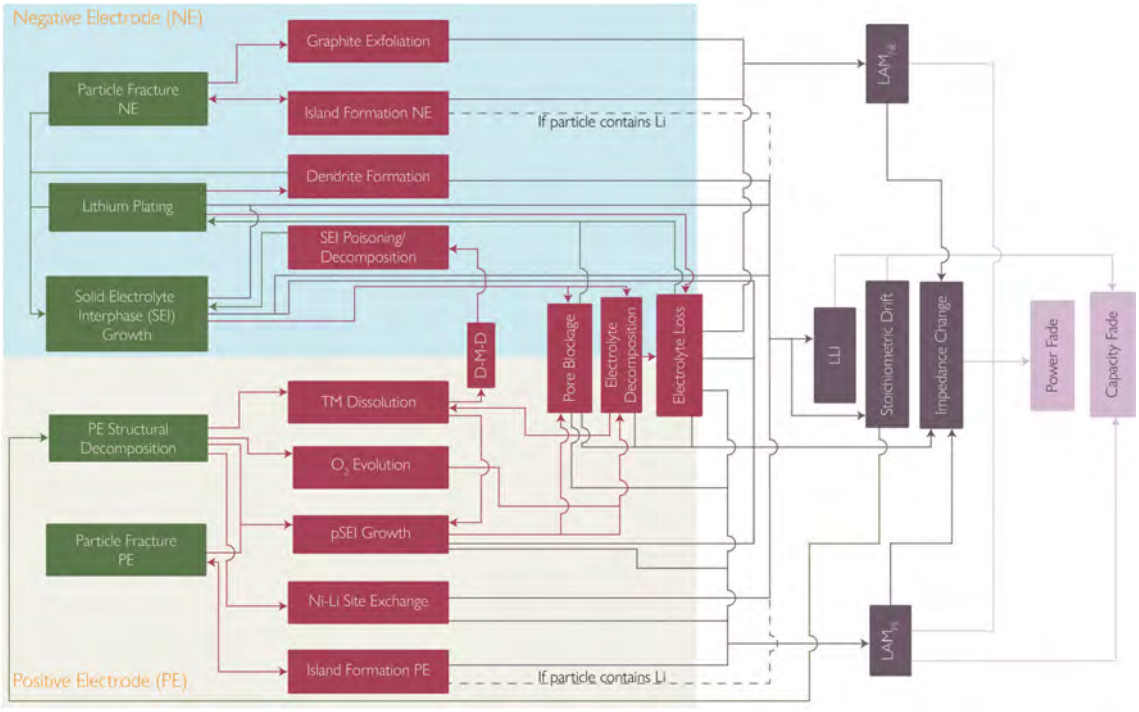

Figure 3.2: Diagram of how aging mechanisms contribute to each mode and the produced effects on cell performance [22].

The main degradation mechanisms are explained in the following lines, along with the relations that they have with other aging mechanisms. Besides, the working and storage conditions that accelerate or slow down these mechanisms are highlighted.

3.1.1.1 *Solid Electrolyte Interphase growth*

The SEI is a passivation layer formed of electrolyte reduction products (which generates electrolyte decomposition) when the liquid electrolyte comes into contact with the active material particles of the negative electrode [22, 126]. This layer stabilizes the reaction between the electrode and the electrolyte by acting as a "solid electrolyte" that enables the intercalation of lithium in the negative electrode while avoiding the fast decomposition of the electrolyte.

This SEI layer is first formed in the formation cycles of the cell, which are the first cycles that are made after assembling the cell [22]. As lithium needs to be consumed to form this layer, LLI takes place. The process results in approximately 10% loss of capacity [22], but it stops further electrolyte decomposition (and further capacity loss) coming from

the contact with the negative electrode. However, once the SEI layer is formed, it keeps growing, even if the battery is not used.

The rate at which this layer grows depends mostly on temperature [22]. At high temperatures, the diffusion rates increase, while making the SEI layer grow faster. In addition to temperature, high C-rates may also create cracks on particles, which increase the rate of SEI growth, as shown in Figure 3.2. Additionally, more side reactions could occur in the plated lithium to form additional SEI [127]. Furthermore, dissolved positive electrode transition metal ions could be deposited on the negative electrode. This continuous growth generates more LLI and consequent capacity fade. In consequence, a high imbalance can be generated between the positive and negative electrodes, accelerating the degradation of the positive electrode due to excessive delithiation at high SOCs. Besides, the continuous increase of the SEI layer can create pore blockage, reducing the porosity of the electrodes.

Peled [128] introduced the concept of SEI in 1979 as an electronically insulating and ionically conducting passivation layer. Since 1979, many experimental research has been made and diverse compounds have been observed within the SEI layer [129]. This makes difficult the understanding of the SEI growth mechanisms that happen in different conditions and in different chemestries [126]. Even the Li^+ transport through the SEI is still debated [126, 130]. This is illustrated in Figure 3.3.

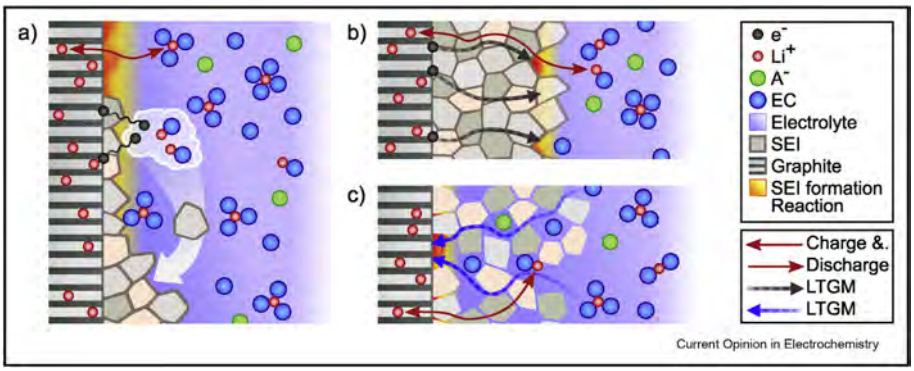

Figure 3.3: Initial SEI formation (a), long term SEI growth by transporting negative charge to the SEI/electrolyte interface (b), and alternatively, long term growth by the diffusion of the electrolyte through the electrode/SEI interface (c) [126].

In Figure 3.3 it is shown how, before the SEI layer is formed, electrons tunnel, electrolyte is reduced and the products of the reduction precipitate as solid film. After the film is formed, two alternatives are considered. In the first one, the electrons are transported from the electrode to the SEI/electrolyte interface, where the electrolyte is reduced. In the second one, the electrolyte is diffused towards the electrode/SEI interface, where the

reaction takes place. Since the mechanisms are not well established yet [126], it is difficult to define one model that describes the SEI growth for any cycling or storage condition.

3.1.1.2 *Lithium plating*

Lithium plating, like the SEI layer growth, is a side reaction that occurs in the negative electrode of lithium-ion batteries. Instead of intercalating into the negative electrode, lithium ions are plated on the surface of the negative electrode forming metallic lithium [131]. As well as being one of the main degradation mechanisms, especially in fast charging applications [22], it can also lead to safety issues [37]. The deposited lithium metal can grow in form of dendrites and perforate the separator resulting in a short circuit, and may cause a thermal runaway [132].

Lithium plating can be caused by fully lithiating the negative electrode, in which case the lithium ions have no option to intercalate into the electrode. However, this does not usually happen, since battery manufacturers add excess capacity in the negative electrode to prevent this. It is more common to generate plating by charging the battery with high C-rates or at low temperatures to high SOCs, in which case the electrostatic potential of the negative electrode may fall below the potential of a reference Li/Li^+ electrode [23,37,38]. In other words, the overpotential of the reaction may become negative, producing the plating reaction. However, lithium plating is not a completely irreversible reaction, and the plated lithium can be stripped through the inverse reaction, which is called stripping [20,21,34,37].

The fact that calendar aging affects very slowly at low temperatures [133], suggests that lithium plating does not occur when the cell is at equilibrium [22]. However, the results reported by Keil *et al.* [134] suggest that the resting periods after fast charging the cells may favour the irreversible lithium deposition instead of the stripping reaction.

The irreversible lithium plating occurs when the plated metallic lithium reacts with the electrolyte to form SEI [18,135]. This SEI layer can isolate the lithium electrically, making it unable to be recovered. This "dead lithium" affects to the LLI mode, as well as the SEI layer generated due to this reaction, and both of them reduce conductivity through pore clogging [18].

3.1.1.3 *Particle cracking and mechanical LAM*

Particle cracking, or particle fracture, is a mechanical degradation mechanism that happens in both electrodes. It is originated by the volume changes that occur in the electrodes due to the stress generated by the intercalation and de-intercalation of lithium

ions [136,137]. This volume changes are very notorious in high specific capacity graphite-Si electrodes, since Si can reach over 300% volume expansion during lithiation [124], creating considerable compressive stress. In delithiation, electrode materials shrink, generating tensile stresses, what can originate battery material fractures. These fractures can lead to electrode pulverization, separating active material from the electrode (island formation), and therefore loosing active material. Also, they might create new surfaces that are in contact with the electrolyte. These new surfaces may react with the electrolyte building new species, accelerating SEI generation [22,138], and consequently loosing lithium inventory and capacity. Furthermore, the volume expansions and contractions can originate loss of electrical contact, increasing their contact and charge transfer resistances [22,122], what generates impedance rise and power fade.

Particle fracture is one of the main contributors in battery degradation [138]. For example, the fragmentation of secondary particles (a form of crack between the primary and the secondary particles) has been observed to be the major degradation mechanism in NMC and NCA cathodes [139–141].

Since particle cracking is originated by electrochemical activity, and higher local current densities are given near the separator, local particle fragmentation has been found close to the separator [137,139]. High currents, and high and low temperatures can also accelerate fracture. At high temperatures more thermal stress is generated, and at low temperatures graphite becomes more fragile and prone to fracture. Besides, since particle cracking is closely related to volume changes, high depth-of-discharges (DODs) will accelerate this phenomenon, as the active particles will be expanded and contracted more, especially in graphite-Si electrodes.

3.1.1.4 *Positive electrode structural change and decomposition*

Positive electrode degradation highly depends on its chemistry. Figure 3.2 shows the main degradation mechanisms for NMC electrodes. Lithiation/delithiation in the positive electrode active material originate stresses that can cause strains called phase transitions [10,22,122]. The layered active material structures can decompose into spinel and rock salt phases, changing the electrode structure and its mechanical properties. Consequently, a passivation layer is formed at the surface of the positive electrode, and generation of different gaseous products can occur. This phenomenon leads to capacity fade. Delithiated states (high cell SOC) enhance these phase transitions [22], as well as high C-rates [10].

Mechanical stresses may also lead to structural disordering, where the crystal structures of the positive electrode are modified by switching lithium atoms with other transition metal atoms of similar ionic radius [22]. This can cause lithium to get trapped, generating LLI, LAM, impedance rise and consequently, capacity and power fade.

In electrode chemistries where nickel can be found, such as NCA or NMC, electrolyte decomposition can occur if highly oxidized nickel contacts the electrolyte. In this case, nickel is dissolved in the electrolyte and surface films are formed on the electrodes [22]. This causes impedance rise and power fade. Furthermore, moisture can react with the electrolyte to form acidic species. These acids can then react with the positive electrode material, dissolving positive electrode active materials, what can poison the negative electrode SEI layer and contribute to the growth of the positive electrode SEI (pSEI).

The pSEI mechanism is very similar to the negative electrode SEI mechanism. Principally, it is formed in the first cycles of the cell [22], however, if it is unstable, continues growing. It is formed by the dissolution products generated by the positive electrode and the electrolyte, which generates LAM. It contributes to the electrolyte decomposition, rising the electrolyte impedance and generating power fade.

The different degradation mechanisms that can occur in the negative electrode, their impact in cell performance and the factors that can reduce or enhance these mechanisms were summarized by Vetter *et al.* as it is shown in Table 3.1. The same information is given for the positive electrode aging mechanisms in Table 3.2.

3.2 AGING MODELING

The understanding and modeling of these degradation phenomena is key to prolong the lifetime of batteries, as well as for the development of advanced control strategies that mitigate aging [122]. As a consequence, physics-based battery aging modeling has been an active research topic in the last years [18, 20, 21, 23, 34–36, 39, 142–146]. Unlike empirical models, which predict the measurable effects of the battery as capacity loss or power fade, physics-based aging models describe specific degradation mechanisms to predict the effects of battery aging, representing with more detail the physical phenomena that will deteriorate the battery.

As mentioned above, several degradation mechanisms can occur in lithium-ion batteries [22, 116], and it would be very difficult, if not impossible, to model all the degradation mechanisms accurately. Therefore, it is essential to select the key degradation mechanisms

Table 3.1: Negative electrode aging causes, effects and influences [120].

Cause	Effect	Leads to	Reduced by	Enhanced by
Electrolyte decomposition (→ SEI) (Continuous side reaction at low rate)	Loss of lithium Impedance rise	Capacity fade Power fade	Stable SEI (additives) Rate decreases with time	High temperatures High SOC (low potential)
Solvent co-intercalation, gas evolution and subsequent cracking formation in particles	Loss of active material (graphite exfoliation) Loss of lithium	Capacity fade	Stable SEI (additives) Carbon pre-treatment	Overcharge
Decrease of accessible surface volume changes, SEI formation and growth	Impedance rise Overpotentials	Power fade	External pressure Stable SEI (additives)	High cycling rate High SOC (low potential)
Changes in porosity due to volume changes, SEI formation and growth	Impedance rise Overpotentials	Power fade	External pressure Stable SEI (additives)	High cycling rate High SOC (low potential)
Contact loss of active material particles due to volume changes during cycling	Loss of active material	Capacity fade	External pressure	High cycling rate High DOD
Decomposition of binder	Overpotentials Impedance rise Inhomogeneous distribution of current and potential	Power fade Enhances other aging mechanisms	Current collector pre-treatment(?)	Overdischarge Low SOC (high potential)
Metallic lithium plating and subsequent electrolyte decomposition by metallic lithium	Loss of lithium (Loss of electrolyte)	Capacity fade (power fade)	Narrow potential window	Low temperature High cycling rates Poor cell balance Geometric misfits

that are the most important to model battery aging adequately. For example, Yang *et al.* [18] used an SEI layer growth model and a lithium plating model that caused a porosity decrease in the negative electrode to justify the nonlinear capacity decay behavior shown in their experimental tests. The same argument was used by Atalay *et al.* [35]. However, these works did not show empirical evidence that the cell was really aging because of the SEI layer growth and the generation of lithium plating. This lack of validation occurs in most of the models presented in the literature [18,35,39,143–146]. While aging mechanisms are modeled using physical equations with physical meaning, the validation and parameter fitting processes are usually performed against capacity measurements, as it is done for empirical models, making the prediction of these models less reliable.

Additional information to the capacity measurements would be needed to improve the validation and parameterization processes. In that regard, invasive methods may be used to measure the SEI layer thickness [147] or the amount of plated lithium [148]. However, these kind of methods would require extensive and complicated experimental work with sophisticated equipment. Therefore, the mid-term solution that was proposed in this

Table 3.2: Positive electrode causes, effects and influences [10].

Cause	Effect	Leads to	Enhanced by
Phase transitions	Crackin of active particles	Capacity fade	High rates, high/low SOC
Structural disordering	Lithium sites lost and lithium trapped	Capacity fade	High rates, high/low SOC
Metal dissolution and/or electrolyte decomposition	Migration of soluble species,	Capacity fade	High/low SOC, high temperature
	Re-precipitation of new phases,	Power fade	
	Surface layer formation	Power fade	
Electrolyte decomposition	Gas evolution		High temperature
Binder decomposition	Loss of contact	Power fade	
Oxidation of conductive agent	Loss of contact	Power fade	
Corrosion of current collector	Loss of contact	Power fade	High SOC

work is to use degradation mode estimates to fit physics-based aging model parameters, and to validate the aging models. The degradation modes estimation procedure that was employed is explained in the following subsection 3.2.1. This method is not able to confirm the existence or the quantities of specific degradation mechanisms, however, it can give information about the type of degradation that happened in the cell; such as LLI or LAM in an electrode. Consequently, the degradation model should be able to adjust well the OCV relation of the cell, and should be able to capture degradation knee trajectories than a capacity-based parameterized model. Furthermore, including higher current cell capacity data (*e.g.* C/5 discharge data) to the parameterization process, the impedance increase can be captured, adding more information and increasing the reliability of the aging model.

In addition to the parameterization process, it is crucial to select the appropriate aging models to represent the aging behavior of a battery. For example, if several LAM is observed in the positive electrode, some mechanism that describes this mode of degradation should be included. Besides, the tendencies of degradation modes can provide information on what mechanisms should be modeled. For example, if the LLI represents a sublinear tendency, the corresponding model for LLI generation should be able to represent this same tendency.

Summing up, with the goal of describing battery aging with more reliability, more physical insight was added to the model selection and parameterization process using degradation mode data.

3.2.1 Degradation mode estimation

The degradation mode estimation tool (ModEst) that was used in this thesis was developed by Sergio Fernandez in Mondragon Unibertsitatea, and a paper was sent for publication in the IEEE ECCE 2024 conference [149].

The tool performs a multi-objective optimization using a genetic algorithm. The multi-objective optimization seeks to minimize the root-mean-square (RMS) errors of the OCV and differential voltage curves, using OCV and BOL OCP data. For that, the algorithm adjusts the 0 % and 100 % SOC stoichiometry values of both electrodes, as well as the total capacities of the electrodes. These stoichiometry values and the electrode capacities are then used to calculate LLI and LAM values. The flowchart of the algorithm is shown in Figure 3.4. The algorithm was validated using different cell chemistries, in simulation and experimentally. Some validation results are shown in Appendix D.

3.3 ANALYSIS OF BATTERY MODELS FOR AGING PREDICTION

The core of this section was published in [75].

One of the first steps that has to be considered when designing a physics-based degradation model is to decide which battery model will be used to couple the degradation mechanisms together. With that question in mind, a comparative study was developed to investigate how accurately would the SPMe represent battery aging compared to the P2D model. As shown in Section 2.4, the SPMe can be a good alternative of the P2D model

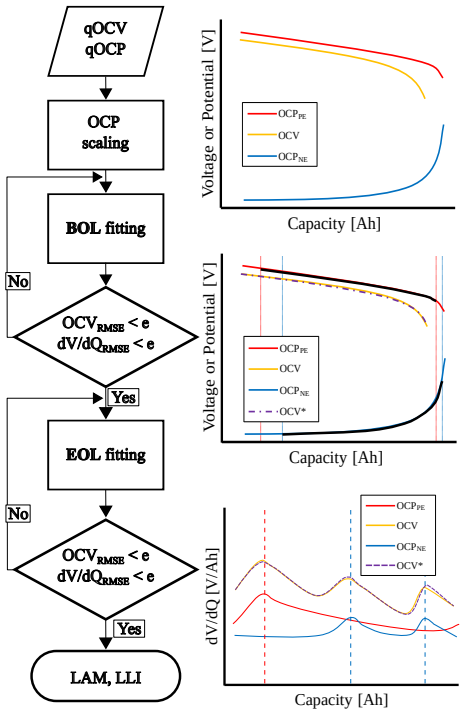

Figure 3.4: Flowchart of the mode estimation tool.

for many applications, since it reduces significantly the computational cost and can be accurate representing the behavior of the battery.

In order to compare the models for many aging mechanisms and have a "realistic" aging representation, the model developed by O'Kane *et al.* [24] was coupled with the SPMe and P2D models, which is probably one of the most complete physics-based aging model that was proposed in the literature, as it considers four degradation modes (LLI, $\mathrm{LAM_n}$, $\mathrm{LAM_p}$ and impedance change). The model considers four degradation mechanisms: SEI layer growth, lithium plating, particle cracking and LAM due to mechanical stress. The last two mechanisms in both electrodes. A representation of the degradation mechanisms implemented in the negative electrode of both models can be seen in Figure 3.5. In the top side of the figure the implementation for the P2D model can be seen, and in the bottom side the implementation for the SPMe. Note that the SPMe models just one average particle, however, since we can calculate the electrolyte concentration and both potentials at any point of the electrode, we can represent the different lithium plating and SEI growth values along the electrode, as in [150]. On contrary, since the solid concentration, c_s is used for the LAM model and for the cracking model, just one average value can be calculated for the entire electrode.

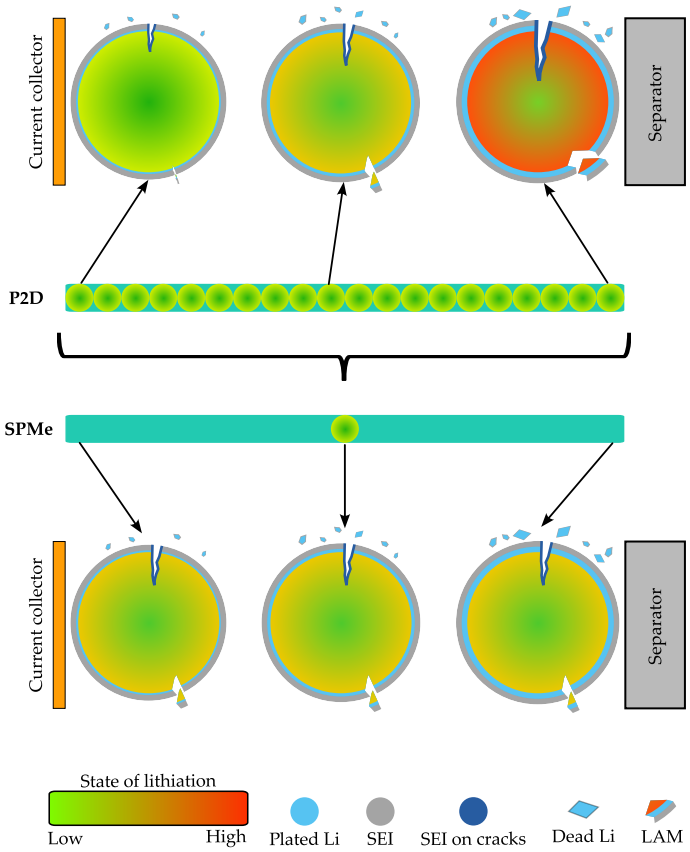

Figure 3.5: Aging model summary for the P2D and SPMe models.

3.3.1 SEI layer growth model

As explained in Section 3.1, SEI layer growth is believed to be one of the most dominant mechanisms in battery aging [22]. Many different models were proposed to explain the long-term growth of the SEI layer [126]: solvent diffusion limited [31, 151], kinetically limited [30], electron tunneling [152]... Among the different models, the solvent diffusion limited model was shown to give one of the best fits to the experimental capacity evolution over time, specially in storage conditions [22]. Hence, a diffusion limited model was used to model the SEI layer growth. This model has a square root of time dependency that results in a sublinear aging trajectory prediction.

The SEI model that was used is based on the work by Single *et al.* [151]. It is assumed that the SEI layer thickness is homogeneous through the surface of the particle. The flux density of the side-reaction is defined by

$$j_{SEI} = -FD_{sol}(T)\nabla c_{sol}, \tag{3.1}$$

where $D_{sol}(T)$ is the diffusion coefficient of the solvent and c_{sol} is the solvent concentration. The solvent concentration at the particle/SEI interface is considered to be zero, and equal to $c_{sol,0}$ (the solvent concentration at the electrolyte) at the SEI/electrolyte interface. Therefore, the equation is rewritten as

$$j_{SEI} = -FD_{sol}\frac{c_{sol,0}}{L_{SEI}}. \tag{3.2}$$

The SEI layer thickness is defined as

$$\frac{\partial L_{SEI}}{\partial t} = \frac{c_{sol,0}D_{sol}V_{SEI}}{L_{SEI}}, \tag{3.3}$$

where V_{SEI} is the mean partial molar volume of the SEI. The consequent voltage decay due to the impedance of the SEI layer is modeled as

$$\eta_{SEI} = \rho_{SEI}L_{SEI}\frac{j}{a_s^n}, \tag{3.4}$$

where ρ_{SEI} is the electrical resistivity of the SEI layer. j is the total lithium flux density, which adds the intercalation flux density and the side reactions' flux density:

$$j = j_{int} + j_{SR}. \tag{3.5}$$

The lithium flux density of the side reactions takes into account three contributions in this model: the flux density that contributes to the SEI layer growth, j_{SEI}, the lithium plating flux density, j_{pl}, and the flux density for the SEI growth on cracks, $j_{SEI,cr}$. These three contributions are taken into account in the side reactions' flux density j_{SR} as

$$j_{SR} = j_{SEI} + j_{pl} + j_{SEI,cr}. \tag{3.6}$$

The SEI layer growth, lithium plating and SEI on cracks mechanisms generate LLI, which is represented in the model by these parasitic flux densities. j_{SR} reduces the intercalation flux density, generating a difference between the de-intercalated lithium in the positive electrode and the intercalated lithium in the negative electrode while charging the cell.

3.3.2 Lithium plating model

The next degradation mechanism that was included for the analysis is the lithium plating. Different plating models can be found in the literature, and they can be principally divided between irreversible [18, 35] and reversible plating models [23, 26, 34]. Reversible models allow the stripping reaction once the lithium plating reaction has occurred, while irreversible models do not. The plating model that was used for the analysis was developed by O'Kane *et al.* [24]. The main difference of this model respect to the previously reported reversible models is the consideration that some amount of the plated lithium may become dead lithium, generating an irreversible loss of lithium.

The plating/stripping flux density is given by:

$$j_{pl} = k_{pl}\left(c_{pl}exp\left(\frac{F\alpha_{a,pl}\eta_{pl}}{RT}\right) - c_e exp\left(-\frac{F\alpha_{c,pl}\eta_{pl}}{RT}\right)\right), \tag{3.7}$$

where k_{pl} is the plating reaction rate, c_{pl} is the plated lithium concentration, $\alpha_{a,pl}$ and $\alpha_{c,pl}$ are the anodic and cathodic transfer coefficients respectively and η_{pl} is the lithium plating overpotential, which is given by

$$\eta_{pl} = \phi_s - \phi_e - \eta_{SEI}. \tag{3.8}$$

The plated lithium concentration is calculated as

$$\frac{\partial c_{pl}}{\partial t} = -a_s^n j_{pl} - \gamma c_{pl}, \tag{3.9}$$

where c_{pl} is the plated lithium concentration and γ is the decay rate for the plated lithium. The dead lithium concentration depends directly on the plated lithium concentration, and is modeled as

$$\frac{\partial c_{dl}}{\partial t} = \gamma c_{pl}. \tag{3.10}$$

The decay rate is given by

$$\gamma = \gamma_0 \frac{L_{SEI,0}}{L_{SEI}}, \tag{3.11}$$

where $L_{SEI,0}$ is the length of the SEI layer at BOL, and γ_0 is the initial decay rate for $L_{SEI} = L_{SEI,0}$.

3.3.3 Particle cracking model

The particle cracking model is based on the stress coupled diffusion equation proposed by Zhang *et al.* [153]:

$$\frac{\partial c_s}{\partial t} = D_s \left[\frac{\partial^2 c_s}{\partial r^2} + \frac{2}{r}\frac{\partial c_s}{\partial r} + \theta \left(\frac{\partial c_s}{\partial r} \right)^2 + \theta c_s \left(\frac{\partial^2 c_s}{\partial r^2} + \frac{2}{r}\frac{\partial c_s}{\partial r} \right) \right], \tag{3.12}$$

where $\theta = \frac{\Omega}{RT}\frac{2\Omega E}{9(1-\nu)}$. Therefore, Equation 2.1 was substituted by Equation 3.12, and the boundary condition 2.3 by

$$D_s(1+\theta c_s)\frac{\partial c_s}{\partial r}\bigg|_{r=R_s} = -j. \tag{3.13}$$

This way, the stress induced by the Li intercalation process is taken into account in the diffusion model.

The particle cracking model is based on the work by Deshpande *et al.* [154]. It assumes identical micro cracks occurring on the surface of the electrode particles. Paris' law [155] is used to model crack length due to mechanical fatigue

$$\frac{\mathrm{d}l_{cr}}{\mathrm{d}t} = \frac{k_{cr}}{t_0}\left(\sigma_t b_{cr}\sqrt{\pi l_{cr}}\right)^{m_{cr}} \quad \sigma_t > 0, \tag{3.14}$$

where k_{cr} is the cracking rate, m_{cr} is the Paris' law exponential term, b_{cr} is the stress intensity factor correction, t_0 is the time needed for one cycle and σ_t is the tangential stress at the surface particle, calculated as

$$\sigma_t = \frac{\Omega E}{1-\nu}(\bar{c}_s - c_{s,e}) \tag{3.15}$$

where E is the Young's modulus, ν is the Poisson's ratio and $\bar{c}_s$ is the average solid concentration. The parameters k_{cr}, m_{cr} and b_{cr} are constants determined from experimental data. The crack surface area to volume ratio is calculated as

$$a_{cr} = 2 l_{cr} w_{cr} \rho_{cr}, \tag{3.16}$$

where w_{cr} and ρ_{cr} are the particle crack width and particle crack number per unit area, which are considered to be constant.

An average SEI growth layer was modeled in the crack surfaces. For that, a new term was added to the diffusion limited SEI model shown in Equation 3.3 to consider the new crack area with smaller SEI layer:

$$\frac{\partial L_{SEI,cr}}{\partial t} = \frac{c_{sol,0} D_{sol}(T) \bar{V}_{SEI}}{L_{SEI,cr}} + \frac{\partial l_{cr}}{\partial t} \frac{L_{SEI,cr0} - L_{SEI,cr}}{l_{cr}}, \tag{3.17}$$

where $L_{SEI,cr}$ is the length of the SEI layer on the particle and $L_{SEI,cr0}$ is the initial SEI layer length in the newly formed crack surface, which can be defined as a thinner initial SEI layer; e. g. $L_{SEI,cr0} = L_{SEI,0}/10000$. The first term will make the SEI layer grow as in the SEI model described by Equation 3.3, and the second term will make the average crack SEI thickness decrease due to the increase in the crack length, l_{cr}.

3.3.4 Loss of active material model

As explained in Section 3.1, several aging mechanisms result in LAM [22], such as electrolyte decomposition and loss, positive electrode dissolution [156] or particle fractures and contact losses due to mechanical stresses [22]. In the LAM model that O'Kane *et al.* [24] used, active material is lost as a consequence of particle cracking, as was proposed by Laresgoiti *et al.* [33]. The reduction of the active material volume fraction is modeled as

$$\frac{\partial \varepsilon_s}{\partial t} = \frac{\beta}{t_0} \left(\frac{\sigma_h}{\sigma_c} \right)^{m_2}, \tag{3.18}$$

where β and m_2 are two fitting constants, σ_c is the critical stress and the hydrostatic stress, σ_h is calculated as

$$\sigma_h = \frac{\sigma_r + 2\sigma_t}{3}, \tag{3.19}$$

where σ_r is the radial stress. However, since the LAM is calculated with the stress values at the surface of the particle, σ_r equals 0.

3.3.5 Porosity change

As the SEI and lithium plating layers grow, the porosity of the negative electrode decreases. This is an important effect for the prediction of battery aging, since the decrease

in the porosity can produce "knees" in the aging trajectory of lithium-ion batteries [18,157]. This is modeled by

$$\frac{\partial \varepsilon_e}{\partial t} = a_s^n \frac{\partial L_{film}}{\partial t}, \tag{3.20}$$

where L_{film} represents the added lengths of the SEI layer and the plating layer:

$$L_{film} = L_{SEI} + L_{pl}. \tag{3.21}$$

The length of the SEI layer is given by Equation 3.3, the length of the SEI layer in the particle cracks is calculated by multiplying the specific surface area of the crack to the length of the SEI layer on the crack, and the length of the plating layer is given by

$$L_{pl} = \frac{c_{pl} + c_{dl}}{a_s^n} V_{Li}, \tag{3.22}$$

where V_{Li} is the partial molar volume of the lithium.

3.3.6 Aging prediction comparison: P2D vs. SPMe

The above-explained aging model was implemented in the P2D and SPMe models to compare the prediction accuracy of both models. The orthogonal collocation method was used to discretize the PDEs and the MATLAB® *ode15s* solver was used to integrate the simulations in time. The cell parameters that were used correspond to a Kokam 1.25 Ah cell and were acquired from [50], summarized in Appendix C. The parameters for the degradation models correspond to the "default values" of [24], except for the solvent diffusion coefficient, which was set to 2.5×10^{-21} $\mathrm{m^2 s^{-1}}$.

Two main aspects were studied in the comparison: the prediction accuracy and the computational cost. To analyze the prediction accuracy, different cycling conditions were simulated, comparing the capacity evolution and the internal variable predictions. In order to analyze the computational cost, the simulation times for the different conditions were evaluated, and the convergence of both models was examined.

3.3.6.1 *Capacity prediction*

One of the most important variables that an aging model should predict accurately is the evolution of capacity of the cell under different operating conditions. In order to see how comparable are the predictions of the P2D and SPMe models, different simulations

were performed. Figure 3.6 shows the evolution of the C/3 discharge capacity of the cell for three different cycling cases with CCCV charging and constant-current (CC) discharging protocol. The capacity was measured by saving the state-vector of the simulation at the end of charge of every 10 cycles, later simulating the C/3 discharges and integrating the discharged current. The end of the simulations was defined by calculating the capacity at the end of every discharge and comparing it to the capacity of the discharge of the first cycle. Once the discharge capacity reached the 80 % SOH value, the simulation is terminated. Since these capacities are calculated from the cycling discharges, they do not match with the 80 % SOH value of the C/3 discharges of Figure 3.6.

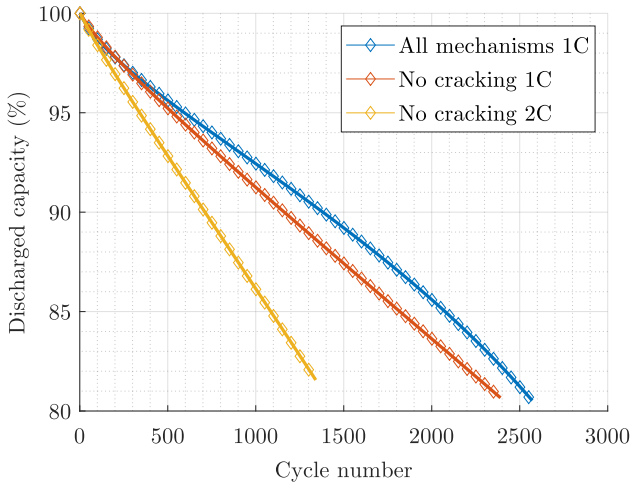

Figure 3.6: Discharged capacity fade comparison:P2D results with solid lines; SPMe results with markers.

The solid lines of Figure 3.6 represent the P2D simulation results, while the markers represent the SPMe results. The simulations in blue were performed with all the mechanisms activated, using 1C constant currents for charging and discharging, and the cut-off current for the constant-voltage (CV) step was set to C/20. The simulations in orange and yellow were carried out without including the particle cracking model. The main reason for this is the computational time required for this model. Since the cracking model can become unstable if the solver is not properly adjusted, a maximum step-time of 1 s was defined to the solver. In this way, the simulation times become much bigger since the variable time-step *ode15s* solver is limited to this maximum step-time.

As can be observed, the capacity prediction of the SPMe is very accurate for the three cases. In the first case, the three phases of battery aging trends can be seen: a sublinear tendency in the first cycles, a linear evolution in the middle and a superlinear behavior (or a “knee”) in the end. The second case shows sublinear and linear tendencies, and the third

one shows a completely linear behavior. It is important to notice that the SPMe model is able to represent the three different tendencies accurately in all these cases.

3.3.6.2 *Internal variable prediction*

As stated above, the main advantage of PBMs compared to empirical or machine learning models is the amount of physical information that can be obtained, thus, it is important to compare the internal variables' behavior for these simulations. The evolution of six aging variables, as well as the positive and negative electrode solid-phase concentrations and the C/3 discharge cell voltage curves, is shown in Figure 3.7. These results were obtained from the above discussed simulation that has all the analyzed mechanisms integrated. The variable values are shown for the entire thickness of the electrode and at different simulation times.

Figure 3.7 a) shows the SEI layer thickness evolution. As explained, the SEI layer growth model calculates the thickness of the layer taking into account constant solvent concentrations at the SEI/electrolyte interface and at the particle/SEI layer interface. Therefore, as can be seen, the response of both models is very similar, since the only variable that changes from the P2D model to the SPMe is the time that takes each model to complete the cycles.

Figure 3.7 b) shows the evolution of dead lithium. As can be observed, the accuracy of the SPMe drops near the separator. The reason for this could be the higher concentration gradients that are generated near the separator while the cell is being charged. This is illustrated in Figure 3.5 with the color gradients that are indicated inside the particles. The P2D is able to represent the different concentration gradients at different electrode positions but the SPMe is not. The solid concentration values are shown in Figure 3.7 g) and h). As mentioned, the results of the solid concentrations in the SPMe are constant for the entire electrode, and this generates some inaccuracies in the degradation variables that depend on c_s. This is the case of the particle cracking model. Figure 3.7 c) shows the particle crack length results in the negative electrode. The SPMe cannot model the different particle crack lengths that models the P2D for different positions. However, it can be seen that the values of the SPMe are very close to an average value of the P2D. The same happens for the LAM values at Figures 3.7 e) and f). Since the average solid concentration value is accurate, the average degradation variable values are accurate, but it is not able to represent the gradient across the electrode.

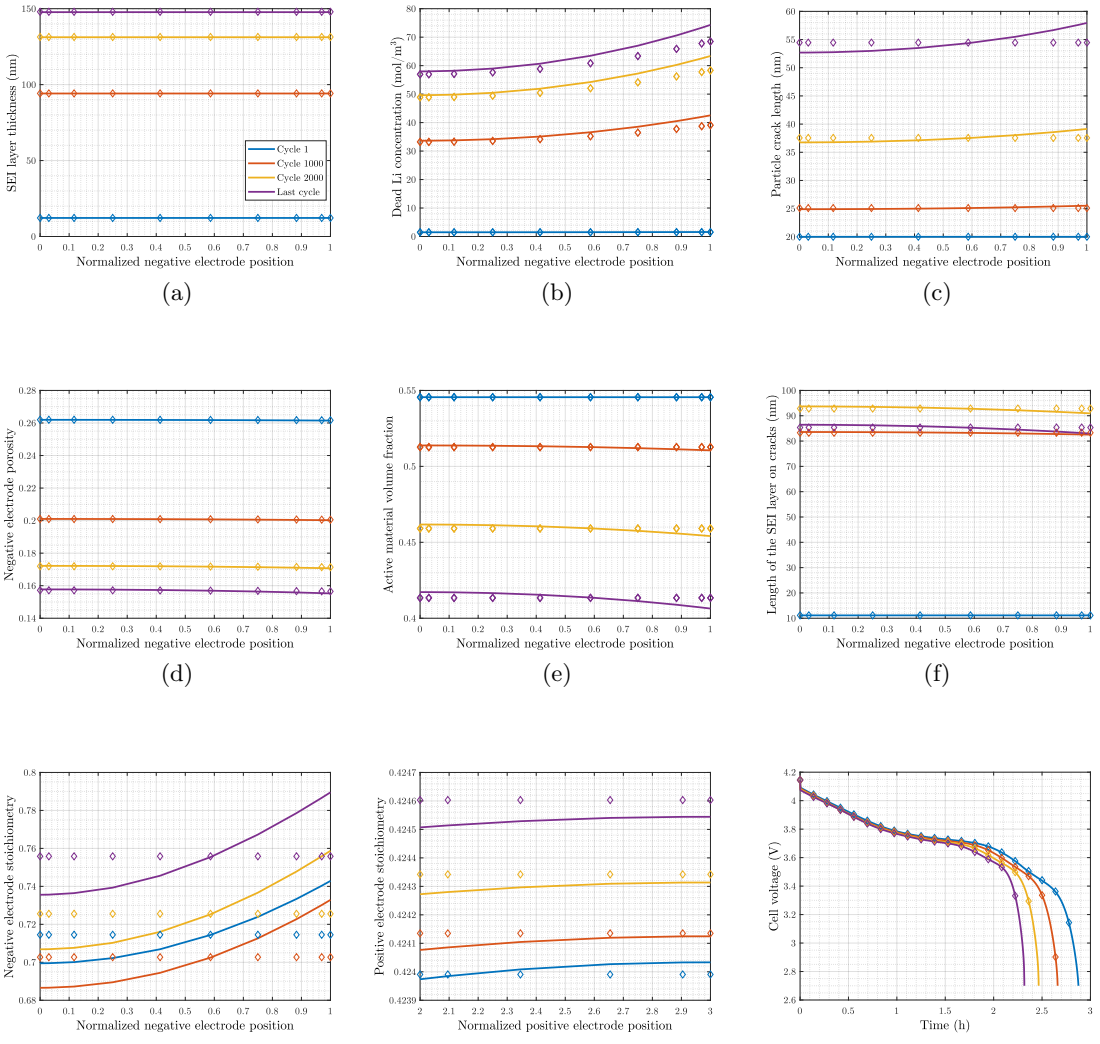

Figure 3.7: Internal aging variable comparison. Solid lines represent the results of the P2D model, and the markers represent the results of the SPMe. In blue the results for the first cycle, in orange the results for the cycle 1000, in yellow for the cycle 2000 and in purple for the last cycle.

Figure 3.7 f) shows the SEI layer growth on cracks. As can be observed, the SEI layer thickness is smaller in the last cycle than in cycle 2000. This phenomenon occurs because the average SEI layer on cracks model of O'Kane *et al.* [24] has two terms: one that makes the layer grow due to solvent diffusion; and another one that makes the average SEI layer decrease due to the increase in particle crack length, creating new surfaces with smaller SEI layer lengths. As can be seen in Figure 3.7 c), the crack length increases exponentially, making the negative term bigger than the positive term. This was also reported by O'Kane *et al.* [24]. The exponential increase in the crack length generates a rapid LLI, which is the cause to see the superlinear aging tendency that is shown in Figure 3.6.

In Figure 3.7 i), the voltage curves of the C/3 discharges that were used to measure capacity are shown. As can be observed, the cell voltage prediction of the SPMe remains accurate at the different points of the aging simulation.

3.3.6.3 *Computational cost analysis*

Regarding the computational cost, the first item that was examined is the time that each model consumed to simulate the three above-mentioned conditions that were studied. The simulations were carried out in a desktop computer with 8 GB of RAM and an Intel®Core™ i7-8700 CPU of 3.20 GHz. Table 3.3 shows the simulation times required for the three cases. As mentioned, the first case requires much more time due to the maximum step-time defined to the solver in order to solve the particle cracking model.

Table 3.3: P2D and SPMe models' simulation times for the aging simulations.

	All 1C	No cracking 1C	No cracking 2C
P2D	19.44 h	11.07 h	6.97 h
SPMe	12.21 h	1.88 h	1.19 h

Aside from the increase in computational time of both models due to the cracking model, it can be observed that the SPMe finishes the simulations between 5 and 6 times faster than the P2D model.

In addition to the reduced computational times required by the SPMe, there is another advantage in using the SPMe instead of the P2D model: robustness. The P2D model is a stiff system of PDAEs that makes its resolution very hard numerically [82]. Whereas once a MOR method is applied (as the FDM, the FEM, the orthogonal collocation method...), the SPMe becomes a well-conditioned system of ordinary differential equations [82]. In order to analyze this difference, a comparison between the number of iterations required to

solve each charging and discharging step is shown in Figure 3.8. As can be seen, the P2D model requires many more steps than the SPMe for every cycle, which shows the better convergence of the SPMe. This is specially notorious in the charging steps, probably due to the CV phase involved, and the additional constraint that is used to solve these phases.

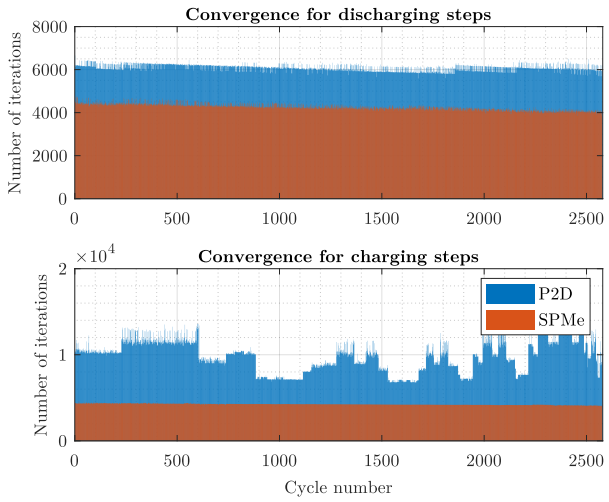

Figure 3.8: Number of iterations needed to compute each discharging and charging step.

3.3.6.4 *Aging parameter fitting*

As explained in Section 3.1, one of the main difficulties when using physics-based aging models is the parameterization of the aging parameters, since they are very hard to measure. Therefore, the aging parameters of PBMs have to be fitted to some experimental data in order to obtain an accurate model. For example, these parameters can be fitted to capacity fade experimental data as in [18, 35].

To evaluate the accuracy and computational time of the SPMe in fitting the aging parameters of a physics-based aging model, the SEI growth model was used to fit the simulated capacity fade to experimental capacity data. A Kokam 1.25 Ah pouch cell of the same batch as the ones used for the parameter measurements of [50] was used for the experiments. The experiments were performed by Dr. Laura Oca at 25 ºC with a Basytec XCTS cycler. The cycles were done between 2.7 V and 4.2 V with 1 C CC charge and discharges with no rest times. Between the cycles, check-up tests that consisted on doing 3 cycles at CC charge and discharge at C/5 current were made. The last discharge cycle was used to measure the capacity.

The MATLAB® particle swarm algorithm was used for the optimization procedure. These optimizations were performed in a workstation with 256 GB of RAM and 2 Intel®Xeon®CPUs E5-2640 v4 of 2.40 GHz. The results for the fitting parameter D_{sol} and

the simulation times can be seen in Table 3.4. The capacity fade simulation results with the fitted parameter for both models are shown in Figure 3.9, as well as the experimental data.

Table 3.4: Optimization results of the P2D and SPMe models.

	D_{sol} (m^2s^{-1})	Time (h)
P2D	3.6596×10^{-20}	62.03
SPMe	3.657×10^{-20}	3.13

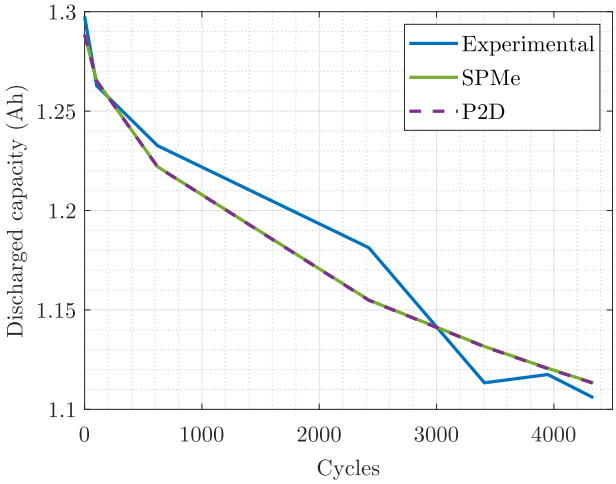

Figure 3.9: Experimental and simulated capacity evolution.

As can be seen in Figure 3.9, the resulting aging models are almost identical, and the simulation times of Table 3.4 show that the SPMe is much faster than the P2D. Therefore, for the fitting of the SEI layer growth model the SPMe would probably be a better approach.

3.3.6.5 *Conclusions of the comparative study*

The results of the analysis showed that the SPMe can predict capacity fade very accurately compared to the P2D model, while reducing the computational cost significantly. However, it has been observed that some internal variables cannot be modeled as accurately as with the P2D model, due to the single particle modeling approach of the SPMe for the solid-phase concentration calculations. Despite these differences, it can be concluded, from the capacity fade predictions and the aging parameter fitting results, that the SPMe can be used to save computational time in control applications and for battery sizing, while maintaining good accuracy. Therefore, the SPMe was used to develop the degradation model presented in Section 3.5.

3.4 EXPERIMENTAL STUDY

As discussed above, the parameterization and validation of physics-based battery aging models needs further research to improve its reliability. For that, in Section 3.2 it was proposed to use degradation mode data to add more physical insight to these processes. The degradation mode estimation tool described in Section 3.2.1 was used to obtain these data. To investigate the degradation model development and parameterization process that was proposed, an experimental research was developed using NMC-graphite LG MH1 cells of 3.2 Ah nominal capacity. The electrochemical and thermal parameters for this cell were obtained by Clara Rojas in her PhD thesis.

3.4.1 Aging matrix

Three different cycling conditions were tested, all of them at 25 ºC to reduce parameter uncertainties and modeling errors. In the first condition, 2 cells were charged at 1C C-rate until they reached the maximum voltage value of 4.2 V. Then, the cells were held in constant voltage for 1h. After the CCCV charge, a rest time of 30 min was set, and to finish, the cells were discharged with 1C C-rate until the minimum voltage of 2.5 V. 50 cycles were performed before doing the check-up cycles. The check-ups were defined as 3 cycles of 0.5C CC charge, CV at 4.2 V for 1 h, rest for 30 min and discharge at 0.2C until 2.5 V. The capacity of the cell was obtained from the third C/5 discharge of the check-up procedure. All these experiments were performed in a Basytec XCTS cycler. After these three cycles, an OCV test was performed to estimate the degradation modes. The OCV tests were performed with a C/30 C-rate on an Arbin LBT cycler to have more accuracy in the OCV current range.

The other two conditions were very similar, but changing the charging and discharging currents for the CC phases. With the intention of increasing the stress of the positive electrode, in the second condition, the cells were charged with the same protocol as the first two cells, but discharged with a 2C C-rate. The increase in the discharging current should generate more stress in the positive electrode due to higher lithium intercalation fluxes. In the third case, the cells were charged and discharged with less current, trying to generate less stress in both electrodes. The cells were charged and discharged with 0.5C C-rates.

All these conditions form a degradation matrix hereafter named as 1C/1C, 1C/2C and 05C/05C, corresponding to the mentioned charge/discharge rates. With this small degradation matrix, it was intended to reduce the experimental cost and time required to develop an accurate aging model using physical information. In addition, the information collected in the first 300 cycles was used to develop the degradation matrix, while the information of the following cycles will be used for validation.

3.4.2 Experimental results

As discussed, to develop an accurate aging model, at least two main features must be taken into account. First, the degradation modes that are taking place with battery aging must be represented in the model. It probably will not be possible to model the exact mechanisms, but at least the degradation modes should describe a similar aging behavior. Hence, degradation modes should be used for parameterization and validation. Second, the trends of degradation should be appropriately followed.

To evaluate those two things, the degradation modes evolution for the above-mentioned aging conditions was calculated using the OCV data collected after every fifty cycles. The evolution of the degradation modes for the six cells is shown in Figure 3.10. The LAM of the negative electrode was observed to be very small (of the order $10^{-4} - 10^{-6}$), and thus, it was believed to be too small for the tool to estimate it with accuracy. Consequently, it can be concluded that when modeling the aging of this cell, at least for these cycling conditions at 25 ºC, the LAM in the negative electrode should not be modeled.

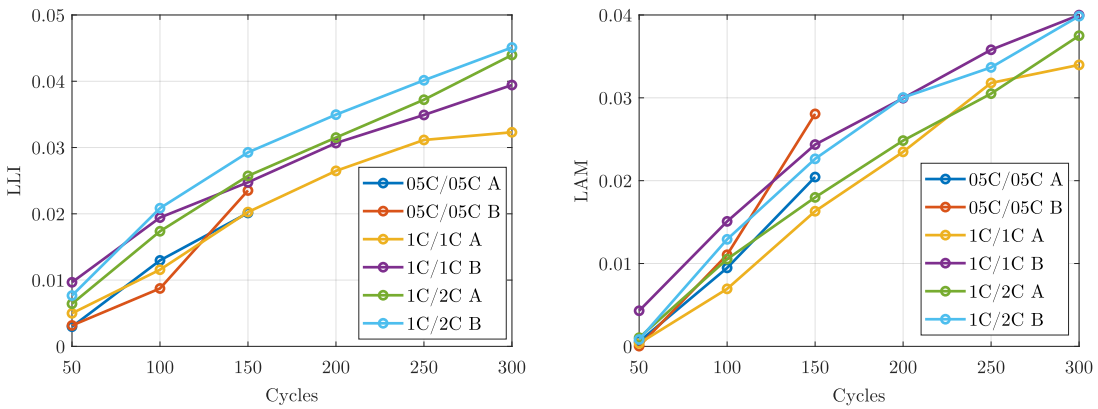

(a) (b)

Figure 3.10: Experimental degradation mode estimates. (a) LLI; (b) Positive electrode LAM.

Regarding the trends of the degradation modes, it can be observed that LLI represents a sublinear tendency in all cases, while the cells that were cycled with 1C charge 2C discharge protocol were the cells that suffered more LLI. In the case of the LAM in the positive electrode, a slightly sublinear trend can be observed. It can be seen that the cells that lost more active material are the ones that were discharged at 2C. The 1C/1C B cell has a similar amount of LAM at the cycle 300, but it can be seen that it had a higher initial LAM value, so with further cycles the 1C/2C A and 1C/2C B cells will probably suffer more LAM.

In addition to the degradation mode values, C/30 and C/5 capacity values were calculated from the OCVs and check-up cycles, respectively. Figure 3.11 shows the capacity evolutions for the 6 cells. As can be observed, the cell capacity values for the C/5 capacities differ considerably from one cell to another in the BOL, up to 5 % of the nominal capacity of the cell. On the other hand, the C/30 capacity discrepancy is below 1 % of the nominal capacity. This could mean that some cells have a higher resistance than others in the BOL. However, since the C/30 capacities and the degradation modes' evolution show that the trends are similar from one another, it was concluded that the capacity measurement value of the C/5 cycles performed with the Basytec XCTS cycler were not accurate. In the 400$^{\text{th}}$ cycle, the capacities measured by the Basytec cycler for the 1C/1C A and B cells was of 2.817 Ah and 2.908 Ah, respectively, and performing the same test with the Arbin LBT cycler the measured C/5 capacities were of 2.936 and 2.9339, respectively. Therefore, it was concluded that the measured C/5 capacity values could not be used for the parameterization process.

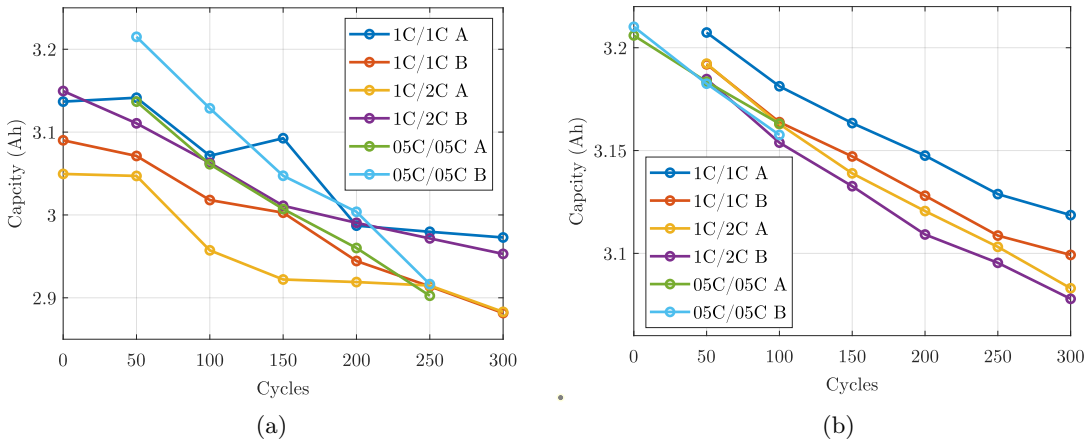

Figure 3.11: Experimental capacity measurements. (a) C/5 capacity; (b) C/30 capacity.

3.5 DEGRADATION MODEL DEVELOPMENT

Based on the aging data that was collected, a physics-based degradation model was developed using the SPMe. To improve the description of the aging phenomena, specially at high C-rates, a thermal model was coupled to the SPMe as in [158]. The parameters for the LG MH1 model were measured and estimated by Clara Rojas for her PhD thesis, and the research will be sent to a journal for publication. The parameters are shown in Appendix C.3.

3.5.1 Model selection

The degradation mode data was used to select the aging mechanisms to describe the degradation of the LG MH1 cell. The first mechanism that was included is the SEI growth. The SEI layer always keeps growing at any condition, resulting in a continuous LLI and a film resistance increase, decreasing negative electrode porosity, and generating capacity and power fade [22]. As is shown in Figure 3.10 (a), LLI has a sublinear aging trend, which fits well with diffusion-limited SEI growth models presented in the literature [22, 126, 130, 151]. Therefore, the SEI layer growth model that was used is the one presented in Section 3.3. In addition, Figure 3.10 (a) shows that the cells that were charged at higher C-rates lost more lithium. This could be due to various reasons, such as particle cracking and SEI growth on cracks, as was modeled in Section 3.3. Nevertheless, the null LAM in the negative electrode suggests that did not occur any particle cracking in the negative electrode. Also, charging the cell at higher C-rates increases the cell temperature, and consequently the parasitic reactions that occur in the cell, such as the SEI growth. The thermal model should capture the faster SEI growth with the increase in temperature. Besides, higher charging current rates may also generate lithium plating. Lithium plating generates LLI and a porosity decrease due to the metallic lithium film generated on the particles. With the goal of modeling LLI more accurately at higher charging currents, a lithium plating model was included.

Regarding the LAM in the positive electrode, it can be observed that considerable degradation occurs in all the studied cases. To model this LAM, the model presented in Section 3.3, was used, but just for the positive electrode and without including the particle cracking model, since it would significantly increase the computational time for the optimizations.

3.5.2 Aging parameter fitting

One of the goals of this degradation model development is to see if the experimental time to obtain a degradation model can be reduced, and thus, a relatively low amount of experiments was used for the fitting of the parameters. The five parameters that were fitted from experimental data to complete the aging model are the following: D_{sol}, k_{pl}, γ_0, β^p, m_2^p.

The fitting strategy that was followed consists of two steps. First, the SEI growth and the LAM models were fitted using the first 150 cycles degradation mode data of the 0.5C/0.5C A cell. This decision was made because lower charging current rates should avoid lithium plating, so the other two degradation mechanisms can be "isolated". The second step consisted on using the 1C/1C and 1C/2C conditions data to fit the lithium plating model parameters.

For the fitting of the SEI growth and LAM models, a multi-objective optimization algorithm was used, setting as objectives to reduce the RMS errors of the LLI and the LAM. The results of the first fitting are shown in Figure 3.12.

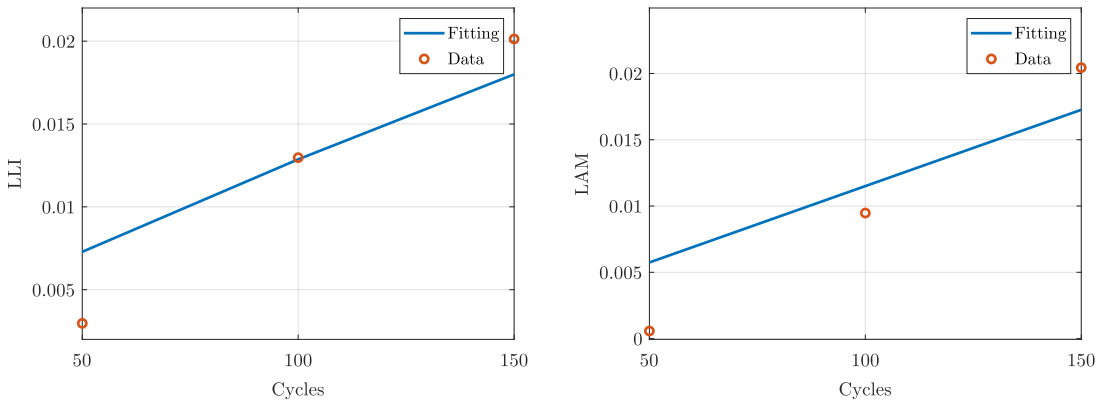

Figure 3.12: Degradation mode prediction results for the 0.5C/0.5C cycling condition after the first fitting.

Using these parameter values, the 1C/1C and 1C/2C cycling conditions were simulated, without including any lithium plating model. Figure 3.13 and Figure 3.14 show the model prediction results and the experimental measurements. As can be observed, the degradation model predicts very accurately the LAM for all the cases, so the fitting of this degradation mode was finished at this point. On the other hand, the LLI shows an appropriate aging

tendency, but it is below the experimental data in both cases, so it is reasonable to add a mechanism that increases the LLI prediction as the current increases.

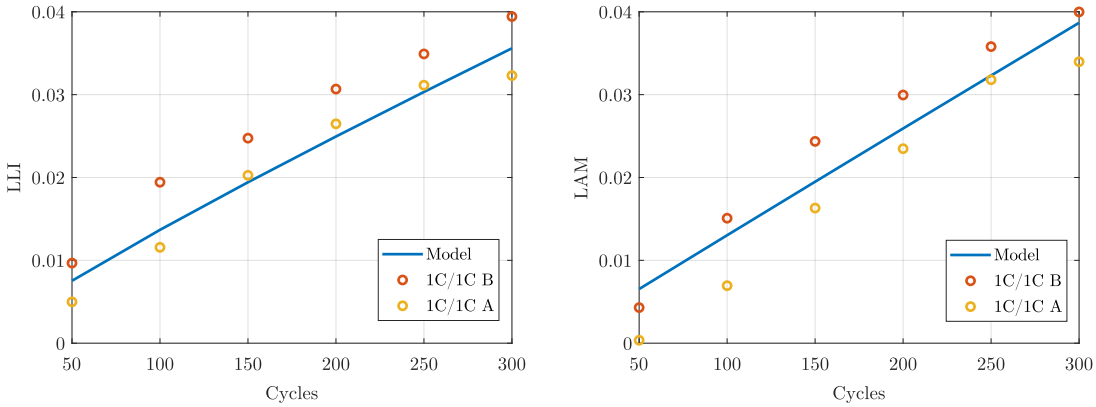

(a) (b)

Figure 3.13: Degradation mode prediction results for the 1C/1C cycling condition after the first fitting.

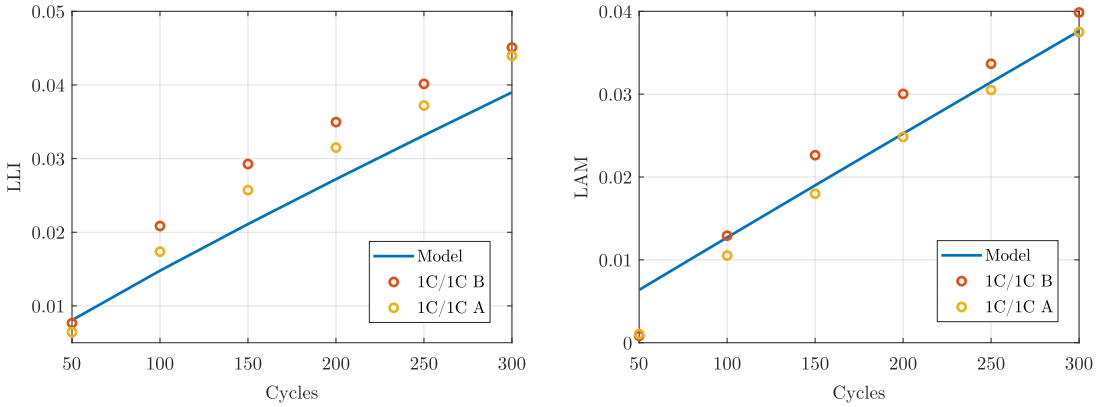

(a) (b)

Figure 3.14: Degradation mode prediction results for the 1C/2C cycling condition after the first fitting.

The lithium plating model was fitted using the 1C/1C B cell data of the first 300 cycles, setting as objective the minimization of the RMS error of the LLI. The fitted parameter values are presented in Table 3.5.

The predictions for the 1C/1C cycles for the first 400 cycles are shown in Figure 3.15, and for the 1C/2C conditions in Figure 3.16. As can be seen, the LAM model gives very accurate results for all the cases, and the LLI model gives better results than in the previous fitting.

As can be seen, the aging model predicts the degradation modes with high accuracy for the first cycles of the cell, and the tendencies are well represented. Nevertheless, it

Table 3.5: Fitted parameter values.

Parameter	Value
D_{sol} $(m^2\,s^{-1})$	3.5219×10^{-21}
β^p	5.5963×10^{-5}
m_2^p	0.3086
k_{pl} $(m\,s^{-1})$	2×10^{-6}
γ_0 (s^{-1})	7.92×10^{-7}

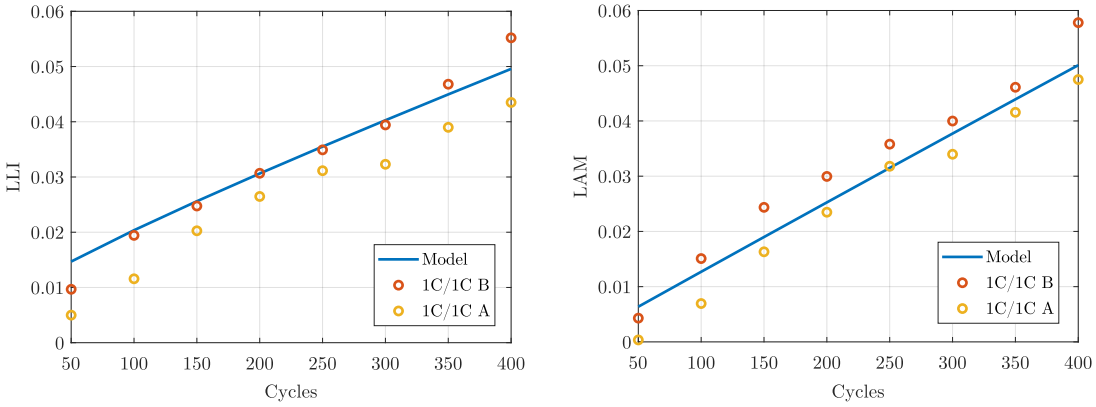

(a) (b)

Figure 3.15: Degradation mode prediction results for the 1C/1C cycling condition after the second fitting.

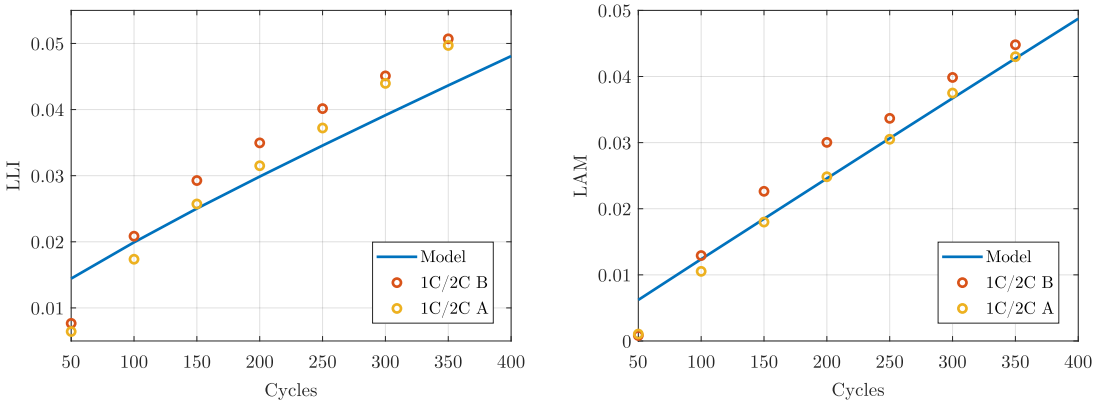

(a) (b)

Figure 3.16: Degradation mode prediction results for the 1C/2C cycling condition after the second fitting.

can be seen that the LLI in the 1C/2C cells is underestimated. As the 1C/1C cell LLI values are well represented, it seems that the additional LAM generated in the 1C/2C cells could come for the additional LAM of the positive electrode. Probably, as active material is lost in the positive electrode, additional parasitic reactions occur in the positive

electrode, resulting in more LLI. The work presented in this chapter is not finished yet, and more experiments will be done to age more these cells, and the effect of the positive electrode LAM in the LLI will be analyzed and modeled. Furthermore, more experimental conditions will be evaluated, focusing on fast charging by increasing the charging C-rate until 2C, to see if the negative electrode suffers LAM. Besides, dynamic profiles are being studied using consecutive charge depleting UDDS profiles, to see if the developed aging model is able to represent its aging accurately.

As mentioned, the objective of this work is to achieve a fast and accurate parameterization of an aging model by means of physical insight. However, the validation process should be extended to at least age the cell until 80 % SOH. Nonetheless, these results are promising, and we will continue with this work on the research group.

In addition, to improve the parameter fitting approach by including power fade measurements, resistance measurements will be made, and the C/5 cycles will be done using the Arbin LBT cycler to circumvent the above-mentioned measurement issues.

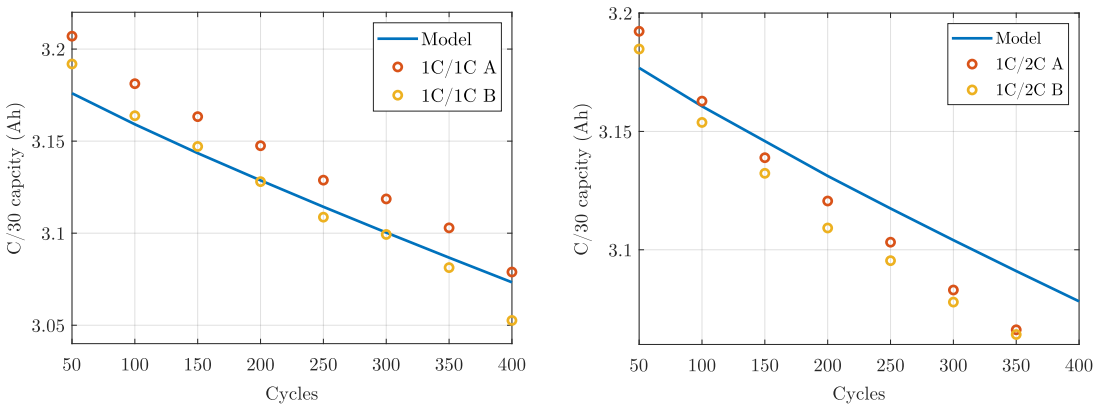

Figure 3.17: C/30 capacity prediction.

3.6 AGING PREDICTION CONCLUSIONS

This chapter summarized the work performed regarding physics-based battery aging modeling and prediction. First, an overview of battery aging was presented, and a variety of models were reviewed, highlighting the need of improving the parameterization and validation of these models. For that, it was proposed to use degradation mode data to add physical insight to the parameter fitting process. Later, an analysis of physics-based battery models was carried out. The performance of the P2D and SPMe models was compared in

terms of computational cost and prediction accuracy, concluding that the SPMe can be an interesting alternative to model battery aging since it can save significant computational effort and give very accurate results compared to the P2D model. Hence, the proposed aging model was developed using the SPMe model. An experimental study was performed with six LG MH1 3.2 Ah high-energy battery cells. The degradation mode evolution was evaluated and concluded that three main aging mechanisms could be modeled to describe the observed battery aging. Using the degradation mode data of only 6 cells, and 150 to 300 cycles, 5 aging parameters were fitted, showing high accuracy in predicting battery capacity fade and degradation mode evolution. Nonetheless, more experimental validation is still pending, since the cells that were used for parameterization have not reached the end of life condition. To further validate the model, more degradation conditions should be used, such as fast charging conditions or dynamic profiles, which will be investigated in future works.

Chapter 4

SOC ESTIMATION

To manage batteries safely, and exploit their energy and power capabilities, it is essential to have insight about their current internal states. However, these internal states are not directly measurable, and, therefore, they have to be estimated. Thus, an internal physical state and SOC estimator was developed. This chapter discusses the proposed algorithm. First, an overview of the state-of-the-art is given, showing the advantages and drawbacks of the main methods reported in the literature. The observability analysis that was performed for the physical states of the battery is presented later, identifying the main challenges for estimating the physical variables. A new algorithm was developed according to this analysis, and was validated in simulation.

4.1 PHYSICS-BASED SOC ESTIMATION REVIEW

SOC estimation is an indispensable feature for BMSs. It is necessary for keeping the battery between safe operation limits, without overcharging or overdischarging it, what would cause its rapid degradation. Furthermore, accurate SOC estimation gives the possibility of exploiting the capacity limits of the battery safely, and hence, not having to oversize the battery capacity in the design process [10].

As mentioned in Section 1.2, nowadays mostly ECMs are used for battery state estimation [8]. However, in recent years, PBMs have been considered and investigated for these applications [9,12,13,53,56]. Due to the information that PBMs can give about the internal physical states of the battery, these models can offer superior performance when attempting to mitigate cell degradation [14,15].

The main challenge that PBMs present nowadays regarding state estimation, is the poor observability of the internal states and parameters of the model from the cell voltage measurement. Since cell voltage is calculated by subtracting the potentials of the negative and positive electrodes, both contributions must be estimated from one voltage measurement, which results in weak observability [11].

Two main approaches have been proposed in the literature to solve this problem. In the first one, it is assumed that there is a conservation of the number of cyclable lithium ions [45,90,159–161]. This method increases the system's observability, but battery cells go through a variety of degradation processes, and the quantity of cyclable lithium ions will not be preserved because of calendar and cycle aging. Because of this, as the cell ages, this assumption tends to result in an increasing estimate inaccuracy.

The second approach was introduced by Bartlett *et al.* [162] and is based on leaving one of the electrodes in open-loop, assuming that its predictions are correct. This way, they estimate only the states of the other electrode. Although this method improves the observability of the estimated states, any incorrect prediction in the open-loop electrode, such as an incorrect initialization, would generate inaccurate estimates.

Allam and Onori [11] created a dual adaptive interconnected observer based on the approach of Bartlett *et al.* [162]. While one of the observers keeps the negative electrode in an open-loop and estimates the states of the positive electrode, the other observer estimates the states of the negative electrode while keeping the positive electrode in open-loop. The estimates are interconnected, feeding the open-loop model of the other observer, correcting the error of each open-loop model, and solving the problems of the previous approaches.

Allam and Onori used this approach to estimate the SOC of a battery cell [11], showing good agreement in the estimated concentrations compared to the reference simulation values, and considerably improving the results of a single observer.

Based on these works, the interconnected-observer approach was used to design a new SOC estimator. The main contributions of this work are summarized below:

- A novel estimator was proposed based on [11], using three interconnected sigma-point Kalman filters (SPKFs) to estimate all the internal physical variables and the SOC of a battery cell, adding electrolyte-concentration estimation to the approach presented in [11].
- An observability analysis of the state variables of the SPMe, comparing the observability of the interconnected approach with the single-filter approach. An observability issue with the electrolyte concentration was identified.
- The robustness of the method was demonstrated by intentionally initializing all the states to incorrect values, not just the SOC, to show that the SPKFs still converge to correct values.

4.2 STATE-SPACE SPME WITH ORTHOGONAL COLLOCATION

As discussed in Section 2.4, the SPM and SPMe are simplified versions of the P2D model, and since the algebraic constraint is removed, they can be solved without a specific differential algebraic equation (DAE) solver, making them more amenable for state estimation applications. Furthermore, the SPMe was found to be a very accurate alternative of the P2D model, correcting one of the main issues of the SPM, incorporating the electrolyte dynamics. Thus, the SPMe was preferred to the SPM and P2D models for the estimation and control tasks of this work.

The orthogonal collocation method was used to convert the partial differential equations (PDEs) of the SPMe into ordinary differential equations (ODEs) as explained in Appendix A. Once the PDEs of the SPMe are converted into ODEs, these can be expressed in state-space form as

$$\dot{x}(t) = Ax(t) + Bu(t), \tag{4.1}$$

where A is the coefficient matrix multiplying to the states x (the discrete solid-phase and electrolyte concentration values), and B is the coefficient vector multiplying to the input u, which is the cell current. The system of equations is then discretized in time using the forward Euler method, giving the state equation with the discrete-time index k,

$$x[k] = A'x[k-1] + B'u[k-1], \tag{4.2}$$

where A' and B' are the equivalent A and B discrete-time matrices. The measurement equation is given by

$$y[k] = \overline{U}_{eq} - \overline{\eta}_r + \overline{\eta}_c - \overline{\Delta\phi}_e - \overline{\Delta\phi}_s. \tag{4.3}$$

The state-space model was solved using 10 collocation points in the negative electrode active material particle, another 10 in the positive electrode active material particle, 3 collocation points for the entire thickness of the negative electrode, another 3 for the positive electrode and 3 for the separator; 29 collocation points in total. However, since the collocation points of the boundaries are not solved in the state equations, as explained in Appendix A, the amount of state-equations is reduced to 19.

The accuracy of a model-based state estimation algorithm strongly depends on the accuracy of the battery model. If the model is inaccurate, it is very unlikely that the estimator will correctly estimate the internal states of the battery. Therefore, it is essential to validate the model before working with the estimator. For that, the discrete-time state-space SPMe that is going to be used for state estimation was compared to the high-fidelity P2D model presented in Section 2.2. The P2D model is solved, as in Appendix A, using the orthogonal collocation method, but with more collocation points than for the state-space model: 6 for each electrode thickness, 3 for the separator and 15 for each active material particle of both electrodes; 195 collocation points in total. The solver *ode15s* from MATLAB® was used to solve the equations of the P2D model.

Figure 4.1 shows a comparison of the voltage and SOC prediction results between the P2D model and the SPMe for a charge-depleting urban dynamometer driving schedule (UDDS) profile that was scaled for cell level, assuming a maximum current of 1C. The SOC is calculated by

$$SOC = \frac{\bar{z} - z_{0\%}}{z_{100\%} - z_{0\%}}, \tag{4.4}$$

where z is the average concentration value of a particle in an electrode, and is calculated as $z = \bar{c}_s / c_{s,max}$. $\bar{z}$ is the average z value through the thickness of an electrode, and $z_{100\%}$ and $z_{0\%}$ are the values of z at 100 % and 0 % SOC respectively.

The maximum cell voltage prediction error is below 15 mV, and the RMS error is 3.2 mV. The RMS error for SOC prediction is 0.0267 %. Therefore, the state-space model was determined to be sufficiently accurate for real-time estimation applications.

4.3 ESTIMATOR DESIGN

Different algorithms can be used for state estimation. Because lithium-ion batteries are nonlinear systems, nonlinear estimation algorithms are required for this task. The most used nonlinear state estimation algorithm is the extended Kalman filter (EKF) [163]. It uses linearization to propagate the mean and covariance of the system, which may cause unreliable estimates if the system is "highly nonlinear" [163]. Better covariance estimates can be obtained using the SPKF [43, 44, 163]. This filter operates by propagating the mean and covariance of the system using a set of function evaluations [43, 44, 163], thus avoiding linearization.

Another approach might involve the use of a deterministic observer, such as the sliding mode observer [11, 12]. However, it was preferred to use stochastic estimators because they can provide useful confidence bounds on the estimates. Therefore, it was decided to use the SPKF as it can generally give better results than the EKF.

4.3.1 Observability analysis of the SPMe

As mentioned above, observability is one of the main concerns regarding physics-based state estimation. As can be seen in the SPMe output Equation 4.3, the cell voltage comprises several different contributions. Among these, $\overline{U}_{eq}$ depends on the state variables c_s^n and c_s^p; while $\overline{\eta}_r$ and $\overline{\eta}_c$ depend on c_e and the input current. Since there is only one cell voltage measurement, it is difficult to discern each contribution, particularly in the case of batteries with graphite-based negative electrodes, which have very flat OCP curves. To further investigate this, an observability analysis was performed to determine how observable the state variables of the SPMe are from the measured output voltage values.

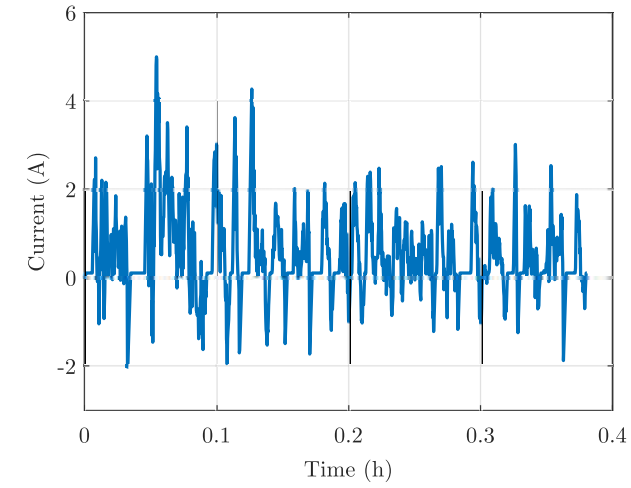

(a)

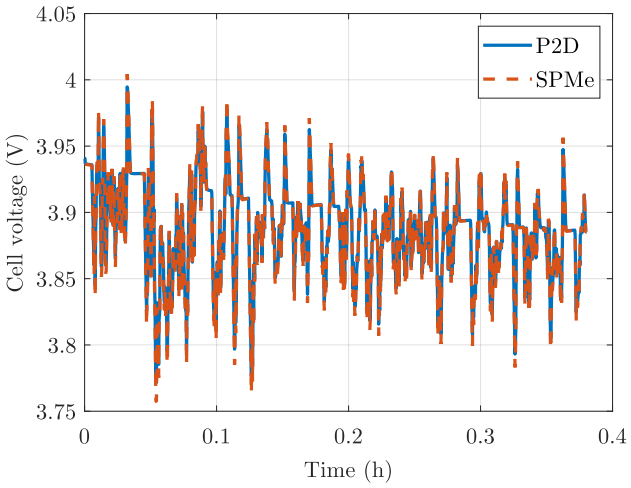

(b)

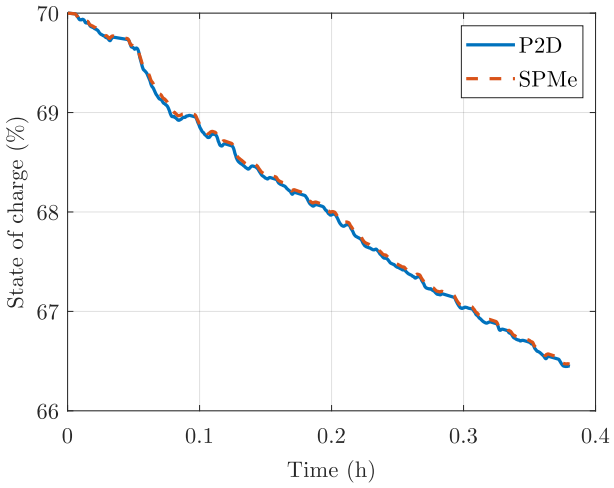

(c)

Figure 4.1: Comparison of the voltage (b) and SOC (c) predictions between the P2D model and the SPMe for a charge depleting UDDS cycle (a).

First, the model was reformulated in a general nonlinear form as,

$$\begin{aligned} \dot{x} &= f(x,u) \\ y &= h(x,u). \end{aligned} \tag{4.5}$$

One measure of the observability of a system can be gleaned from the condition number of its observability matrix, where the condition number is defined as the ratio of the maximum to the minimum singular value. By calculating the condition number of the observability matrix, we can analyze how close the matrix is from being singular. The bigger the condition number, the closer will be the matrix from being singular, and hence, less observable. If the observability matrix has not full rank, the system will be unobservable for the estimator. In the case of nonlinear systems, the observability matrix can be obtained using the Lie derivatives of h [164], which are calculated as

$$L_f^k h(x) = \nabla \left(L_f^{k-1} h \right) f, \tag{4.6}$$

where $L_f^0 h = h(x,u)$. The observability matrix is then defined with the Jacobian of the Lie derivatives as

$$\mathcal{O} = \begin{bmatrix} \nabla L_f^0 h \\ \nabla L_f^1 h \\ \nabla L_f^2 h \\ \vdots \\ \nabla L_f^n h \end{bmatrix}, \tag{4.7}$$

where n is the state vector dimension. $\mathcal{O}$ is an $n \times n$ matrix that must have full rank for the system to be observable.

After constructing the observability matrix of the SPMe by calculating its Lie derivatives, the degree of observability of the system was analyzed by evaluating its condition number. The condition number was assessed for several scenarios since it changes based on the input current and the values of the state variables. It was found out that in the case of no current, the condition number is of the order $10^{24} - 10^{26}$ for the entire SOC range, and the observability matrix is not full rank, indicating that one or more variables are not observable. In the case of a 1C current, the condition number of the system for the entire SOC range decreases to the order of $10^{13} - 10^{14}$, and the matrix becomes full rank, showing that the

system is observable. However, the condition number is relatively high, meaning that the system has poor observability. Low observability leads to numerically-ill conditioned error covariance matrices [165, 166], resulting in slow state estimation convergence, which makes the tuning process of the state estimator algorithm more difficult. The condition numbers for the 1C and no current cases for the entire SOC range are shown in Figure 4.2.

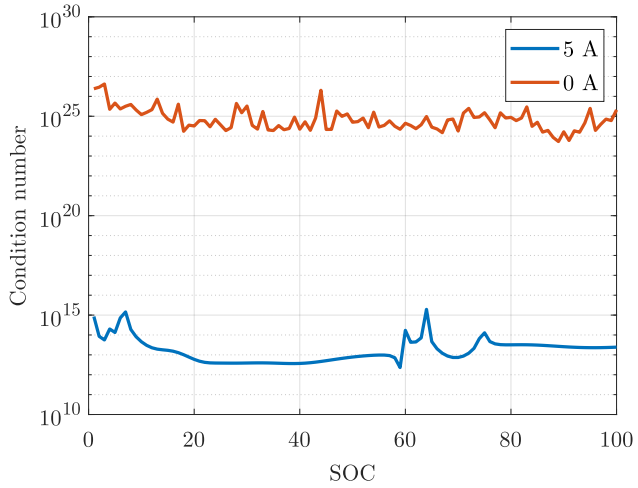

Figure 4.2: Condition number of the SPMe from 0 % to 100 % SOC for 0 A and 5 A.

In order to improve the observability of an SPM, Allam and Onori proposed to estimate the solid-phase concentration of each electrode by interconnecting two observers, where each one estimates the solid-phase concentration of one electrode and leaves the other in open-loop mode [11], to later interconnect the estimations and update the open-loop variables. In this case, since an SPMe was employed, three state variables have to be estimated instead of two, so the observability of each variable was analyzed, leaving the other two in an open-loop configuration. In this way, the observability issues of the model can be analyzed in more detail, and the origin of any weak observability can be located easier.

For the analysis of each variable, an observability matrix was created using the same method mentioned above. Then, the condition number of each observability matrix was analyzed by searching for different SOC, c_e and current values. Figure 4.3 shows the results of the analysis.

It can be seen that the observability of each system is improved compared to the full SPMe results of Figure 4.2, since the condition numbers decrease considerably. However, we noticed that the electrolyte concentration is not observable in the absence of input current because the corresponding observability matrix does not have full rank. This is shown in Figure 4.3 (c), where the condition number increases up to 10^{17} when the current is 0.

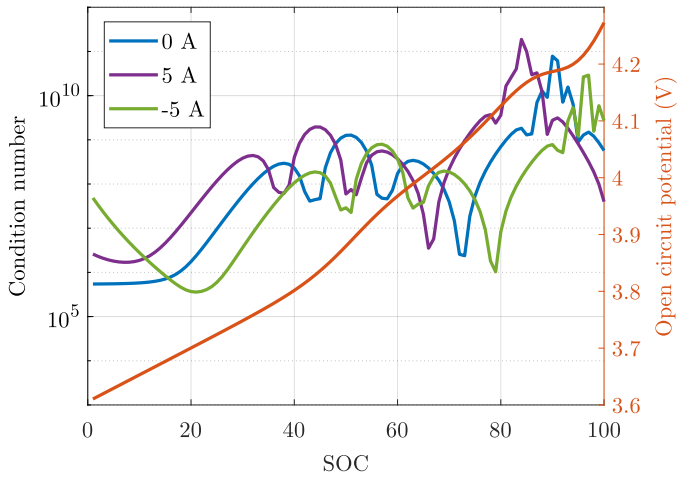

(a)

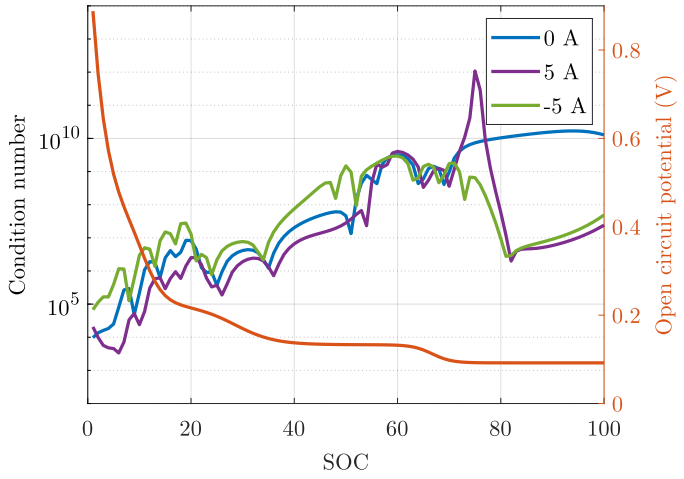

(b)

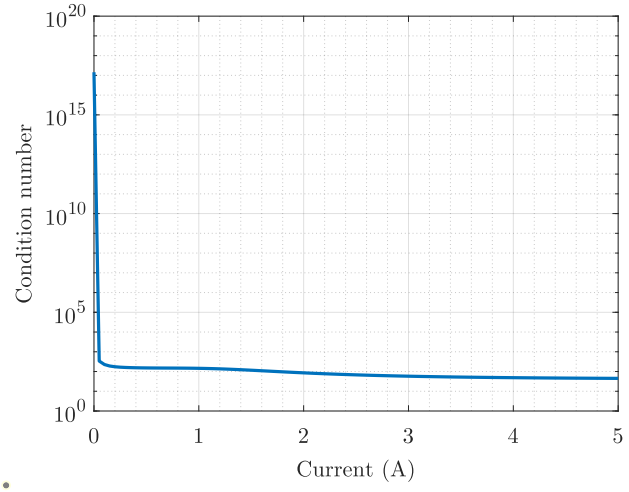

(c)

Figure 4.3: Observability analysis for the SPMe variables. (a) Positive electrode solid-phase concentration analysis, (b) negative electrode solid-phase concentration analysis and (c) electrolyte concentration analysis.

Therefore, it can be concluded that the main observability issues occur with the electrolyte concentration when the input current is 0. This agrees with the results of the full SPMe shown in Figure 4.2. If we look at the SPMe equations, we can see that the contribution of electrolyte concentration to the output equation comes in the form of overpotentials η_c and η_r. η_r becomes 0 immediately in the absence of current because $j = 0$. In the case of η_c, we encounter the same ambiguity problem as with the contribution of the two electrodes to a single voltage measurement. Since the same value for η_c can be obtained with infinite combinations of c_e^n and c_e^p, the electrolyte concentration becomes unobservable. Note that this happens in the SPMe model because of its assumption of a uniform reaction current density over the entire electrodes, but may not happen in the same way in the P2D model, where a difference in the electrolyte concentration would generate a flux of ions that might be observable.

Note that the electrolyte concentration becomes observable when the input current is not 0. However, the observability must not be mistaken with the *sensitivity* of the variable. Because the electrolyte concentration contribution is smaller in the output equation compared to the solid-phase concentrations, accurate electrolyte concentration estimation becomes challenging.

Figure 4.3 a) and b) show that the variables c_s^n and c_s^p are observable in the absence of current. As can be seen, the current affects the condition number curves by shifting them, but the condition number magnitude does not change in the same way as it does in the electrolyte concentration. Besides, the lithiation state of the electrodes has a greater effect on the observability of these variables, since their contribution to the voltage equation is directly related to the OCPs. Consequently, it can be seen that the condition number increases when the OCPs of the electrode become flatter, denoting less observability at those regions.

4.3.2 The interconnected SPKF

As explained above, the observability of the system can be improved by separating and interconnecting the estimation of the different variables of the SPMe. To achieve this, the state x was divided into x_n, x_p, and x_e. The state equations were divided correspondingly, where it is necessary to separate the A' and B' matrices of the state Equation 4.2 into the matrices; A'_n and B'_n for the negative electrode solid-phase concentration state equation, A'_p and B'_p for the positive electrode, and A'_e and B'_e for the electrolyte concentration.

A diagram of the interconnected SPKF is illustrated in Figure 4.4. As shown, the estimator can be divided into two main phases: the prediction phase and the correction phase. For the prediction phase, the three state and covariance estimates of the previous time step are taken. Then, the three state-space systems are used to obtain the state and covariance predictions. Afterwards, all the predictions, which are based on the three separated estimates of the previous time step, are interconnected to obtain three output predictions. In the correction phase, the prediction information is compared with the cell voltage measurement and used to obtain the filter gains. Then, these gains are used to compute the three state and covariance estimates.

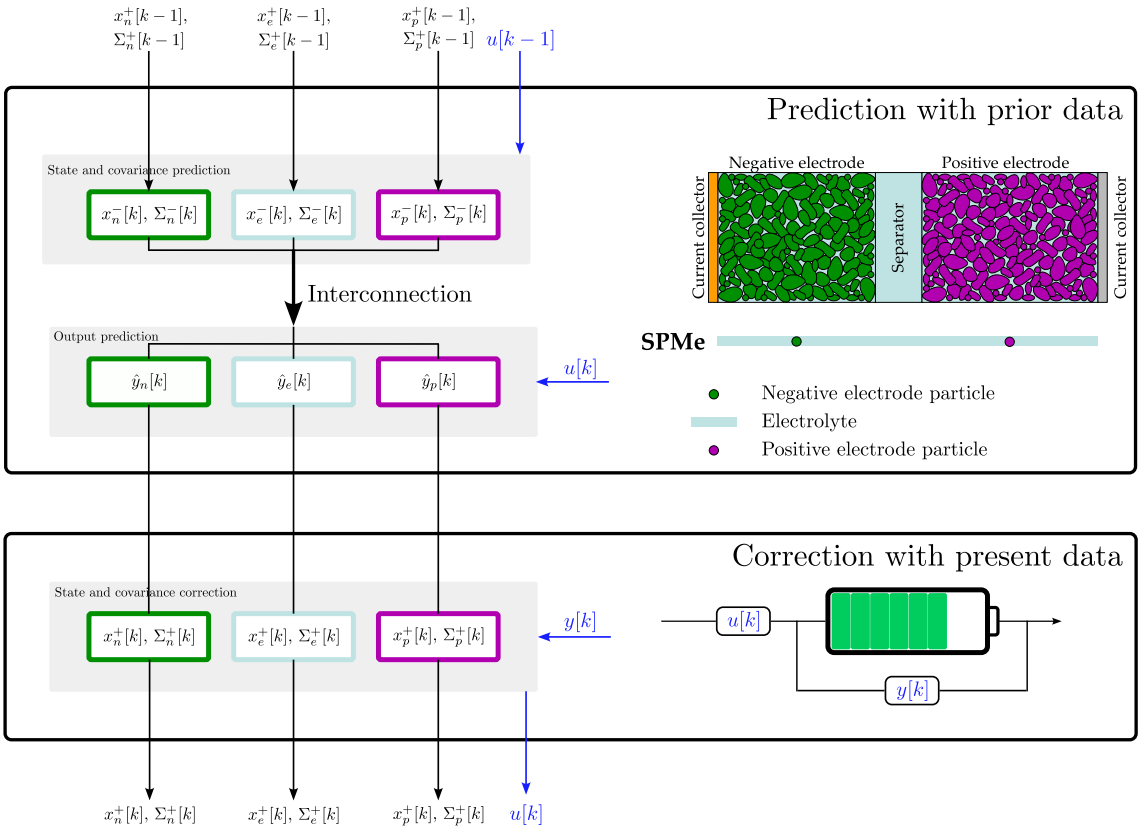

Figure 4.4: Diagram of the triple interconnected SPKF.

A detailed description of the six recursive steps of the estimator is given below:

Step 1a: State prediction time update. In this step the new state is predicted based on previous information. The standard SPKF algorithm procedure uses sigma points of the state, process noise, and measurement noise vectors to represent the randomness of the system. However, since the state equations of our model are linear, we can simplify the state prediction to

$$\hat{x}^-[k] = A'\hat{x}^+[k-1] + B'u[k-1], \tag{4.8}$$

where $\hat{x}^+$ is the state estimate and $\hat{x}^-$ the state prediction. While k and $k-1$ denote the present and previous time steps, respectively.

In our interconnected estimator, this step is computed for the three estimators. This way, the prediction of each state variable is done with the state-space matrices of each individual estimator and the previous time-step estimation as

$$\begin{aligned}\hat{x}_n^-[k] &= A_n'\hat{x}_n^+[k-1] + B_n'u[k-1]\\ \hat{x}_p^-[k] &= A_p'\hat{x}_p^+[k-1] + B_p'u[k-1]\\ \hat{x}_e^-[k] &= A_e'\hat{x}_e^+[k-1] + B_e'u[k-1].\end{aligned} \tag{4.9}$$

Step 1b: Error covariance time update. The error covariance is defined by

$$\Sigma_{\tilde{x}}^-[k] = \mathbb{E}[(x[k] - \hat{x}^-[k])(x[k] - \hat{x}^-[k])^T], \tag{4.10}$$

which leads to the three covariance matrices

$$\begin{aligned}\Sigma_{\tilde{x}_n}^-[k] &= (A_n')^T\Sigma_{\tilde{x}_n}^+[k-1]A_n' + \Sigma_{\tilde{w}_n}\\ \Sigma_{\tilde{x}_p}^-[k] &= (A_p')^T\Sigma_{\tilde{x}_p}^+[k-1]A_p' + \Sigma_{\tilde{w}_p}\\ \Sigma_{\tilde{x}_e}^-[k] &= (A_e')^T\Sigma_{\tilde{x}_e}^+[k-1]A_e' + \Sigma_{\tilde{w}_e}.\end{aligned} \tag{4.11}$$

Step 1c: Output prediction. Since the output equation is nonlinear, unlike the state equation, the sigma points $\mathcal{X}_n^-[k]$, $\mathcal{X}_p^-[k]$, and $\mathcal{X}_e^-[k]$ (for the three estimators) must be calculated first. The set of sigma points for each estimator is calculated as

$$\begin{aligned}\mathcal{X}_n^-[k] &= \left\{\hat{x}_n^-[k], \hat{x}_n^-[k] + h\sqrt{\Sigma_{\tilde{x}_n}^-}, \hat{x}_n^-[k] - h\sqrt{\Sigma_{\tilde{x}_n}^-}\right\}\\ \mathcal{X}_p^-[k] &= \left\{\hat{x}_p^-[k], \hat{x}_p^-[k] + h\sqrt{\Sigma_{\tilde{x}_p}^-}, \hat{x}_p^-[k] - h\sqrt{\Sigma_{\tilde{x}_p}^-}\right\}\\ \mathcal{X}_e^-[k] &= \left\{\hat{x}_e^-[k], \hat{x}_e^-[k] + h\sqrt{\Sigma_{\tilde{x}_e}^-}, \hat{x}_e^-[k] - h\sqrt{\Sigma_{\tilde{x}_e}^-}\right\},\end{aligned} \tag{4.12}$$

where h is a tuning variable for the SPKF and $\sqrt{\Sigma_{\tilde{x}_n}^-}$, $\sqrt{\Sigma_{\tilde{x}_p}^-}$ and $\sqrt{\Sigma_{\tilde{x}_e}^-}$ are the lower-triangular matrix square roots of the error covariance matrices, which were computed using a Cholesky decomposition. The sigma points (the vectors of the set $\mathcal{X}$) are then used to compute the output equation and to obtain the output sigma points,

$$\begin{aligned}\mathcal{Y}_{n,i} &= h(\mathcal{X}_{n,i}^-[k], \hat{x}_p^-[k], \hat{x}_e^-[k], u[k])\\ \mathcal{Y}_{p,i} &= h(\hat{x}_n^-[k], \mathcal{X}_{p,i}^-[k], \hat{x}_e^-[k], u[k])\\ \mathcal{Y}_{e,i} &= h(\hat{x}_n^-[k], \hat{x}_p^-[k], \mathcal{X}_{e,i}^-[k], u[k]).\end{aligned} \tag{4.13}$$

The three cell voltage predictions are then calculated as the weighted mean of these sigma points:

$$\begin{aligned}\hat{y}_n[k] &= \sum_{i=0}^{2N_{x_n}+1} \alpha_{n,i}^{(m)} \mathcal{Y}_{n,i}[k] \\ \hat{y}_p[k] &= \sum_{i=0}^{2N_{x_p}+1} \alpha_{p,i}^{(m)} \mathcal{Y}_{p,i}[k] \\ \hat{y}_e[k] &= \sum_{i=0}^{2N_{x_e}+1} \alpha_{e,i}^{(m)} \mathcal{Y}_{e,i}[k],\end{aligned} \tag{4.14}$$

where $\alpha_{n,i}^{(m)}$, $\alpha_{p,i}^{(m)}$ and $\alpha_{e,i}^{(m)}$ are the constants used to calculate the weighted mean.

Step 2a: Estimator gain matrix. In order to update the predictions with the present information, the estimator gain matrix is calculated. For that, we compute the required covariance matrices:

$$\begin{aligned}\Sigma_{\tilde{y}_n}[k] &= \sum_{i=0}^{2N_{x_n}+1} \alpha_{n,i}^{(c)} (\mathcal{Y}_{n,i}[k] - \hat{y}_n[k])(\mathcal{Y}_{n,i}[k] - \hat{y}_n[k])^T \\ \Sigma_{\tilde{y}_p}[k] &= \sum_{i=0}^{2N_{x_p}+1} \alpha_{p,i}^{(c)} (\mathcal{Y}_{p,i}[k] - \hat{y}_p[k])(\mathcal{Y}_{p,i}[k] - \hat{y}_p[k])^T \\ \Sigma_{\tilde{y}_e}[k] &= \sum_{i=0}^{2N_{x_e}+1} \alpha_{e,i}^{(c)} (\mathcal{Y}_{e,i}[k] - \hat{y}_e[k])(\mathcal{Y}_{e,i}[k] - \hat{y}_e[k])^T,\end{aligned} \tag{4.15}$$

$$\begin{aligned}\Sigma^-_{\tilde{x}_n\tilde{y}_n}[k] &= \sum_{i=0}^{2N_{x_n}+1} \alpha_{n,i}^{(c)} (\mathcal{X}^-_{n,i}[k] - \hat{x}^-_n[k])(\mathcal{Y}_{n,i}[k] - \hat{y}_n[k])^T \\ \Sigma^-_{\tilde{x}_p\tilde{y}_p}[k] &= \sum_{i=0}^{2N_{x_p}+1} \alpha_{p,i}^{(c)} (\mathcal{X}^-_{p,i}[k] - \hat{x}^-_p[k])(\mathcal{Y}_{p,i}[k] - \hat{y}_p[k])^T \\ \Sigma^-_{\tilde{x}_e\tilde{y}_e}[k] &= \sum_{i=0}^{2N_{x_e}+1} \alpha_{e,i}^{(c)} (\mathcal{X}^-_{e,i}[k] - \hat{x}^-_e[k])(\mathcal{Y}_{e,i}[k] - \hat{y}_e[k])^T,\end{aligned} \tag{4.16}$$

where $\alpha_{n,i}^{(c)}$, $\alpha_{p,i}^{(c)}$ and $\alpha_{e,i}^{(c)}$ are the constants used to calculate the weighted covariance.

Once these matrices are computed we calculate the gains of the estimators:

$$\begin{aligned}L_n[k] &= \Sigma^-_{\tilde{x}_n\tilde{y}_n}[k](\Sigma_{\tilde{y}_n}[k])^{-1} \\ L_p[k] &= \Sigma^-_{\tilde{x}_p\tilde{y}_p}[k](\Sigma_{\tilde{y}_p}[k])^{-1} \\ L_e[k] &= \Sigma^-_{\tilde{x}_e\tilde{y}_e}[k](\Sigma_{\tilde{y}_e}[k])^{-1}.\end{aligned} \tag{4.17}$$

Step 2b: State estimate measurement update. The state estimates are calculated by

$$\begin{aligned}\hat{x}_n^+[k] &= \hat{x}_n^-[k] + L_n(y[k] - \hat{y}_n[k]) \\ \hat{x}_p^+[k] &= \hat{x}_p^-[k] + L_p(y[k] - \hat{y}_p[k]) \\ \hat{x}_e^+[k] &= \hat{x}_e^-[k] + L_e(y[k] - \hat{y}_e[k]).\end{aligned} \tag{4.18}$$

Step 2c: Error covariance measurement update. The error covariance matrices are updated by computing

$$\begin{aligned}\Sigma_{\tilde{x}_n}^+[k] &= \Sigma_{\tilde{x}_n}^-[k] - L_n[k]\Sigma_{\tilde{y}_n}[k]\left(L_n[k]\right)^T \\ \Sigma_{\tilde{x}_p}^+[k] &= \Sigma_{\tilde{x}_p}^-[k] - L_p[k]\Sigma_{\tilde{y}_p}[k]\left(L_p[k]\right)^T \\ \Sigma_{\tilde{x}_e}^+[k] &= \Sigma_{\tilde{x}_e}^-[k] - L_e[k]\Sigma_{\tilde{y}_e}[k]\left(L_e[k]\right)^T.\end{aligned} \tag{4.19}$$

4.4 SOC ESTIMATOR VALIDATION

In order to validate the proposed method, the state estimates were compared with the results of the orthogonal collocation P2D model. In this way, in addition to the voltage and SOC estimates, the internal variables can also be compared with the true values.

The algorithm was evaluated for three types of inconveniences. The first step consisted of incorrectly initializing all the states of the system. In this way, the convergence of all the states was analyzed. Later, current and voltage measurement uncertainties were simulated to evaluate the robustness of the filter against measurement noise. Finally, parametric uncertainties were inserted to analyze how modeling errors and cell degradation could affect the proposed method.

4.4.1 SOC and internal variable estimation

The first step in the validation process was to ensure that the estimator is able to estimate the SOC and the internal physical variables under incorrect initialization. For this, the estimator was initialized with 20 % SOC error and 20 % electrolyte concentration error. These errors are very challenging and should be rare to encounter such high errors in real applications.

To analyze all the dynamics of the internal variables properly, five charge/discharge cycles with charge-depleting UDDS profiles were simulated. The cell was discharged with

consecutive dynamic profiles until it reached the minimum cell voltage. Then, it was charged with C/2 current until it reached the maximum voltage and then discharged again using consecutive charge-depleting UDDS profiles.

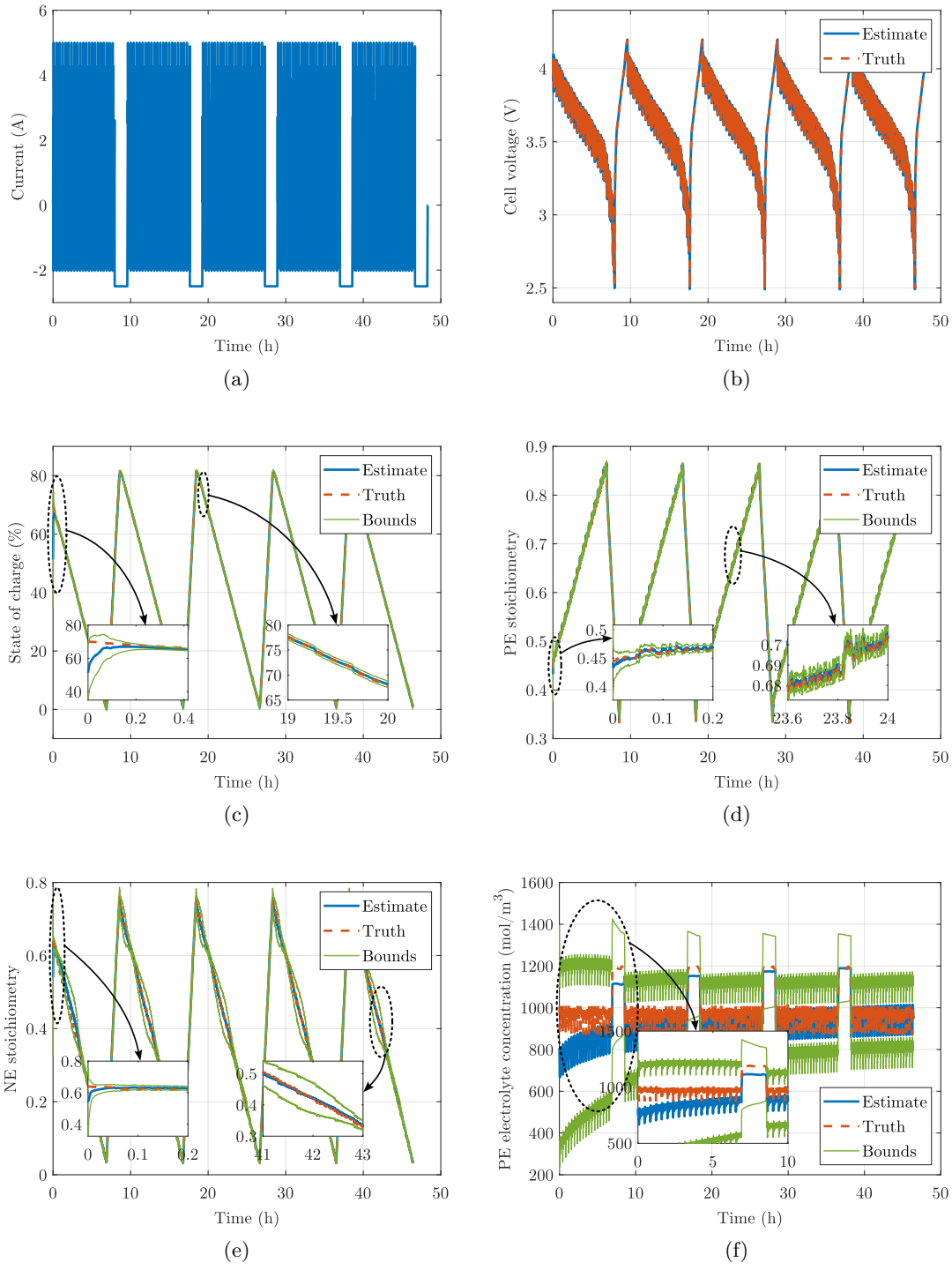

Figure 4.5: Results of the interconnected SPKF estimator with incorrect initialization. (a) Cell current, (b) cell voltage, (c) SOC, (d) positive electrode stoichiometry, (e) average electrolyte concentration in the positive electrode and (f) negative electrode stoichiometry.

The results of this simulation are shown in Figure 4.5, where the input current and the voltage response are shown in Figure 4.5 (a) and (b), respectively. The RMS error for the entire simulation is 2.1 mV. Figure 4.5 (c) shows that the 20 % SOC error is corrected immediately, and the confidence bounds converge quickly. The RMS error of the SOC estimation is 0.61 %. The response of the positive electrode stoichiometry shown in Figure 4.5 (d) is very similar, as it rapidly corrects the estimate and the bounds converge. The RMS error for the entire simulation is 0.28 %. Figure 4.5 (f) shows the negative electrode stoichiometry. It can be observed that the initial estimate correction is fast and the bounds converge. However, the bounds diverge at the beginning and middle of the discharge. Since the open circuit potential of the negative electrode (shown in Figure 4.3 (b)) is very flat around 80 % SOC and 50 % SOC, its observability is lower than the observability of the positive electrode, which makes estimation of the positive electrode concentration more reliable. Its RMS error of 0.88 % is also higher than the error of the positive electrode. Figure 4.5 (e) shows the results of the mean electrolyte concentration value on the positive electrode. As can be seen, the estimate of the electrolyte concentration is the slowest to correct its value. This is also shown in its bounds, which take longer to converge and need to be larger because its estimate is not as reliable as the solid-phase concentrations. Since the electrolyte concentration contribution to the cell voltage equation is the lowest among the three state variables, it seems reasonable that its estimate is the slowest one to converge. Nevertheless, despite being the slowest variable, it should be noted that it converges well to the correct value starting with a very high error of 20 %. Due to this slow convergence, the RMS error of the normalized electrolyte concentration ($\theta_e = c_e/c_{e,0}$) for the entire simulation is 6.2 %, however, the RMS error in the last cycle is decreased to 0.5 %.

The same estimation analysis was then performed by introducing current and voltage measurement uncertainties, as well as incorrect state initializations. Zero-mean Gaussian noises with standard deviation of 100 mA and 25 mV were used to corrupt the current and voltage measurements respectively. The results of these simulations are shown in Figure 4.6. The input current profile and the reference voltage values are the same as those shown in Figure 4.5 (a) and (b), so they are not shown in Figure 4.6.

As can be seen in the results of Figure 4.6, the estimator is robust to measurement uncertainties. The SOC estimate converges very quickly as in the case without sensor noise, as well as the positive and negative electrodes' solid-phase concentrations. The electrolyte concentration estimate is slower than that of the other variables as in the previous case,

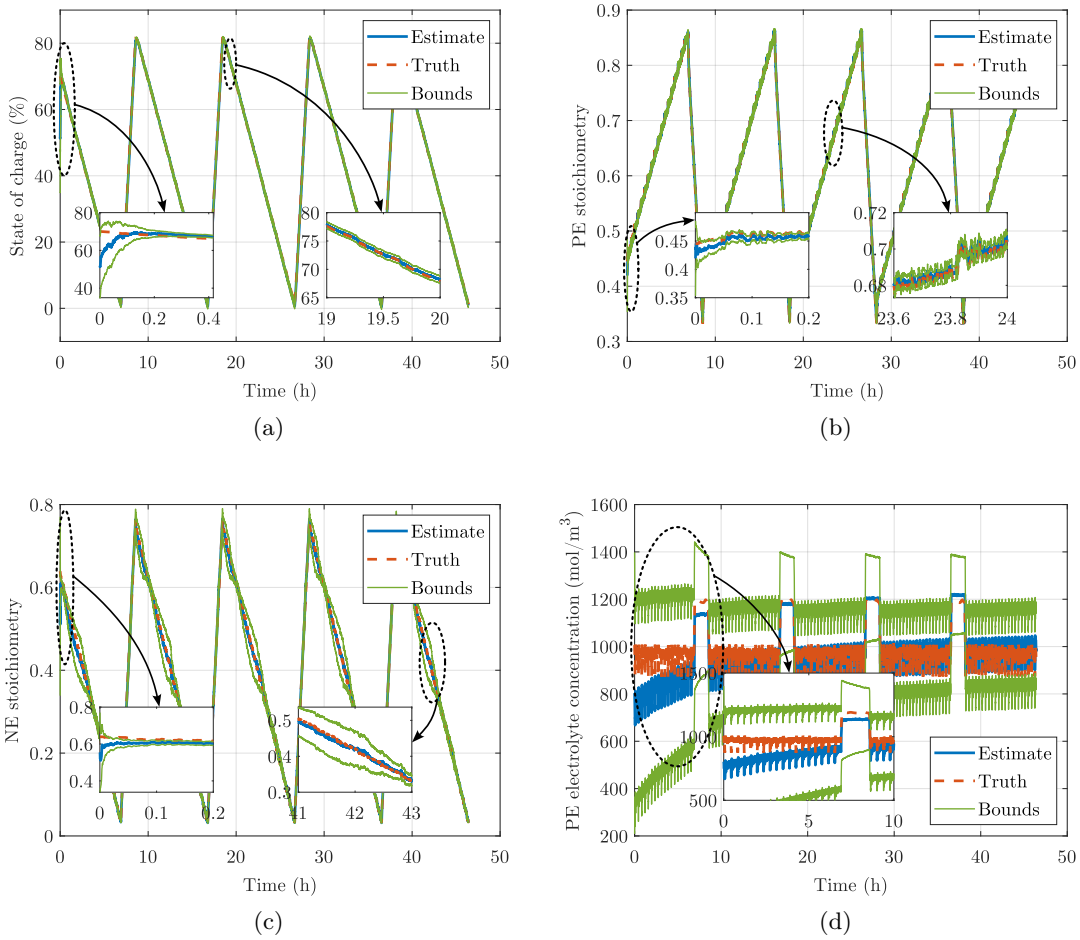

Figure 4.6: Results of the interconnected SPKF estimator under measurement uncertainties. (a) SOC, (b) positive electrode stoichiometry, (c) average electrolyte concentration in the positive electrode, and (d) negative electrode stoichiometry.

but converges accurately. The RMS errors of the estimates are very similar to the errors of the case without noise; the voltage estimate has an RMS error of 4.8 mV, the SOC estimate an error of 0.52 %, the positive electrode stoichiometry 0.23 %, the negative electrode stoichiometry 0.76 % and the normalized electrolyte concentration estimate has an RMS error of 5.56 %.

4.4.2 SOC estimation with parametric uncertainty

To evaluate the response of the algorithm under parameter uncertainties, two different cases were studied; first, aged parameter values were introduced in the reference P2D model by changing the eSOH parameters. These parameters are directly related to the OCV of the cell, so they generate a large impact on the cell voltage outcome. Later, the case of an incorrect parameterization due to parameter measurement errors, inaccuracies,

or cell-to-cell variations was analyzed. In this case, the values of active material and electrolyte diffusivities were changed, as well as the normalized reaction rate values. These parameters were selected because they are very challenging to measure and, hence, prone to uncertainties.

To alter the eSOH parameters for the first analysis, an LAM value of 10 % was set in the negative electrode, and 5 % for LLI. The resulting changes in the parameters of the P2D model can be seen in Table 4.1.

Table 4.1: eSOH parameters' variations.

Parameter	Fresh	Aged
ε_s^n	0.75	0.675
ε_s^p	0.665	0.665
$z_{0\%}^n$	0.027	0.0256
$z_{0\%}^p$	0.8536	0.8148
$z_{100\%}^n$	0.9014	0.9350
$z_{100\%}^p$	0.27	0.2661

These changes in the parameters were inserted into the P2D model, and the same 5 charge/discharge cycles simulated to obtain the truth results of an aged cell. The results of this first analysis, with incorrect eSOH parameters, are shown in Figure 4.7.

Figure 4.7 (b) shows the positive electrode stoichiometry. The initial error is corrected in a few seconds, and the estimation closely follows the truth value throughout the simulation. However, the RMS error is larger than the error for the previous analyses: 0.9 %. Besides, it can be seen that the truth value exceeds the confidence bounds at some points. The response of the negative electrode stoichiometry, shown in Figure 4.7 (d), is similar to the positive electrode stoichiometry, as the estimate converges well and the RMS error is 1.78 %. This larger error most likely arises from the incorrect negative electrode active material volume fraction, which affects the reaction flux. Nonetheless, it can be seen that the estimate is accurate for most of the simulation. Therefore, it can be concluded that the estimator is able to reduce, or correct, the model errors introduced by small differences in the active material volume fractions.

In the case of the electrolyte concentration, it can be observed in Figure 4.7 (c) that the overall response is worse than the previous result, since the estimator is not able to correct the estimate during the simulation. As mentioned above, the contribution of the electrolyte concentration in the cell voltage value is smaller than the contributions of the electrode stoichiometries. This probably makes the estimation slower, and the fact that the

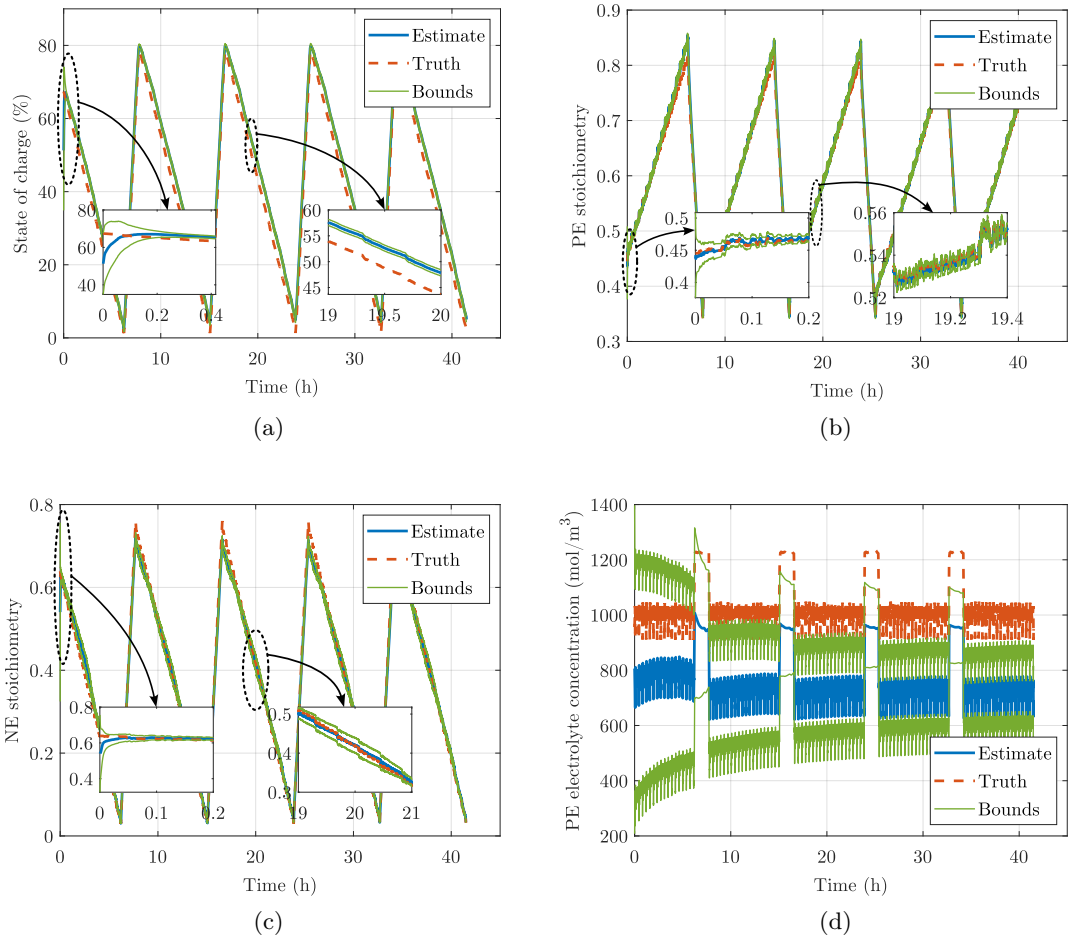

Figure 4.7: Results of the interconnected SPKF estimator with incorrect eSOH parameters. (a) SOC, (b) positive electrode stoichiometry, (c) average electrolyte concentration in the positive electrode, and (d) negative electrode stoichiometry.

wrong negative electrode active material volume fraction affects the reaction flux generates modeling errors, aggravating the initial issue.

Lastly, the estimate of the SOC is shown in Figure 4.7 (a). The SOC estimation error is quite high, with an RMS error of 3.63 %, while the filter is very confident about the estimate. As the estimates of both stoichiometries converge to the true value and give quite accurate results for almost the entire simulation, the SOC estimate is also very confident. However, the SOC is calculated with Equation 4.4, and since the aged $z^n_{0\%}$, $z^p_{0\%}$, $z^n_{100\%}$ and $z^p_{100\%}$ values are unknown by the filter, the SOC calculation is wrong. This can be seen in the zooms of Figure 4.7 (a), (b) and (d), where between 19 and 20 hours both stoichiometry estimates are correct, but the SOC estimate is inaccurate. This shows the importance of estimating correctly the operating window of the battery, as we cannot obtain accurate SOC estimates otherwise.

Finally, to analyze the parametric uncertainties that can arise from cell-to-cell variations or parameter measurement/estimation errors, the filter response was evaluated under 25 % change of the parameters D_s^n, D_s^p, D_e^p, $k_{0,norm}^n$ and $k_{0,norm}^p$. All of these parameters were multiplied by 0.75 in the state-space model, and the reference voltage and current values presented in Figure 4.5 were used.

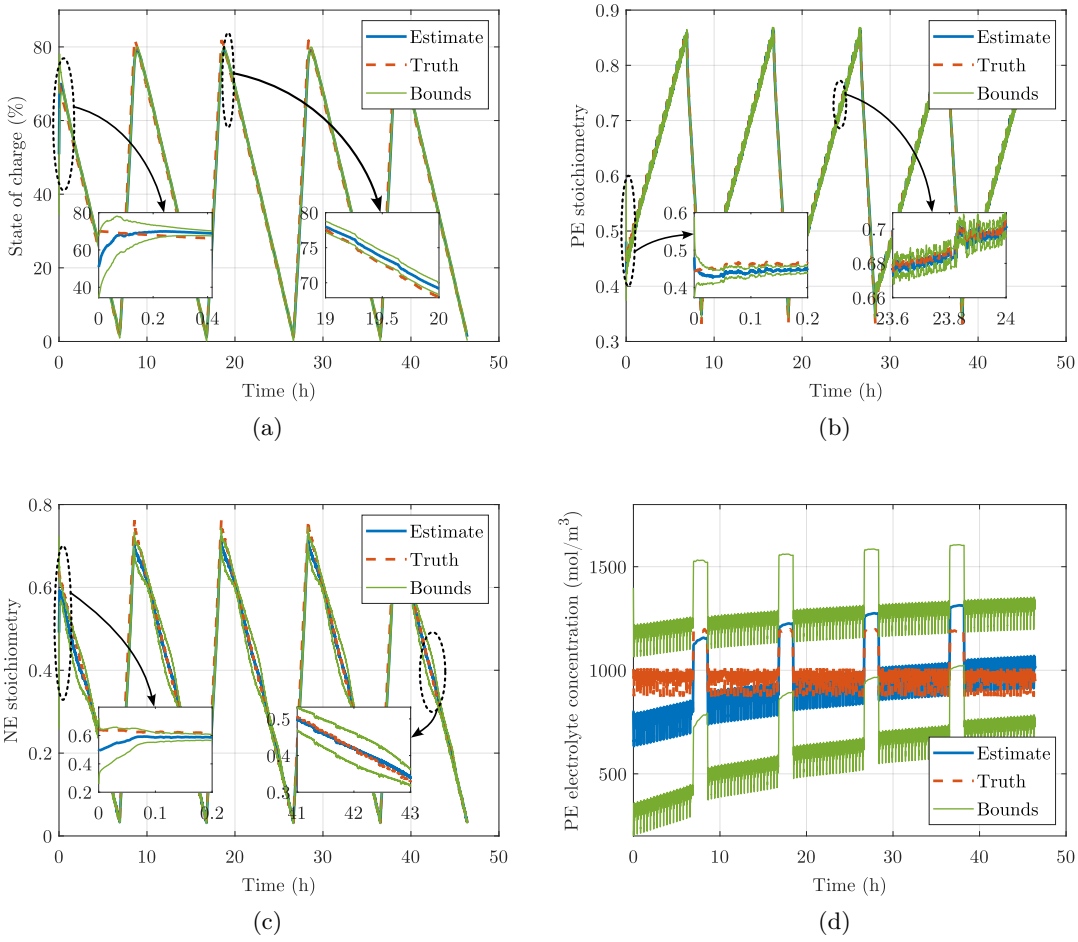

Figure 4.8: Results of the interconnected SPKF estimator with parameter measurement uncertainties. (a) SOC, (b) positive electrode stoichiometry, (c) average electrolyte concentration in the positive electrode, and (d) negative electrode stoichiometry.

Figure 4.8 shows the results of the analysis with parametric uncertainties. The RMS error of the SOC estimation in this case is 1.91 %. The electrolyte concentration has an error of 9 % for the entire simulation and 6.8 % in the last cycle. For the positive and negative electrode stoichiometry estimates, the RMS errors are 0.57 % and 2.05 %, respectively. As can be seen, the estimation errors increased compared to the other cases. This seems logical due to the relatively large parametric errors inserted into the model. However, it can be seen that the estimator is able to correct the estimates adequately, especially the solid-phase concentrations, and it can estimate the SOC more accurately

than in the previous case with eSOH parameter uncertainties. It should be noted that the differences in eSOH parameter inserted in the previous case are significantly smaller than in this case, and still the SOC estimation is more accurate in the case without deviations of the eSOH parameters.

Since 25 % parameter errors should be rarely encountered in real applications, the same analysis was performed with 5 % errors instead of 25 %. The goal of this analysis was to evaluate how the estimator behaves under more "realistic" parameter uncertainties, which may be caused by aging, cell-to-cell variations or measurement/estimation errors. The resulting RMS errors are the following: 0.78 % for the SOC estimate, 0.33 % for the positive electrode stoichiometry, 0.97 % for the negative electrode stoichiometry, 7.05 % for the electrolyte concentration throughout the entire simulation and 1.59 % for the last cycle. These results are comparable to the results reported for the two discussed cases without parametric uncertainties.

As can be observed, the importance of eSOH parameter estimation is critical for accurate physics-based SOC estimation, since the most significant errors in the SOC estimates can arise from these deviations. Other parametric deviations can result in poorer estimates, but if the differences are not very large, the filter can produce very accurate estimates.

4.5 CONCLUSIONS

A novel method for estimating SOC and internal variables was presented using an SPMe with three interconnected SPKF estimators. Interconnection was shown to improve the observability of the system, making the filter tuning faster and more robust. The validation process showed that the estimator is able to estimate all the internal variables accurately under initialization errors and measurement uncertainties. Additionally, modeling and parametric uncertainties that can be encountered due to battery aging, errors in the parameter estimation process, or cell-to-cell variations were evaluated. The importance of accurately estimating the eSOH parameters was highlighted, as SOC estimates can become inaccurate with slight parametric changes. This issue is addressed in more detail in Chapter 5. Moreover, since model-based estimators rely on voltage predictions, it is key to have accurate estimates of the OCV curve. On the other hand, other parametric uncertainties that can arise from measurement errors were analyzed by changing the values of diffusivities and reaction rates. The results showed that the estimator is capable of

correcting modest parametric uncertainties; however, if the errors become severe, it could give inaccurate estimates.

Chapter 5

PHYSICS-BASED BATTERY HEALTH ESTIMATION

This chapter discusses one of the most critical factors to implement advanced control algorithms in lithium-ion batteries; battery health estimation. Battery health estimation algorithms should adapt the model parameters according to the new aged cell characteristics, allowing the control algorithm to manage the battery optimally according to its state. To begin, an overview of current methods is given and the strengths and weaknesses of each method identified. Afterwards, the new health estimation approach that was developed in this work is presented and validated. Finally, conclusions are drawn about the algorithm that was developed.

5.1 BATTERY HEALTH ESTIMATION REVIEW

The SOH of a battery cell is usually defined as

$$SOH = \frac{Q}{Q_{nom}}, \tag{5.1}$$

where Q is the present total capacity of the battery between the maximum and minimum voltage limits, and Q_{nom} is the nominal capacity of the cell, measured with a fresh cell using the protocol specified by the manufacturer. This value represents the health of the cell at a certain time in terms of how its past usage has affected its capacity; however, it does not provide enough information to determine how quickly the capacity of the battery will drop from this point onward and when it is going to reach the end-of-life (EOL) condition. Therefore, it does not seem fair to call it the SOH of the battery. This is similar to defining the health of a person depending on how old he/she is, without taking into account any medical diagnosis.

One of the main reasons for defining SOH in this way is the lack of information that the state estimation algorithm has about the actual internal state of the battery. As mentioned in Chapter 4, nowadays empirical and ECMs are used almost exclusively for battery state estimation [8]. These are phenomenological models that cannot represent the actual physical behaviors that occur within the battery. As an alternative, in recent years, PBMs have been considered and investigated for these tasks [8, 9, 11–14, 56]. Due to the information PBMs can provide about the internal physical states of the battery, these models can offer superior performance while avoiding operating conditions known to induce degradation [8, 14]. Furthermore, they can provide more information on battery aging than the traditional estimate of SOH based on cell capacity, providing information on various degradation mechanisms and modes [22].

In addition to the SOH value, the importance of estimating eSOH parameters has been referenced in many works [167–171]. The errors that can occur in the estimation of SOC and internal variables, if these parameters of eSOH are not accurately estimated, were highlighted in Chapter 4. The eSOH parameters used here define the utilization window (the concentration values reached when the cell is at maximum and minimum voltages) and the total capacity of each electrode. This information can be used to calculate the LAM and the LLI as in [168]. This eSOH parameter estimation approach gives much more

information about the actual health of the battery than the cell capacity value, and can be used to improve the prognosis and control of a battery.

Lee *et al.* studied the identifiability of individual electrode capacity and utilization windows, showing that phase transition data improved the identifiability [167]. Mohtat *et al.* estimated electrode capacities and utilization windows using cell expansion measurements and a constrained Cramer-Rao bound formulation [168], showing that adding expansion measurements to the voltage measurements increased the observability of their system and helped in estimating the eSOH parameters. Lee *et al.* used voltage fitting and differential voltage analysis to estimate the eSOH parameters [169]. Fan *et al.* [170] performed optimizations on specific check-up profiles using a particle swarm optimization algorithm to obtain the values of the eSOH parameters and other degradation parameters. Li *et al.* [171] used a Cuckoo search algorithm to optimize the eSOH parameters and impedance-related parameters of their ECM using low-dynamic and high-dynamic operation data. These methods can be used to estimate eSOH parameters; however, they require constant-current or low-dynamic operation data, which are generally not available in most applications, or additional sensors be added to commonly used current and voltage sensors. Furthermore, these methods use optimization algorithms to obtain eSOH parameters, which is not an ideal solution for online estimation due to its computational requirements. Additionally, these optimizations depend on the quality of the data, so if the application cannot obtain and store all the necessary high-quality data, these methods might not work properly. Therefore, it would be desirable to have a filter-based estimation method, such as is often used to estimate SOC, to estimate these eSOH parameters without having to acquire constant-current data or use additional sensors. This would facilitate the implementation of these algorithms in real-world BMSs.

Some physics-based SOH estimation methods that do not require these specific data or additional sensors have been reported in the literature [12, 55, 56]. Allam and Onori [12] added a SEI layer growth model to the SPM to estimate cell capacity, as well as SOC. The results showed that the system was able to estimate these values adequately. However, despite showing good capacity estimation in their results, this approach is based on an SEI layer growth model, which is not the only degradation mechanism that can occur in a battery cell [22]. Furthermore, since the SEI layer only models the LLI, the other two degradation modes (the LAM in both electrodes) cannot be estimated, leading to incorrect estimates of SOC and internal variables, as shown in Chapter 4. Thus, this SOH estimation approach is not able to obtain eSOH parameter values.

Gao *et al.* [56] used a dual EKF to estimate the SOC and SOH of a cell. They used open-loop simulations of the positive electrode and the electrolyte phase to improve the observability of the negative electrode solid-phase concentration. Consequently, if the positive electrode or electrolyte variables are incorrectly initialized, these estimates will be incorrect. The solid-phase concentration, the active material volume fraction and the resistance increase, all in the negative electrode, were estimated with the SOC/SOH estimator. One of the inconveniences that result from this approach is that the stoichiometry limits of the negative electrode can only be estimated once the cell is fully charged or discharged. Since 100 % and 0 % SOC stoichiometry values are not directly observable from the cell voltage, they propose to use the estimated concentration values at the cell voltage limits. Therefore, if the cell does not reach one of these values, this information would be unknown. Furthermore, the approach only considers negative electrode degradation, which will generate an estimation error as the positive electrode ages. Summing up, this method can only give the negative electrodes' total capacity value, and since positive electrode aging is not taken into account, the utilization window cannot be well estimated, and will result in an erroneous SOC estimation. Besides, the utilization window values can only be obtained if the cell is fully charged and discharged.

Smiley *et al.* [55] used an interacting multiple-model (IMM) Kalman filter to estimate the SOH of a battery using a PBM. There, the authors precomputed different models that represented different aging scenarios by changing some parameters of the model that affect cell SOH. They then used the filter to select the model that most accurately represented the current aging state. One of the issues with this implementation is that LAM in the negative electrode was not considered. Therefore, this method is prone to the same SOC and internal variable estimation issue when the positive electrode ages as in the works by Allam and Onori [12], and Gao *et al.* [56]. Another shortcoming of this implementation is that it loses accuracy if the aging case is not similar to one of the precomputed models. Additionally, all the precomputed models have to be stored, and a subset must be continuously executed by the IMM, which increases the memory requirements of the implementation.

Compared to the previous work mentioned above, the proposed method makes significant contributions: (i) it does not depend on constant-current data, nor does it require additional sensors, and it can compute all the eSOH parameters from online measurements of current and voltage values. To the best of the author's knowledge, this is the first method that is able to estimate all the eSOH parameters, as well as the SOC and the internal physical

variables; (ii) it obtains LLI and both electrodes' LAM values; (iii) it can work with dynamic current profiles; and (iv) it does not need to fully charge or discharge the cell.

5.2 AGING PARAMETER SELECTION AND OBSERVABILITY ANALYSIS

As batteries age due to usage and parasitic effects that accumulate over time, their internal characteristics change, making cell voltage predictions of the battery model inaccurate (if the model is not adjusted to account for this aging), and results in incorrect state estimates. To maintain the accuracy of the state estimates shown Chapter 4 throughout the lifetime of the battery, we seek to adapt certain parameters of our model to consider the effects of aging. To represent battery aging as faithfully as possible, it is key to select appropriate parameters to estimate with the parameter estimation algorithm. These parameters will define how accurate battery cell voltage prediction is compared to the true cell voltage value, which will affect the accuracy of the estimation algorithm.

Two of the main contributors to the cell voltage value are the OCPs of both electrodes. Therefore, it is crucial that the OCP estimates remain accurate throughout the lifetime of the battery. It can be assumed that the shape of the SOL vs. OCP curves does not change with battery aging, since these curves are inherent properties of the electrode materials. However, the electrode capacity vs. OCP curves change when electrode capacity is lost. In addition, when lithium is lost due to side reactions or other aging mechanisms, a shift between the OCPs of both electrodes occurs, changing the shape of the OCV curve [119]. The estimates of the OCPs can be used to calculate the amount of lithium that was lost in the cell, as well as the amount of active material that was lost in each electrode. Many degradation mechanisms can occur in a battery cell [22], and it is extremely difficult, if not impossible, to discern which mechanisms are the ones that are taking place in the battery and at which rate they are degrading its elements. However, these mechanisms can be grouped in three degradation modes that can be estimated from the OCV and OCP curves [119]: LLI, LAM^{n} and LAM^{p}. Since these degradation modes can be observed from the cell OCV value, its estimation is more tractable than the estimation of each degradation mechanism and could give very useful information to improve battery control and prognosis. Therefore, it was determined that the parameters that must be updated to maintain accurate state estimates are the eSOH parameters.

As mentioned above, the eSOH parameters define the total capacities of the electrodes and their operating windows between some fixed cell voltage limits. When these parameters are estimated, all degradation modes can be calculated. To adapt the model to the new utilization windows, we would like to actualize the parameters $\theta^n_{0\%}$, $\theta^p_{0\%}$, $\theta^n_{100\%}$, and $\theta^p_{100\%}$ of the SPMe, which denote the stoichiometry values of the electrodes when the cell is fully charged or discharged, and therefore they define the operating windows of the electrodes. For the change in capacity of each electrode, known as LAM^{n} and LAM^{p}, we also want to adapt the volume fractions of the active material ε^n_s and ε^p_s. These two parameters define the amount of active material per volume unit that can be used for lithium intercalation and deintercalation. Thus, by estimating ε^n_s and ε^p_s, and knowing the electrode dimensions and maximum lithium concentrations, the amount of capacity that each electrode has, in Ah, can be calculated as

$$Q^r = A^r F c^r_{s,max} L^r \varepsilon^r_s / 3600, \tag{5.2}$$

where superscript r denotes the negative or positive electrode.

In order to estimate these six parameters using a filter, we first have to ensure that they are observable from the output equation. On the one hand, by examining the SPMe equations, it can be seen that the active material volume fractions affect the output voltage equation because they are related to a^n_s and a^p_s by the relation $a^r_s = 3\varepsilon^r_s / R^r_s$ (where the superscript r denotes the negative or positive electrode). These two parameters contribute to the calculation of the reaction flux j, resulting in a change in the cell voltage value. On the other hand, it can be observed that the stoichiometric limits are not directly related to the output voltage equation. The solid-phase concentration changes the OCPs of the electrodes, but the fact that the 100 % and 0 % SOC stoichiometric limits are higher or lower does not directly affect the output. Hence, some other method to estimate these four parameters should be found.

To define how observable the volume fractions of active material are, and to confirm that the stoichiometry limits do not directly contribute to the output voltage equation, the same method that was presented in Section 4.3.1 was used. First, the model was reformulated in a general nonlinear form as follows

$$\begin{aligned} \dot{x} &= f(x, u) \\ y &= h(x, u), \end{aligned} \tag{5.3}$$

where x denotes the eSOH parameters in this case. The observability of a system can be evaluated by calculating the condition number of its observability matrix. The condition number is defined as the ratio of the maximum to the minimum singular value, and it indicates how close is a matrix from being singular. The condition number was calculated using the MATLAB® *cond* function. Evaluating the condition number of the observability matrix, it can be analyzed if the system is well-conditioned or ill-conditioned. If the matrix has a low condition number, the system is said to be well-conditioned. On the other hand, the system is said to be ill-conditioned if it has a high condition number, and in the case the observability matrix has not full rank, the estimator would not be able to estimate some of the system states.

In the case of nonlinear systems, the observability matrix can be obtained using the Lie derivatives of h [164], which are calculated as

$$L_f^k h(x) = \nabla \left(L_f^{k-1} h \right) f, \tag{5.4}$$

where $L_f^0 h = h(x, u)$. The observability matrix is then defined with the Jacobian of the Lie derivatives as

$$\mathcal{O} = \begin{bmatrix} \nabla L_f^0 h \\ \nabla L_f^1 h \\ \nabla L_f^2 h \\ \vdots \\ \nabla L_f^n h \end{bmatrix}, \tag{5.5}$$

where n is the state vector dimension. $\mathcal{O}$ is an $n \times n$ matrix that must be of full rank for the system to be observable.

Using this method, the observability of the active material volume fractions was analyzed. To do so, the observability matrix of the system was obtained with respect to these two parameters. By analyzing its condition number for different parameter values, we saw that in all cases, except when the current was 0, the matrix was full rank and had a relatively low condition number, meaning that these parameters are observable from the output equation. This can be observed in Figure 5.1, where the condition number of the observability matrix is shown for different currents. When there is no current in the cell, the observability matrix is not full rank, and the condition number grows to infinity.

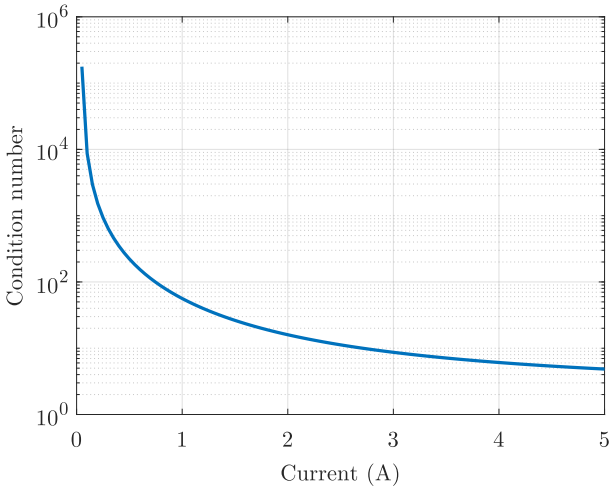

Figure 5.1: Condition number of the observability matrix of the volume fractions of the active materials for different input currents.

After analyzing the observability matrix of the stoichiometry limits, we found that the matrix does not have a full rank and, thus, the parameters cannot be calculated directly using the output voltage equation. In summary, it was determined that the active material volume fractions are observable from the cell voltage equation, unless there is no current, and thus, can be estimated using a filter. However, the analysis of the stoichiometry limits has shown that these parameters are not direct contributors to the cell voltage equation, meaning that they are not representative to the present voltage value, unless the cell is at 100 % or 0 % SOC of course. Therefore, another method must be designed to estimate these parameters.

5.3 ESTIMATOR DESIGN

Based on the observability analysis presented above, an estimation approach to obtain updated values of the six eSOH parameters was designed. The method is divided into two parts. The first part consists of estimating the active material volume fractions of both electrodes, which are observable from the output voltage equation, meaning that they can be estimated using an SPKF algorithm, for example. The second part is related to the four stoichiometry limits. Since it was determined that these parameters cannot be estimated with a filter using the present voltage value, another method was developed.

5.3.1 Active material volume fraction estimation

As explained above, the active material volume fractions are observable from the cell voltage equation, so they were added to the SPKF-based estimation approach presented in Chapter 4. This way, together with the internal states of the battery, the active material volume fractions are estimated periodically by the filter. To do so, the state estimates, x, were interconnected with the parameter estimates, ε, as in a dual state and parameter estimator [10].

The state equations for the internal physical states are given by

$$\begin{aligned} x_n[k] &= A'_n x_n[k-1] + B'_n u[k-1] \\ x_p[k] &= A'_p x_p[k-1] + B'_p u[k-1] \\ x_e[k] &= A'_e x_e[k-1] + B'_e u[k-1], \end{aligned} \tag{5.6}$$

where x_n, x_p and x_e are the negative electrode solid-phase lithium concentration, positive electrode solid-phase lithium concentration and electrolyte concentration estimates respectively. A'_n, B'_n, A'_p, B'_p, A'_e and B'_e are the state-space form discrete-time A and B matrices presented in Chapter 4, and u denotes the input of the system, which is the cell current.

For the eSOH parameter estimation, two additional estimators were included. These additional estimators are used to estimate the active material volume fraction, ε_s, of each electrode. The state equations for the parameter estimators are given by

$$\begin{aligned} \varepsilon_n[k] &= A'_{\varepsilon_n} \varepsilon_n[k-1] + B'_{\varepsilon_n} u[k-1] \\ \varepsilon_p[k] &= A'_{\varepsilon_p} \varepsilon_p[k-1] + B'_{\varepsilon_p} u[k-1], \end{aligned} \tag{5.7}$$

where ε_n and ε_p denote the negative electrode and positive electrode active material volume fraction estimates respectively. These parameters are assumed to change very slowly in time compared to the states, so the A'_{ε_n} and A'_{ε_p} matrices are equal to 1, while B'_{ε_n} and B'_{ε_p} are equal to 0.

The interconnected state estimator has been updated to estimate the two active material volume fractions as follows:

Step 1a: State prediction time update. The prediction of the two parameters is added to the rest of the predictions as

$$\begin{aligned}\hat{\varepsilon}_n^-[k] &= A'_{\varepsilon_n}\hat{\varepsilon}_n^+[k-1] + B'_{\varepsilon_n}u[k-1]\\ \hat{\varepsilon}_p^-[k] &= A'_{\varepsilon_p}\hat{\varepsilon}_p^+[k-1] + B'_{\varepsilon_p}u[k-1].\end{aligned} \tag{5.8}$$

Step 1b: Error covariance time update. The error covariance matrices for the parameters are given by

$$\begin{aligned}\Sigma_{\tilde{\varepsilon}_n}^-[k] &= (A'_{\varepsilon_n})^T\Sigma_{\tilde{\varepsilon}_n}^+[k-1]A'_{\varepsilon_n} + \Sigma_{\tilde{w}_{\varepsilon_n}}\\ \Sigma_{\tilde{\varepsilon}_p}^-[k] &= (A'_{\varepsilon_p})^T\Sigma_{\tilde{\varepsilon}_p}^+[k-1]A'_{\varepsilon_p} + \Sigma_{\tilde{w}_{\varepsilon_p}}.\end{aligned} \tag{5.9}$$

Step 1c: Output prediction. To predict the output, the sigma points of the active material volume fractions have to be calculated together with the sigma points of the state variables. The set of sigma points for the two parameter estimators are calculated as

$$\begin{aligned}\mathcal{W}_{\varepsilon_n}^-[k] &= \left\{\hat{\varepsilon}_n^-[k], \hat{\varepsilon}_n^-[k] + h\sqrt{\Sigma_{\tilde{\varepsilon}_n}^-}, \hat{\varepsilon}_n^-[k] - h\sqrt{\Sigma_{\tilde{\varepsilon}_n}^-}\right\}\\ \mathcal{W}_{\varepsilon_p}^-[k] &= \left\{\hat{\varepsilon}_p^-[k], \hat{\varepsilon}_p^-[k] + h\sqrt{\Sigma_{\tilde{\varepsilon}_p}^-}, \hat{\varepsilon}_p^-[k] - h\sqrt{\Sigma_{\tilde{\varepsilon}_p}^-}\right\},\end{aligned} \tag{5.10}$$

where h is a tuning variable for the SPKF and $\sqrt{\Sigma_{\tilde{\varepsilon}_n}^-}$ and $\sqrt{\Sigma_{\tilde{\varepsilon}_p}^-}$ are the lower-triangular matrix square root of the error covariance matrices, which have been computed using a Cholesky decomposition. The sigma points (the vectors of the sets $\mathcal{W}$) are then used to compute the output equation and obtain the output sigma points. Since the volume fractions of active materials affect the output equation, the output sigma points of the state estimators, $\mathcal{Y}$, must be calculated considering the changes in these parameters.

$$\begin{aligned}\mathcal{Y}_{n,i} &= h(\mathcal{X}_{n,i}^-[k], \hat{x}_p^-[k], \hat{x}_e^-[k], \hat{\varepsilon}_n^-[k], \hat{\varepsilon}_p^-[k], u[k])\\ \mathcal{Y}_{p,i} &= h(\hat{x}_n^-[k], \mathcal{X}_{p,i}^-[k], \hat{x}_e^-[k], \hat{\varepsilon}_n^-[k], \hat{\varepsilon}_p^-[k], u[k])\\ \mathcal{Y}_{e,i} &= h(\hat{x}_n^-[k], \hat{x}_p^-[k], \mathcal{X}_{e,i}^-[k], \hat{\varepsilon}_n^-[k], \hat{\varepsilon}_p^-[k], u[k])\\ \mathcal{D}_{\varepsilon_n,i} &= h(\hat{x}_n^-[k], \hat{x}_p^-[k], \hat{x}_{e,i}^-[k], \mathcal{W}_{\varepsilon_n}^-[k], \hat{\varepsilon}_p^-[k], u[k])\\ \mathcal{D}_{\varepsilon_p,i} &= h(\hat{x}_n^-[k], \hat{x}_p^-[k], \hat{x}_{e,i}^-[k], \hat{\varepsilon}_n^-[k], \mathcal{W}_{\varepsilon_p}^-[k], u[k]),\end{aligned} \tag{5.11}$$

The five cell voltage predictions are calculated as the weighted mean of these sigma points:

$$\begin{aligned}
\hat{y}_n[k] &= \sum_{i=0}^{2N_{x_n}+1} \alpha_{n,i}^{(m)} \mathcal{Y}_{n,i}[k] \\
\hat{y}_p[k] &= \sum_{i=0}^{2N_{x_p}+1} \alpha_{p,i}^{(m)} \mathcal{Y}_{p,i}[k] \\
\hat{y}_e[k] &= \sum_{i=0}^{2N_{x_e}+1} \alpha_{e,i}^{(m)} \mathcal{Y}_{e,i}[k] \\
\hat{d}_{\varepsilon_n}[k] &= \sum_{i=0}^{2N_{\varepsilon_n}+1} \alpha_{\varepsilon_n,i}^{(m)} \mathcal{D}_{\varepsilon_n,i}[k] \\
\hat{d}_{\varepsilon_p}[k] &= \sum_{i=0}^{2N_{\varepsilon_p}+1} \alpha_{\varepsilon_p,i}^{(m)} \mathcal{D}_{\varepsilon_p,i}[k],
\end{aligned} \tag{5.12}$$

where $\alpha_{n,i}^{(m)}$, $\alpha_{p,i}^{(m)}$, $\alpha_{e,i}^{(m)}$, $\alpha_{\varepsilon_n,i}^{(m)}$ and $\alpha_{\varepsilon_p,i}^{(m)}$ are the constants used to calculate the weighted mean.

Step 2a: Estimator gain matrix. The covariance matrices for the parameter estimators are calculated in the same way as for the state estimator:

$$\begin{aligned}
\Sigma_{\tilde{d}_{\varepsilon_n}}[k] &= \sum_{i=0}^{2N_{\varepsilon_n}+1} \alpha_{\varepsilon_n,i}^{(c)} (\mathcal{D}_{\varepsilon_n,i}[k] - \hat{d}_{\varepsilon_n}[k])(\mathcal{D}_{\varepsilon_n,i}[k] - \hat{d}_{\varepsilon_n}[k])^T \\
\Sigma_{\tilde{d}_{\varepsilon_p}}[k] &= \sum_{i=0}^{2N_{\varepsilon_p}+1} \alpha_{\varepsilon_p,i}^{(c)} (\mathcal{D}_{\varepsilon_p,i}[k] - \hat{d}_{\varepsilon_p}[k])(\mathcal{D}_{\varepsilon_p,i}[k] - \hat{d}_{\varepsilon_p}[k])^T,
\end{aligned} \tag{5.13}$$

$$\begin{aligned}
\Sigma^-_{\tilde{\varepsilon}_n \tilde{d}_{\varepsilon_n}}[k] &= \sum_{i=0}^{2N_{\varepsilon_n}+1} \alpha_{\varepsilon_n,i}^{(c)} (\mathcal{W}^-_{\varepsilon_n,i}[k] - \hat{\varepsilon}^-_n[k])(\mathcal{D}_{\varepsilon_n,i}[k] - \hat{d}_{\varepsilon_n}[k])^T \\
\Sigma^-_{\tilde{\varepsilon}_p \tilde{d}_{\varepsilon_p}}[k] &= \sum_{i=0}^{2N_{\varepsilon_p}+1} \alpha_{\varepsilon_p,i}^{(c)} (\mathcal{W}^-_{\varepsilon_p,i}[k] - \hat{\varepsilon}^-_p[k])(\mathcal{D}_{\varepsilon_p,i}[k] - \hat{d}_{\varepsilon_p}[k])^T.
\end{aligned} \tag{5.14}$$

where $\alpha_{\varepsilon_n,i}^{(c)}$ and $\alpha_{\varepsilon_p,i}^{(c)}$ are the constants used to calculate the weighted covariance.

Once these matrices are computed we calculate the gains of the estimators:

$$\begin{aligned}
L_{\varepsilon_n}[k] &= \Sigma^-_{\tilde{\varepsilon}_n \tilde{d}_{\varepsilon_n}}[k](\Sigma_{\tilde{d}_{\varepsilon_n}}[k])^{-1} \\
L_{\varepsilon_p}[k] &= \Sigma^-_{\tilde{\varepsilon}_p \tilde{d}_{\varepsilon_p}}[k](\Sigma_{\tilde{d}_{\varepsilon_p}}[k])^{-1}.
\end{aligned} \tag{5.15}$$

Step 2b: State estimate measurement update. The parameter estimates are then calculated as

$$\begin{aligned}\hat{\varepsilon}_n^+[k] &= \hat{\varepsilon}_n^-[k] + L_{\varepsilon_n}(d[k] - \hat{d}_{\varepsilon_n}[k]) \\ \hat{\varepsilon}_p^+[k] &= \hat{\varepsilon}_p^-[k] + L_{\varepsilon_p}(d[k] - \hat{d}_{\varepsilon_p}[k]).\end{aligned} \tag{5.16}$$

Step 2c: Error covariance measurement update. Lastly, the error covariance matrices are updated as

$$\begin{aligned}\Sigma_{\tilde{\varepsilon}_n}^+[k] &= \Sigma_{\tilde{\varepsilon}_n}^-[k] - L_{\varepsilon_n}[k]\Sigma_{\tilde{d}_{\varepsilon_n}}[k]\left(L_{\varepsilon_n}[k]\right)^T \\ \Sigma_{\tilde{\varepsilon}_p}^+[k] &= \Sigma_{\tilde{\varepsilon}_p}^-[k] - L_{\varepsilon_p}[k]\Sigma_{\tilde{d}_{\varepsilon_p}}[k]\left(L_{\varepsilon_p}[k]\right)^T.\end{aligned} \tag{5.17}$$

With this combined state/parameter estimator, solid-phase and electrolyte concentrations, as well as active material volume fractions, are estimated for both electrodes, which has not been reported in literature to the best of our knowledge. The following state variables x and parameters ε are obtained from these five SPKF estimators' interconnection:

$$\begin{aligned}x &= [c_s^n; c_s^p; c_e] \\ \varepsilon &= [\varepsilon_s^n; \varepsilon_s^p].\end{aligned} \tag{5.18}$$

It is not mandatory to interconnect one estimator per state variable and per parameter. As has been shown in the observability analysis, the parameters could be estimated using a single estimator, as its observability matrix has a relatively low condition number. However, the interconnection makes the tuning of the filters easier and, as we have seen in our simulations, more stable and robust.

5.3.2 Stoichiometric window estimation

As mentioned above, as the stoichiometry limits are not direct contributors to the voltage equation of our SPMe, another method to estimate this variables was designed. For that, a system of four equations was defined, which can be solved to obtain the rest of the eSOH parameters (the 100 % and 0 % SOC stoichiometries). The procedure to obtain each equation is explained below.

The available capacity, in Ah, of an electrode between some defined voltage limits is given by

$$Q^r = A^r F c^r_{s,max} L^r \varepsilon^r_s (\theta^r_{100\%} - \theta^r_{0\%})/3600, \tag{5.19}$$

where superscript r denotes the negative, n, or positive, p, electrode.

Since the lost capacity over a full discharging process is relatively small compared to the capacities of the electrodes, it can be assumed that the usable capacities of both electrodes are equivalent:

$$Q_{dch} \approx Q^n \approx Q^p. \tag{5.20}$$

The same occurs in the charging process,

$$Q_{ch} \approx Q^n \approx Q^p. \tag{5.21}$$

Therefore,

$$A^n c^n_{s,max} L^n \varepsilon^n_s (\theta^n_{100\%} - \theta^n_{0\%}) = A^p c^p_{s,max} L^p \varepsilon^p_s (\theta^p_{0\%} - \theta^p_{100\%}). \tag{5.22}$$

Equation 5.22 shows the six eSOH parameters that we want to estimate: $\theta^n_{100\%}, \theta^n_{0\%}, \theta^n_{100\%}, \theta^p_{0\%}, \varepsilon^p_s$ and ε^p_s.

If the useful capacities of both electrodes are equivalent, then the remaining useful capacities until full charge or discharge must also be the same. The full discharge equivalency is given by

$$A^n c^n_{s,max} L^n \varepsilon^n_s (z^n - \theta^n_{0\%}) = A^p c^p_{s,max} L^p \varepsilon^p_s (\theta^p_{0\%} - z^p), \tag{5.23}$$

and for a full charge:

$$A^n c^n_{s,max} L^n \varepsilon^n_s (\theta^n_{100\%} - z^n) = A^p c^p_{s,max} L^p \varepsilon^p_s (z^p - \theta^p_{100\%}), \tag{5.24}$$

where z^p and z^n are the current lithiation states of the electrodes at any given moment. Note that we use z^n and z^p instead of θ^n and θ^p. This is because the stoichiometry limits are defined using OCP values, which are obtained when the surface concentration is equal to, or almost equal to, the SOL of the active material particle. When operating the battery with higher C-rates, the intercalation process in both electrodes can be different, as the

surface concentration may change faster or slower depending on the diffusion coefficients or the exchange current densities of the electrodes. This can generate a difference between the available capacities of both electrodes. Thus, it is more accurate to define the available electrode capacities using the SOL rather than the stoichiometry. In this way, any difference caused by the different parameters of the positive and negative electrodes is avoided.

Since we also know our fixed operation voltage limits, we know that the 100 % and 0 % positive and negative stoichiometries must fulfill

$$U^p_{ocp}(\theta_{100\%}) - U^n_{ocp}(\theta_{100\%}) = V_{max} \tag{5.25}$$

and

$$U^p_{ocp}(\theta_{0\%}) - U^n_{ocp}(\theta_{0\%}) = V_{min}. \tag{5.26}$$

We assume that the OCPs are fixed functions of active materials that do not change with battery aging, nor do the values of A^r, $c^r_{s,max}$, L^r and F. Therefore, the only unknowns of this four-equation system are the six eSOH parameters and the SOL of both electrodes z^n and z^p. Nonetheless, z^n and z^p are estimated by the SOC estimator with the interconnected SPKFs. ε^n_s and ε^p_s are also obtained from the new two additional interconnected SPKFs that we have defined above. Thus, the resulting system of equations has four equations to solve for four variables. By solving this system of equations, the remaining four eSOH parameters can be obtained, which completes the estimation of the eSOH parameters.

As mentioned above, the stoichiometry limits are not estimated every time step by the interconnected SPKF filter, instead, for the validation process, the equation system was solved numerically using the MATLAB® *vpasolve* solver. In the simulations, the system was solved at the end of the charging process, however, it can be performed at any other moment. This is less demanding computationally, and since the eSOH parameters will not change its value often, it is not necessary to change their values in every time step. The equation system was solved for several values of c_s and ε_s of the last discharge/charge cycle for each end-of-charge event. These estimates were taken every 1000 s from the last cycle. Later, the $\theta^n_{100\%}$, $\theta^p_{100\%}$, $\theta^n_{0\%}$ and $\theta^p_{0\%}$ values obtained from all the solutions are filtered (using the MATLAB® function *rmoutliers*) and averaged. This is the approach that we decided to follow to obtain the results; however, the equation system can be solved for just one point if it is preferable. The reason for doing so is that, in this way, an overall estimate value was obtained from the different estimates of the entire discharge/charge cycle.

5.3.3 Degradation mode and SOH estimation

Once the eSOH parameters are estimated, the three degradation modes LLI, LAM^{n} and LAM^{p} can be calculated. The LAM of each electrode, in %, can be defined as

$$LAM^r = \left(1 - \frac{Q_a^r}{Q_f^r}\right) \times 100 \tag{5.27}$$

where r denotes the positive or negative electrode, Q_a^r is the total capacity of the aged electrode r, calculated as

$$Q_a^r = A^r F c_{s,max}^r L^r \varepsilon_{s,a}^r / 3600, \tag{5.28}$$

where $\varepsilon_{s,a}^r$ is the estimated active material volume fraction. Q_f^r is the total capacity of a fresh electrode r, calculated as

$$Q_f^r = A^r F c_{s,max}^r L^r \varepsilon_{s,f}^r / 3600, \tag{5.29}$$

where $\varepsilon_{s,f}^r$ is the initial active material volume fraction of the fresh cell. Therefore, since the only variable that changes is ε_s^r, the LAM can be defined as

$$LAM^r = \left(1 - \frac{\varepsilon_{s,a}^r}{\varepsilon_{s,f}^r}\right) \times 100. \tag{5.30}$$

The total amount of intercalated lithium in the cell at any SOC can be calculated as

$$n_{Li} = \frac{3600}{F} \left(z^p Q^p + z^n Q^n\right). \tag{5.31}$$

Any z^n and z^p values can be chosen from the entire SOC range (both from the same SOC). In our case, we have chosen to take the 0 % SOC values. Then, the LLI can be calculated as

$$LLI = \left(1 - \frac{n_{Li}^a}{n_{Li}^f}\right) \times 100, \tag{5.32}$$

where n_{Li}^a is the aged lithium inventory, and n_{Li}^f is the fresh lithium amount in the cell. Since the total electrode capacities, Q^n and Q^p, are calculated with the ε_s estimates, and the lithiation states were also estimated, the calculation of LLI is straightforward.

In addition, an SOH value can be calculated by comparing the fresh cell capacity with the aged cell capacity. The available capacity of the aged cell can be obtained by substituting the estimated eSOH parameter values in the electrode capacity Equation 5.19. Then, the SOH of the cell can be calculated as

$$SOH = \frac{Q_a}{Q_f}, \tag{5.33}$$

where Q_a is the aged cell capacity calculated with the estimated eSOH parameters, and Q_f is the fresh cell capacity.

5.4 STATE AND PARAMETER ESTIMATION VALIDATION

To validate the proposed estimator, the accuracy of the state and parameter estimates was analyzed. For that, the estimates were compared to the high-fidelity P2D model mentioned above, which was used to obtain the true values of the states and parameters. A charge-depleting UDDS current profile, scaled to cell level for a 1C maximum current, was used as dynamic input for the simulations. The profile is shown in Figure 5.2.

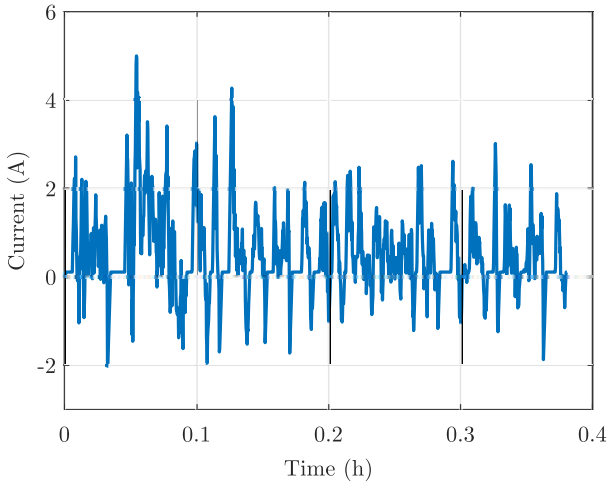

Figure 5.2: Charge-depleting UDDS current profile.

Two different aging scenarios were studied to assess the performance of the estimator. The robustness of the algorithm was evaluated under incorrect state and parameter initializations in both cases. First, the same SOC and internal variable estimation with incorrect eSOH parameters shown in Section 4.4.2 was performed with the state/parameter estimator to see if the estimator was able to correct the SOC and internal variable estimates.

Later, larger eSOH parameter differences were used, including significant LAM values in both electrodes, to discuss the estimation performance in harsher conditions. Note that these degradation mode values could arise from different degradation mechanisms, such as SEI growth or lithium plating for the LLI, and particle cracking for the LAM, for example. However, even without knowing which aging mechanisms have happened in the cell, the estimator should be able to estimate the effects that these mechanisms have generated in the capacities of both electrodes and the OCV of the cell.

In the first case, a 10 % LAM value was applied in the negative electrode by reducing 10 % the active material volume fraction of the active material, and 5 % LLI in the cell by changing the stoichiometry limits of both electrodes. Equations 5.27-5.32 were used to calculate the parameter values. In Chapter 4, it was concluded that without estimating these eSOH parameters, the SOC and internal variable estimation was inaccurate. The SOC estimate RMS error was 3.63 %, the electrolyte concentration estimate was very poor, and the solid-phase concentration estimates were significantly worse than in the cases with no eSOH parameter uncertainties. In this case, the eSOH parameters are estimated and updated during the simulation as defined above. The results of this simulation are shown in Figure 5.3.

To analyze all the dynamics of the parameters, 15 charge/discharge cycles were simulated. In each cycle, the cell was discharged using consecutive charge-depleting UDDS profiles, as the one shown in Figure 5.2, until the minimum cell voltage was reached. Subsequently, the cell was charged at constant current C/2 until the maximum voltage value was reached. The SOC was initialized with 20 % error and the volume fractions of active materials were initialized at 80 % of their values at BOL. The differences in eSOH parameters with respect to the fresh cell are shown in Table 5.1.

Table 5.1: Variations of the eSOH parameters for the first aging case.

Parameter	Fresh	Aged
ε_s^n	0.75	0.675
ε_s^p	0.665	0.665
$z^n_{0\%}$	0.027	0.0256
$z^p_{0\%}$	0.8536	0.8148
$z^n_{100\%}$	0.9014	0.9350
$z^p_{100\%}$	0.27	0.2661

Looking at Figure 5.3, it can be observed that the initial state and parameter estimates are inaccurate. However, as the volume fractions of the active materials are slowly corrected,

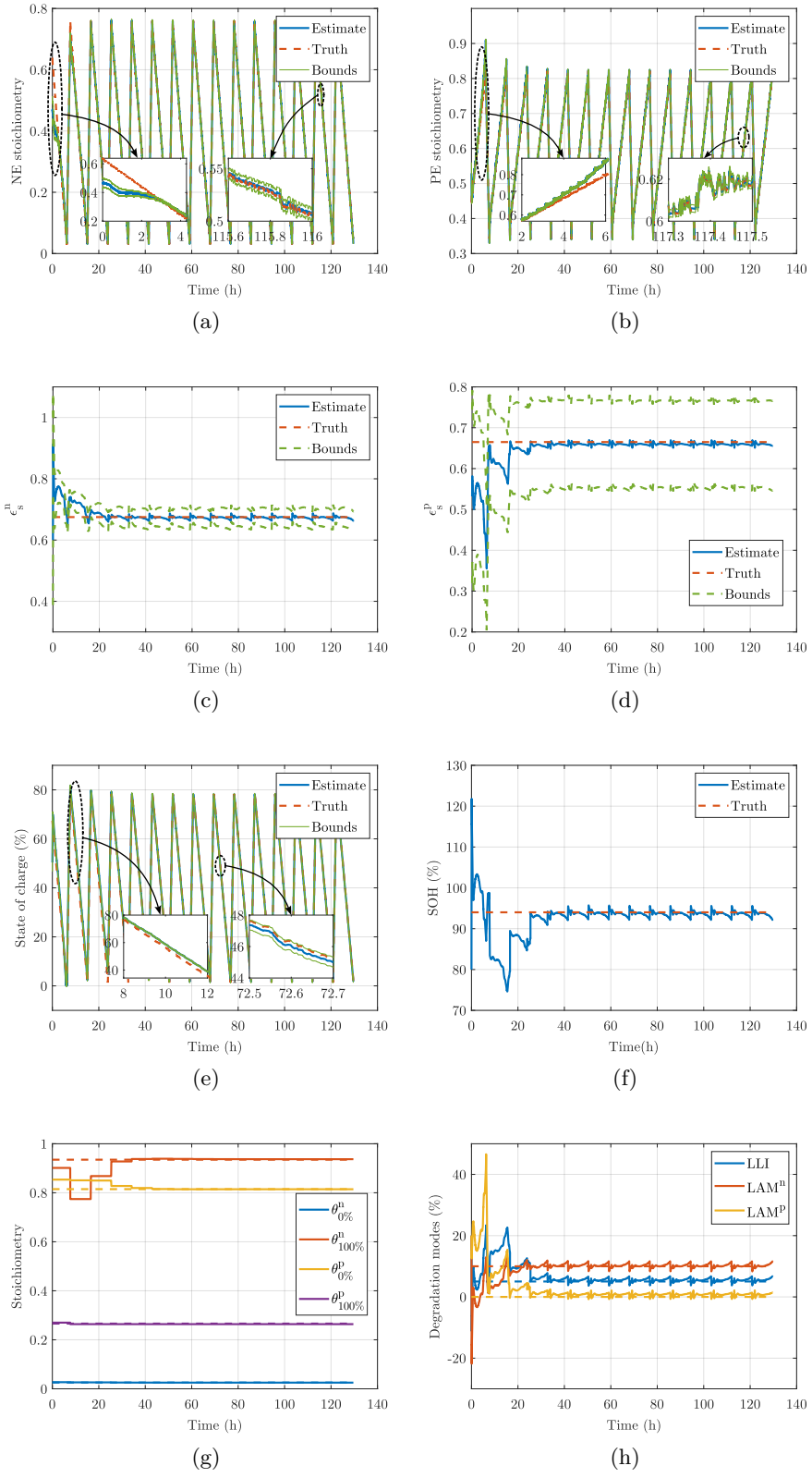

Figure 5.3: Estimation of states and parameters with 10 % LAM in the negative electrode and 5 % LLI. (a)-(b) Negative and positive electrode stoichiometries, respectively; (c) and (d) negative and positive electrode volume fractions of active materials, respectively; (e) SOC estimate; (f) SOH estimate; (g) 100 % and 0 % SOC stoichiometries; (h) degradation modes.

the state estimates improve. This can be seen in the SOC estimate of Figure 5.3 (e). The SOC estimate is poor at first, as the stoichiometry limits shown in Figure 5.3 (g) are inaccurate. Little by little, estimates of active material volume fractions of Figure 5.3 (c) and (d) are corrected and, electrode stoichiometry estimates shown in Figure 5.3 (a) and (b) become more accurate. The RMS error of the SOC in the full simulation is 1.4 %, while the RMS error in the last cycle is 0.29 %. This shows how the parameter estimator improves the SOC estimate by updating the volume fractions of the aged active material and the stoichiometry limits. The same happens in the negative and positive stoichiometries, which have 1.72 % and 0.73 % RMS errors, respectively, for the entire simulation, while in the last cycle both stoichiometry estimates have 0.11 % RMS errors. Regarding the parameters, the negative and positive volume fractions of the active materials have 2.94 % and 6.2 % RMS error, respectively (normalized with the values of the fresh cell), while they have 0.59 % and 0.85 % RMS error in the last cycle.

As these four estimates converge to the true values, the equation system (5.23-5.26) to solve $\theta^n_{100\%}$, $\theta^p_{100\%}$, $\theta^n_{0\%}$ and $\theta^p_{0\%}$ provides better estimates, improving the SOC estimate. Normalized to the values at the BOL, $\theta^n_{100\%}$, $\theta^p_{100\%}$, $\theta^n_{0\%}$ and $\theta^p_{0\%}$ have 5.14 %, 0.9 %, 1.94 %, and 1.94 % errors, respectively, in the entire simulation, while in the last cycle the RMS errors are 0.22 %, 0.85 %, 1.34 % and 0.05 %.

As the eSOH parameters are estimated, the degradation modes can be calculated using Equations 5.30-5.32. The results of these estimates can be seen in Figure 5.3 (h). As happens with the rest of the estimates, the results are accurate once the eSOH parameters are corrected. Additionally, an SOH estimate was obtained by computing Equation 5.33. As can be observed, the estimate converges accurately to the true value.

The results for a different aging scenario are shown in Figure 5.4. In this case, in contrast to the previous case, both electrodes suffer from LAM, not just the negative electrode. The LAM for the positive electrode is 20 %, 10 % for the negative electrode, and 16 % LLI. The eSOH parameters of this case are shown in Table 5.2.

Figures 5.4 (a) and (b) show the stoichiometries of the negative and positive electrodes, respectively. The estimates of both variables are inaccurate in the first cycles, especially the positive electrode stoichiometry, due to the incorrect initialization of the active material volume fractions, shown in Figure 5.4 (c) and (d), which affect the SPMe predictions of these variables due to the change in the reaction flux, j. After the first cycle, the positive electrode stoichiometry is corrected as the positive electrode active material volume fraction converges to its true value. The RMS errors for negative and positive

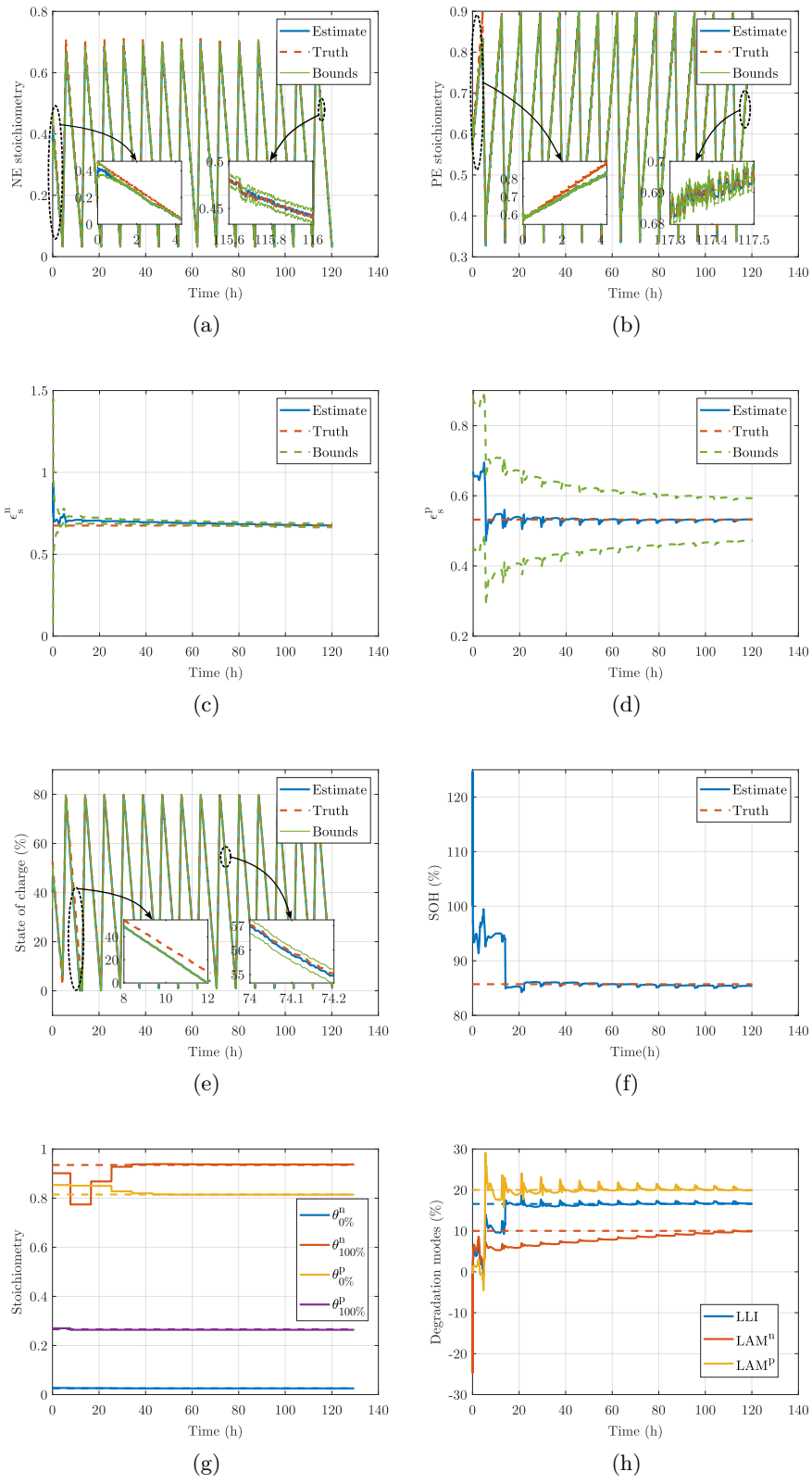

Figure 5.4: State and parameter estimation results with 10 % LAM in the negative electrode, 20 % LAM in the positive electrode, and 16 % LLI. (a)-(b) Negative and positive electrode stoichiometries, respectively; (c) and (d) negative and positive electrode volume fractions of active materials, respectively; (e) SOC estimate; (f) SOH estimate; (g) 100 % and 0 % SOC stoichiometries; (h) degradation modes.

Table 5.2: Variations of the eSOH parameters for the second aging case.

Parameter	Fresh	Aged
ε_s^n	0.75	0.675
ε_s^p	0.665	0.532
$z_{0\%}^n$	0.027	0.0278
$z_{0\%}^p$	0.8536	0.891
$z_{100\%}^n$	0.9014	0.8566
$z_{100\%}^p$	0.27	0.2657

electrode stoichiometries are 1.04 % and 0.67 %, respectively, for the entire simulation and 0.11 % and 0.06 % in the last cycle. The negative electrode active material volume fraction estimate takes longer than the positive. This is probably due to the higher sensitivity of the positive electrode stoichiometry to cell voltage. For the end of the simulation, the active material volume fraction of the negative electrode converges well to the true value, improving the negative electrode stoichiometry estimate. The RMS errors of the negative and positive active material volume fractions are 2.72 % and 4.14 % respectively, while in the last cycle are 0.11 % and 0.29 %.

In the case of the SOC estimation, shown in Figure 5.4 (e), a higher error can be seen in the first cycles compared to the last cycles. This error comes from two sides; First, the stoichiometry estimates are not accurate until the volume fractions are corrected, and second, the stoichiometry limits shown in Figure 5.4 (g) have a considerable error until the volume fractions and the solid-phase concentrations are corrected. After some cycles, the SOC estimate improves considerably, and in the last cycles becomes very accurate as it is shown in Figure 5.4 (e). The SOC RMS error of the full simulation is 1.73 %, while in the last cycle the error decreases to 0.33 %. In the case of $\theta_{100\%}^n$, $\theta_{100\%}^p$, $\theta_{0\%}^n$ and $\theta_{0\%}^p$, the RMS errors are 2.49 %, 0.75 %, 2.78 % and 2.28 % respectively, while in the last cycle the errors are 0.14 %, 0.68 %, 1.64 % and 0.26 %.

Regarding the estimates of SOH and degradation modes shown in Figures 5.4 (f) and (h), respectively, the SOH estimate improves considerably for the second cycle and remains very accurate until the end of the simulation. LAM^{p} and LLI estimates are very accurate from the second cycle on. Since the LAM^{n} value is obtained from the estimate of the active material volume fraction of the negative electrode, it takes more time to correct its value, but it converges accurately.

5.5 DISCUSSION

The parameter estimation method proposed in this chapter can be used to estimate all the eSOH parameters, and thus all the degradation modes, which group any aging mechanism that can occur inside a cell [119], allowing the acquisition of very valuable information for prognosis and control. Additionally, other parameters could be added to the estimation approach to obtain better voltage predictions from the model. Nevertheless, many parameters of the SPMe are bulk properties of the materials, and therefore, unless the composition of the electrode and electrolyte materials changes, it should not be necessary to update them. In addition to the eSOH parameters, it would be interesting to add parameters that represent power fade in the battery to this estimation approach; such as the electric resistance growth or the porosity decrease. These updates in the estimator would improve SOP and internal variable estimates, helping control algorithms.

The main drawback of the proposed estimation method is probably the equation system that has to be solved numerically to obtain the stoichiometry values at 100 % and 0 % SOH. It is not desirable for a BMS to require of numerical computations to obtain these parameter values. However, since the eSOH parameters change very slowly over time, it is not necessary to do these calculations online. The stoichiometry limits can be obtained apart from the online state/parameter estimation procedure, ideally after the estimates become stable. For example, if the eSOH parameters of an electric vehicle (EV) battery have to be obtained, the numerical computations can be done when the EV arrives at a charging station or whenever it has a connection to a more powerful computing source.

One of the benefits of this estimation method is the estimation of degradation modes. These estimates would certainly aid in the prediction of battery degradation "knee" trajectories [157, 172], and several battery applications could benefit from this added knowledge. For example, second-life batteries could be more reliable if the degradation modes were well known and if there were a way to know the probability that a battery would be near a degradation "knee". Moreover, electric vehicle or stationary applications could improve battery control algorithms based on this degradation modes and internal variables knowledge.

Accurate physics-based state estimation algorithms could prevent accelerated battery degradation and safety issues. Besides, accurate stoichiometry estimates as the ones shown in this paper could be used to define dynamic SOAs in future BMSs, increasing the energy and power capabilities, while providing longer battery lifespans.

5.6 CONCLUSIONS

In this chapter, a novel eSOH parameter estimation method was presented which is capable of estimating all degradation modes from current and voltage measurements in normal battery operation; with dynamic input current profiles and without the need of any additional experiment. The method was validated in simulation for two different aging scenarios; one of them with 10 % LAM in the negative electrode and 5 % LLI, and the other with 20 % LAM in the positive electrode, 10 % in the negative electrode and 16 % LLI in the battery. The results showed very good agreement with the true values. The internal variable estimates were accurately corrected by the filter and improved while the eSOH parameter estimates converged. Besides, degradation modes and SOH were estimated with high accuracy in both studied cases.

In this work, a first step of the validation process was performed by validating the algorithm in simulation. However, experimental validation is paramount in the validation process, and future work will develop an experimental study for this purpose. Additionally, the estimation of parameters that represent power fade is crucial for battery control and, therefore, future work will add these parameters to the estimator. The resulting algorithm would be able to add a power fade estimate to the previously developed eSOH, degradation mode and capacity fade estimates.

Chapter 6

BATTERY AGING-AWARE CONTROL

This chapter discusses the aging-aware control strategies that were implemented and evaluated throughout this thesis. A new fast charging strategy is proposed to minimize lithium plating based on the previously developed degradation model, which could be coupled with the state/parameter estimator to improve fast charging throughout the lifetime of a battery. First, the relevant literature is reviewed. Later, the most popular control strategy found in the literature is evaluated and compared to the new fast charging algorithm developed in this work. Finally, the conclusions drawn from this work are presented.

6.1 DEGRADATION-AWARE CONTROL REVIEW

As explained in Section 1.2.3, lithium-ion battery control has been widely studied in the literature [63]. However, not many works focused on controlling the cell based on physical insight. The approaches that can be adopted when developing a control strategy can be classified into two groups; passive and active methods. Passive methods are based on optimizing a charging profile offline, while active methods work online and use present cell data to control its operation.

Focusing on passive strategies, Lin *et al.* [173] used an SPM and dynamic programming to develop degradation-aware fast charging strategies, showing significant improvements in charging time and capacity loss compared to typical CCCV protocols. They applied physics-based constraints on solid-phase and electrolyte concentrations to mitigate aging. However, they did not used any additional degradation model to predict specific degradation phenomena, and semi-empirical cost functions were applied for the optimization. Gao *et al.* [61] used an SPM coupled to a thermal model and an SEI growth model to design degradation-aware charging strategies. They tried to minimize the SEI growth on the cost function, while they applied a hard constraint on the negative electrode overpotential to mitigate lithium plating. The results show that their "health-aware" strategy reduced battery aging, while their "minimum-time" strategy, despite reducing the charging time, reduced significantly the lifetime of the cell.

Regarding active control strategies, Yin *et al.* [69] used a reduced-order P2D model for the negative electrode and an SPM for the positive electrode to reduce SEI growth and lithium plating. They employed an NMPC algorithm with the objective of reducing SEI growth in the charging process, and to reduce lithium plating, they proposed to include discharging pulses every 50 s if the side reaction's overpotential went below 0. The state estimation was performed with an SPKF algorithm. The results showed that the method was able to increase the lifetime of the battery compared to similar time CCCV charging protocols.

The most complete degradation-aware control strategy was reported by Zhou *et al.* [16]. They used an SPMe coupled to a thermal model and to SEI growth and lithium plating aging models. They used an unscented Kalman filter (UKF) to estimate the internal variables of the SPMe, and an MPC algorithm to minimize charging time while maintaining both side-reactions' overpotential above their minimum values. The main improvement with respect to previously reported control architectures is the experimental validation

procedure. While previous works compared capacity loss between the degradation-aware control strategy and CCCV strategies [61, 69], Zhou *et al.* [16] used differential voltage analysis to analyze the degradation modes occurring in the cell. Hence, obtaining a deeper analysis of the aging that has occurred with and without the optimized charging protocol. In their case, the battery suffered from significant LAM in the negative electrode and considerable LLI. The authors suggested that the LAM could come from the pore blockage occurring due to the SEI and lithium plating films. However, in their results can be seen that LAM in the negative electrode occurs before LLI, contradicting their argument. Therefore, another aging model could be used to model the LAM occurring in the negative electrode, and the control strategy could be improved. Nonetheless, the results show that there is a significant improvement on LAM and LLI by using the optimized charging algorithm.

Summing up, this literature review showed that most physics-based degradation-aware control strategies, both active and passive, aim to reduce aging by limiting the side-reactions' overpotential. Most authors tried to mitigate lithium plating, while some of them tried also to mitigate SEI growth. However, none of the analyzed works developed a control strategy using the recently published plating/stripping models, and tried to use the stripping reaction to allow faster charging while mitigating plating. Furthermore, it was observed that none of the reported strategies tried to mitigate LAM, while it was seen in Chapter 3 that it can be a major contributor to the aging of a battery.

In this work we have focused on active control strategies, since the developed health and state estimation algorithm could be very useful to couple with the control algorithms. For that, as most authors did, we used an MPC algorithm. Taking into account the research gaps that were discussed above, and using the degradation model developed in Chapter 3, different control strategies were implemented, and their performance on mitigating battery aging was analyzed. A new control strategy was developed using the plating/stripping model introduced in Chapter 3, showing in simulation that it can outperform previously reported strategies in mitigating plating for fast charging applications.

6.2 MODEL PREDICTIVE CONTROL

Several control algorithms could be used to control lithium-ion batteries, however, as discussed in the literature review of Section 6.1, most authors that focused on active control strategies employed MPC algorithms. MPC is based on predicting the future response of a

system, and using those predictions to make control decisions [68]. For that, it employs a look-ahead strategy to compute an optimal sequence of future inputs to produce the optimal outputs for the desired objective [17]. Figure 6.1 describes the MPC strategy.

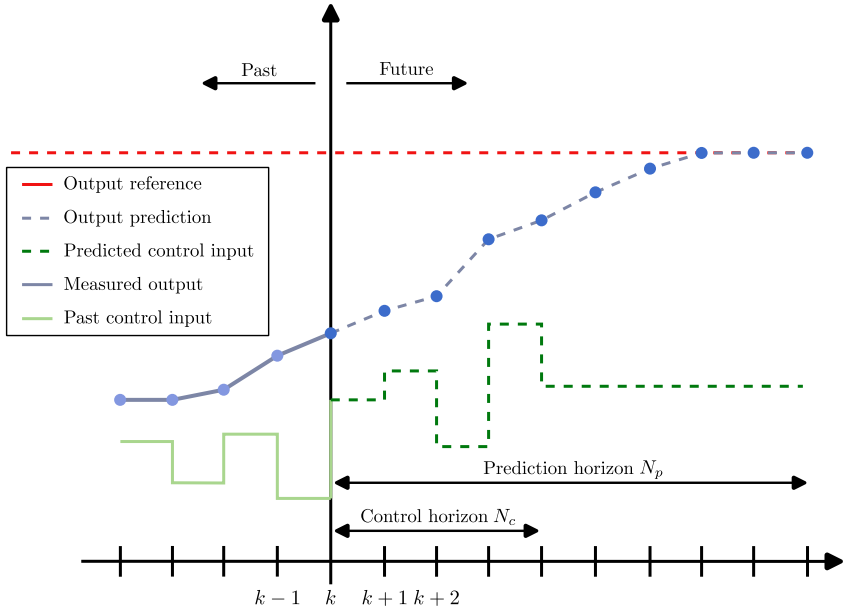

Figure 6.1: MPC illustration (adapted from [174]).

As shown in Figure 6.1, the MPC utilizes two time horizons to solve the optimal control problem: the prediction horizon (N_p) and the control horizon (N_c). The prediction horizon determines how long into the future is the forecast going to be computed, while the control horizon determines the time-horizon at which the inputs are going to be optimized. This control scheme allows the use of aging prediction models to forecast the future aging state of the battery. Furthermore, another advantage of MPC algorithms is the ability of handling hard constraints [17], such as the widely used $\eta_{pl} \geq 0$ V to limit lithium plating [16, 61]. These features have made MPC one of the most popular control algorithms for lithium-ion battery control in the literature.

Given that minimizing degradation is the main goal of this thesis, and that degradation models were created to predict battery aging behavior, its predictive capability makes the MPC appropriate for this work. Due to the nonlinear nature of lithium-ion batteries, a discrete-time NMPC algorithm was used based on the MATLAB® implementation of Liuping Wang [175]. Aloisio Kawakita de Souza *et al.* [174] showed that a linearized SPMe with a linear MPC could give very accurate results compared to an NMPC implementation, and save considerable computational time. However, since the goal of this work is to develop new and effective degradation-aware control strategies, less attention was put into

the computational cost and the implementability of the strategies, and more in the aging reduction.

For the implementation of the battery model, the orthogonal collocation based state-space model presented in Chapter 4 was augmented as in [17] to include integral action in the feedback loop. The state vector was redefined as

$$\boldsymbol{X}[k] = \begin{bmatrix} x[k] & u[k] \end{bmatrix}^T, \tag{6.1}$$

and the state equation as

$$\boldsymbol{X}[k+1] = \tilde{A}\boldsymbol{X}[k] + \tilde{B}[k]\Delta\boldsymbol{u}, \tag{6.2}$$

where

$$\tilde{A} = \begin{bmatrix} A & B \\ 0 & I \end{bmatrix} \quad \text{and} \quad \tilde{B} = \begin{bmatrix} 0 \\ I \end{bmatrix}, \tag{6.3}$$

and $\Delta\boldsymbol{u}$ is the control-input increment $\Delta\boldsymbol{u}[k+1] = \boldsymbol{u}[k+1] - \boldsymbol{u}[k]$. The outputs of the model were calculated using the nonlinear equations of the SPMe presented in Chapter 2. Additionally, the lithium plating model presented in Chapter 3 was added to the state-space model to predict the evolution of the plated lithium and dead lithium concentrations.

6.3 DEVELOPMENT OF DEGRADATION-AWARE CONTROL STRATEGIES

The first thing to define when designing a control strategy, is the control objective. As mentioned above, a typical objective of lithium-ion battery control works is to optimize a fast charging algorithm, which is critical for EVs. For that, a minimum-time problem has to be solved. In this section, different control strategies are implemented and analyzed, and the results are compared using the degradation model developed in Chapter 3.

6.3.1 Fast charging with side-reaction overpotential constraint

It is widely accepted that lithium plating is one of the main aging mechanisms that is affected by fast charging [22]. In addition, this phenomenon can generate safety hazards [58], so its prevention is of critical importance for fast charging applications. Therefore, the

developed lithium plating model was utilized to design fast charging algorithms and compare their performance. Several strategies were evaluated, and the lithium plating generated in the charging process was quantified using the above-mentioned model. All the charging strategies were simulated starting from 10 % SOC value, and the target SOC was defined at 80 %.

The first approach that was adopted to design a degradation-aware fast charging control strategy is the most common approach presented in the literature; which consists on maintaining lithium plating overpotential above 0 V. The lithium plating overpotential in the SPMe is given by

$$\eta_{pl}[k] = \frac{RT}{\alpha F} asinh\left(\frac{j^n[k]F}{2i_0^n[k]} + U_{ocp}^n(c_{s,e}^n[k]) + R_f^n F j^n[k]\right). \tag{6.4}$$

As explained above, minimum-time problems such as fast charging are very challenging to solve, and generally not amenable for real-time controls [17]. Thus, to circumvent the minimum-time problem, the pseudo-minimum-time approach proposed by Xavier and Trimboli [68] was adopted, defining the cost function as

$$J[k] = (\underrightarrow{\boldsymbol{R}}[k+1] - \underrightarrow{\boldsymbol{Y}}[k+1])^T Q(\underrightarrow{\boldsymbol{R}}[k+1] - \underrightarrow{\boldsymbol{Y}}[k+1]) + \rho \underrightarrow{\Delta \boldsymbol{U}}^T[k+1] \underrightarrow{\Delta \boldsymbol{U}}[k+1], \tag{6.5}$$

where $\underrightarrow{\boldsymbol{Y}}$ denotes the set of future outputs, $\underrightarrow{\Delta \boldsymbol{U}}$ the set of future control input increments, $\underrightarrow{\boldsymbol{R}}$ the set of future reference values, and Q and ρ are weighting matrices. The output is defined to be the SOC of the cell, and the reference is defined as the target SOC value.

In addition to the side-reaction overpotential constraint, a maximum charging current was defined, and the performance of the control was evaluated compared to a CCCV protocol using the same current limit. For these simulations, a prediction horizon of 3 s was used, since a longer horizon did not improve the control significantly. The following hard constraints were set for the control strategy:

$$\begin{aligned} V &\leq V_{max} \\ \eta_{pl} &\geq 0\,\mathrm{V} \\ I &\leq I_{max}. \end{aligned} \tag{6.6}$$

Using this control approach and defining the maximum cell current to 2C, the results depicted in Figure 6.2 were obtained. As can be seen, the MPC algorithm effectively reduces the cell current when the plating overpotential reaches the 0 V value. Consequently, the cell needs more charging time to reach the target SOC value of 80 %. Figure 6.2 (c)

shows that the overpotential control also affects the temperature of the cell, preventing the temperature increase, which will affect positively to other degradation mechanisms such as the SEI growth. Figure 6.2 (f) shows the amount of dead lithium caused by the charging process. As can be seen, the plating/stripping model proposed by O'Kane *et al.* [24] predicts a dead lithium amount even when the side reaction overpotential does not fall below 0 V. However, it can be seen that the overpotential control mitigates certain amount of lithium plating, therefore, despite increasing the charging time, this strategy reduces degradation successfully.

As mentioned, many authors employed this type of control strategy, and showed that it can be used to reduce degradation [16]. However, this charging strategy relies on a predefined maximum current value, which may be imposed by the manufacturer, or may be proposed by the control engineer. Thus, it does not utilize physical limits to define this value, and it would remain the same for the entire lifetime of the battery. This could be inappropriate when the internal characteristics of the batteries change, and since the estimator developed in Chapter 5 allows to adapt the parameters of the battery through its lifetime, a better approach should be developed to take full advantage of the estimator. Trying to improve this, an adaptable maximum charging current strategy was developed using a similar approach. For that, the following hard constraints were set in the NMPC algorithm:

$$\begin{aligned} V &\leq V_{max} \\ \eta_{pl} &\geq 0\,\mathrm{V} \\ c_e^n &\geq 300\,\mathrm{mol\ m^{-3}} \\ c_{s,max}^r - 500\ \mathrm{mol\ m^{-3}} \leq c_s^r &\geq 500\,\mathrm{mol\ m^{-3}}. \end{aligned} \tag{6.7}$$

The objective of these constraints is to maintain the physical limits of the concentrations within reasonable values. For that, the electrolyte concentration is constrained to a minimum value, and the solid-phase concentrations of both electrodes are maintained within maximum and minimum concentration values. This should be useful to prevent hazardous working conditions and reduce battery aging. Figure 6.3 shows the results for this charging strategy. As shown, the MPC algorithm seeks to maximize the charging current while maintaining the side reaction overpotential above 0 V. The maximum and minimum concentration constraints are not activated at any point of the charging, since the current is completely limited by the overpotential constraint in the first phase, and by the maximum voltage constraint in the final phase. By avoiding the maximum current

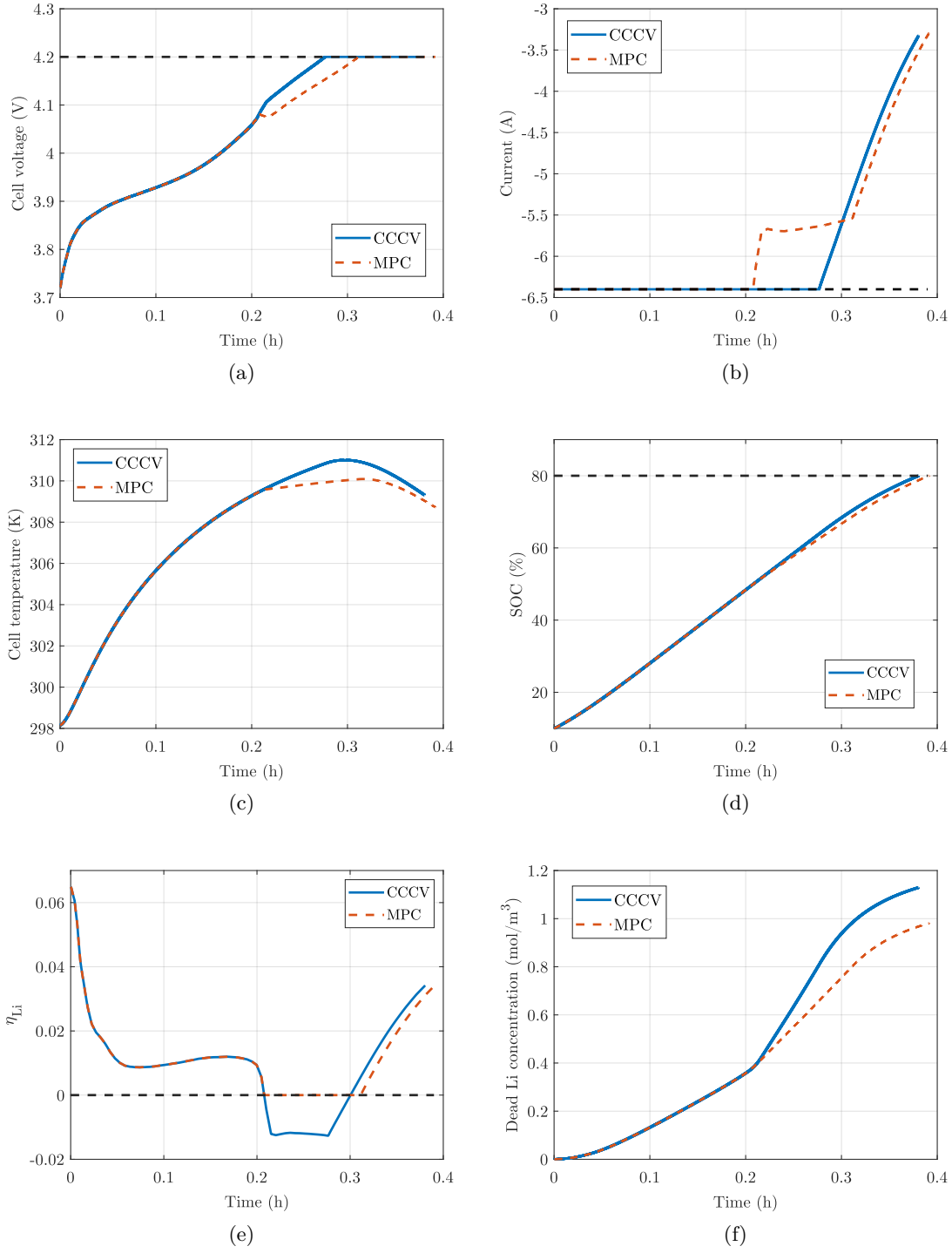

Figure 6.2: Comparison of 2C CCCV charge to fast charging strategy with side-reaction overpotential constraint. (a) Cell voltage evolution; (b) Charging current; (c) Cell temperature; (d) SOC; (e) Lithium plating overpotential; (f) Dead lithium concentration.

constraint, it is achieved to charge the battery faster, finishing the charge in 1323 s, around 80 s faster than the current limited strategy, however, the temperature of the cell reaches higher values, and the final dead lithium amount increases according to the model.

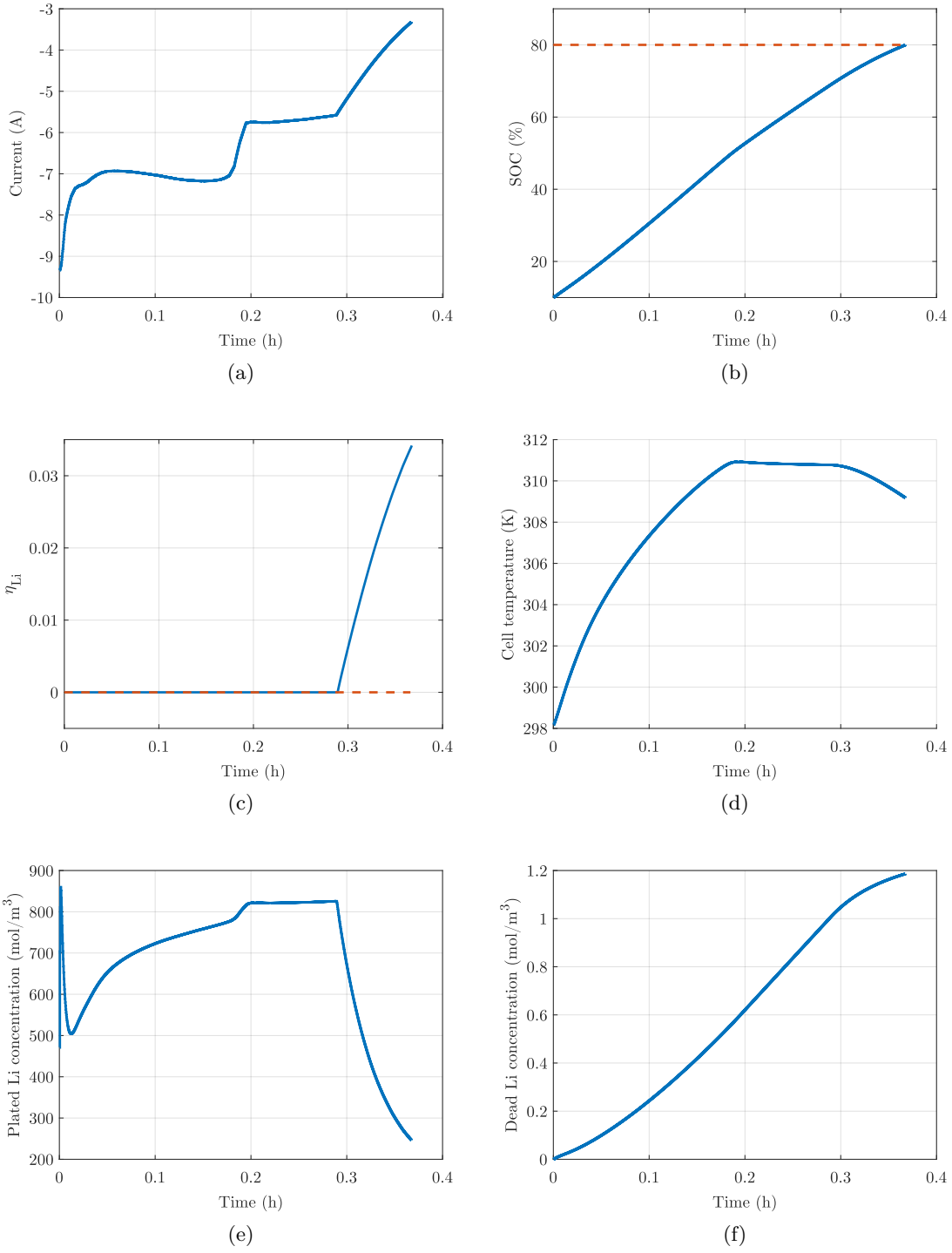

Figure 6.3: Fast charging strategy with side-reaction overpotential constraint and no maximum current constraint. (a) Charging current; (b) SOC ; (c) Lithium plating overpotential; (d) Cell temperature; (e) Plated lithium concentration; (f) Dead lithium concentration.

Another important factor that must be controlled in fast charging applications is the temperature of the cell [17], since it can cause safety issues and increase the degradation rate of the battery. Hence, a temperature constraint was set in the same MPC algorithm to avoid cell temperature rise above 35 ºC (308.15 K). The results are shown in Figure 6.4.

As expected, the temperature constraint slows down the charging process to maintain the cell temperature below the 35 ºC limit. The effect of the temperature limit can be seen in the plated and dead lithium concentrations shown in Figure 6.4 (e) and (f), as the plated lithium concentration drops abruptly, slowing the growth of dead lithium. Consequently, the charging time increases around 200 s from the previous case, but generates considerably less dead lithium, showing that appropriate physics-based constraints can help in mitigating lithium plating.

These approaches can get good results as is shown above, but they do not take advantage of physics-based degradation models that could do prognosis of battery aging in a predictive algorithm such as the MPC. In this sense, the plating/stripping model that was developed could be helpful by providing future lithium plating concentration predictions, which could be potentially used to generate optimal controls for plating minimization. Therefore, in the following subsection 6.3.2 a new fast charging algorithm is proposed using the lithium plating model predictions.

6.3.2 Fast charging using lithium plating predictions

As explained in Chapter 3, lithium plating is a reversible side-reaction that generates LLI. Many authors suggested that pulsed charging profiles could help mitigating lithium plating by reducing lithium concentration polarization and favouring the stripping reaction [69,176]. However, the previous approach of constraining side-reaction overpotential cannot make use of the stripping reaction as a way of minimizing lithium plating. For that, the developed lithium plating/stripping model could be used with the aim of finding the minimum-time solution with the minimum dead lithium amount that predicts the model. To the best of the author's knowledge, no lithium plating/stripping model has been used in the literature in control applications to mitigate plating.

For the sake of readability, the lithium plating/stripping model equations are expressed again here. The plating/stripping flux density is given by:

$$j_{pl} = k_{pl}\left(c_{pl}exp\left(\frac{F\alpha_{a,pl}\eta_{pl}}{RT}\right) - c_e exp\left(-\frac{F\alpha_{c,pl}\eta_{pl}}{RT}\right)\right). \tag{6.8}$$

The plated lithium concentration is given by

$$\frac{\partial c_{pl}}{\partial t} = -a_s^n j_{pl} - \gamma c_{pl}, \tag{6.9}$$

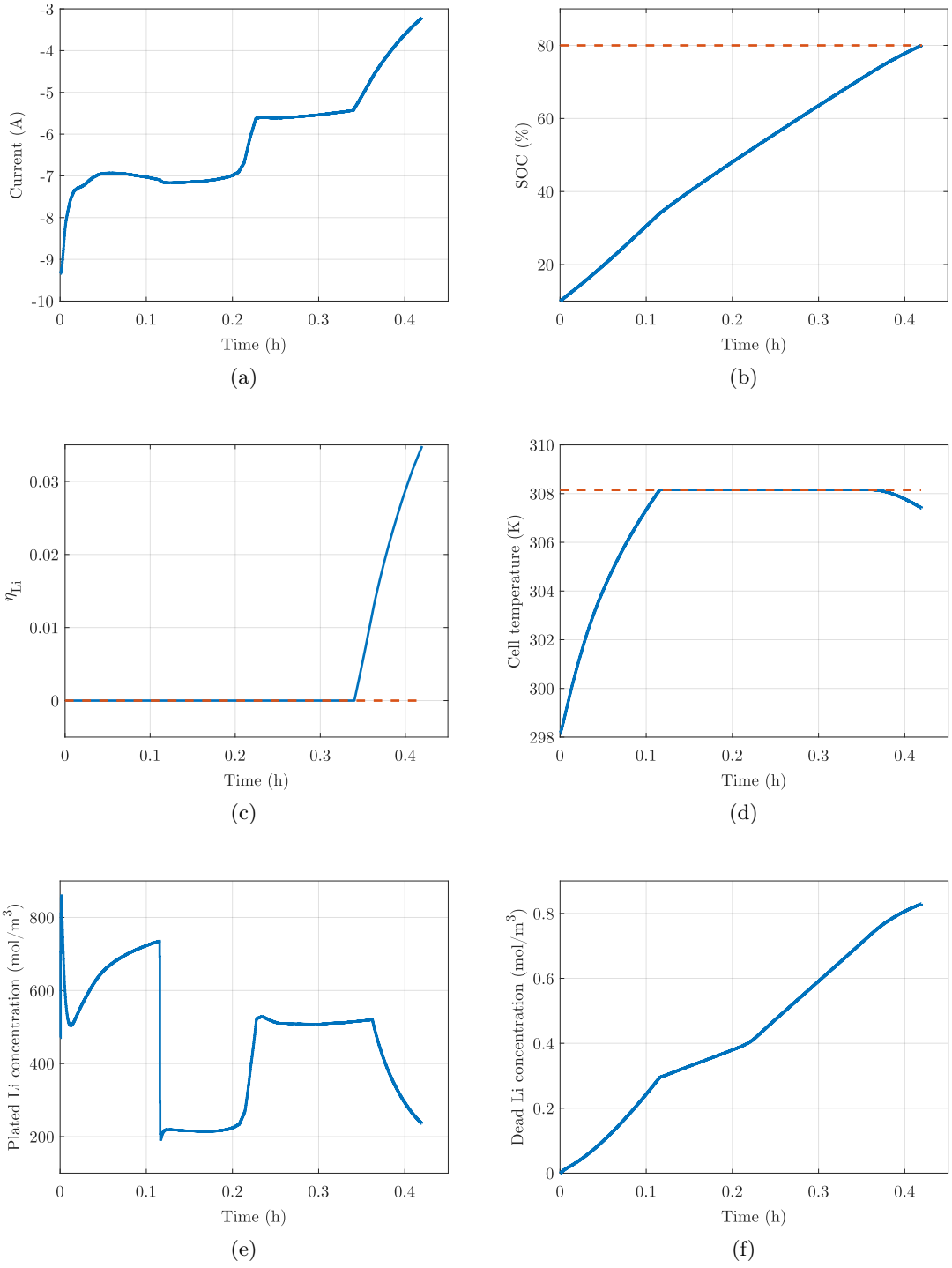

Figure 6.4: Fast charging strategy with side-reaction overpotential constraint, no maximum current constraint, and 35 ºC temperature constraint. (a) Charging current; (b) SOC ; (c) Lithium plating overpotential; (d) Cell temperature; (e) Plated lithium concentration; (f) Dead lithium concentration.

and the dead lithium concentration is modeled as

$$\frac{\partial c_{dl}}{\partial t} = \gamma c_{pl}. \tag{6.10}$$

Different approaches can be adopted to develop a lithium plating minimization control strategy using this model. For fast charging applications, as well as minimizing the dead lithium amount, we would also like to minimize the charging time, thus, it makes sense to maintain the pseudo-minimum-time cost function defined in Equation 6.5. To minimize the amount of dead lithium, it can be observed in Equation 6.10 that the dead lithium is directly related to the lithium plating concentration. Thus, a reasonable approach to limit the growth of dead lithium could be to set a constraint on the plated lithium concentration. In this way, the growth of dead lithium would be limited by the maximum amount of plated lithium. Thus, the following constraints were set in the NMPC algorithm

$$\begin{aligned} V &\leq V_{max} \\ c_{pl} &\leq c_{pl}^{max} \\ c_e^n &\geq 300\,\text{mol m}^{-3} \\ c_{s,max}^r - 500\,\text{mol m}^{-3} \leq c_s^r &\geq 500\,\text{mol m}^{-3}. \end{aligned} \tag{6.11}$$

By tuning the c_{pl}^{max} value, different charging results can be obtained. If higher maximum plating concentration values are allowed, faster charging profiles should be obtained (until other constraint such as the maximum cell voltage value is the limiting factor). Thus, two charging strategies were tested using this approach. First, a very fast charge was sought. For that, a maximum plated lithium concentration of 300 mol m^{-3} was set. Figure 6.5 shows the results of the control algorithm. As can be seen, the NMPC uses a pulsed charging current to minimize the charging time while maintaining the plated lithium concentration value below 300 mol m^{-3}. As a result, it was achieved to reduce the charging time, compared to all the above-discussed approaches, and the amount of dead lithium at the end of charge, reducing it to almost a half of the amount obtained with the temperature constrained control.

After obtaining a very fast charging with reduced lithium plating, it was tried to reduce more the lithium plating without increasing too much the charging time. For that, the constraint $c_{pl} \leq 15$ mol m^{-3} was applied. The results of the charging method are shown in Figure 6.6. It can be seen that the approach reduces dead lithium remarkably, to almost 1 % of the 2C CCCV protocol. Interestingly, in this case the NMPC decides to insert discharging pulses in the end of charge process to help more to the lithium stripping reaction. In addition to the significant reduction in the amount of dead lithium, it can be seen that the temperature of the cell increases much less than in previous cases, reducing also the impact of other aging mechanisms.

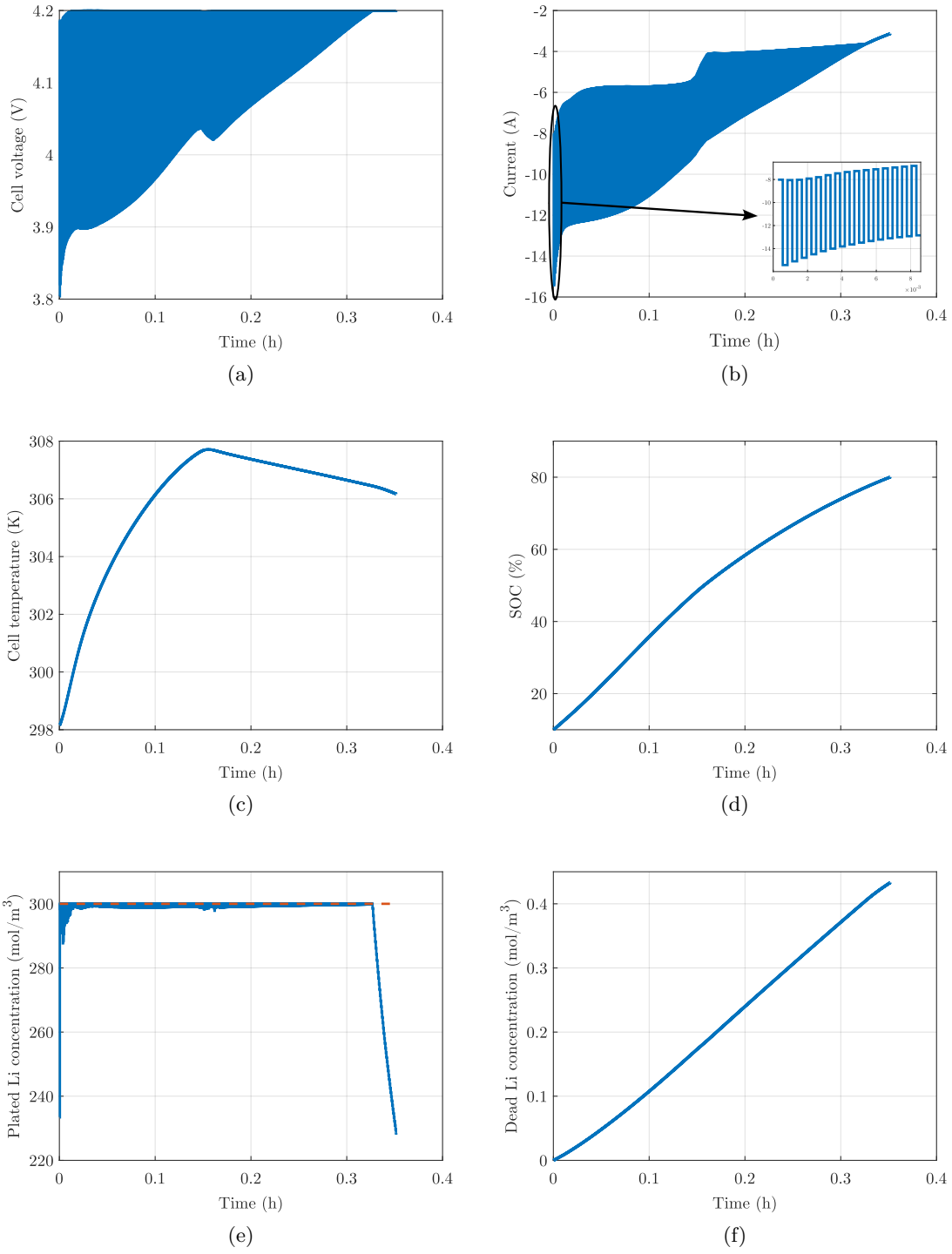

Figure 6.5: Fast charging strategy with $c_{pl} \leq 300$ mol m^{-3} constraint. (a) Cell voltage; (b) Charging current ; (c) Cell temperature; (d) SOC; (e) Plated lithium concentration; (f) Dead lithium concentration.

6.4 CONCLUSIONS

This chapter presented and discussed the work performed on degradation-aware control strategies for lithium-ion batteries. First, a literature review was performed to analyze

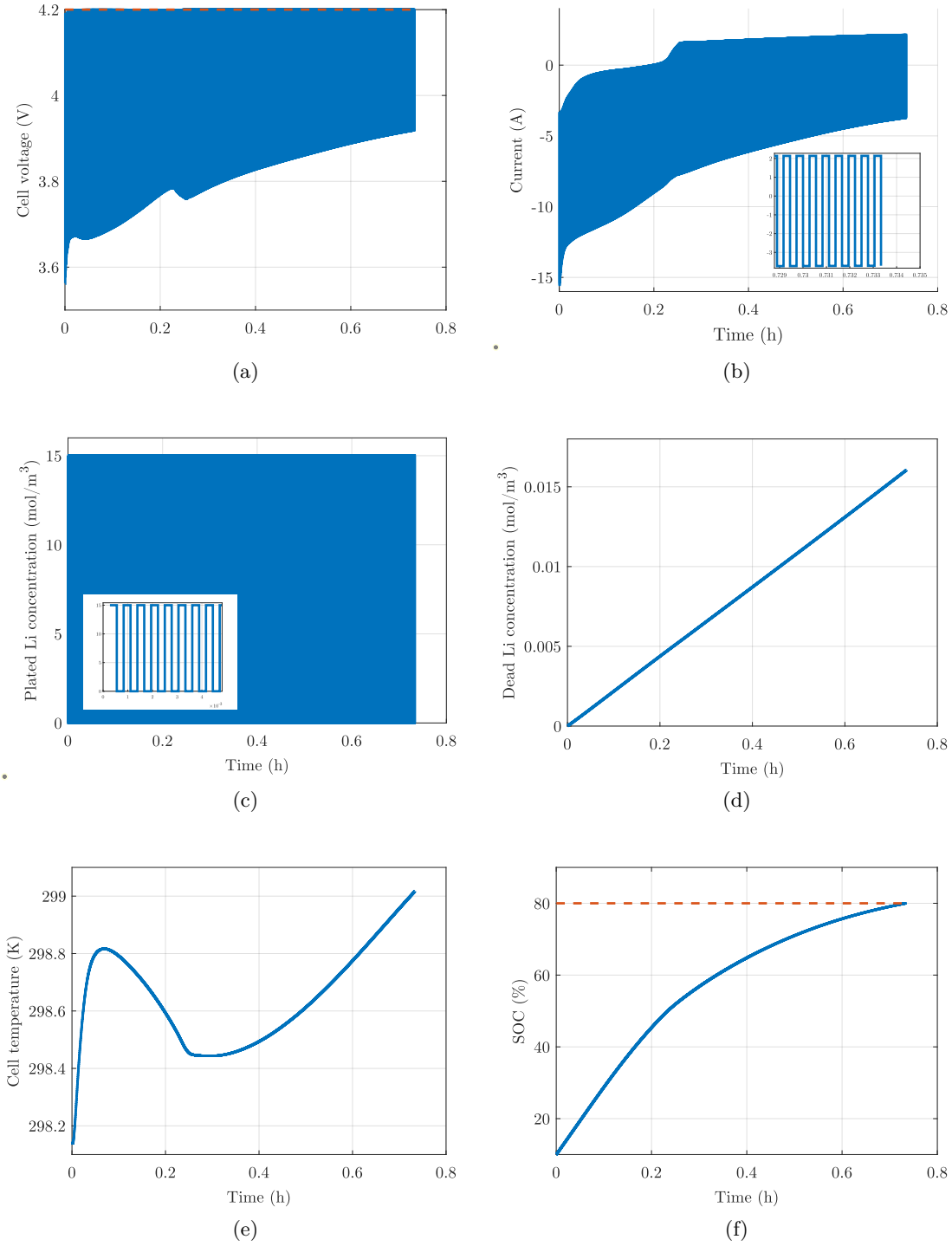

Figure 6.6: Fast charging strategy with $c_{pl} \leq 15$ mol m^{-3} constraint. (a) Cell voltage; (b) Charging current ; (c) Cell temperature; (d) SOC; (e) Plated lithium concentration; (f) Dead lithium concentration.

what control approaches were reported in the literature. The analysis showed that many authors developed fast charging strategies due to its critical importance in EVs. For this, most of the works tried to minimize lithium plating by limiting the overpotential of the side-reaction. Thus, this strategy was implemented using three different approaches; the

first one using a maximum current constraint, the second one without maximum current constraint and the third one including a maximum temperature constraint. The results showed that these strategies can effectively mitigate lithium plating compared to a fast charge CCCV protocol, but it still produced significant lithium plating according to the lithium plating model. Therefore, a new strategy was proposed to minimize lithium plating using the lithium plating/stripping model, based on limiting the amount of plated lithium in the cell. With this strategy, the NMPC algorithm uses a pulsed charging profile to minimize the charging time as well as the amount of lithium plating. The simulations showed that this approach can significantly improve the results from the side-reaction overpotential constraint control according to the used lithium plating/stripping model. Nonetheless, further work must be done to validate the control strategy experimentally.

Chapter 7

CONCLUSIONS AND FUTURE WORK

This chapter contains the main conclusions that were drawn from this PhD thesis. The performed investigation is summarized in the conclusions first, stating which was the main objective and which the directions of the research. The conclusions obtained from each chapter are presented later, to finally introduce the main general conclusion of the thesis. Later, future lines of work are discussed, stating which are the lines to follow in each investigation that was performed throughout this dissertation.

7.1 CONCLUSIONS

This PhD thesis focused on the improvement of lithium-ion battery management with the goal of reducing aging. For that the main objective of the thesis was defined as follows:

Design a control strategy to reduce lithium-ion battery aging, applicable to any operation moment, and adaptable throughout its lifetime.

To fulfill this objective, three main aspects to work were identified: battery aging modeling, battery state estimation, and control. For that, the use of PBMs was recognized as the most promising approach because of their ability to capture the internal physical behavior of battery cells. Since PBMs are generally computationally expensive, reduced-order P2D and SPMs were implemented using the orthogonal collocation method, obtaining fast and accurate PBMs. An analysis was performed to compare the performance of the SPMe and the P2D model, concluding that the SPMe can be a very good alternative of the more computationally expensive P2D model for control oriented applications.

To reduce battery aging, battery aging has to be understood first, and hence, the present literature was reviewed to evaluate the predominant aging mechanisms that can occur in lithium-ion battery cells and the modes of aging that these mechanisms generate. Subsequently, many physics-based aging models were reviewed, and a combined aging model was implemented in the SPMe and the P2D models. It was shown that the predictions of the SPMe were very similar to the predictions of the P2D model, and therefore, it was determined that, for control oriented applications, the SPMe could be a more interesting approach due to its lower computational cost. After this analysis was completed and certain knowledge about lithium-ion battery aging was obtained, a new parameterization approach was defined. This was motivated by the lack of physical insight used in the parameterization process in the literature. For that, degradation modes were determined to be a key additional information for the fitting. The parameterization approach was used in an experimental study and an aging model was developed for 3.2 Ah LG MH1 cells. The prediction results for the first cycles were accurate, but more aging information must be obtained to complete the validation of the aging model. Nonetheless, the results are promising, since the degradation modes predicted with the aging model are accurate compared to the experimental mode measures.

Regarding battery state estimation, a research gap was identified in the field of physics-based battery health estimation. The importance of estimating all degradation modes was highlighted to maintain accurate OCV estimates and give accurate SOC and internal

variable estimates, which will be key for advanced control algorithms. The effectiveness of the eSOH estimation algorithm was evaluated in simulation, obtaining very promising results. To the best of the author's knowledge the first eSOH estimation algorithm was developed that can work in real-time and does not need any specific low-current test data. Hence, it is believed that the method aids in the inclusion of PBMs in advanced BMSs, and could be helpful for many applications such as EVs, consumer electronics, second-life batteries, etc.

Using the developed aging models and state estimation methods, all the ingredients to perform degradation-aware control strategies were prepared. Therefore, using a MPC algorithm with the developed state-space orthogonal collocation SPMe and the lithium plating/stripping model, a new fast charging strategy was developed to charge lithium-ion batteries fast and safely, reducing the lithium plating significantly compared to traditional CCCV charging profiles and previously reported fast charging control approaches. The experimental validation of the proposed control strategy is still pending, but the simulation results show that the method is promising and could be of great benefit for many applications. Therefore, the main goal of the thesis was accomplished.

7.2 FUTURE LINES

The significance of physics-based lithium-ion battery control cannot be overstated in the pursuit of enhancing battery performance, longevity, and safety. As we look towards the future, our research will focus on advancing this critical area through several key avenues.

[1] **Advancement of Degradation Model Development.** We will continue with the development of degradation models by conducting additional experiments under various conditions. These experiments will encompass a broader range of operating parameters, including temperature, charge/discharge rates, and cycling protocols. Furthermore, we aim to complete the parameterization process by incorporating data from calendar cycling experiments. These experiments will involve systematic cycling of batteries under controlled conditions to simulate real-world usage patterns over extended periods. Additionally, we will conduct more comprehensive measurements of capacity and internal resistance and implement specific tests to isolate individual degradation mechanisms. This work is of upmost importance, as accurate degradation models are essential for predicting battery performance and optimizing control strategies.

[2] **2. Validation of eSOH Estimation.** In parallel, we will continue our efforts to validate the eSOH estimation algorithm using experimental data. This validation process will involve including power fade parameters to improve the eSOH estimation. By comparing the estimated eSOH with empirical measurements obtained from experimental testing, we aim to improve the accuracy and reliability of our predictive models. Validating eSOH estimation is crucial for ensuring the effectiveness of prognostic algorithms to mitigate battery degradation.

[3] **Integration of Physics-Based State Estimation and Model Predictive Control (MPC).** Finally, we will explore the integration of physics-based state estimation, aging prediction models, and MPC control algorithms to validate our holistic control approach. By experimentally implementing these integrated systems, we seek to demonstrate their efficacy in optimizing battery operation while simultaneously managing degradation effects. This approach represents a significant advancement in battery management technology, as it leverages predictive models to proactively mitigate aging-related performance degradation. The experimental validation of this control approach will provide crucial insights into its real-world applicability and pave the way for its widespread adoption in diverse battery-powered systems.

In conclusion, our ongoing research endeavors aim to further establish the importance of physics-based lithium-ion battery control through rigorous experimentation and validation. By advancing degradation models, validating eSOH estimation techniques, and integrating predictive control strategies, we strive to contribute to the development of more efficient, reliable, and sustainable battery management systems.

Appendix A

THE ORTHOGONAL COLLOCATION METHOD

As has been mentioned in section 2.3, the orthogonal collocation method is a spectral MOR technique, which implies that the PDEs of the model are approximated with a sum of basis functions. In this case, as in [54, 80, 115], the approximation functions that have been selected are Chebyshev polynomials of the first kind. The truncated Chebyshev expansion is used to approximate the solution $u(x,t)$ of the PDE:

$$u_N(x,t) = \sum_{k=0}^{N} \hat{u}_k(t) T_k(x), \quad x \in [-1,1] \tag{A.1}$$

where T_k are the Chebyshev polynomials of first kind and degree k and $\hat{u}_k(t)$ are the $N+1$ coefficients that have to be solved. The collocation points in the interval $[-1,1]$ are determined by:

$$x_i = \cos\left(\frac{i\pi}{N}\right) \quad i = 0, 1, ..., N. \tag{A.2}$$

It can be proved [177] that by choosing the coefficients $\hat{u}_k(t)$ to make $u_N(x_i,t) = u(x_i,t)$, u_N can be expressed in terms of the discrete values of the solution at the collocation points $u_j(t) = u(x_j,t) = u_n(x_j,t)$ according to,

$$u_N(x,t) = \sum_{j=0}^{N} u_j(t) \phi_j(x), \quad x \in [-1,1] \tag{A.3}$$

where the functions ϕ_j are given by:

$$\phi_j(x) = \frac{(-1)^{j+1}(1-x^2)T'_N(x)}{\bar{c}_j N^2 (x - x_j)}, \quad x \in [-1,1] \tag{A.4}$$

with $\bar{c}_j = 2$ for $j = 0$ and $j = N$ and $\bar{c}_j = 1$ otherwise.

As the variables of the model appear in differential form in the governing equations of the model, the approximation equation A.3 has to be derived to insert it in the governing PDEs. To express these derivatives in compact and computationally efficient form, differentiation matrices are used. The coefficients of the differentiation matrices are obtained by evaluating the derivative of equation A.3 at the collocation points. The resulting matrices are used to express the derivative of u in the collocation points:

$$u' = \mathrm{D}'_N u. \tag{A.5}$$

Weideman and Reddy provided the MATLAB® function *chebdif.m* in [177] to compute the Chebyshev differentiation matrices. However, these differentiation matrices do not account for any boundary condition, and therefore, they have to be modified to satisfy the boundary conditions of the model before using them to reformulate the governing equations.

As for differentiation, the calculations of integrals of the variables at the collocation points are performed with integration matrices. Integration matrices are used in the same way as the differentiation matrices. The matrix is multiplied with the vector of variable's discrete values at the collocation points:

$$u = \mathrm{I}_N u'. \tag{A.6}$$

These integration matrices can be computed by inverting the differentiation matrices. However, since the inversion of the matrices neglects the value $f(-1)$ and introduces numerical approximations [115], it is not the most appropriate way to generate them. Instead, the Clenshaw-Curtis quadrature [178] is used to compute the coefficients of the integration matrices. The MATLAB® function *cumsummat.m* [177] was used to generate the integration matrices. To calculate definite integrals over the domain [-1,1], the first row of the integration matrix is extracted, which is the row corresponding to the integration of the collocation point placed at $x_i = 1$. This Clenshaw-Curtis quadrature weights, w_i, are computed with the function *clencurt.m* given by Trefethen in [179].

In the following subsections the reformulation of all the equations of the model is detailed. For that, the discretization process of the model is explained, as well as how the differentiation matrices are adjusted to fulfil the boundary conditions of the model.

Notation *The i^{th} row and j^{th} column element of a matrix* M *is denoted* $[\mathrm{M}]_{i,j}$ *and a range of rows or columns is denoted i:j. Where the first row or column corresponds to*

the surface of the particle and the last row or column to the surface of the particle. Bold variables denote vectors containing the discrete values of those variables.

A.1 SOLID DIFFUSION MODEL

The solid diffusion equation given by 2.1 can be reformulated as

$$\frac{\partial c_s}{\partial t} = D_s \left(\frac{\partial^2 c_s}{\partial r^2} + \frac{2}{r} \frac{\partial c_s}{\partial r} \right), \tag{A.7}$$

subject to the Neumann boundary conditions 2.2 and 2.3.

In order to simplify the discretization process of the model, the new variable u_s is defined as $u_s = c_s r$. Inserting u_s in the solid diffusion equation:

$$\frac{\partial u_s}{\partial t} = D_s \frac{\partial^2 u_s}{\partial r^2}. \tag{A.8}$$

With this change of variable, the homogeneous Neumann boundary condition at the particle center, given by Equation 2.2, results in the homogeneous Dirichlet boundary condition

$$u_s(r = 0) = 0, \tag{A.9}$$

which ensures that $c_s = u_s/r$ remains finite as r tends to 0. The Neumann boundary condition 2.3 at the particle surface is replaced by the mixed boundary condition

$$\frac{1}{R_s} \frac{\partial u_s}{\partial r}\bigg|_{r=R_s} - \frac{u_s(r = R_s)}{R_s^2} = \frac{-j}{D_s}. \tag{A.10}$$

These equations are defined in the domain $r \in [0, R_s]$. However, since the Chebyshev collocation points are defined in the domain [-1,1], all the equations need to be scaled to the [-1,1] domain. To do so, the coordinate transformation

$$\bar{r} = \frac{2r}{R_s} - 1 \tag{A.11}$$

is defined. With this coordinate transformation the partial derivatives are substituted by

$$\frac{\partial}{\partial r} = \frac{2}{R_s} \frac{\partial}{\partial \bar{r}} \quad \text{and} \quad \frac{\partial^2}{\partial r^2} = \frac{4}{R_s^2} \frac{\partial^2}{\partial \bar{r}^2}. \tag{A.12}$$

Therefore, Equations A.8, A.9 and A.10 are reformulated as the solid diffusion equation

$$\frac{\partial u_s}{\partial t} = \frac{4D_s}{R_s^2}\frac{\partial^2 u_s}{\partial r^2}, \tag{A.13}$$

subject to the homogeneous Dirichlet boundary condition at the center of the particle

$$u_s(\bar{r} = -1) = 0, \tag{A.14}$$

and to the inhomogeneous mixed boundary condition at the surface of the particle

$$\left.\frac{\partial u_s}{\partial \bar{r}}\right|_{\bar{r}=1} - \frac{u_s(\bar{r}=1)}{2} = -\frac{R_s^2}{2D_s}j. \tag{A.15}$$

The next step that has been taken is to discretize the spherical particle domain $\bar{r}$ with R Chebyshev collocation points, with $R \in \mathbb{N}$. The amount of collocation points used for the discretization, R, determines the size of the differentiation matrix $D''_R \in \mathbb{R}^{(R\times R)}$ that will be used to approximate the linear differential operator $\partial^2/\partial\bar{r}^2$.

After, the differentiation matrix is modified by using the boundary conditions A.14 and A.15, which provide two additional constraints to the discrete values of u_s. First, the boundary condition A.14 states that the value of u_s at the center of the particle is equal to zero, therefore the R^{th} $\mathbf{u}_s$ element equals 0 ($\mathbf{u}_{s,R} = 0$). This allows to reduce the size of the differentiation matrix D''_R by one, removing the last row and column of the matrix. The second boundary condition A.15 at the surface of the particle allows to express the value of u_s at the surface ($\mathbf{u}_{s,1}$) in terms of the other collocation points values:

$$[\mathrm{D}'_R]_{1,1}\,\mathbf{u}_{s,1} + [\mathrm{D}'_R]_{1,2:R-1}\,\bar{\mathbf{u}}_s + [\mathrm{D}'_R]_{1,R}\,\mathbf{u}_{s,R} - \frac{1}{2}\mathbf{u}_{s,1} = -\frac{R_s^2}{2D_s}j, \tag{A.16}$$

where $\bar{\mathbf{u}}_s \in \mathbb{R}^{(R-2)}$ is the vector that contains the values of the interior collocation points, which is obtained removing the first and last values of $\mathbf{u}_s$. Since $\mathbf{u}_{s,R} = 0$, $\mathbf{u}_{s,1}$ can be related to the interior points by

$$\mathbf{u}_{s,1} = \frac{1}{1 - 2\,[\mathrm{D}'_R]_{1,1}}\left(2\,[\mathrm{D}'_R]_{1,2:R-1}\,\bar{\mathbf{u}}_s + \frac{R_s^2}{D_s}j\right). \tag{A.17}$$

As $\mathbf{u}_{s,R} = 0$, the second derivative of $\bar{\mathbf{u}}_s$, $\bar{\mathbf{u}}''_s$, is given by

$$\bar{\mathbf{u}}''_s = [\mathrm{D}''_R]_{2:R-1,1}\,\mathbf{u}_{s,1} + [\mathrm{D}''_R]_{2:R-1,2:R-1}\,\bar{\mathbf{u}}_s. \tag{A.18}$$

Introducing the expression A.17 for $\mathbf{u}_{s,1}$:

$$\bar{\mathbf{u}}_s'' = \left([\mathrm{D}_R'']_{2:R-1,2:R-1} + \frac{2\,[\mathrm{D}_R'']_{2:R-1,1}\,[\mathrm{D}_R']_{1,2:R-1}}{1-2\,[\mathrm{D}_R']_{1,1}} \right) \bar{\mathbf{u}}_s + \frac{[\mathrm{D}_N'']_{2:R-1,1}}{1-2\,[\mathrm{D}_R']_{1,1}} \frac{R_s^2}{D_s} j. \tag{A.19}$$

This expression is then used to approximate the term $\partial^2 u_s/\partial r^2$ in the reformulated solid diffusion Equation A.13:

$$\frac{\partial \bar{\mathbf{u}}_s}{\partial t} = \frac{4D_s}{R_s^2} \bar{\mathbf{u}}_s''. \tag{A.20}$$

This equation is used to obtain the values of u_s at the interior collocation points. However, since the model also needs the solid concentration value at the surface of the particle, the relation between the interior points and the surface point, given in Equation A.17, is used. To obtain the concentrations, the $\mathbf{u}_s$ values can be divided by their respective r value. Therefore, to obtain the surface concentration value, the expression given in Equation A.17 is divided by the particle radius R_s:

$$\mathbf{c}_{s,e} = \frac{1}{1-2\,[\mathrm{D}_R']_{1,1}} \left(\frac{2}{R_s} [\mathrm{D}_R']_{1,2:R-1}\,\bar{\mathbf{u}}_s + \frac{R_s}{D_s} j \right). \tag{A.21}$$

Equations A.20 and A.21 have to be solved in every collocation point used to discretize the domains of the electrodes.

A.2 ELECTROLYTE DIFFUSION MODEL

As done for the solid diffusion equation, the linear differential operators that appear in the electrolyte diffusion equation have to be approximated by Chebyshev differentiation matrices. The derivation of the electrolyte diffusion model has been done taking into account that the electrolyte diffusivity D_e is a function of the electrolyte concentration, and therefore, its spatial derivative has to be calculated.

First, the electrolyte diffusion model presented in Equation 2.4 is reformulated using the chain rule:

$$\frac{\partial c_e}{\partial t} = \varepsilon_e^{brug} D \frac{\partial^2 c_e}{\partial x^2} + \varepsilon_e^{brug} \frac{\partial D}{\partial c_e} \left(\frac{\partial c_e}{\partial x} \right)^2 + \frac{a_s\,(1-t_0^+)}{\varepsilon_e} j. \tag{A.22}$$

Since there are two linear differential operators, $\partial/\partial x$ and $\partial^2/\partial x^2$, two differentiation matrices have to be defined to approximate each operator.

The electrolyte concentration equation has to be solved in three different domains, and therefore, Equation A.22 is divided into three parts. To ensure the continuity of the electrolyte concentration across the cell, these three equations have to satisfy the following continuity conditions:

$$c_e^{neg}\left(x = L^{neg}\right) = c_e^{sep}\left(x = L^{neg}\right) \tag{A.23}$$

$$c_e^{sep}\left(x = L^{neg} + L^{sep}\right) = c_e^{pos}\left(x = L^{neg} + L^{sep}\right). \tag{A.24}$$

First, the electrolyte concentration at the electrode/separator interfaces must have the same value with both equations. Second, the exchange of lithium between the contiguous domains must be the same:

$$D\left(\varepsilon_e^{neg}\right)^{brug} \frac{\partial c_e^{neg}}{\partial x}\bigg|_{x=L^{neg}} = D\left(\varepsilon_e^{sep}\right)^{brug} \frac{\partial c_e^{sep}}{\partial x}\bigg|_{x=L^{neg}} \tag{A.25}$$

$$D\left(\varepsilon_e^{sep}\right)^{brug} \frac{\partial c_e^{sep}}{\partial x}\bigg|_{x=L^{neg}+L^{sep}} = D\left(\varepsilon_e^{pos}\right)^{brug} \frac{\partial c_e^{pos}}{\partial x}\bigg|_{x=L^{neg}+L^{sep}}. \tag{A.26}$$

As for the solid concentration model, a coordinate transformation has been done to scale each macro-scale domain to the [-1,1] domain by applying the following equations:

$$\begin{cases} \bar{x} = \dfrac{2}{L^{neg}}\left(x - \dfrac{L^{neg}}{2}\right) & \text{for} \quad x \in [0, L^{neg}] \\ \bar{x} = \dfrac{2}{L^{sep}}\left(x - L^{neg} - \dfrac{L^{sep}}{2}\right) & \text{for} \quad x \in [L^{neg}, L^{neg} + L^{sep}] \\ \bar{x} = \dfrac{2}{L^{pos}}\left(x - L^{neg} - L^{sep} - \dfrac{L^{pos}}{2}\right) & \text{for} \quad x \in [L^{neg} + L^{sep}, L^{tot}] \end{cases} \tag{A.27}$$

Using the chain rule, the partial derivatives after the coordinate transformation are defined as

$$\frac{\partial}{\partial x} = \frac{2}{L^i}\frac{\partial}{\partial \bar{x}} \quad \text{and} \quad \frac{\partial^2}{\partial x^2} = \frac{4}{{L^i}^2}\frac{\partial^2}{\partial \bar{x}^2}. \tag{A.28}$$

Applying the coordinate transformation, the three electrolyte diffusion equations are defined as

$$\begin{cases} \dfrac{\partial c_e^{neg}}{\partial t} = \dfrac{4\left(\varepsilon_e^{neg}\right)^{brug}}{{L^{neg}}^2}\left(D\dfrac{\partial^2 c_e^{neg}}{\partial \bar{x}^2} + \dfrac{\partial D}{\partial c_e^{neg}}\left(\dfrac{\partial c_e^{neg}}{\partial \bar{x}}\right)^2\right) + \dfrac{a_s^{neg}}{\varepsilon_e^{neg} F}\left(1 - t_0^+\right) j^{neg} \\ \dfrac{\partial c_e^{sep}}{\partial t} = \dfrac{4\left(\varepsilon_e^{sep}\right)^{brug}}{{L^{sep}}^2}\left(D\dfrac{\partial^2 c_e^{sep}}{\partial \bar{x}^2} + \dfrac{\partial D}{\partial c_e^{sep}}\left(\dfrac{\partial c_e^{sep}}{\partial \bar{x}}\right)^2\right) \\ \dfrac{\partial c_e^{pos}}{\partial t} = \dfrac{4\left(\varepsilon_e^{pos}\right)^{brug}}{{L^{pos}}^2}\left(D\dfrac{\partial^2 c_e^{pos}}{\partial \bar{x}^2} + \dfrac{\partial D}{\partial c_e^{pos}}\left(\dfrac{\partial c_e^{pos}}{\partial \bar{x}}\right)^2\right) + \dfrac{a_s^{pos}}{\varepsilon_e^{pos} F}\left(1 - t_0^+\right) j^{pos} \end{cases} \tag{A.29}$$

The boundary conditions at the current collectors are reformulated as

$$\left.\frac{\partial c_e^{neg}}{\partial \bar{x}}\right|_{\bar{x}=-1} = 0 \tag{A.30}$$

$$\left.\frac{\partial c_e^{pos}}{\partial \bar{x}}\right|_{\bar{x}=1} = 0. \tag{A.31}$$

While the continuity conditions are expressed as

$$c_e^{neg}\left(\bar{x}=1\right) = c_e^{sep}\left(\bar{x}=-1\right) \tag{A.32}$$

$$c_e^{sep}\left(\bar{x}=1\right) = c_e^{pos}\left(\bar{x}=-1\right), \tag{A.33}$$

and the interface lithium exchange conditions as

$$2D\frac{\left(\varepsilon_e^{neg}\right)^{brug}}{L^{neg}}\left.\frac{\partial c_e^{neg}}{\partial x}\right|_{\bar{x}=1} = 2D\frac{\left(\varepsilon_e^{sep}\right)^{brug}}{L^{sep}}\left.\frac{\partial c_e^{sep}}{\partial x}\right|_{\bar{x}=-1} \tag{A.34}$$

$$2D\frac{\left(\varepsilon_e^{sep}\right)^{brug}}{L^{sep}}\left.\frac{\partial c_e^{sep}}{\partial x}\right|_{\bar{x}=1} = 2D\frac{\left(\varepsilon_e^{pos}\right)^{brug}}{L^{pos}}\left.\frac{\partial c_e^{pos}}{\partial x}\right|_{\bar{x}=-1}. \tag{A.35}$$

After reformulating all the equations according to the coordinate transformation, the Chebyshev differentiation matrices that are used to approximate the derivatives of the equations are computed. For that the negative electrode, the separator and the positive electrode are discretized with N, S and P collocation points respectively, with $N, S, P \in \mathbb{N}$.

Notation *The differentiation matrices for the negative electrode are defined as* D'_N *and* D''_N; *for the separator* D'_S *and* D''_S; *and for the positive electrode* D'_P *and* D''_P.

In order to take into account the boundary and continuity conditions, the differentiation matrices are modified. First, the continuity conditions A.32 and A.33 are used. These conditions imply that a single concentration value can be used to describe the value at the electrode/separator interface. Therefore, the amount of discrete concentration values that have to be solved is reduced by two, ensuring that the continuity condition is satisfied.

The four remaining conditions A.30, A.31, A.34 and A.35, are then used to express the electrolyte concentrations at the current collector/negative electrode interface c_e^{cn}, negative electrode/ separator interface c_e^{ns}, separator/ positive electrode interface c_e^{sp} and positive electrode/ current collector interface c_e^{pc}, in terms of the interior points of the domains, denoted as $\bar{c_e}^{neg}$, $\bar{c_e}^{sep}$ and $\bar{c_e}^{pos}$ (as it has been done in the solid concentration differentiation matrix for the surface concentration value). To do so, the scaled first

derivative differentiation matrices that account for the domain length and porosity are defined as

$$\tilde{\mathrm{D}}'_N = \frac{2\left(\varepsilon_e^{neg}\right)^{brug}}{L^{neg}}\mathrm{D}'_N \quad , \quad \tilde{\mathrm{D}}'_S = \frac{2\left(\varepsilon_e^{sep}\right)^{brug}}{L^{sep}}\mathrm{D}'_S \quad , \quad \tilde{\mathrm{D}}'_S = \frac{2\left(\varepsilon_e^{pos}\right)^{brug}}{L^{pos}}\mathrm{D}'_P. \tag{A.36}$$

With the scaled first derivative differentiation matrices, the discrete version of the boundary conditions A.30 and A.31 are given by

$$\left[\tilde{\mathrm{D}}'_N\right]_{N,N} c_e^{cn} + \left[\tilde{\mathrm{D}}'_N\right]_{N,1} c_e^{ns} = -\left[\tilde{\mathrm{D}}'_N\right]_{N,2:N-1} \bar{\mathbf{c}_e}^{neg} \tag{A.37}$$

$$\left[\tilde{\mathrm{D}}'_P\right]_{1,1} c_e^{pc} + \left[\tilde{\mathrm{D}}'_P\right]_{1,P} c_e^{sp} = -\left[\tilde{\mathrm{D}}'_P\right]_{1,2:P-1} \bar{\mathbf{c}_e}^{pos}, \tag{A.38}$$

while the discrete versions of the lithium flux equality conditions A.34 and A.35 are given by

$$\begin{aligned}\left[\tilde{\mathrm{D}}'_S\right]_{S,1} c_e^{sp} - \left(\left[\tilde{\mathrm{D}}'_N\right]_{1,1} - \left[\tilde{\mathrm{D}}'_S\right]_{S,S}\right) c_e^{ns} - \left[\tilde{\mathrm{D}}'_N\right]_{1,N} c_e^{cn} = \\ - \left[\tilde{\mathrm{D}}'_S\right]_{S,2:S-1} \bar{\mathbf{c}_e}^{sep} + \left[\tilde{\mathrm{D}}'_N\right]_{1,2:N-1} \bar{\mathbf{c}_e}^{neg}\end{aligned} \tag{A.39}$$

$$\begin{aligned}\left[\tilde{\mathrm{D}}'_P\right]_{P,1} c_e^{pc} - \left(\left[\tilde{\mathrm{D}}'_S\right]_{1,1} - \left[\tilde{\mathrm{D}}'_P\right]_{P,P}\right) c_e^{sp} - \left[\tilde{\mathrm{D}}'_S\right]_{1,S} c_e^{ns} = \\ - \left[\tilde{\mathrm{D}}'_P\right]_{P,2:P-1} \bar{\mathbf{c}_e}^{pos} + \left[\tilde{\mathrm{D}}'_S\right]_{1,2:S-1} \bar{\mathbf{c}_e}^{sep}.\end{aligned} \tag{A.40}$$

These four equations form a linear system of equations which relates the concentration values at the domain boundaries to the concentration values at the interior collocation points. Rewriting the system of equations in matrix form:

$$\mathrm{A} \begin{bmatrix} c_e^{pc} \\ c_e^{sp} \\ c_e^{ns} \\ c_e^{cn} \end{bmatrix} = \mathrm{B} \begin{bmatrix} \bar{\mathbf{c}_e}^{pos} \\ \bar{\mathbf{c}_e}^{sep} \\ \bar{\mathbf{c}_e}^{neg} \end{bmatrix} \tag{A.41}$$

where matrix $\mathrm{A} \in \mathbb{R}^{4\times 4}$ is given by

$$\mathrm{A} = \begin{bmatrix} \left[\tilde{\mathrm{D}}'_P\right]_{1,1} & \left[\tilde{\mathrm{D}}'_P\right]_{1,P} & 0 & 0 \\ \left[\tilde{\mathrm{D}}'_P\right]_{P,1} & \left[\tilde{\mathrm{D}}'_P\right]_{P,P} - \left[\tilde{\mathrm{D}}'_S\right]_{1,1} & -\left[\tilde{\mathrm{D}}'_S\right]_{1,S} & 0 \\ 0 & \left[\tilde{\mathrm{D}}'_S\right]_{S,1} & \left[\tilde{\mathrm{D}}'_S\right]_{S,S} - \left[\tilde{\mathrm{D}}'_N\right]_{1,1} & -\left[\tilde{\mathrm{D}}'_N\right]_{1,N} \\ 0 & 0 & -\left[\tilde{\mathrm{D}}'_N\right]_{N,1} & -\left[\tilde{\mathrm{D}}'_S\right]_{N,N} \end{bmatrix}, \tag{A.42}$$

and matrix $\mathrm{B} \in \mathbb{R}^{4\times(P+S+N-6)}$ by

$$\mathrm{B} = \begin{bmatrix} -\left[\tilde{\mathrm{D}}'_P\right]_{1,2:P-1} & 0 & 0 \\ -\left[\tilde{\mathrm{D}}'_P\right]_{P,2:P-1} & \left[\tilde{\mathrm{D}}'_S\right]_{1,2:S-1} & 0 \\ 0 & -\left[\tilde{\mathrm{D}}'_S\right]_{S,2:S-1} & \left[\tilde{\mathrm{D}}'_N\right]_{1,2:N-1} \\ 0 & 0 & -\left[\tilde{\mathrm{D}}'_N\right]_{N,2:N-1} \end{bmatrix}. \tag{A.43}$$

Assuming that A is non singular, a matrix $\mathrm{M} \triangleq \mathrm{A}^{-1}\mathrm{B}$ can be defined to relate the interior and boundary points:

$$\begin{bmatrix} c_e^{pc} \\ c_e^{sp} \\ c_e^{ns} \\ c_e^{cn} \end{bmatrix} = \mathrm{M} \begin{bmatrix} \bar{\mathbf{c}}_e{}^{pos} \\ \bar{\mathbf{c}}_e{}^{sep} \\ \bar{\mathbf{c}}_e{}^{neg} \end{bmatrix} \tag{A.44}$$

Once the concentration values of the domain boundaries are related to the inner concentration values by the system of Equations A.44, the same system of equations can be used to derive differentiation matrices for the second derivative. This way the second derivative differentiation matrices will satisfy the boundary and continuity conditions.

The second derivative approximations for the interior points of the three macro-scale domains are given by

$$\left(\bar{\mathbf{c}}_e{}^{pos}\right)'' = [\mathrm{D}''_P]_{2:P-1,1}\, c_e^{pc} + [\mathrm{D}''_P]_{2:P-1,2:P-1}\, \bar{\mathbf{c}}_e{}^{pos} + [\mathrm{D}''_P]_{2:P-1,P}\, c_e^{sp} \tag{A.45}$$

$$\left(\bar{\mathbf{c}}_e{}^{sep}\right)'' = [\mathrm{D}''_S]_{2:S-1,1}\, c_e^{sp} + [\mathrm{D}''_S]_{2:S-1,2:S-1}\, \bar{\mathbf{c}}_e{}^{sep} + [\mathrm{D}''_S]_{2:S-1,S}\, c_e^{ns} \tag{A.46}$$

$$\left(\bar{\mathbf{c}}_e{}^{neg}\right)'' = [\mathrm{D}''_N]_{2:N-1,1}\, c_e^{ns} + [\mathrm{D}''_P]_{2:N-1,2:N-1}\, \bar{\mathbf{c}}_e{}^{neg} + [\mathrm{D}''_N]_{2:N-1,N}\, c_e^{cn}. \tag{A.47}$$

Writing these equations in matrix form:

$$\begin{bmatrix} (\bar{\mathbf{c}_e}^{pos})'' \\ (\bar{\mathbf{c}_e}^{sep})'' \\ (\bar{\mathbf{c}_e}^{neg})'' \end{bmatrix} = \begin{bmatrix} [\mathrm{D}''_P]_{2:P-1,2:P-1} & 0 & 0 \\ 0 & [\mathrm{D}''_S]_{2:S-1,2:S-1} & 0 \\ 0 & 0 & [\mathrm{D}''_N]_{2:N-1,2:N-1} \end{bmatrix} \begin{bmatrix} \bar{\mathbf{c}_e}^{pos} \\ \bar{\mathbf{c}_e}^{sep} \\ \bar{\mathbf{c}_e}^{neg} \end{bmatrix} + \begin{bmatrix} [\mathrm{D}''_P]_{2:P-1,1} & [\mathrm{D}''_P]_{2:P-1,P} & 0 & 0 \\ 0 & [\mathrm{D}''_S]_{2:S-1,1} & [\mathrm{D}''_S]_{2:S-1,S} & 0 \\ 0 & 0 & [\mathrm{D}''_N]_{2:N-1,1} & [\mathrm{D}''_N]_{2:N-1,N} \end{bmatrix} \begin{bmatrix} c_e^{pc} \\ c_e^{sp} \\ c_e^{ns} \\ c_e^{cn} \end{bmatrix} \tag{A.48}$$

Using Equation A.44 to substitute the domain boundary values and defining the vectors $\bar{\mathbf{c}_e} = [\bar{\mathbf{c}_e}^{pos}, \bar{\mathbf{c}_e}^{sep}, \bar{\mathbf{c}_e}^{neg}]^T$ and $\bar{\mathbf{c}_e}'' = [(\bar{\mathbf{c}_e}^{pos}), (\bar{\mathbf{c}_e}^{sep}), (\bar{\mathbf{c}_e}^{neg})]^{\mathbf{T}}$, the second derivative of the electrolyte concentration at the interior points is given by

$$\bar{\mathbf{c}_e}'' = \bar{\mathrm{D}}''_{PSN} \bar{\mathbf{c}_e}, \tag{A.49}$$

where $\bar{\mathrm{D}}''_{PSN}$ is the second derivative differentiation matrix for the three macro-scale domains. It is a square matrix of size $P + S + N - 6$ that satisfies the boundary and continuity conditions. It is defined as

$$\bar{\mathrm{D}}''_{PSN} = \begin{bmatrix} [\mathrm{D}''_P]_{2:P-1,2:P-1} & 0 & 0 \\ 0 & [\mathrm{D}''_S]_{2:S-1,2:S-1} & 0 \\ 0 & 0 & [\mathrm{D}''_N]_{2:N-1,2:N-1} \end{bmatrix} + \begin{bmatrix} [\mathrm{D}''_P]_{2:P-1,1} & [\mathrm{D}''_P]_{2:P-1,P} & 0 & 0 \\ 0 & [\mathrm{D}''_S]_{2:S-1,1} & [\mathrm{D}''_S]_{2:S-1,S} & 0 \\ 0 & 0 & [\mathrm{D}''_N]_{2:N-1,1} & [\mathrm{D}''_N]_{2:N-1,N} \end{bmatrix} \mathrm{M}. \tag{A.50}$$

Similarly, the first derivative differentiation matrix is given by $\bar{\mathbf{c}_e}' = \bar{\mathrm{D}}'_{PSN}\bar{\mathbf{c}_e}$, where $\bar{\mathrm{D}}'_{PSN}$ is a square matrix of size $P+S+N-6$:

$$\begin{aligned}\bar{\mathbf{D}}'_{PSN} = &\begin{bmatrix} [\mathbf{D}'_P]_{2:P-1,2:P-1} & 0 & 0 \\ 0 & [\mathbf{D}'_S]_{2:S-1,2:S-1} & 0 \\ 0 & 0 & [\mathbf{D}'_N]_{2:N-1,2:N-1} \end{bmatrix} \\ &+ \begin{bmatrix} [\mathbf{D}'_P]_{2:P-1,1} & [\mathbf{D}'_P]_{2:P-1,P} & 0 & 0 \\ 0 & [\mathbf{D}'_S]_{2:S-1,1} & [\mathbf{D}'_S]_{2:S-1,S} & 0 \\ 0 & 0 & [\mathbf{D}'_N]_{2:N-1,1} & [\mathbf{D}'_N]_{2:N-1,N} \end{bmatrix} M.\end{aligned} \tag{A.51}$$

Hence, the first derivative differentiation matrix $\bar{\mathbf{D}}'_{PSN}$ and the second derivative differentiation matrix $\bar{\mathbf{D}}''_{PSN}$ can be used to approximate the linear operators of the electrolyte diffusion Equation A.22:

$$\frac{\partial \bar{\mathbf{c}_e}}{\partial t} = \varepsilon_e^{brug}\mathrm{diag}\left(\bar{\mathbf{D}}\right)\left(\bar{\mathrm{D}}''_{PSN}\bar{\mathbf{c}_e}\right) + \varepsilon_e^{brug}\mathrm{diag}\left(\bar{\mathbf{D}}'_{c_e}\right)\left(\mathrm{D}'_{PSN}\bar{\mathbf{c}_e}\right)^2 + \frac{a_s\left(1-t_0^+\right)}{\varepsilon_e}\bar{\mathbf{j}}, \tag{A.52}$$

where $\bar{\mathbf{c}_e}, \bar{\mathbf{j}}, \bar{\mathbf{D}}, \bar{\mathbf{D}}'_{c_e} \in \mathbb{R}^{P+S+N-6}$ are the vectors containing the concatenated values of the interior collocation points of the electrolyte concentration c_e, the flux of lithium between the solid and the electrolyte phase j, concentration-dependent diffusivity D and the partial derivative of the diffusivity $\partial D/\partial c_e$ respectively. Note that the parameters ε_e, $brug$ and a_s have different values in each domain, and therefore, they must be expressed as diagonal matrices of size $P+S+N-6$ in Equation A.52.

Once the values of the interior points are solved in the model, these values can be used to obtain the domain boundary values by applying the relation given by Equation A.44.

A.3 SOLID AND ELECTROLYTE POTENTIALS

Another form of Equation 2.10 was used to solve the solid potential:

$$\frac{i_s}{\sigma_{eff}} = -\frac{\partial \phi_s}{\partial x}, \tag{A.53}$$

where i_s is the solid-phase current density:

$$i_s = i_{app} - i_e, \tag{A.54}$$

where i_e is the electrolyte current density. Since the separator is electronically insulating, the electrolyte current density i_e is equal to the total current density i_{app}. At the electrodes, the local lithium flux j is equal to the divergence of the electrolyte current density i_e,

$$\frac{\partial i_e}{\partial x} = a_s F j. \tag{A.55}$$

Introducing the expression A.55 in Equation 2.6, the electrolyte-phase potential equation can be represented as

$$-i_e = \kappa_{eff} \frac{\partial \phi_e}{\partial x} + \kappa_{D,eff} \frac{\partial \ln c_e}{\partial x}. \tag{A.56}$$

In order to reduce the number of algebraic variables that have to be solved, the integral form of Equation A.55 is used to obtain the electrolyte current density, which is given by

$$i_e(x,t) = a_s F \int_{x=0}^{x} j(x,t)dx + C_N \quad \text{for} \quad x \in [0, L^{neg}] \tag{A.57}$$

for the negative electrode, and by

$$i_e(x,t) = a_s F \int_{x=L^{neg}+L^{sep}}^{x} j(x,t)dx + C_P \quad \text{for} \quad x \in \left[L^{neg} + L^{sep}, L^{tot}\right] \tag{A.58}$$

for the positive electrode. Two charge conservation constraints can be obtained from Equations A.57 and A.58. Since at the collector/electrode interfaces the electrolyte current density i_e must equal zero, and at the electrode/separator interfaces must equal i_{app}, it can be concluded that, defining the integral over the entire negative electrode domain, Equation A.57 constraints the lithium ion flux as

$$i_{app}(t) = a_s F \int_{x=0}^{L^{neg}} j(x,t)dx \quad \text{for} \quad x \in [0, L^{neg}], \tag{A.59}$$

and defining the integral of Equation A.58 for the entire positive electrode, the lithium flux is constrained by

$$-i_{app}(t) = a_s F \int_{x=L^{neg}+L^{sep}}^{L^{tot}} j(x,t)dx \quad \text{for} \quad x \in \left[L^{neg} + L^{sep}, L^{tot}\right]. \tag{A.60}$$

Equations A.59 and A.60 are charge conservation constraints that ensure that the amount of lithium exchange in the electrode particles and the electrolyte is equal to the electronic flux going through the external load i_{app}. Since the lithium flux is calculated with the Butler-Volmer Equation 2.12, which relates the flux of lithium on the surface of the particles with the local overpotential 2.13, these flux constraints can be used to

determine the values of the solid-phase potential at both current collectors $\phi_{s,CC}^{neg}$ and $\phi_{s,CC}^{pos}$. This way, just $\phi_{s,CC}^{neg}$ and $\phi_{s,CC}^{pos}$ are considered as algebraic variables, and the model only needs to solve these two constraints instead of solving one solid potential equation for each collocation point. Once the current collector values are obtained, the solid-phase potential values at the rest of the collocation points are obtained by using Equation A.53 in its integral form, which gives the spatial evolution of the solid potential. Adding this spatial evolution to the current collector values, the solid potential values at all the collocation points of the electrodes are obtained. The integral form of Equation A.53 in the negative electrode is given by

$$\tilde{\phi}_s^{neg}(x) = \frac{-1}{\sigma_{eff}} \int_{x=0}^{x} i_s^{neg}(x)dx \quad \text{for} \quad x \in [0, L^{neg}], \tag{A.61}$$

and in the positive electrode by

$$\tilde{\phi}_s^{neg}(x) = \frac{-1}{\sigma_{eff}} \left(\int_{x=L^{neg}+L^{sep}}^{x} i_s^{pos}(x)dx - \int_{x=L^{neg}+L^{sep}}^{L^{tot}} i_s^{pos}(x)dx \right) \quad \text{for} \quad x \in \left[L^{neg} + L^{sep}, L^{tot}\right]. \tag{A.62}$$

Choosing the integration constants so that the potential $\tilde{\phi}_s$ is equal to zero at the current collectors, the discrete values of the solid-phase potential in the negative and positive electrodes are respectively given by

$$\tilde{\Phi}_s^{neg} = \frac{-1}{\sigma_{eff}^{neg}} \frac{L^{neg}}{2} \left(\mathbf{I}_N \mathbf{i}_s^{neg}\right) \tag{A.63}$$

$$\tilde{\Phi}_s^{pos} = \frac{-1}{\sigma_{eff}^{pos}} \frac{L^{pos}}{2} \left(\mathbf{I}_P - 1_P \mathbf{w}_P^{\mathbf{T}}\right) \mathbf{i}_s^{pos}, \tag{A.64}$$

where $\tilde{\Phi}_s^{pos} \in \mathbb{R}^P$ and $\tilde{\Phi}_s^{neg} \in \mathbb{R}^N$ denote the discrete $\tilde{\phi}_s$ values at the collocation points, $\mathbf{I}_N$ and $\mathbf{I}_P$ are the integration matrices for the negative and positive electrodes respectively, and $\mathbf{i}_s^{neg} \in \mathbb{R}^N$ and $\mathbf{i}_s^{pos} \in \mathbb{R}^P$ are the vectors of the solid-phase current density. The terms $\frac{L^{neg}}{2}$ and $\frac{L^{pos}}{2}$ arise from the scaling of the model equation on the domain [-1,1]. $1_P \in \mathbb{R}^P$ denotes a column vector of ones and $\mathbf{w}_P^{\mathbf{T}}$ are the Clenshaw-Curtis quadrature weights at the positive electrode. To obtain the vectors $\mathbf{i}_s^{pos} \in \mathbb{R}^P$ and $\mathbf{i}_s^{neg} \in \mathbb{R}^N$, Equation A.54 is used. Hence, before obtaining the solid-phase current densities, the electrolyte current densities must be obtained. For that, Equation A.55 is used in its integral form

$$\mathbf{i}_e^{neg} = a_s^{neg} F \frac{L^{neg}}{2} \left(\mathbf{I}_N \mathbf{j}^{neg}\right) \tag{A.65}$$

for the negative electrode, and

$$\mathbf{i}_e^{pos} = a_s^{pos} F \frac{L^{pos}}{2} \left(\mathbf{I}_P \mathbf{j}^{pos}\right) + \mathbf{i}_{app} \tag{A.66}$$

for the positive electrode. $\mathbf{i}_e^{pos}, \mathbf{j}^{pos} \in \mathbb{R}^P$ and $\mathbf{i}_e^{neg}, \mathbf{j}^{neg} \in \mathbb{R}^N$ denote the vectors containing the discrete values of the electrolyte current density and the lithium flux at the surface of the particles in the positive electrode and in the negative electrode. $\mathbf{i}_{app} \in \mathbb{R}^P$ is a column vector, which elements are equal to the applied current density i_{app}. After obtaining the electrolyte current densities, and using Equation A.54 the solid current densities, the solid-phase potentials are caculated.

For the electrolyte-phase potentials, Equation A.56 is used. Integrating the equation, the electrolyte potential of the domain i can be expressed as

$$\phi_e^i(\bar{x}) = -\frac{L^i}{2} \int_{\bar{x}=-1}^{\bar{x}} \frac{i_e\left(\bar{x}\right)}{\kappa_{eff}(\bar{x}} d\bar{x} - \frac{2\left(1-t_0^+\right) RT}{F} \ln c_e^i\left(\bar{x}\right) + C_i, \tag{A.67}$$

where C_i is the integration constant. By enforcing the continuity of the electrolyte potential at the boundary domains, i.e. $\phi_e^{neg}(1) = \phi_e^{sep}(-1)$ and $\phi_e^{sep}(1) = \phi_e^{pos}(-1)$, and setting as reference potential the electrolyte potential at the positive electrode/current collector interface, $\phi_e^{pos}(1) = 0$, the integration constants are given by

$$C_{pos} = \frac{L^{pos}}{2} \int_{-1}^{1} \frac{i_e^{pos}\left(\bar{x}\right)}{\kappa_{eff}^{pos}} d\bar{x} - \frac{2\left(1-t_0^+\right) RT}{F} \ln c_e^{pos}(1) \tag{A.68}$$

$$C_{sep} = \frac{L^{sep}}{2} \int_{-1}^{1} \frac{i_e^{sep}\left(\bar{x}\right)}{\kappa_{eff}^{sep}} d\bar{x} - \frac{2\left(1-t_0^+\right) RT}{F} \ln c_e^{sep}(1) + \phi_e^{pos}(-1) \tag{A.69}$$

$$C_{neg} = \frac{L^{neg}}{2} \int_{-1}^{1} \frac{i_e^{neg}\left(\bar{x}\right)}{\kappa_{eff}^{neg}} d\bar{x} - \frac{2\left(1-t_0^+\right) RT}{F} \ln c_e^{neg}(1) + \phi_e^{sep}(-1). \tag{A.70}$$

By inserting the discrete $\mathbf{i}_e$ and $\mathbf{c}_e$ values and substituting the integral operators by the integration matrices, the discrete values of the electrolyte potential at the collocation points $\mathbf{\Phi}_e$ can be calculated.

A.4 LITHIUM EXCHANGE AT THE SURFACE OF THE PARTICLES

To finish, the lithium flux at the surface of the particles $\mathbf{j}$ are calculated by solving algebraic constraints at the collocation points of the electrodes using the Butler-Volmer Equation 2.12:

$$0 = \mathbf{j} - \frac{\text{diag}\left(\mathbf{i}_0\right)}{F}\left[exp\left(\frac{\alpha^{neg}F}{RT}\eta\right) - exp\left(\frac{-\alpha^{pos}F}{RT}\eta\right)\right], \tag{A.71}$$

where the exchange current density values $\mathbf{i}_0$ are calculated using Equation 2.14 and substituting the continuous variables by the discrete values $\mathbf{c}_{s,e}$ and $\mathbf{c}_e$. Discrete values for η are calculated using Equation 2.13 and substituting the discrete potential values.

A.5 DAE SYSTEM

The model reformulation described above results in a semi-explicit DAE system of index one. The system of equations is composed of $(R-2)\times(N+P)+N+S+P-6$ ODEs, that describe the solid and electrolyte concentration models, and $N+P+2$ algebraic constraints, which are used to compute the lithium exchange values at the surface of the particles in both electrodes' collocation points, $\mathbf{j}$, and the solid-phase potentials at the current collectors $\phi^{neg}_{s,CC}$ and $\phi^{pos}_{s,CC}$. This system can be expressed by

$$\dot{\mathbf{x}} = \mathbf{f}\left(\mathbf{x}, \mathbf{z}, u\right) \tag{A.72}$$

$$0 = \mathbf{g}\left(\mathbf{x}, \mathbf{z}, u\right) \tag{A.73}$$

where $\mathbf{f}$ and $\mathbf{g}$ are nonlinear mapping functions derived from the reformulated equations. The state vector $\mathbf{x}$, associated with the time-differential equations, contains the discrete values of the solid concentration $u_s = rc_s$ and the electrolyte concentration c_e:

$$\mathbf{x} = \left[\bar{\mathbf{u}}^{pos}_s, \bar{\mathbf{u}}^{neg}_s, \bar{\mathbf{c}_e}\right]^{\mathbf{T}}. \tag{A.74}$$

$\bar{\mathbf{u}}^{pos}_s \in \mathbb{R}^{(R-2)\times P}$ and $\bar{\mathbf{u}}^{neg}_s \in \mathbb{R}^{(R-2)\times N}$ are the concatenated vectors of u_s at the interior collocation points for all the collocation points in the electrodes.

The state vector $\mathbf{z}$ associated with the algebraic equations, contains the discrete values of the lithium flux at the particles' surface $\mathbf{j}^{pos} \in \mathbb{R}^P$ and $\mathbf{j}^{neg} \in \mathbb{R}^N$ at the collocation

points of the positive and negative electrodes respectively, and the solid-phase potentials at the current collectors $\phi_{s,CC}^{pos}$ and $\phi_{s,CC}^{neg}$:

$$\mathbf{z} = \left[\mathrm{j}^{pos}, \mathrm{j}^{neg}, \phi_{s,CC}^{pos}, \phi_{s,CC}^{neg}\right]^{\mathbf{T}}. \tag{A.75}$$

To solve this system of equations, the MATLAB® *ode15s* [180] solver has been used. This solver uses a variable time-step to solve stiff DAE systems. Due to the functions that the solver uses, it is not directly implementable in real-time systems. Nevertheless, it can be adapted to make it suitable for real-time implementation, as it is shown in [53]. In this work, they adapted the *ode15s* solver to implement a similar ROM to the previously explained one, using the orthogonal collocation technique.

Appendix B

VALIDATION OF THE ROM

In order to validate the ROM, high fidelity results were obtained from a higher order solution of the P2D model (the FOM). The FOM was solved using FEM in COMSOL Multiphysics® while the ROM was computed in MATLAB ®. All the simulations were carried out in a personal computer with an 8th generation Intel Core i5 processor and 8 GB of RAM. The COMSOL Multiphysics® model was implemented by G. Plett *et al.* [8]. The parameter values that were used correspond to the work by Doyle *et al.* [181] and its values can be found in Tables B.1 and B.2. The cell is composed of a graphite (Li_xC_6) negative electrode and a lithium manganese oxide ($Li_yMn_2O_4$) positive electrode. The electrolyte is a mixture of lithium hexafluorophosphate salt ($LiPF_6$) and commonly used organic carbonate solvents (ethylene carbonate (EC) and dimethyl carbonate (DMC)).

Table B.1: Doyle cell electrode parameters (25 ^{o}C) [181].

Parameter	Description	Negative electrode	Positive electrode
D_s (m^2 s^{-1})	Solid diffusion	3.9×10^{-14}	10^{-13}
σ (S m^{-1})	Electric conductivity	100	3.8
$c_{s,max}$ (mol m^{-3})	Max. Li concentration	26390	22860
$c_{s,0}$ (mol m^{-3})	Initial Li concentration	14870	3900
L (m)	Thickness	1.28×10^{-4}	1.9×10^{-4}
R_s (m)	Particle radius	12.5×10^{-6}	8.5×10^{-6}
ε	Liquid volume fraction	0.357	0.444
ε_s	Solid volume fraction	0.471	0.297
$brug$	Bruggeman coefficient	1.5	1.5
k (mol m^{-2} s^{-1})	Reaction rate	2.29×10^{-5}	2.21×10^{-5}
R_{film} (Ω) *	Film resistance	0	0

* The value for R_{film}^{neg} was changed from the original value by Doyle *et al.* [181], which was 0.07 Ω.

Table B.2: Doyle cell separator and electrolyte parameters (25ºC) [181].

Parameter	Description	Separator	Electrolyte
L (m)	Thickness	0.76×10^{-4}	-
ε_e	Liquid volume fraction	0.724	-
$\kappa_{ref,0}$ (S m^{-1})	Initial conductivity	-	0.105
$brug$ *	Bruggeman coefficient	1.5	-
α	Transfer coefficient	-	0.5
D_e (m^2 s^{-1})	Diffusion coefficient	-	7.5×10^{-11}
t_0^+	Transport number	-	0.363
$c_{e,0}$ (mol m^{-3})	Initial concentration	-	2000

* The value for *brug* in the electrolyte was changed from the original value by Doyle *et al.* [181], which was 3.3.

For the implementation in COMSOL Multiphysics®, the macro-scale was represented with a 1D geometry divided into three domains (the electrodes and the separator). The micro-scale was represented with a 2D geometry and the diffusion coefficients were set to zero in the x direction. This limits the solid diffusion model just to the y direction distributed along the cell thickness. This y direction then becomes equivalent to the r direction. The equations solved in both geometries are coupled using the *linear extrusion* COMSOL Multiphysics® function to project the surface concentration $c_{s,e}$ from the 2D geometry to the 1D geometry. Each domain of the 1D geometry was discretized with 20 elements. The 2D geometries of the electrodes were discretized with 249 triangular elements.

To begin with the validation of the ROM, constant-current discharges at different C-rates were simulated and the evolution of the internal variables in time and space were compared with the FOM. Afterwards, to validate the ROM with application-oriented dynamic current profiles, a UDDS profile was used. The UDDS is used by the United States Environmental Protection Agency to test the performance and efficiency of light duty vehicles in city driving conditions. The UDDS gives a speed versus time profile, but it was translated into current versus time using the method described in Section 2.4 of [10]. Figure B.1 shows the current profile of the UDDS cycle.

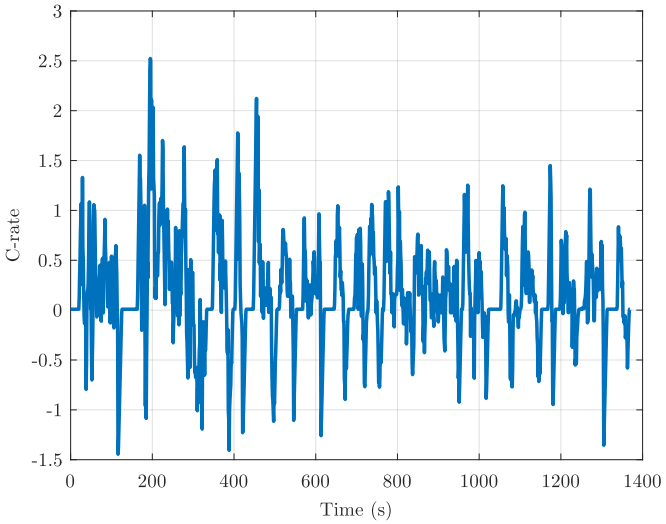

Figure B.1: UDDS current profile.

B.1 CONSTANT CURRENT

Figure B.2 shows constant-current discharges at different C-rates. As can be observed, the voltage response of the ROM agrees very well with the FOM. The number of collocation points used to compute the ROM for the discharges are $N_p = 6$, $N_s = 3$, $N_n = 6$ and $N_r = 15$, which denote the number of collocation points used to discretize the positive electrode, the separator, the negative electrode and the solid particles respectively.

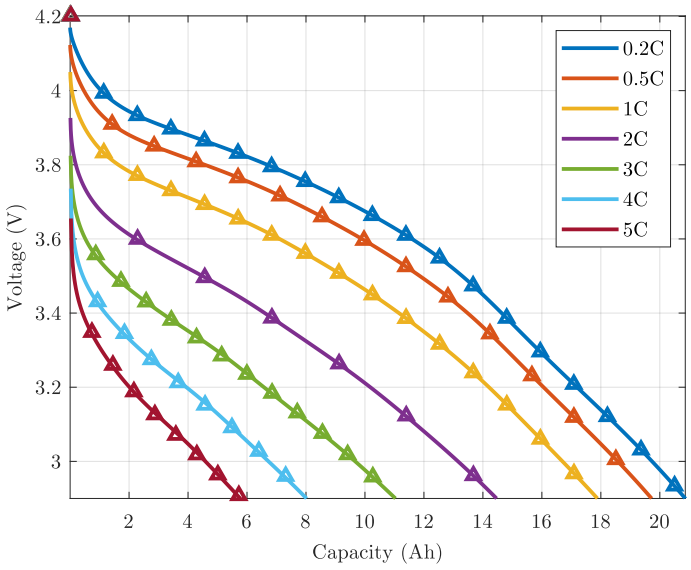

Figure B.2: Constant-current discharges for various C-rates. The markers show the FOM response and the lines the ROM response.

Regarding the computational cost, the ROM is about 10 times faster than the FOM to obtain the solutions for the constant-current discharge profiles. The ROM needed approximately 0.5-2 s to obtain the results while the FOM needed around 5-30 s. The RMS errors of the different discharges can be seen in Table B.3. These root-mean-square errors (RMSEs) are obtained applying the following equation:

$$RMSE = \sqrt{(FOM - ROM)^2}. \tag{B.1}$$

Table B.3: RMSEs for different constant-current discharges.

C-rate	0.2C	0.5C	1C	2C	3C	4C	5C
RMSE (mV)	0.257	0.326	0.732	1.523	2.256	4.08	4.647

In order to evaluate how the internal variables perform, the results obtained for a 1C discharge were used. In Figure B.3 the cell voltage evolution can be seen, which is calculated by subtracting the negative electrode/current collector interface solid-phase potential to the positive electrode/current collector interface solid-phase potential. The cell voltage absolute error of the ROM with respect to the FOM is shown, of which maximum value is of 2 mV and its RMSE is of 0.732 mV.

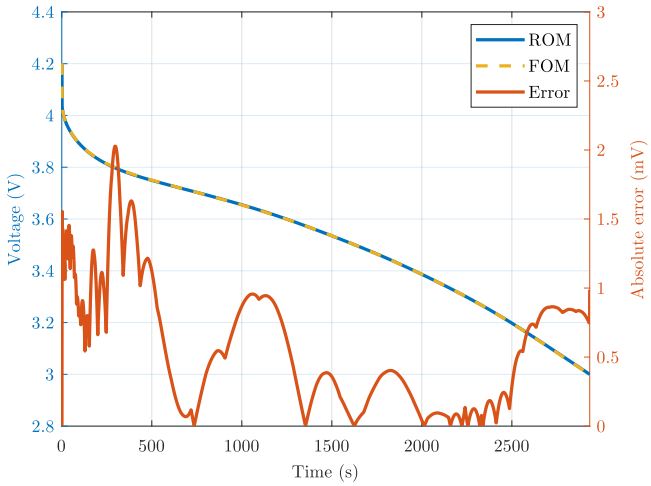

Figure B.3: Cell voltage response for a 1C discharge with the ROM and the FOM.

Regarding the electrolyte and solid-phase concentrations, Figures B.4 and B.5 show that the time evolution of both variables are very close to the results obtained from the FOM, being its maximum relative error value of around 1 % for both variables.

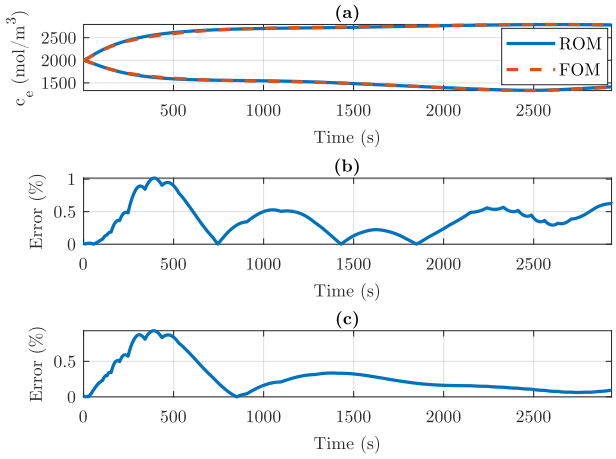

Figure B.4: a) Electrolyte concentration response for a 1C discharge at the cell boundaries with the ROM and the FOM. b) Relative error of the positive electrode response. c) Relative error of the negative electrode response.

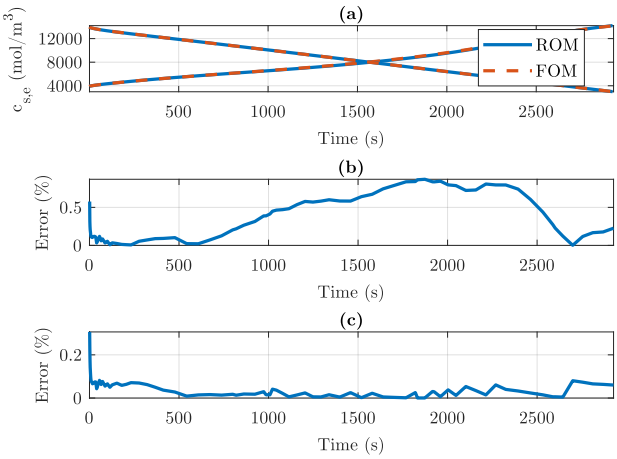

Figure B.5: a) Particle surface concentration response for a 1C discharge at the cell boundaries with the ROM and the FOM. b) Relative error of the positive electrode response. c) Relative error of the negative electrode response.

In Figure B.6 and Figure B.7 the spatial evolution of both concentration variables at different times is shown.

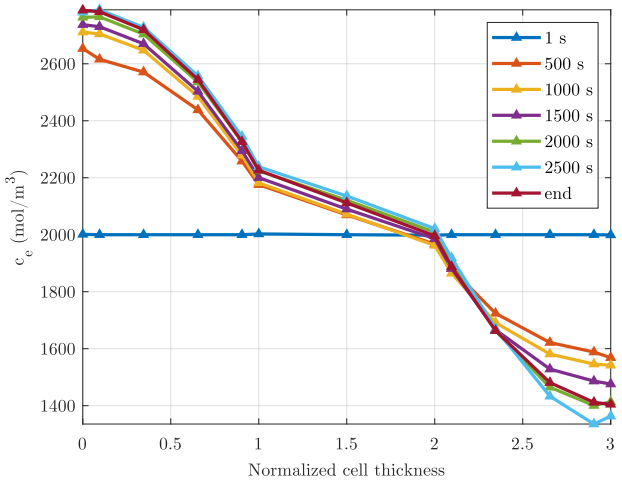

Figure B.6: Electrolyte lithium concentration across the thickness of the cell at different times for a 1C discharge.

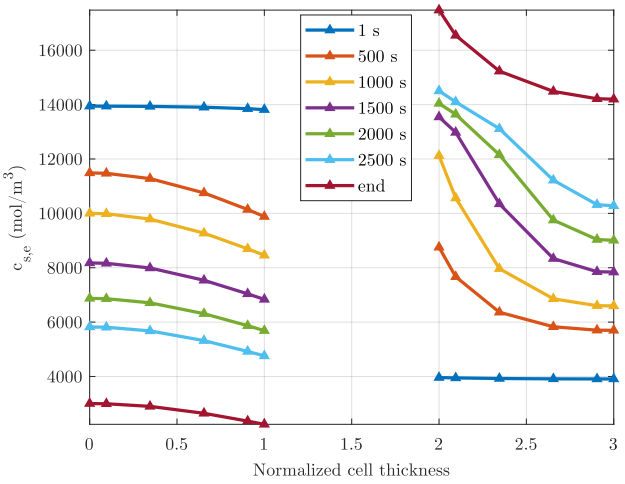

Figure B.7: Particle surface lithium concentration across the thickness of the cell at different times for a 1C discharge.

The variable that shows the biggest error compared to the FOM is the reaction flux at the particle/electrolyte interface. This is logical since all the variables of the model are coupled by the reaction flux and all the errors of the rest of the variables are added into the calculus of j. However, despite being the least precise variable, the response remains being very accurate, while having a maximum relative error of about 4%.

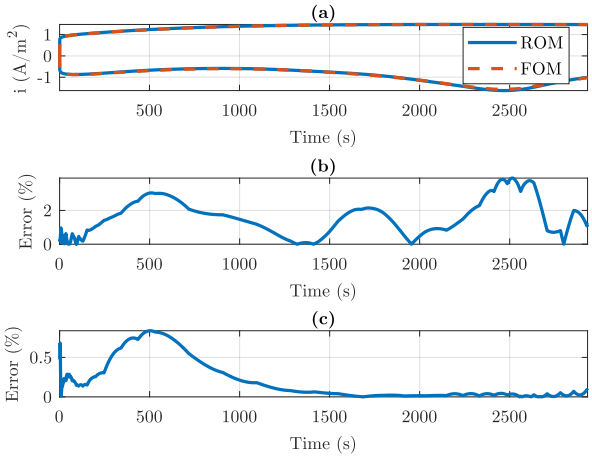

Figure B.8: a) Current density response for a 1C discharge at the cell boundaries with the ROM and the FOM. b) Relative error of the positive electrode response. c) Relative error of the negative electrode response.

In Table B.4 an evaluation of the ROM with different number of collocation points can be seen. To compare the accuracies obtained with different discretizations, the RMSEs obtained for 1 C discharges are shown. To see the computational requirements for each discretization, the computational time required to obtain the solution, the size of the biggest matrix and the RAM memory needed to store the biggest matrix are given. The size of the matrix is calculated by adding the number of equations that have to be solved, which is given by

$$size = (N_r - 2)(N_n + N_p) + 2N_n + N_s + 2N_p - 4. \tag{B.2}$$

Each element of this double-precision numerical matrix requires 8 bytes, so knowing the size of the matrix, the memory required to store it can be calculated with the formula

$$Memory(\text{kB}) = rc8/10^3, \tag{B.3}$$

where r denotes the number of rows and c denotes the number of columns.

Table B.4: RMS error and required computational time to simulate a 1C discharge with the ROM with different number of collocation points (positive electrode, separator, negative electrode and solid-phase particles number of points).

	6,3,6,15	6,3,6,10	6,3,6,5	6,3,6,30	12,6,12,15	4,2,4,15
RMSE (mV)	0.732	0.725	2.091	0.723	0.668	4.092
Time (s)	1.55	1.17	0.88	3.01	3.04	1.39
Size	179×179	119×119	59×59	359×359	362×362	118×118
Memory (kB)	256	113	28	1031	1048	111

Overall, these constant-current discharge results show that the performance of the ROM with constant inputs is very accurate. Furthermore, the time savings are considerable comparing to the FOM. To compare the memory requirements with the FOM, the COMSOL® model has 1528 degrees of freedom, which means that its matrix size is of 1528×1528. This results in a memory requirement of 18.68 MB, which is 73 times bigger than the matrix for the 6,3,6,15 collocation points ROM.

B.2 DYNAMIC CURRENT PROFILES

The variable input of dynamic current profiles generate sharper concentration gradients in the model, making the numerical solution of the model more time consuming. Furthermore, since the current input changes every second or every few seconds, the variable time-step solver cannot be used to simulate more than one second. Therefore, the solver needs to solve the model every second. In consequence, dynamic current profile simulations take much longer than constant-current simulations for methods that use variable time-step solvers. The COMSOL Multiphysics® model needed around 376 s to solve the UDDS profile shown in Figure B.1. In Table B.5 the computational time required to solve the UDDS profile with the ROM is shown for different numbers of collocation points. As can be seen, the ROM remains being around 10 times faster than the FOM for the case of 6,3,6,15 collocation points, however the total time savings are much bigger since the solution of the UDDS profile is more time consuming.

Table B.5: RMS error and required computational time to simulate the UDDS cycle with the ROM.

	6,3,6,15	6,3,6,12	6,3,6,5	6,3,6,20	10,5,10,15	15,8,15,15	4,2,4,15
RMSE (mV)	0.751	1.01	11.768	0.833	0.827	0.938	0.625
Time (s)	37.67	32.36	19.03	44.64	51.25	82.75	29.95

In Figure B.9 the voltage responses of the FOM and the ROM with 6,3,6,15 collocation points are shown for the UDDS cycle. In Figure B.10 the absolute error for the ROM can be observed. As can be seen, the voltage response is very accurate, almost as accurate as for the constant-current discharges, as can be concluded by comparing the RMS errors of Tables B.4 and B.5.

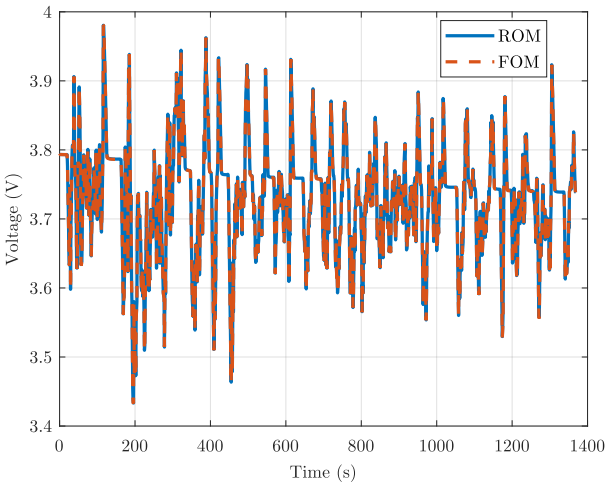

Figure B.9: Cell voltage response of the ROM and the FOM for the UDDS profile with an initial SOC of 60%.

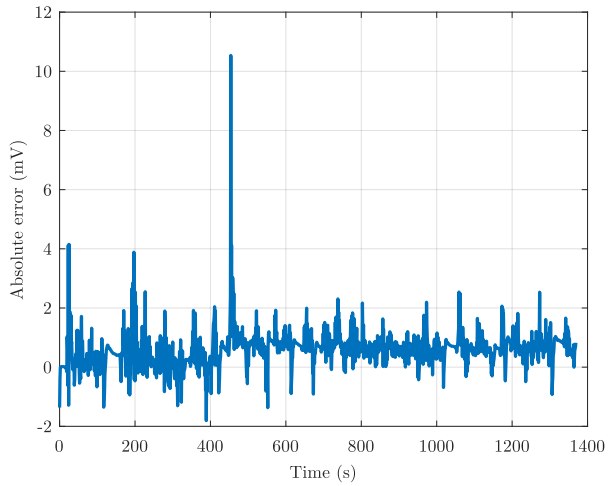

Figure B.10: Absolute voltage error of the ROM compared to the FOM for the UDDS profile.

Appendix C

CELL PARAMETERS FOR THE PBMS

C.1 LG M50

The parameters of the LG M50 cell are given in Table C.1.

Table C.1: LG M50 cell parameters [49].

Parameter	Negative	Separator	Positive
D_s (m^2 s^{-1})	3.3×10^{-14}		4×10^{-15}
σ (S m^{-1})	215		0.18
$c_{s,max}$ (kmol m^{-3})	33.133		63.104
$c_{e,0}$ (kmol m^{-3})	1	1	1
A (m^2)	0.1027	0.1027	0.1027
L (m)	8.52×10^{-5}	1.2×10^{-5}	7.56×10^{-5}
R_s (m)	5.86×10^{-6}		5.22×10^{-6}
α	0.5		0.5
$R_f(\Omega)$	0.02		0
ε_s	0.75		0.665
ε_e	0.25	0.47	0.335
$brug$	1.5	1.5	1.5
$z_{0\%}$	0.027		0.8536
$z_{100\%}$	0.9014		0.27
$k_{0,norm}$ (mol m^{-2} s^{-1})	7.04×10^{-6}		7.07×10^{-5}
t_+^0	0.2594	0.2594	0.2594

The functions for the negative and positive open circuit potentials are given by

$$\begin{aligned} U^n_{ocp}(\theta) = 1.9793e^{-39.3631\theta} + 0.2482 \\ -0.0909 \times \tanh(29.8538(\theta - 0.1234)) \\ -0.04478 \times \tanh(14.9159(\theta - 0.2769)) \\ -0.0205 \times \tanh(30.4444(\theta - 0.6103)) \end{aligned} \tag{C.1}$$

and

$$\begin{aligned} U^p_{ocp}(\theta) = -0.809\theta + 4.4875 \\ -0.0428 \times \tanh(18.5138(\theta - 0.5542)) \\ -17.7326 \times \tanh(15.789(\theta - 0.3117)) \\ +17.5842 \times \tanh(15.9308(\theta - 0.312)), \end{aligned} \tag{C.2}$$

respectively. The ionic conductivity of the electrolyte is given by

$$\kappa_e(c_e) = 1.297 \times 10^{-10} c_e^3 - 7.94 \times 10^{-5} c_e^{1.5} + 3.329 \times 10^{-3} c_e, \tag{C.3}$$

and the electrolyte diffusivity $D_e(c_e)$ by

$$D_e(c_e) = 8.794 \times 10^{-17} c_e^2 - 3.972 \times 10^{-13} c_e + 4.862 \times 10^{-10}. \tag{C.4}$$

C.2 28 AH POWER CELL PARAMETERS

The parameters of the LG M50 cell are given in Table C.2.

Table C.2: 28 Ah power cell parameters [47].

Parameter	Negative	Separator	Positive
D_s (m^2 s^{-1})	1.99×10^{-14}		5×10^{-15}
σ (S m^{-1})	1000		10
$c_{s,max}$ (kmol m^{-3})	31.390		48.390
$c_{e,0}$ (kmol m^{-3})	1	1	1
A (m^2)	1.7775	1.7775	1.7775
L (m)	46.6×10^{-6}	18.7×10^{-6}	43×10^{-6}
R_s (m)	6.3×10^{-6}		2.1×10^{-6}
α	0.5		0.5
$R_f(\Omega)$	0		0.0
ε_s	0.4925		0.5724
ε_e	0.292	0.3949	0.209
$brug$	1.52	1.62	1.44
$z_{0\%}$	0.014		0.9615
$z_{100\%}$	0.884		0.4352
$k_{0,norm}$ (mol m^{-2} s^{-1})	1.54×10^{-4}		1.04×10^{-4}
t_+^0	0.26	0.26	0.26
$D_e(m^2 s^{-1})$	2.79×10^{-10}	2.79×10^{-10}	2.79×10^{-10}

The positive and negative electrode OCPs are shown in Figure C.1.

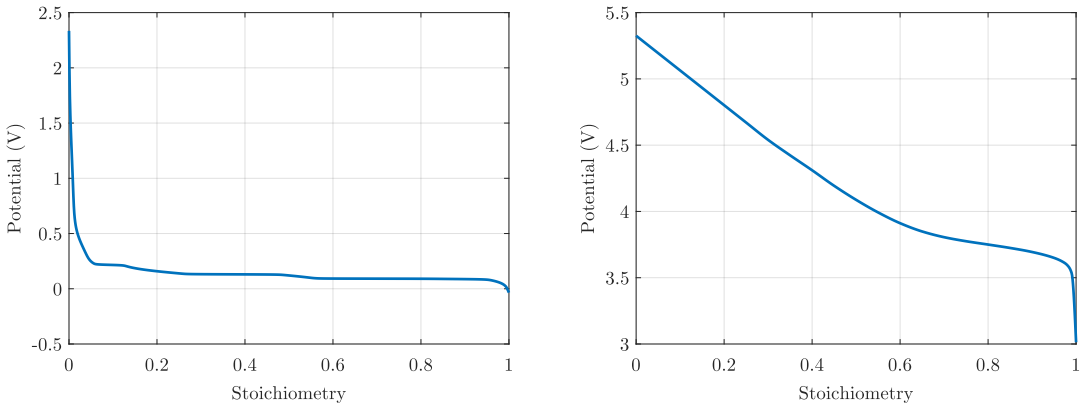

(a) (b)

Figure C.1: OCPs of the negative (a) and positive (b) electrodes for the 28 Ah power cell [47].

The ionic conductivity of the electrolyte is given by

$$\kappa_e(c_e) = c_e(0.042 - 1.0972 \times 10^{-5} c_e + 0.0132 e^{-0.0022 c_e})^2. \tag{C.5}$$

C.3 LG MH1 CELL PARAMETERS

The parameters of the LG M50 cell are given in Table C.3.

Table C.3: LG M50 cell parameters [49].

Parameter	Negative	Separator	Positive
D_s (m^2 s^{-1})	5.94×10^{-14}		6.51×10^{-15}
σ (S m^{-1})	136		1.964
$c_{s,max}$ (kmol m^{-3})	29.561		48.902
$c_{e,0}$ (kmol m^{-3})	1	1	1
A (m^2)	0.0748	0.0748	0.0748
L (m)	8.7×10^{-5}	1.3×10^{-5}	6.7×10^{-5}
R_s (m)	8.5×10^{-6}		4.1×10^{-6}
α	0.5		0.5
$R_f(\Omega)$	0.02		0.047
ε_s	0.667		0.7
ε_e	0.313	0.41	0.26
$brug$	1.48	1.5	1.47
$z_{0\%}$	0.005		0.9314
$z_{100\%}$	0.9412		0.2386
$k_{0,norm}$ (mol m^{-2} s^{-1})	3.11×10^{-5}		6.07×10^{-5}
t_+^0	0.2594	0.2594	0.2594

The positive and negative electrode OCPs are shown in Figure C.2.

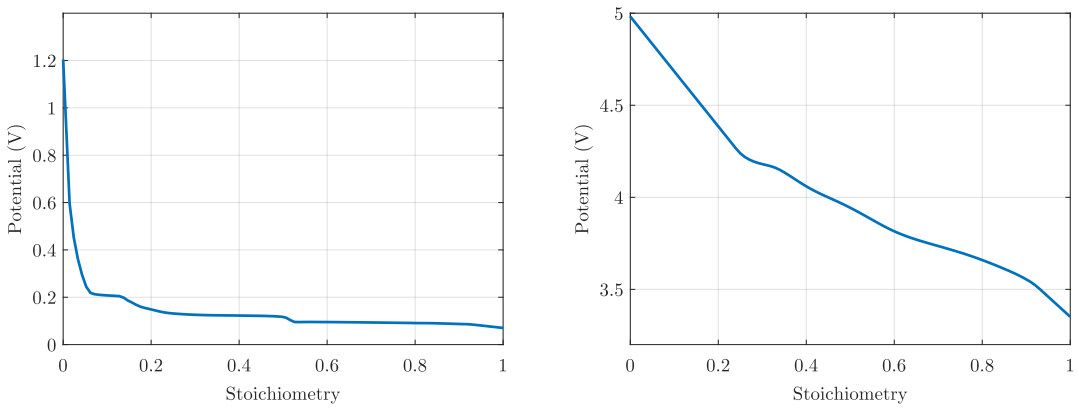

(a) (b)

Figure C.2: OCPs of the negative (a) and positive (b) electrodes for the LG MH1 cell.

Appendix D

DEGRADATION MODE ESTIMATION TOOL VALIDATION

Simulation results for an NMC-graphite 28 Ah cell, which parameters were obtained from [47, 48] are shown in Figure D.1, and for an LFP cell in Figure D.2.

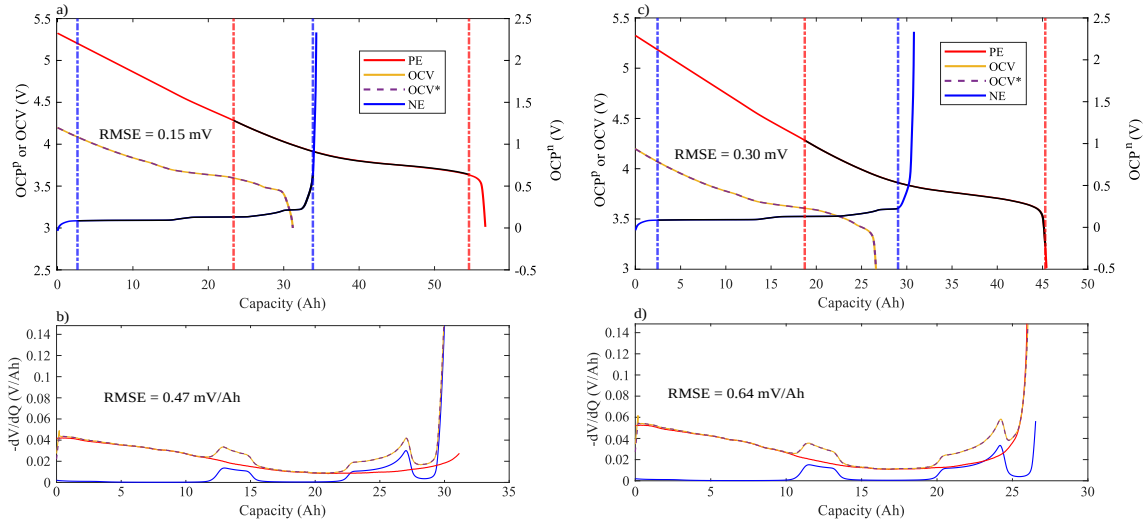

Figure D.1: Mode estimation for a 28 Ah high-power NMC-graphite cell.

The estimated and real degradation mode values for these two simulation cases are given in Table D.1.

Table D.1: Simulation degradation modes estimation.

		LAM^n	LAM^p	LLI
NMC	Estimated	9.80 %	20.00 %	14.51 %
	Expected	10.00 %	20.00 %	14.48 %
LFP	Estimated	9.74 %	19.86 %	12.09 %
	Expected	10.00 %	20.00 %	12.00 %

The experimental results for a Kokam 1.25 Ah cell, of which parameters were acquired from [50], are shown in D.3.

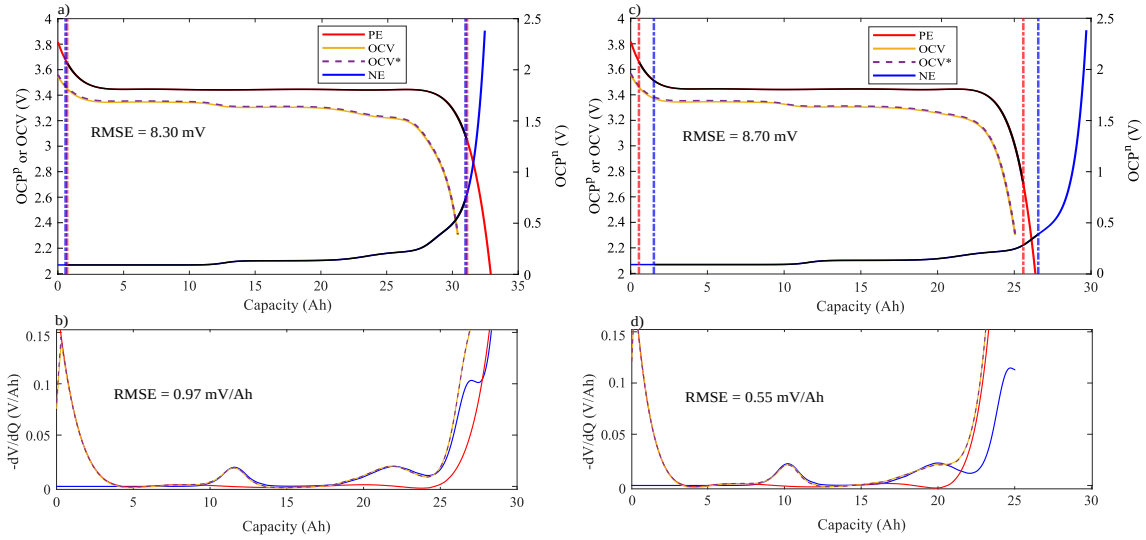

Figure D.2: Mode estimation for an LFP cell.

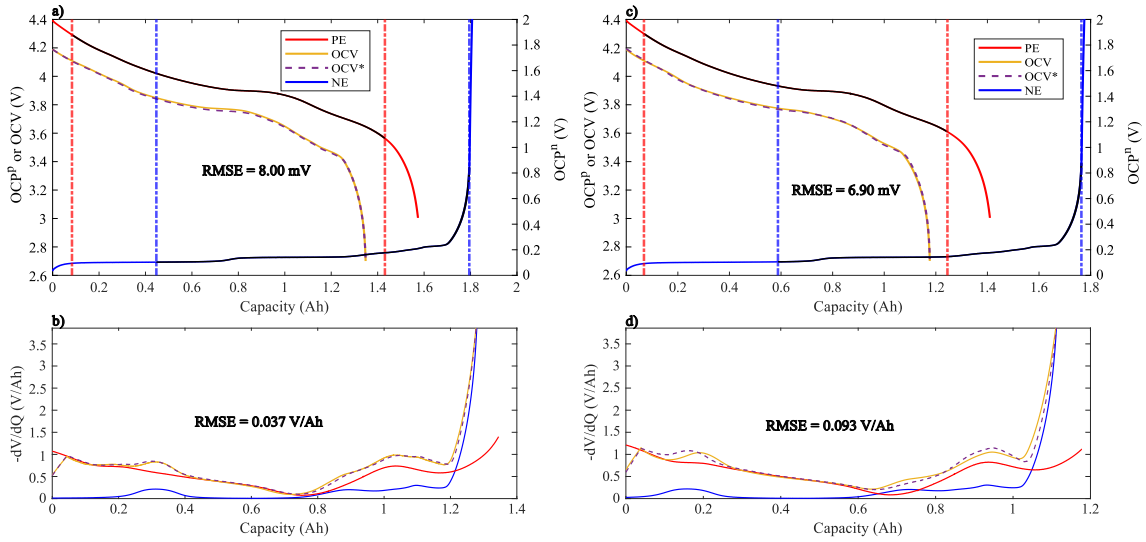

Figure D.3: Mode estimation for a 1.25 Ah Kokam cell.

LIST OF FIGURES

LIST OF TABLES

REFERENCES

[1] European Commission, "Horizon Europe. Strategic Plan 2021-2024," European Commission, Tech. Rep., 2021.

[2] P. R. Shukla, J. Skea, R. Slade, A. Al Khourdajie, R. Van Diemen, D. McCollum, M. Pathak, S. Some, P. Vyas, R. Fradera *et al.*, "Climate change 2022: Mitigation of climate change," *Contribution of working group III to the sixth assessment report of the Intergovernmental Panel on Climate Change*, vol. 10, p. 9781009157926, 2022.

[3] D. Choi, N. Shamim, A. Crawford, Q. Huang, C. K. Vartanian, V. V. Viswanathan, M. D. Paiss, M. J. E. Alam, D. M. Reed, and V. L. Sprenkle, "Li-ion battery technology for grid application," *Journal of Power Sources*, vol. 511, no. August, p. 230419, 2021. [Online]. Available: https://doi.org/10.1016/j.jpowsour.2021.230419

[4] A. Khan, S. Yaqub, M. Ali, A. W. Ahmad, H. Nazir, H. A. Khalid, N. Iqbal, Z. Said, and K. Sopian, "A state-of-the-art review on heating and cooling of lithium-ion batteries for electric vehicles," *Journal of Energy Storage*, vol. 76, p. 109852, 2024.

[5] Z. Wang, C. Dai, K. Chen, Y. Wang, Q. Liu, Y. Liu, B. Ma, L. Mi, and W. Mao, "Perspectives on strategies and techniques for building robust thick electrodes for lithium-ion batteries," *Journal of Power Sources*, vol. 551, p. 232176, 2022.

[6] B. S. Vishnugopi, A. Verma, and P. P. Mukherjee, "Fast charging of lithium-ion batteries via electrode engineering," *Journal of The Electrochemical Society*, vol. 167, no. 9, p. 090508, 2020.

[7] E. Logan and J. Dahn, "Electrolyte design for fast-charging li-ion batteries," *Trends in Chemistry*, vol. 2, no. 4, pp. 354–366, 2020.

[8] G. L. Plett, *Battery Management Systems, Volume 1: Battery Modeling.* Artech House, 2015, vol. 1.

[9] K. D. Stetzel, L. L. Aldrich, M. S. Trimboli, and G. L. Plett, "Electrochemical state and internal variables estimation using a reduced-order physics-based model of a

lithium-ion cell and an extended Kalman filter," *Journal of Power Sources*, vol. 278, pp. 490–505, 2015. [Online]. Available: http://dx.doi.org/10.1016/j.jpowsour.2014.11.135

[10] G. L. Plett, *Battery Management Systems, Volume 2: Equivalent-Circuit Methods*. Artech House, 2016, vol. 2.

[11] A. Allam and S. Onori, "An Interconnected Observer for Concurrent Estimation of Bulk and Surface Concentration in the Cathode and Anode of a Lithium-ion Battery," *IEEE Transactions on Industrial Electronics*, vol. 65, no. 9, pp. 7311–7321, sep 2018.

[12] ——, "Online Capacity Estimation for Lithium-Ion Battery Cells via an Electrochemical Model-Based Adaptive Interconnected Observer," *IEEE Transactions on Control Systems Technology*, vol. 29, no. 4, pp. 1636–1651, sep 2020.

[13] E. Miguel, G. L. Plett, M. S. Trimboli, I. Lopetegi, L. Oca, U. Iraola, and E. Bekaert, "Electrochemical Model and Sigma Point Kalman Filter Based Online Oriented Battery Model," *IEEE Access*, vol. 9, pp. 98 072–98 090, 2021.

[14] G. Florentino and M. S. Trimboli, "Lithium-ion Battery Management Using Physics-based Model Predictive Control and DC-DC Converters," *2018 IEEE Transp. Electrif. Conf. Expo, ITEC 2018*, pp. 1046–1053, 2018.

[15] M. Xu, R. Wang, P. Zhao, and X. Wang, "Fast charging optimization for lithium-ion batteries based on dynamic programming algorithm and electrochemical-thermal-capacity fade coupled model," *Journal of Power Sources*, vol. 438, p. 227015, 2019.

[16] B. Zhou, G. Fan, Y. Wang, Y. Liu, S. Chen, Z. Sun, C. Meng, J. Yang, and X. Zhang, "Life-extending optimal charging for lithium-ion batteries based on a multi-physics model and model predictive control," *Applied Energy*, vol. 361, p. 122918, 2024.

[17] G. L. Plett and M. S. Trimboli, *Battery Management Systems, Volume 3: Physics-Based Methods*. Artech House, 2024, vol. 3.

[18] X. G. Yang, Y. Leng, G. Zhang, S. Ge, and C. Y. Wang, "Modeling of lithium plating induced aging of lithium-ion batteries: Transition from linear to nonlinear aging," *Journal of Power Sources*, vol. 360, pp. 28–40, 2017. [Online]. Available: http://dx.doi.org/10.1016/j.jpowsour.2017.05.110

[19] D. Yang, Y. Wang, R. Pan, R. Chen, and Z. Chen, "State-of-health estimation for the lithium-ion battery based on support vector regression,"

Applied Energy, vol. 227, no. May 2017, pp. 273–283, 2018. [Online]. Available: https://doi.org/10.1016/j.apenergy.2017.08.096

[20] D. Ren, K. Smith, D. Guo, X. Han, X. Feng, L. Lu, M. Ouyang, and J. Li, "Investigation of Lithium Plating-Stripping Process in Li-Ion Batteries at Low Temperature Using an Electrochemical Model," *Journal of The Electrochemical Society*, vol. 165, no. 10, pp. A2167–A2178, 2018.

[21] C. von Lüders, J. Keil, M. Webersberger, and A. Jossen, "Modeling of lithium plating and lithium stripping in lithium-ion batteries," *Journal of Power Sources*, vol. 414, no. December 2018, pp. 41–47, 2019. [Online]. Available: https://doi.org/10.1016/j.jpowsour.2018.12.084

[22] J. S. Edge, S. O'Kane, R. Prosser, N. D. Kirkaldy, A. N. Patel, A. Hales, A. Ghosh, W. Ai, J. Chen, J. Yang, S. Li, M.-C. Pang, L. Bravo Diaz, A. Tomaszewska, M. W. Marzook, K. N. Radhakrishnan, H. Wang, Y. Patel, B. Wu, and G. J. Offer, "Lithium ion battery degradation: what you need to know," *Physical Chemistry Chemical Physics*, vol. 23, no. 14, pp. 8200–8221, 2021.

[23] S. E. J. O'Kane, I. D. Campbell, M. W. J. Marzook, G. J. Offer, and M. Marinescu, "Physical Origin of the Differential Voltage Minimum Associated with Lithium Plating in Li-Ion Batteries," *Journal of The Electrochemical Society*, vol. 167, no. 9, p. 090540, may 2020.

[24] S. E. O'Kane, W. Ai, G. Madabattula, D. Alonso-Alvarez, R. Timms, V. Sulzer, J. S. Edge, B. Wu, G. J. Offer, and M. Marinescu, "Lithium-ion battery degradation: how to model it," *Physical Chemistry Chemical Physics*, vol. 24, no. 13, pp. 7909–7922, 2022.

[25] W. Vermeer, G. R. Chandra Mouli, and P. Bauer, "A comprehensive review on the characteristics and modeling of lithium-ion battery aging," *IEEE Transactions on Transportation Electrification*, vol. 8, no. 2, pp. 2205–2232, 2022.

[26] P. Arora, "Mathematical Modeling of the Lithium Deposition Overcharge Reaction in Lithium-Ion Batteries Using Carbon-Based Negative Electrodes," *Journal of The Electrochemical Society*, vol. 146, no. 10, p. 3543, 1999. [Online]. Available: https://doi.org/10.1149%2F1.1392512

[27] R. Spotnitz, "Simulation of capacity fade in lithium-ion batteries," *Journal of power sources*, vol. 113, no. 1, pp. 72–80, 2003.

[28] S. B. Peterson, J. Apt, and J. Whitacre, "Lithium-ion battery cell degradation resulting from realistic vehicle and vehicle-to-grid utilization," *Journal of Power Sources*, vol. 195, no. 8, pp. 2385–2392, 2010.

[29] M. Schimpe, M. E. von Kuepach, M. Naumann, H. C. Hesse, K. Smith, and A. Jossen, "Comprehensive modeling of temperature-dependent degradation mechanisms in lithium iron phosphate batteries," *Journal of The Electrochemical Society*, vol. 165, no. 2, p. A181, 2018.

[30] P. Ramadass, B. Haran, P. M. Gomadam, R. White, and B. N. Popov, "Development of First Principles Capacity Fade Model for Li-Ion Cells," *Journal of the Electrochemical Society*, vol. 151, no. 2, pp. 196–203, 2004.

[31] H. J. Ploehn, P. Ramadass, and R. E. White, "Solvent Diffusion Model for Aging of Lithium-Ion Battery Cells," *Journal of The Electrochemical Society*, vol. 151, no. 3, p. A456, 2004.

[32] M. Safari, M. Morcrette, A. Teyssot, and C. Delacourt, "Multimodal Physics-Based Aging Model for Life Prediction of Li-Ion Batteries," *Journal of The Electrochemical Society*, vol. 156, no. 3, p. A145, 2009.

[33] I. Laresgoiti, S. Käbitz, M. Ecker, and D. U. Sauer, "Modeling mechanical degradation in lithium ion batteries during cycling: Solid electrolyte interphase fracture," *Journal of Power Sources*, vol. 300, pp. 112–122, 2015.

[34] X. G. Yang, S. Ge, T. Liu, Y. Leng, and C. Y. Wang, "A look into the voltage plateau signal for detection and quantification of lithium plating in lithium-ion cells," *Journal of Power Sources*, vol. 395, no. April, pp. 251–261, 2018. [Online]. Available: https://doi.org/10.1016/j.jpowsour.2018.05.073

[35] S. Atalay, M. Sheikh, A. Mariani, Y. Merla, E. Bower, and W. D. Widanage, "Theory of battery ageing in a lithium-ion battery : Capacity fade , nonlinear ageing and lifetime prediction," *Journal of Power Sources*, vol. 478, p. 229026, 2020. [Online]. Available: https://doi.org/10.1016/j.jpowsour.2020.229026

[36] S. Pannala, H. Movahedi, T. R. Garrick, A. G. Stefanopoulou, and J. B. Siegel, "Consistently tuned battery lifetime predictive model of capacity

loss, resistance increase, and irreversible thickness growth," *Journal of The Electrochemical Society*, vol. 171, no. 1, p. 010532, jan 2024. [Online]. Available: https://dx.doi.org/10.1149/1945-7111/ad1294

[37] D. Anseán, M. Dubarry, A. Devie, B. Liaw, V. García, J. Viera, and M. González, "Operando lithium plating quantification and early detection of a commercial LiFePO4 cell cycled under dynamic driving schedule," *Journal of Power Sources*, vol. 356, pp. 36–46, jul 2017. [Online]. Available: https://linkinghub.elsevier.com/retrieve/pii/S0378775317305670

[38] I. D. Campbell, M. Marzook, M. Marinescu, and G. J. Offer, "How Observable Is Lithium Plating? Differential Voltage Analysis to Identify and Quantify Lithium Plating Following Fast Charging of Cold Lithium-Ion Batteries," *Journal of The Electrochemical Society*, vol. 166, no. 4, pp. A725–A739, 2019.

[39] J. M. Reniers, G. Mulder, and D. A. Howey, "Review and Performance Comparison of Mechanical-Chemical Degradation Models for Lithium-Ion Batteries," *Journal of The Electrochemical Society*, vol. 166, no. 14, pp. A3189–A3200, 2019.

[40] G. L. Plett, "Extended Kalman filtering for battery management systems of LiPB-based HEV battery packs - Part 3. State and parameter estimation," *Journal of Power Sources*, vol. 134, no. 2, pp. 277–292, 2004.

[41] ——, "Extended Kalman filtering for battery management systems of LiPB-based HEV battery packs - Part 1. Background," *Journal of Power Sources*, vol. 134, no. 2, pp. 252–261, 2004.

[42] ——, "Extended Kalman filtering for battery management systems of LiPB-based HEV battery packs - Part 2. Modeling and identification," *Journal of Power Sources*, vol. 134, no. 2, pp. 262–276, 2004.

[43] ——, "Sigma-point Kalman filtering for battery management systems of LiPB-based HEV battery packs: Part 1: Introduction and state estimation," *Journal of Power Sources*, vol. 161, no. 2, pp. 1356–1368, 2006.

[44] ——, "Sigma-point Kalman filtering for battery management systems of LiPB-based HEV battery packs: Part 2: Simultaneous state and parameter estimation," *Journal of power sources*, vol. 161, no. 2, pp. 1369–1384, 2006.

[45] D. Di Domenico, A. Stefanopoulou, and G. Fiengo, "Lithium-ion battery state of charge and critical surface charge estimation using an electrochemical model-based extended Kalman filter," *Journal of Dynamic Systems, Measurement and Control, Transactions of the ASME*, vol. 132, no. 6, pp. 1–11, 2010.

[46] R. Jobman, M. S. Trimboli, and G. L. Plett, "Identification of Lithium-Ion Physics-Based Model Parameter Values," *Journal of Energy Challenges and Mechanics*, vol. 2, no. 2, pp. 45–55, 2015.

[47] J. Schmalstieg, C. Rahe, M. Ecker, and D. U. Sauer, "Full Cell Parameterization of a High-Power Lithium-Ion Battery for a Physico-Chemical Model: Part I. Physical and Electrochemical Parameters," *J. Electrochem. Soc.*, vol. 165, no. 16, pp. A3799–A3810, 2018.

[48] J. Schmalstieg and D. U. Sauer, "Full Cell Parameterization of a High-Power Lithium-Ion Battery for a Physico-Chemical Model: Part II. Thermal Parameters and Validation," *Journal of The Electrochemical Society*, vol. 165, no. 16, pp. A3811–A3819, 2018.

[49] C.-H. Chen, F. B. Planella, K. O'regan, D. Gastol, W. D. Widanage, and E. Kendrick, "Development of experimental techniques for parameterization of multi-scale lithium-ion battery models," *Journal of The Electrochemical Society*, vol. 167, no. 8, p. 080534, 2020.

[50] L. Oca, E. Miguel, E. Agirrezabala, A. Herran, E. Gucciardi, L. Otaegui, E. Bekaert, A. Villaverde, and U. Iraola, "Physico-chemical parameter measurement and model response evaluation for a pseudo-two-dimensional model of a commercial lithium-ion battery," *Electrochimica Acta*, vol. 382, p. 138287, 2021. [Online]. Available: https://doi.org/10.1016/j.electacta.2021.138287

[51] D. Lu, M. S. Trimboli, G. Fan, R. Zhang, and G. L. Plett, "Nondestructive pulse testing to estimate a subset of physics-based-model parameter values for lithium-ion cells," *Journal of The Electrochemical Society*, vol. 168, no. 8, p. 080533, aug 2021. [Online]. Available: https://dx.doi.org/10.1149/1945-7111/ac1cfa

[52] D. Lu, M. S. Trimboli, G. Fan, Y. Wang, and G. L. Plett, "Nondestructive eis testing to estimate a subset of physics-based-model parameter values for lithium-ion cells," *Journal of The Electrochemical Society*, vol. 169, no. 8, p. 080504, aug 2022. [Online]. Available: https://dx.doi.org/10.1149/1945-7111/ac824a

[53] J. Sturm, S. Ludwig, J. Zwirner, B. Heinrich, M. F. Horsche, and A. Jossen, "Suitability of physicochemical models for embedded systems regarding a nickel-rich , silicon-graphite lithium-ion battery," *Journal of Power Sources*, vol. 436, no. July, p. 226834, 2019. [Online]. Available: https://doi.org/10.1016/j.jpowsour.2019.226834

[54] A. M. Bizeray, S. Zhao, S. R. Duncan, and D. A. Howey, "Lithium-ion battery thermal-electrochemical model-based state estimation using orthogonal collocation and a modified extended Kalman filter," *Journal of Power Sources*, vol. 296, pp. 400–412, 2015. [Online]. Available: http://dx.doi.org/10.1016/j.jpowsour.2015.07.019

[55] A. Smiley and G. L. Plett, "An adaptive physics-based reduced-order model of an aged lithium-ion cell , selected using an interacting multiple-model Kalman fi lter," *Journal of Energy Storage*, vol. 19, no. July, pp. 120–134, 2018. [Online]. Available: https://doi.org/10.1016/j.est.2018.07.004

[56] Y. Gao, K. Liu, C. Zhu, X. Zhang, and D. Zhang, "Co-estimation of state-of-charge and state-of- health for lithium-ion batteries using an enhanced electrochemical model," *IEEE Transactions on Industrial Electronics*, vol. 69, no. 3, pp. 2684–2696, 2022.

[57] S. Wang, Q. Wang, L. Xu, Y. Sun, X. Feng, and H. Wang, "A review on mechanisms, characteristics and relating hazards of vent gases from thermally abused li-ion batteries," *Journal of Energy Storage*, vol. 84, p. 110892, 2024.

[58] G. Zhang, W. Shen, and X. Wei, "Lithium-ion battery thermal safety evolution during high-temperature nonlinear aging," *Fuel*, vol. 362, p. 130845, 2024.

[59] T. Yin, L. Jia, X. Li, L. Zheng, and Z. Dai, "Effect of high-rate cycle aging and over-discharge on ncm811 (lini0. 8co0. 1mn0. 1o2) batteries," *Energies*, vol. 15, no. 8, p. 2862, 2022.

[60] M. A. Xavier, A. K. de Souza, and M. S. Trimboli, "A split-future mpc algorithm for lithium-ion battery cell-level fast-charge control," *IFAC-PapersOnLine*, vol. 53, no. 2, pp. 12 459–12 464, 2020.

[61] Y. Gao, X. Zhang, B. Guo, C. Zhu, J. Wiedemann, L. Wang, and J. Cao, "Health-aware multiobjective optimal charging strategy with coupled electrochemical-thermal-aging model for lithium-ion battery," *IEEE Transactions on Industrial Informatics*, vol. 16, no. 5, pp. 3417–3429, 2020.

[62] A. K. de Souza, G. L. Plett, and M. S. Trimboli, "A model predictive control-based state of power estimation algorithm using adaptive weighting," *Proc. of EVS-35, Oslo, Norway, June 2022*, 2022.

[63] Y. Gao, X. Zhang, Q. Cheng, B. Guo, and J. Yang, "Classification and review of the charging strategies for commercial lithium-ion batteries," *IEEE Access*, vol. 7, pp. 43 511–43 524, 2019.

[64] K. Liu, C. Zou, K. Li, and T. Wik, "Charging pattern optimization for lithium-ion batteries with an electrothermal-aging model," *IEEE transactions on industrial informatics*, vol. 14, no. 12, pp. 5463–5474, 2018.

[65] P. H. Notten, J. O. het Veld, and J. Van Beek, "Boostcharging li-ion batteries: A challenging new charging concept," *Journal of Power Sources*, vol. 145, no. 1, pp. 89–94, 2005.

[66] F. Savoye, P. Venet, S. Pelissier, M. Millet, and J. Groot, "Impact of periodic current pulses on li-ion batteries lifetime in vehicular application," *International Journal of Electric and Hybrid Vehicles*, vol. 7, no. 4, pp. 323–341, 2015.

[67] A. Bryson and Y. Ho, "Applied optimal control: optimization, estimation, and control, rev. printing ed," *Hemisphere Pub. Corp*, 1975.

[68] M. A. Xavier and M. S. Trimboli, "Lithium-ion battery cell-level control using constrained model predictive control and equivalent circuit models," *Journal of Power Sources*, vol. 285, pp. 374–384, 2015.

[69] Y. Yin, Y. Bi, Y. Hu, and S.-Y. Choe, "Optimal fast charging method for a large-format lithium-ion battery based on nonlinear model predictive control and reduced order electrochemical model," *Journal of The Electrochemical Society*, vol. 167, no. 16, p. 160559, 2021.

[70] J. Yeregui, L. Oca, I. Lopetegi, E. Garayalde, M. Aizpurua, and U. Iraola, "State of charge estimation combining physics-based and artificial intelligence models for lithium-ion batteries," *Journal of Energy Storage*, vol. 73, p. 108883, 2023. [Online]. Available: https://www.sciencedirect.com/science/article/pii/S2352152X23022818

[71] C. Rojas, L. Oca, I. Lopetegi, U. Iraola, and J. Carrasco, "A critical look at efficient parameter estimation methodologies of electrochemical models for lithium-ion

cells," *Journal of Energy Storage*, vol. 80, p. 110384, 2024. [Online]. Available: https://www.sciencedirect.com/science/article/pii/S2352152X23037830

[72] I. Lopetegi, G. L. Plett, M. S. Trimboli, A. Kawakita de Souza, L. Oca, E. Miguel, and U. Iraola, "A new battery soc/soh/esoh estimation method using a pbm and interconnected spkfs: Part i. soc and internal variable estimation," *Journal of The Electrochemical Society*, 2024. [Online]. Available: http://iopscience.iop.org/article/10.1149/1945-7111/ad30d4

[73] I. Lopetegi, G. L. Plett, M. S. Trimboli, L. Oca, E. Miguel, and U. Iraola, "A new battery soc/soh/esoh estimation method using a pbm and interconnected spkfs: Part ii. soh and esoh estimation," *Journal of The Electrochemical Society*, 2024. [Online]. Available: http://iopscience.iop.org/article/10.1149/1945-7111/ad30d5

[74] X. Dorronsoro, I. Lopetegi, E. Garayalde, U. Iraola, and J. Yeregui, "Modular battery energy storage systems for available energy increase," in *2022 IEEE Vehicle Power and Propulsion Conference (VPPC)*, 2022, pp. 1–7.

[75] I. Lopetegi, G. L. Plett, M. S. Trimboli, J. Yeregui, L. Oca, C. Rojas, E. Miguel, and U. Iraola, "Lithium-ion battery aging prediction with electrochemical models: P2d vs spme," in *2023 IEEE Vehicle Power and Propulsion Conference (VPPC)*, 2023, pp. 1–7.

[76] L. Cai and R. E. White, "Reduction of Model Order Based on Proper Orthogonal Decomposition for Lithium-Ion Battery Simulations," *Journal of The Electrochemical Society*, vol. 156, no. 3, p. A154, 2009.

[77] ——, "An Efficient Electrochemical – Thermal Model for a Lithium-Ion Cell by Using the Proper Orthogonal Decomposition Method," *Journal of The Electrochemical Society*, vol. 157, pp. 1188–1195, 2010.

[78] P. W. Northrop, V. Ramadesigan, S. De, and V. R. Subramanian, "Coordinate transformation, orthogonal collocation, model reformulation and simulation of electrochemical-thermal behavior of lithium-ion battery stacks," *Journal of the Electrochemical Society*, vol. 158, no. 12, 2011.

[79] J. L. Lee, A. Chemistruck, and G. L. Plett, "One-dimensional physics-based reduced-order model of lithium-ion dynamics," *Journal of Power Sources*, vol. 220, pp. 430–448, 2012. [Online]. Available: http://dx.doi.org/10.1016/j.jpowsour.2012.07.075

[80] A. Bizeray, S. R. Duncan, and D. A. Howey, "Advanced battery management systems using fast electrochemical modelling," *IET Conference Publications*, vol. 2013, no. 621 CP, pp. 1–6, 2013.

[81] A. Rodríguez, G. L. Plett, and M. S. Trimboli, "Comparing four model-order reduction techniques, applied to lithium-ion battery-cell internal electrochemical transfer functions," *eTransportation*, vol. 1, p. 100009, 2019. [Online]. Available: https://doi.org/10.1016/j.etran.2019.100009

[82] S. G. Marquis, V. Sulzer, R. Timms, C. P. Please, and S. J. Chapman, "An Asymptotic Derivation of a Single Particle Model with Electrolyte," *Journal of The Electrochemical Society*, vol. 166, no. 15, nov 2019.

[83] Y. Li, D. Ralahamilage, M. Vilathgamuwa, Y. Mishra, T. Farrell, S. S. Choi, and C. Zou, "Model Order Reduction Techniques for Physics-Based Lithium-Ion Battery Management: A Survey," *IEEE Industrial Electronics Magazine*, pp. 2–18, 2021.

[84] S. Atlung, K. West, and T. Jacobsen, "Dynamic aspects of solid solution cathodes for electrochemical power sources," *Journal of The Electrochemical Society*, vol. 126, no. 8, pp. 1311–1321, 1979.

[85] P. Kemper and D. Kum, "Extended single particle model of li-ion batteries towards high current applications," *2013 9th IEEE Vehicle Power and Propulsion Conference, IEEE VPPC 2013*, pp. 158–163, 2013.

[86] S. Khaleghi Rahimian, S. Rayman, and R. E. White, "Extension of physics-based single particle model for higher charge-discharge rates," *Journal of Power Sources*, vol. 224, pp. 180–194, 2013. [Online]. Available: http://dx.doi.org/10.1016/j.jpowsour.2012.09.084

[87] J. Li, N. Lotfi, R. G. Landers, and J. Park, "A Single Particle Model for Lithium-Ion Batteries with Electrolyte and Stress-Enhanced Diffusion Physics," *Journal of The Electrochemical Society*, vol. 164, no. 4, pp. A874–A883, 2017.

[88] X. Han, M. Ouyang, L. Lu, and J. Li, "Simpli fi cation of physics-based electrochemical model for lithium ion battery on electric vehicle . Part II : Pseudo-two-dimensional model simpli fi cation and state of charge estimation," *Journal of Power Sources*, vol. 278, pp. 814–825, 2015. [Online]. Available: http://dx.doi.org/10.1016/j.jpowsour.2014.08.089

[89] H. E. Perez, S. Dey, X. Hu, and S. J. Moura, "Optimal Charging of Li-Ion Batteries via a Single Particle Model with Electrolyte and Thermal Dynamics," *Journal ofThe Electrochemical Society*, vol. 164, no. 7, pp. 1679–1687, 2017.

[90] S. J. Moura, F. B. Argomedo, R. Klein, A. Mirtabatabaei, and M. Krstic, "Battery State Estimation for a Single Particle Model With Electrolyte Dynamics," *IEEE Transactions on Control Systems Technology*, vol. 25, no. 2, mar 2017.

[91] G. Richardson, I. Korotkin, R. Ranom, M. Castle, and J. M. Foster, "Generalised single particle models for high-rate operation of graded lithium-ion electrodes : Systematic derivation and validation," *Electrochimica Acta*, vol. 339, 2020. [Online]. Available: https://doi.org/10.1016/j.electacta.2020.135862

[92] C. M. Bender and S. A. Orszag, *Advanced mathematical methods for scientists and engineers I: Asymptotic methods and perturbation theory.* Springer Science & Business Media, 2013.

[93] M. Doyle, T. Fuller, and J. Newman, "Modeling of galvanostatic charge and discharge of the lithium/ polymer/insertion cell," *Journal of the Electrochemical Society*, vol. 140, no. 6, pp. 1526–1533, 1993.

[94] M. Doyle and J. Newman, "The use of mathematical modeling in the design of lithium/polymer battery systems," *Electrochimica Acta*, vol. 40, no. 13-14, pp. 2191–2196, 1995.

[95] T. F. Fuller, M. Doyle, and J. Newman, "Simulation and Optimization of the Dual Lithium Ion Insertion Cell," *Journal of the Electrochemical Society*, vol. 141, no. 1, pp. 1–10, 1994.

[96] J. Newman and W. Tiedemann, "Porous-electrode theory with battery applications. [Porous-electrode theory with applications to batteries (and fuel cells)]," *AIChE J.; (United States)*, vol. 21, pp. 25–41, 1975.

[97] K. H. Xue and G. L. Plett, "A convective transport theory for high rate discharge in lithium ion cells," *Electrochimica Acta*, vol. 87, pp. 575–590, 2013. [Online]. Available: http://dx.doi.org/10.1016/j.electacta.2012.09.109

[98] A. Falconi, "Electrochemical Li-Ion battery modeling for electric vehicles," Ph.D. dissertation, Communaute Universite Grenoble Alpes, 2017.

[99] L. Oca, "Pouch cell fabrication process optimisation through physico-chemical modelling and characterisation," Ph.D. dissertation, Mondragon Unibertsitatea, 2020.

[100] E. Miguel, G. L. Plett, M. S. Trimboli, L. Oca, U. Iraola, and E. Bekaert, "Review of computational parameter estimation methods for electrochemical models," *Journal of Energy Storage*, vol. 44, p. 103388, 2021. [Online]. Available: https://doi.org/10.1016/j.est.2021.103388

[101] V. D. A. G. Bruggeman, "Berechnung verschiedener physikalischer Konstanten von heterogenen Substanzen. I. Dielektrizitätskonstanten und Leitfähigkeiten der Mischkörper aus isotropen Substanzen," *Annalen der physik*, vol. 416, no. 7, pp. 636–664, 1935.

[102] T. G. Zavalis, "Mathematical Models for Investigation of Performance, Safety, and Aging in Lithium-Ion Batteries," Ph.D. dissertation, Royal Institute of Technology KTH, 2013.

[103] W. B. Gu and C. Y. Wang, "Thermal-electrochemical modeling of battery systems," *Journal of the Electrochemical Society*, vol. 147, no. 8, pp. 2910–2922, 2000.

[104] M. Ecker, T. K. D. Tran, P. Dechent, S. Kabitz, A. Warnecke, and D. U. Sauer, "Parameterization of a Physico-Chemical Model of a Lithium-Ion Battery: I. Determination of Parameters," *J. Electrochem. Soc.*, vol. 162, no. 9, pp. A1836–A1848, 2015.

[105] D. R. Baker and M. W. Verbrugge, "Intercalate Diffusion in Multiphase Electrode Materials and Application to Lithiated Graphite," *Journal of the Electrochemical Society*, vol. 159, no. 8, pp. A1341–A1350, 2012.

[106] G. Fan, K. Pan, and M. Canova, "A comparison of model order reduction techniques for electrochemical characterization of Lithium-ion batteries," *Proceedings of the IEEE Conference on Decision and Control*, vol. 54rd IEEE, pp. 3922–3931, 2015.

[107] F. Chinesta, A. Ammar, A. Leygue, and R. Keunings, "An overview of the proper generalized decomposition with applications in computational rheology," *Journal of Non-Newtonian Fluid Mechanics*, vol. 166, no. 11, pp. 578–592, 2011.

[108] E. Jané, R. Medeiros, F. Varas, and M. Higuera, "A time-adaptive order reduction technique for the doyle-fuller-newman electrochemical model of lithium-ion batteries," *Journal of The Electrochemical Society*, vol. 170, no. 3, p. 030539, 2023.

[109] J. L. Lee, A. Chemistruck, and G. L. Plett, "One-dimensional physics-based reduced-order model of lithium-ion dynamics," *Journal of Power Sources*, vol. 220, pp. 430–448, 2012. [Online]. Available: http://dx.doi.org/10.1016/j.jpowsour.2012.07.075

[110] A. Rodríguez, G. L. Plett, and M. S. Trimboli, "Improved transfer functions modeling linearized lithium-ion battery-cell internal electrochemical variables," *Journal of Energy Storage*, vol. 20, no. April, pp. 560–575, 2018. [Online]. Available: https://doi.org/10.1016/j.est.2018.06.015

[111] J. C. Forman, S. Bashash, J. L. Stein, and H. K. Fathy, "Reduction of an electrochemistry-based li-ion battery model via quasi-linearization and Padé approximation," *Journal of the Electrochemical Society*, vol. 158, no. 2, 2011.

[112] N. T. Tran, M. Vilathgamuwa, T. Farrell, S. S. Choi, Y. Li, and J. Teague, "A Padé Approximate Model of Lithium Ion Batteries," *Journal of The Electrochemical Society*, vol. 165, no. 7, pp. A1409–A1421, 2018.

[113] T. S. Dao, C. P. Vyasarayani, and J. McPhee, "Simplification and order reduction of lithium-ion battery model based on porous-electrode theory," *Journal of Power Sources*, vol. 198, pp. 329–337, 2012. [Online]. Available: http://dx.doi.org/10.1016/j.jpowsour.2011.09.034

[114] G. Fan, X. Li, and M. Canova, "A reduced-order electrochemical model of li-ion batteries for control and estimation applications," *IEEE Transactions on Vehicular Technology*, vol. 67, no. 1, pp. 76–91, 2018.

[115] A. Bizeray, "State and parameter estimation of physics-based lithium-ion battery models," Ph.D. dissertation, University of Oxford, 2016. [Online]. Available: https://ora.ox.ac.uk/catalog/uuid:f326b332-b912-4bf6-a9b3-d5e61d3a9596/download_file?file_format=pdf&safe_filename=DPhil_Thesis___Adrien_M_Bizeray.pdf&type_of_work=Thesis

[116] A. Barré, B. Deguilhem, S. Grolleau, M. Gérard, F. Suard, and D. Riu, "A review on lithium-ion battery ageing mechanisms and estimations for automotive applications," *Journal of Power Sources*, vol. 241, pp. 680–689, 2013. [Online]. Available: http://dx.doi.org/10.1016/j.jpowsour.2013.05.040

[117] M. Dubarry, C. Truchot, and B. Y. Liaw, "Synthesize battery degradation modes via a diagnostic and prognostic model," *Journal of power sources*, vol. 219, pp. 204–216, 2012.

[118] M. Dubarry and D. Anseán, "Best practices for incremental capacity analysis," *Frontiers in Energy Research*, vol. 10, p. 1023555, 2022.

[119] C. R. Birkl, M. R. Roberts, E. McTurk, P. G. Bruce, and D. A. Howey, "Degradation diagnostics for lithium ion cells," *Journal of Power Sources*, vol. 341, pp. 373–386, 2017. [Online]. Available: http://dx.doi.org/10.1016/j.jpowsour.2016.12.011

[120] J. Vetter, P. Novák, M. R. Wagner, C. Veit, K. C. Möller, J. O. Besenhard, M. Winter, M. Wohlfahrt-Mehrens, C. Vogler, and A. Hammouche, "Ageing mechanisms in lithium-ion batteries," *Journal of Power Sources*, vol. 147, pp. 269–281, 2005.

[121] C. R. Birkl, E. McTurk, M. R. Roberts, P. G. Bruce, and D. A. Howey, "A parametric open circuit voltage model for lithium ion batteries," *Journal of the Electrochemical Society*, vol. 162, no. 12, pp. A2271–A2280, 2015.

[122] M. M. Kabir and D. E. Demirocak, "Degradation mechanisms in Li-ion batteries: a state-of-the-art review," *International Journal of Energy Research*, vol. 41, no. 14, pp. 1963–1986, 2017. [Online]. Available: https://onlinelibrary.wiley.com/doi/abs/10.1002/er.3762

[123] J. P. Pender, G. Jha, D. H. Youn, J. M. Ziegler, I. Andoni, E. J. Choi, A. Heller, B. S. Dunn, P. S. Weiss, R. M. Penner, and C. B. Mullins, "Electrode Degradation in Lithium-Ion Batteries," *ACS Nano*, vol. 14, no. 2, pp. 1243–1295, 2020. [Online]. Available: https://doi.org/10.1021/acsnano.9b04365

[124] S. N. S. Hapuarachchi, Z. Sun, and C. Yan, "Advances in In Situ Techniques for Characterization of Failure Mechanisms of Li-Ion Battery Anodes," *Advanced Sustainable Systems*, vol. 1700182, pp. 1–29, 2018.

[125] M. Woody, M. Arbabzadeh, G. M. Lewis, G. A. Keoleian, and A. Stefanopoulou, "Strategies to limit degradation and maximize Li-ion battery service lifetime - Critical review and guidance for stakeholders," *Journal of Energy Storage*, vol. 28, no. January, p. 101231, 2020. [Online]. Available: https://doi.org/10.1016/j.est.2020.101231

[126] B. Horstmann, F. Single, and A. Latz, "Review on multi-scale models of solid-electrolyte interphase formation," *Current Opinion in Electrochemistry*, vol. 13, pp. 61–69, 2019. [Online]. Available: https://doi.org/10.1016/j.coelec.2018.10.013

[127] X. Zhao, Y. Yin, Y. Hu, and S.-y. Choe, "Electrochemical-thermal modeling of lithium plating / stripping of Li temperatures," *Journal of Power Sources*, vol. 418, no. January, pp. 61–73, 2019. [Online]. Available: https://doi.org/10.1016/j.jpowsour.2019.02.001

[128] E. Peled, "The Electrochemical Behavior of Alkali and Alkaline Earth Metals in Nonaqueous Battery Systems—The Solid Electrolyte Interphase Model," *Journal of The Electrochemical Society*, vol. 126, no. 12, pp. 2047–2051, 1979.

[129] T. Liu, L. Lin, X. Bi, L. Tian, K. Yang, J. Liu, M. Li, Z. Chen, J. Lu, K. Amine, K. Xu, and F. Pan, "In situ quantification of interphasial chemistry in Li-ion battery," *Nature Nanotechnology*, vol. 14, no. 1, pp. 50–56, 2019. [Online]. Available: http://dx.doi.org/10.1038/s41565-018-0284-y

[130] F. Single, B. Horstmann, and A. Latz, "Revealing SEI Morphology: In-Depth Analysis of a Modeling Approach," *Journal of The Electrochemical Society*, vol. 164, no. 11, pp. E3132–E3145, 2017.

[131] M. Petzl and M. A. Danzer, "Nondestructive detection, characterization, and quantification of lithium plating in commercial lithium-ion batteries," *Journal of Power Sources*, vol. 254, pp. 80–87, 2014. [Online]. Available: http://dx.doi.org/10.1016/j.jpowsour.2013.12.060

[132] M. C. Smart and B. V. Ratnakumar, "Effects of Electrolyte Composition on Lithium Plating in Lithium-Ion Cells," *Journal of The Electrochemical Society*, vol. 158, no. 4, pp. A379–A389, 2011.

[133] M. Dubarry, N. Qin, and P. Brooker, "Calendar aging of commercial Li-ion cells of different chemistries – A review," *Current Opinion in Electrochemistry*, vol. 9, pp. 106–113, 2018. [Online]. Available: https://doi.org/10.1016/j.coelec.2018.05.023

[134] J. Keil, N. Paul, V. Baran, P. Keil, R. Gilles, and A. Jossen, "Linear and Nonlinear Aging of Lithium-Ion Cells Investigated by Electrochemical Analysis and In-Situ Neutron Diffraction," *Journal of The Electrochemical Society*, vol. 166, no. 16, pp. A3908–A3917, 2019.

[135] J. Wandt, P. Jakes, J. Granwehr, R.-a. Eichel, and H. A. Gasteiger, "Quantitative and time-resolved detection of lithium plating on graphite anodes in lithium ion batteries," *Materials Today*, vol. 21, no. 3, pp. 231–240, 2018. [Online]. Available: https://doi.org/10.1016/j.mattod.2017.11.001

[136] M. Ebner, F. Marone, M. Stampanoni, and V. Wood, "Visualization and quantification of electrochemical and mechanical degradation in li ion batteries," *Science*, vol. 342, no. 6159, pp. 716–720, 2013.

[137] W. Ai, L. Kraft, J. Sturm, A. Jossen, and B. Wu, "Electrochemical Thermal-Mechanical Modelling of Stress Inhomogeneity in Lithium-Ion Pouch Cells," *Journal of The Electrochemical Society*, vol. 167, no. 1, p. 013512, 2020.

[138] P. Li, Y. Zhao, Y. Shen, and S. H. Bo, "Fracture behavior in battery materials," *JPhys Energy*, vol. 2, no. 2, 2020.

[139] R. Xu, Y. Yang, F. Yin, P. Liu, P. Cloetens, Y. Liu, F. Lin, and K. Zhao, "Heterogeneous damage in Li-ion batteries: Experimental analysis and theoretical modeling," *Journal of the Mechanics and Physics of Solids*, vol. 129, no. 2019, pp. 160–183, 2020. [Online]. Available: https://doi.org/10.1016/j.jmps.2019.05.003

[140] S. Watanabe, M. Kinoshita, T. Hosokawa, K. Morigaki, and K. Nakura, "Capacity fading of LiAlyNi1-x-yCoxO 2 cathode for lithium-ion batteries during accelerated calendar and cycle life tests (effect of depth of discharge in charge-discharge cycling on the suppression of the micro-crack generation of LiAlyNi 1-x-yCoxO2 parti," *Journal of Power Sources*, vol. 260, pp. 50–56, 2014. [Online]. Available: http://dx.doi.org/10.1016/j.jpowsour.2014.02.103

[141] H. H. Ryu, K. J. Park, C. S. Yoon, and Y. K. Sun, "Capacity fading of ni-rich li[NixCoyMn1-x-y]O2 ($0.6 \leq x \leq 0.95$) Cathodes for High-Energy-Density Lithium-Ion Batteries: Bulk or Surface Degradation?" *Chemistry of Materials*, vol. 30, no. 3, pp. 1155–1163, 2018.

[142] R. D. Deshpande and D. M. Bernardi, "Modeling Solid-Electrolyte Interphase (SEI) Fracture: Coupled Mechanical/Chemical Degradation of the Lithium Ion Battery," *Journal of The Electrochemical Society*, vol. 164, no. 2, pp. A461–A474, 2017.

[143] J. Li, R. G. Landers, and J. Park, "A comprehensive single-particle-degradation model for battery state-of-health prediction," *Journal of Power Sources*, vol. 456, p. 227950, 2020.

[144] X. Jin, A. Vora, V. Hoshing, T. Saha, G. Shaver, O. Wasynczuk, and S. Varigonda, "Applicability of available li-ion battery degradation models for system and control algorithm design," *Control Engineering Practice*, vol. 71, pp. 1–9, 2018.

[145] J. Keil and A. Jossen, "Electrochemical modeling of linear and nonlinear aging of lithium-ion cells," *Journal of The Electrochemical Society*, vol. 167, no. 11, p. 110535, 2020.

[146] G. Dong and J. Wei, "A physics-based aging model for lithium-ion battery with coupled chemical/mechanical degradation mechanisms," *Electrochimica Acta*, vol. 395, p. 139133, 2021.

[147] S. Bhattacharya, A. R. Riahi, and A. T. Alpas, "Thermal cycling induced capacity enhancement of graphite anodes in lithium-ion cells," *Carbon*, vol. 67, pp. 592–606, 2014. [Online]. Available: https://www.sciencedirect.com/science/article/pii/S0008622313009792

[148] E. Gucciardi, F. Torre, M. A. Cabañero, L. Oca, and E. Bekaert, "A direct method to quantify lithium plating on graphite negative electrode of commercial li-ion cells," *Electrochemistry Communications*, vol. 151, p. 107496, 2023.

[149] S. Fernandez, I. Lopetegi, L. Oca, J. Yeregui, E. Garayalde, and U. Iraola, "Intuitive degradation mode estimation tool: Modest," in *2024 IEEE Energy Conversion Congress & Expo (ECCE)*, 2024. - Under review.

[150] F. B. Planella and W. D. Widanage, "A Single Particle Model with Electrolyte and Side Reactions for degradation of lithium-ion batteries," *Appl. Math. Model.*, 2022.

[151] F. Single, A. Latz, and B. Horstmann, "Identifying the Mechanism of Continued Growth of the Solid–Electrolyte Interphase," *ChemSusChem*, vol. 11, no. 12, pp. 1950–1955, 2018.

[152] M. Tang, S. Lu, and J. Newman, "Experimental and Theoretical Investigation of Solid-Electrolyte-Interphase Formation Mechanisms on Glassy Carbon," *Journal of The Electrochemical Society*, vol. 159, no. 11, pp. A1775–A1785, 2012.

[153] X. Zhang, W. Shyy, and A. Marie Sastry, "Numerical Simulation of Intercalation-Induced Stress in Li-Ion Battery Electrode Particles," *J. Electrochem. Soc.*, vol. 154, no. 10, p. A910, 2007.

[154] R. Deshpande, M. Verbrugge, Y.-T. Cheng, J. Wang, and P. Liu, "Battery Cycle Life Prediction with Coupled Chemical Degradation and Fatigue Mechanics," *J. Electrochem. Soc.*, vol. 159, no. 10, pp. A1730–A1738, 2012.

[155] P. Paris and F. Erdogan, "A critical analysis of crack propagation laws," *Journal of Basic Engineering*, 1963.

[156] F. M. Kindermann, J. Keil, A. Frank, and A. Jossen, "A SEI Modeling Approach Distinguishing between Capacity and Power Fade," *Journal of The Electrochemical Society*, vol. 164, no. 12, pp. E287–E294, 2017.

[157] P. M. Attia, A. Bills, F. B. Planella, P. Dechent, G. dos Reis, M. Dubarry, P. Gasper, R. Gilchrist, S. Greenbank, D. Howey, O. Liu, E. Khoo, Y. Preger, A. Soni, S. Sripad, A. G. Stefanopoulou, and V. Sulzer, "Review—"knees" in lithium-ion battery aging trajectories," *Journal of The Electrochemical Society*, vol. 169, no. 6, p. 060517, jun 2022. [Online]. Available: https://dx.doi.org/10.1149/1945-7111/ac6d13

[158] F. B. Planella, M. Sheikh, and W. D. Widanage, "Systematic derivation and validation of a reduced thermal-electrochemical model for lithium-ion batteries using asymptotic methods," *Electrochimica Acta*, vol. 388, p. 138524, 2021.

[159] S. J. Moura, N. A. Chaturvedi, and M. Krstić, "Adaptive partial differential equation observer for battery state-of-charge/state-of-health estimation via an electrochemical model," *Journal of Dynamic Systems, Measurement and Control, Transactions of the ASME*, vol. 136, no. 1, pp. 1–11, 2014.

[160] S. Dey, B. Ayalew, and P. Pisu, "Combined estimation of State-of-Charge and State-of-Health of Li-ion battery cells using SMO on electrochemical model," in *2014 13th International Workshop on Variable Structure Systems (VSS)*. IEEE, jun 2014, pp. 1–6. [Online]. Available: http://ieeexplore.ieee.org/document/6881140/

[161] ——, "Nonlinear Robust Observers for State-of-Charge Estimation of Lithium-Ion Cells Based on a Reduced Electrochemical Model," *IEEE Transactions on Control Systems Technology*, vol. 23, no. 5, pp. 1935–1942, 2015.

[162] A. Bartlett, J. Marcicki, S. Onori, G. Rizzoni, X. G. Yang, and T. Miller, "Electrochemical Model-Based State of Charge and Capacity Estimation for a Composite Electrode Lithium-Ion Battery," *IEEE Transactions on Control Systems Technology*, vol. 24, no. 2, pp. 384–399, 2016.

[163] D. Simon, *Optimal state estimation: Kalman, H infinity, and nonlinear approaches*. John Wiley & Sons, 2006.

[164] R. Hermann and A. Krener, "Nonlinear controllability and observability," *IEEE Transactions on automatic control*, vol. 22, no. 5, pp. 728–740, 1977.

[165] F. M. Ham, *Determination of the degree of observability in linear control systems*. Iowa State University, 1980.

[166] G. H. Florentino, "Model predictive control implementations for management of lithium-ion battery cells and packs using reduced-order electrochemical models," Ph.D. dissertation, University of Colorado Colorado Springs. Kraemer Family Library, 2018.

[167] S. Lee, P. Mohtat, J. B. Siegel, and A. G. Stefanopoulou, "Beyond estimating battery state of health: Identifiability of individual electrode capacity and utilization," in *2018 Annual American Control Conference (ACC)*. IEEE, 2018, pp. 2288–2293.

[168] P. Mohtat, S. Lee, J. B. Siegel, and A. G. Stefanopoulou, "Towards better estimability of electrode-specific state of health: Decoding the cell expansion," *Journal of Power Sources*, vol. 427, pp. 101–111, 2019.

[169] S. Lee, J. B. Siegel, A. G. Stefanopoulou, J.-W. Lee, and T.-K. Lee, "Electrode State of Health Estimation for Lithium Ion Batteries Considering Half-cell Potential Change Due to Aging," *J. Electrochem. Soc.*, vol. 167, no. 9, p. 090531, 2020.

[170] G. Fan, D. Lu, M. S. Trimboli, G. L. Plett, C. Zhu, and X. Zhang, "Nondestructive diagnostics and quantification of battery aging under different degradation paths," *Journal of Power Sources*, vol. 557, p. 232555, 2023.

[171] W. Li, J. Chen, K. Quade, D. Luder, J. Gong, and D. U. Sauer, "Battery degradation diagnosis with field data, impedance-based modeling and artificial intelligence," *Energy Storage Materials*, vol. 53, pp. 391–403, 2022.

[172] N. Costa, D. Anseán, M. Dubarry, and L. Sánchez, "Icformer: A deep learning model for informed lithium-ion battery diagnosis and early knee detection," *Journal of Power Sources*, vol. 592, p. 233910, 2024.

[173] X. Lin, S. Wang, and Y. Kim, "A framework for charging strategy optimization using a physics-based battery model," *Journal of Applied Electrochemistry*, vol. 49, pp. 779–793, 2019.

[174] A. H. K. de Souza, "Physics-based modeling, estimation and control for lithium-ion and lithium-metal batteries," Ph.D. dissertation, University of Colorado Colorado Springs, 2023.

[175] L. Wang, *Model predictive control system design and implementation using MATLAB*. Springer, 2009, vol. 3.

[176] A. Tomaszewska, Z. Chu, X. Feng, S. O'kane, X. Liu, J. Chen, C. Ji, E. Endler, R. Li, L. Liu *et al.*, "Lithium-ion battery fast charging: A review," *ETransportation*, vol. 1, p. 100011, 2019.

[177] J. A. Weideman and S. C. Reddy, "A MATLAB differentiation matrix suite," *ACM Transactions on Mathematical Software*, vol. 26, no. 4, pp. 465–519, 2000.

[178] C. W. Clenshaw and A. R. Curtis, "A method for numerical integration on an automatic computer," *Numerische Mathematik*, vol. 2, no. 1, pp. 197–205, 1960.

[179] L. N. Trefethen, "Spectral methods in MATLAB, volume 10 of Software, Environments, and Tools," *Society for Industrial and Applied Mathematics (SIAM), Philadelphia, PA*, vol. 24, 2000.

[180] L. F. Shampine and M. W. Reichelt, "The MATLAB ode suite," *SIAM Journal of Scientific Computing*, vol. 18, no. 1, pp. 1–22, 1997.

[181] M. Doyle, J. Newman, A. S. Gozdz, C. N. Schmutz, and J.-M. Tarascon, "Comparison of Modeling Predictions with Experimental Data from Plastic Lithium Ion Cells," *J. Electrochem. Soc.*, vol. 143, no. 6, pp. 1890–1903, 1996.